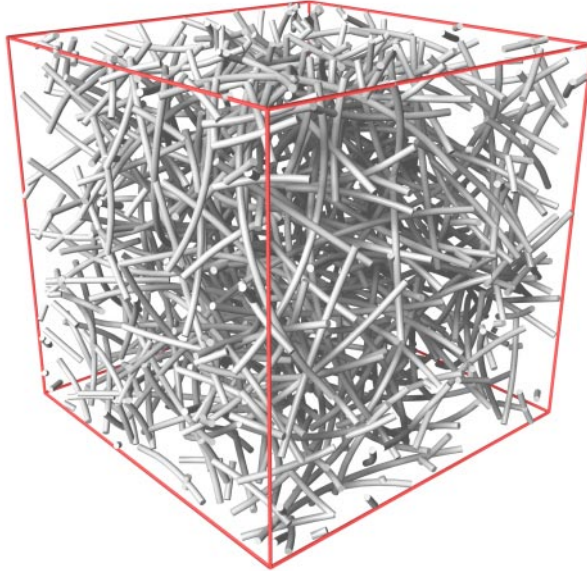




**LUND**  
UNIVERSITY



# **NETWORK MODELLING FOR THE EVALUATION OF MECHANICAL PROPERTIES OF CELLULOSE FIBRE FLUFF**

SUSANNE HEYDEN

Department  
of  
Mechanics  
and  
Materials

Structural Mechanics

*Doctoral Thesis*

*Department of Mechanics and Materials*  
Structural Mechanics

ISRN LUTVDG/TVSM--00/1011--SE (1-208)  
ISBN 91-7874-076-2 ISSN 0281-6679

NETWORK MODELLING FOR  
THE EVALUATION OF MECHANICAL  
PROPERTIES OF CELLULOSE FIBRE FLUFF

Doctoral Thesis by  
SUSANNE HEYDEN

Copyright © 2000 by Structural Mechanics, LTH, Sweden.  
Printed by KFS i Lund AB, Lund, Sweden, March 2000.

For information, address:  
Division of Structural Mechanics, LTH, Lund University, Box 118, SE-221 00 Lund, Sweden.  
Homepage: <http://www.byggmek.lth.se>

# ACKNOWLEDGEMENTS

The research presented in this thesis was carried out at the Division of Structural Mechanics, Department of Mechanics and Materials, Lund University. The work was carried out within the framework of the Forest Products Industry Research College (FPIRC). Financial support from the Foundation for Strategic Research (the Forest Products Industry Research College Programme), Bo Rydin's Foundation for Scientific Research and the Swedish National Board for Industrial and Technical Development (NUTEK), is gratefully acknowledged.

I would like to thank my supervisor, Dr Per Johan Gustafsson, for his excellent guidance and support during the course of this work. He has supplied numerous ideas, has remarkable scientific intuition and is always enthusiastic.

The industrial partners in this project were SCA Research AB and Mölnlycke AB, and I am grateful for the ideas, information and comments which their representatives have supplied.

Thanks are also due to Jonas Lindemann, for help with the visualisation, to Mats Gustavsson, for sharing a solver interface, to Christer Nilsson, for interesting discussions, to Per-Anders Wernberg, Kent Persson and Peter Davidsson, for general help with the computer system, and to Bo Zadig, for his skilful drawing of the more complicated figures. I would also like to thank my other colleagues at the Division of Structural Mechanics for their support.

Finally, I wish to express my gratitude to Anders for always being there.

Lund, March 2000

Susanne Heyden



# ABSTRACT

A network mechanics model for cellulose fibre fluff is proposed. 2D and 3D versions of the model have been implemented and the influence of various micro-level parameters on the global mechanical performance has been determined by means of computer simulations.

Model networks composed of bonded fibres of arbitrary distribution in length, curvature, cross-section, stiffness and strength were investigated. The bonds were modelled as non-linear coupling elements representing stick-slip performance. The bonds were arbitrarily distributed in stiffness and strength. The fibres were arranged in a random structure according to an arbitrary orientation distribution. The network geometry was periodic, enabling a cell under observation to be regarded as one of many identical cells making up a global structure. Periodic boundary and loading conditions were used to obtain relevant results, even in the case of small network cells. The networks were analysed by means of the finite element method, and homogenized mechanical properties such as stress versus strain performance, initial anisotropic 2D and 3D stiffness properties, strength and fracture energy were calculated. Fracture localization and geometric quantities, such as the number of bonds and active part were also studied.

Simulations showed that a cell 1.2 times the fibre length is sufficient for calculation of the initial stiffness values. The dependence of initial stiffness on fibre and bond stiffness, network density, fibre curl, fibre orientation and fibre length was studied. Fracture simulations showed that bond ductility is a very important parameter for 2D networks, giving a stronger and more ductile network. The influence on fracture of network density, fibre length and fibre orientation distribution was also examined. A comparison was made between 3D network simulation results and experimental results for cellulose fibre fluff. Reasonable agreement was observed up to peak stress. Analysis of the post-peak stress performance requires that size dependence due to strain localization and heterogeneity in the material, be taken into consideration.

The models enable systematic analysis and design of network structures. The 2D version has the advantage of requiring less computer capacity, but in order to be able to draw quantitative conclusions regarding cellulose fibre fluff it is advisable to use the 3D version.

**Keywords:** network mechanics, fibre network, cellulose fibres, fracture, stiffness, computer simulation, 3D model



# CONTENTS

<b>1</b>	<b>Introduction</b>	<b>1</b>
1.1	General remarks . . . . .	1
1.2	Aim and scope of the investigation . . . . .	3
1.3	Organisation of this thesis . . . . .	5
1.4	Notations . . . . .	6
<b>2</b>	<b>Earlier cellulose fibre network mechanics modelling</b>	<b>9</b>
2.1	Geometry models . . . . .	9
2.2	Uniform strain models . . . . .	10
2.3	Semi-analytical models . . . . .	15
2.4	Computer simulations . . . . .	16
<b>3</b>	<b>The model</b>	<b>21</b>
3.1	Fibres . . . . .	21
3.2	Inter-fibre bonds . . . . .	24
3.2.1	Bond model consisting of coupled springs . . . . .	24
3.2.2	Bond model consisting of uncoupled springs . . . . .	27
3.3	Network cell geometry . . . . .	27
3.4	Remarks on heterogeneity and periodic geometry . . . . .	31
<b>4</b>	<b>Generation and analysis of geometry</b>	<b>33</b>
4.1	Input data . . . . .	33
4.2	Generation of network geometry . . . . .	34
4.3	Analysis of network geometry . . . . .	37
4.4	Output from geometry unit . . . . .	39
<b>5</b>	<b>Results of geometry analysis</b>	<b>41</b>
5.1	Basic example networks . . . . .	41
5.2	Number of fibre crossings . . . . .	48
5.3	Percolation and the active part of a network . . . . .	51
<b>6</b>	<b>FEM model and analysis of initial stiffness</b>	<b>55</b>
6.1	Element stiffness matrices . . . . .	55
6.1.1	Beam elements . . . . .	56
6.1.2	Bond elements . . . . .	62
6.1.3	Transformation to global coordinates . . . . .	65

6.2	Methods of applying strain . . . . .	65
6.3	Solution of the system of equations . . . . .	67
6.4	Evaluation of resultant forces and D matrix . . . . .	69
6.5	Anisotropic, orthotropic and isotropic materials . . . . .	70
6.6	Approximation of a near isotropic D matrix . . . . .	73
6.7	Approximation of a near orthotropic D matrix . . . . .	79
<b>7</b>	<b>Results from the analysis of initial global stiffness properties</b>	<b>83</b>
7.1	Effect of boundary conditions and sample size . . . . .	83
7.2	Global elastic stiffness vs stiffness of components . . . . .	89
7.3	Global elastic stiffness vs network density and degree of fibre-to-fibre interaction . . . . .	95
7.4	Global elastic stiffness vs fibre curl . . . . .	98
7.5	Global elastic stiffness vs orientation distribution . . . . .	102
7.6	Global elastic stiffness vs length distribution . . . . .	108
<b>8</b>	<b>Analysis of the fracture process</b>	<b>113</b>
8.1	Input parameters for fracture analysis . . . . .	113
8.2	Method of analysis . . . . .	115
8.3	Output parameters from fracture analysis . . . . .	119
<b>9</b>	<b>Results from the analysis of the fracture process</b>	<b>127</b>
9.1	Fracture in 2D networks . . . . .	127
9.1.1	Effect of sample size . . . . .	127
9.1.2	Fracture of an example network . . . . .	134
9.1.3	Influence of properties of bonds . . . . .	140
9.1.4	Influence of network density . . . . .	148
9.1.5	Simulation of complex 2D example network . . . . .	152
9.2	Fracture in 3D networks . . . . .	157
9.2.1	Influence of network density . . . . .	157
9.2.2	Influence of fibre orientation . . . . .	159
9.2.3	Influence of properties of bonds . . . . .	161
9.2.4	Influence of fibre length . . . . .	163
9.2.5	Comparison with experimental results . . . . .	168
<b>10</b>	<b>Numerical considerations</b>	<b>175</b>
10.1	Correctness of solutions . . . . .	175
10.2	Speed of simulations . . . . .	176
<b>11</b>	<b>Concluding remarks</b>	<b>177</b>
11.1	Summary and conclusions . . . . .	177
11.2	Future developments . . . . .	179
<b>A</b>	<b>Generation of fibres</b>	<b>181</b>

<b>B</b>	<b>Analysis of connectedness of networks</b>	<b>185</b>
<b>C</b>	<b>Effective bending stiffness of a spiral beam</b>	<b>189</b>
<b>D</b>	<b>Transformation of the D matrix</b>	<b>191</b>
	<b>References</b>	<b>195</b>



# 1. INTRODUCTION

## 1.1. General remarks

Cellulose fibres are in general obtained by defibration of wood, by either chemical, mechanical or combined chemical-mechanical processing. A major part of the pulp is used for making paper, which is manufactured by forming the wet fibres into sheets. Another important product made from pulp is dry-shaped cellulose fibre fluff, see Figures 1.1 and 1.2. This kind of material is produced by blowing the fibres, in a dry condition, into the desired shape. The result is a material used mainly in disposable nappies and health-care products. It is also possible to blow the fibres together with an adhesive aerosol. In this case, the bonds between the fibres are stronger, and fields of application include insulation boards and various moulded products, the latter being of higher density.

The main functions of some of the products mentioned above are the absorption of liquid or the prevention of heat transfer, but it is of course also necessary that they can withstand the mechanical load to which they are subjected when in use. This study deals with the mechanical properties of dry-shaped cellulose fibre materials, and examines which factors are of importance for mechanical properties such as stiffness, strength, strain localization and fracture process of a cellulose fibre fluff.

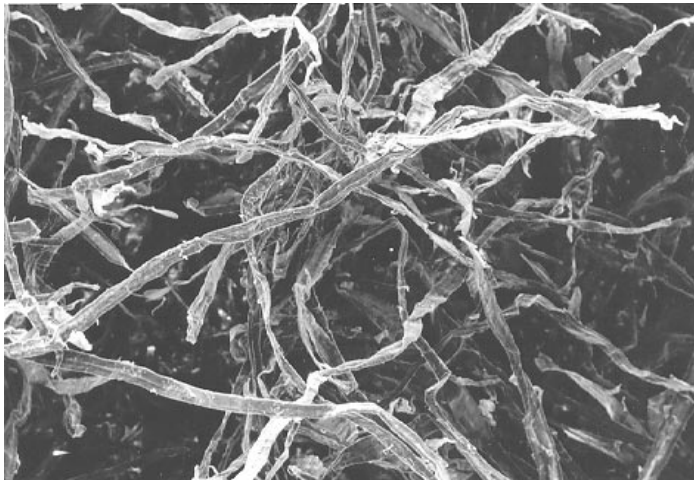


Figure 1.1: *Cellulose fibre fluff seen in a microscope.*

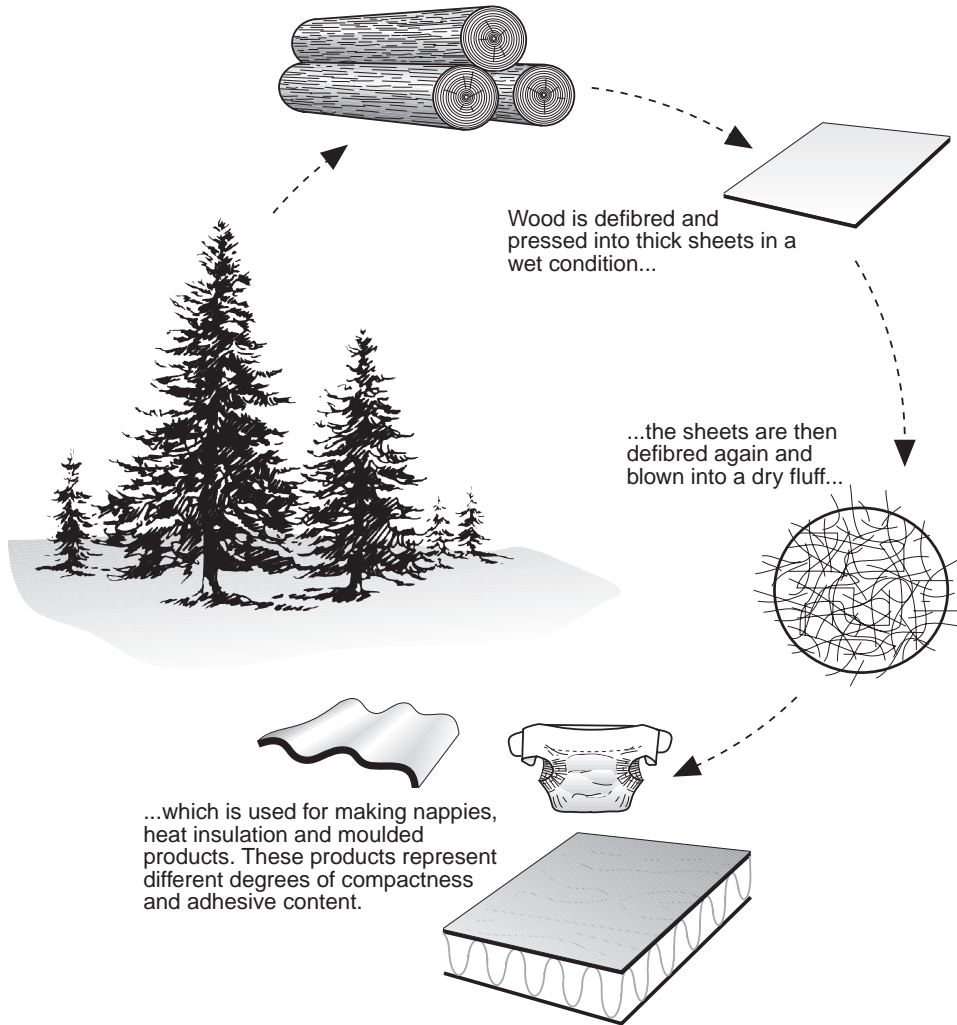


Figure 1.2: *Dry-shaped cellulose fibre fluff is made from wood, and is used for disposable nappies, insulation and moulded products.*

## 1.2. Aim and scope of the investigation

Due to strong competition, the absorbent-product industry is very research intensive. The need within this industry for methods for the rational analysis of the mechanical behaviour of fibre materials has been emphasized. The aim of the present study was to develop a model that enables such mechanical and geometrical analysis of materials made of cellulose fibres.

Micro-mechanical modelling is an established concept within structural mechanics which consists of making assumptions regarding the properties and behaviour of the components of a material on a lower structural level, and thereby calculating the expected behaviour of the material on a higher structural level. The micro-mechanical model used in this work is a network model, which is particularly suitable for a material like cellulose fibre fluff due to its network character. In this study, assumptions are made regarding the fibres, inter-fibre bonds and network geometry, see Figure 1.3, partly from [60], and the properties on the continuum level are obtained by computer simulations.

A theoretical model of the fibre material is introduced in terms of fibres, inter-fibre bonds and the structure into which these are assembled. The model has been formulated and implemented in a two-dimensional as well as a three-dimensional version. The implementation involves two separate steps. First a network structure is generated according to prescribed statistical distributions of the various properties that define the micro-structure of the material. The resulting structure is then assumed to be subjected to strain, and the finite element method is used to obtain the global stiffness properties. Through introducing fracture criteria for fibres and bonds, non-linear simulation of the fracture process can be carried out.

Computer simulations allow relations to be obtained between parameters on the microlevel and the global level. The pertinent microlevel parameters include the length distribution, the orientation distribution, the geometrical and the constitutive properties of the fibres, the constitutive properties of the bonds, the degree of heterogeneity of the network and also the network density. The corresponding global characteristics can be divided into geometrical and mechanical properties. Interesting geometrical properties include the number of bonds and the percentage of the network that is active. Concerning the mechanics, practical interest is focused on the stiffness properties and on the fracture process, the latter involving strength, strain localization and softening. From the application point of view, strain localization is of particular interest, since it may initiate crumbling in the case of cyclic loading.

Particular attention is paid to the network size needed to obtain relevant computational results. The choice of boundary conditions is important in this context, and a concept of periodic geometry and boundary conditions is used in an effort to minimize the required network size, and thereby minimize the number of degrees of freedom.

Viscous effects and dynamic behaviour of the material are not dealt with in this study.

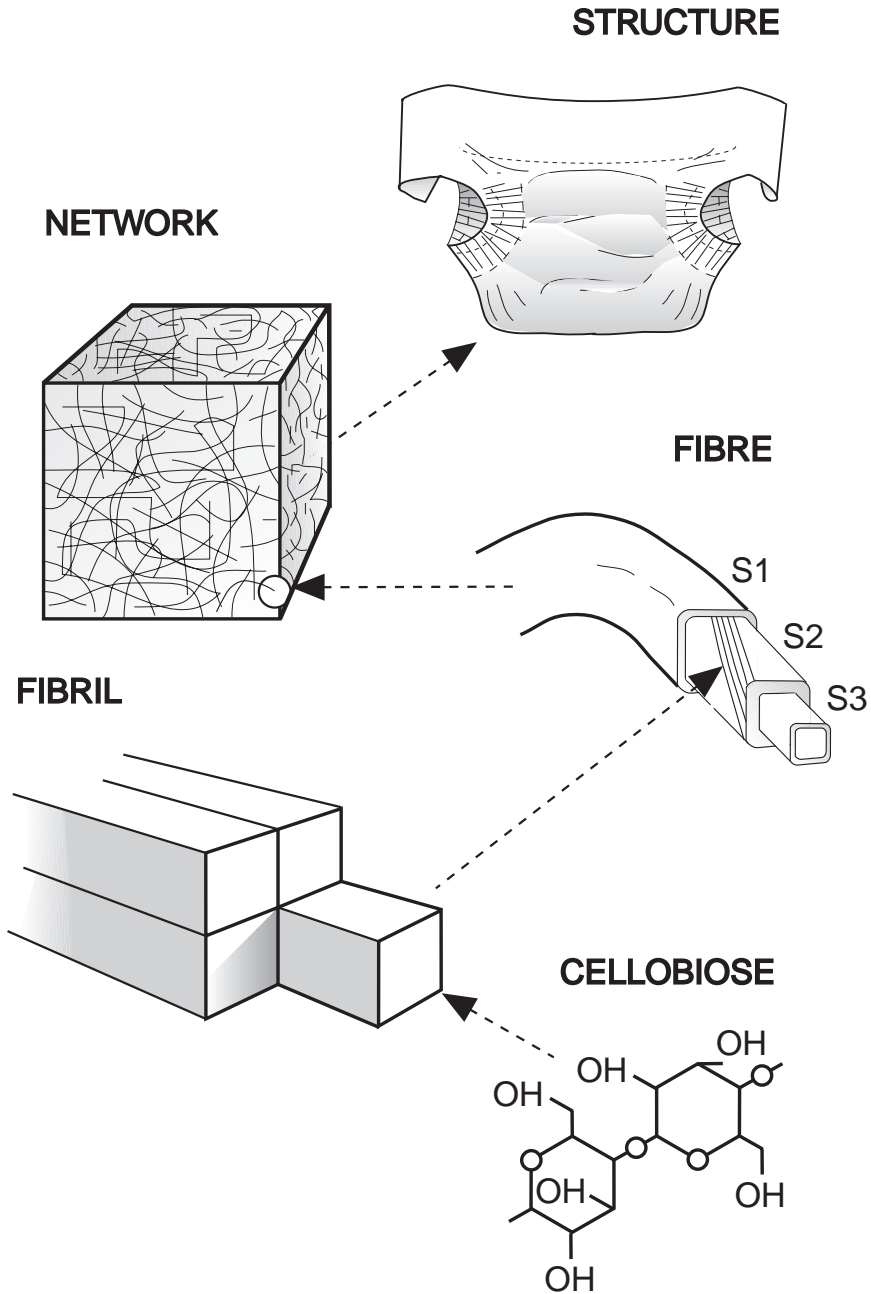


Figure 1.3: *Modelling and analysis can be performed at different structural levels. This study deals with the transition from the fibres to the network. Partly from [60].*

### 1.3. Organisation of this thesis

In Chapter 2 some earlier work on cellulose fibre network mechanics is summarized. This includes both analytical network modelling and computer simulations.

In Chapter 3 the proposed 2D and 3D models of fibre networks are presented. The parameters that define a network are listed and discussed.

Chapter 4 describes how a network is generated and prepared for the analysis of mechanical performance.

Chapter 5 presents results concerning the purely geometrical properties of a network, such as the number of bonds and the mechanically active part of the network.

In Chapter 6, methods for obtaining the global initial stiffness properties of a network are thoroughly discussed. Different boundary conditions are considered.

In Chapter 7, simulation results of global initial stiffness properties are presented, in terms of elastic modulus and Poisson's ratio of networks. These results illustrate how stiffness properties are affected by boundary conditions, network size, network density, stiffness properties of fibres and bonds, as well as curl, length and orientation distribution of the fibres.

Chapter 8 deals with the fracture process. Output parameters of interest are defined and discussed, and the methods used to obtain them are presented.

Chapter 9 presents results from the analysis of the fracture process. It is demonstrated how global parameters such as strength, fracture energy and localization depend on sample size, network density, properties of bonds and other micro-level parameters.

Chapter 10 contains a discussion of numerical aspects of the study, the problems that have arisen and how they have been solved.

Conclusions are presented and future plans are outlined in Chapter 11.

Finally, in Appendices A to D, some algorithms and calculations are given.

## 1.4. Notations

Notations are explained in the text when they first occur. In addition, a list of the main notations is given below, together with the corresponding SI units. Bold face is used to denote vector quantities. A barred letter denotes the arithmetic mean value of the parameter in question.

### Roman upper-case letters

$A_b$	area of bond	$[\text{m}^2]$
$A_f$	cross-sectional area of fibre	$[\text{m}^2]$
$\mathbf{D}$	constitutive matrix	$[\text{Pa}], [\text{N/m}]$
$D_{ij}$	element in row $i$ , column $j$ of $\mathbf{D}$	$[\text{Pa}], [\text{N/m}]$
$E$	homogenized elastic modulus for a network	$[\text{Pa}], [\text{N/m}]$
$E_f$	elastic modulus of fibre	$[\text{Pa}]$
$F_{ult}$	ultimate resultant force in bond	$[\text{N}]$
$G$	homogenized shear modulus for a network	$[\text{Pa}], [\text{N/m}]$
$G_F$	fracture energy of network, see Section 8.3	$[\text{Nm/m}], [\text{Nm/m}^2]$
$G_f$	shear modulus of fibre	$[\text{Pa}]$
$I_f$	moment of inertia of fibre	$[\text{m}^4]$
$J_{yf}$	out-of-plane bending section constant, curved fibre	$[\text{m}^4]$
$J_{zf}$	in-plane bending section constant, curved fibre	$[\text{m}^4]$
$\mathbf{K}$	system stiffness matrix	$[\text{Nm}], [\text{N}], [\text{N/m}]$
$\mathbf{K}_e$	element stiffness matrix	$[\text{Nm}], [\text{N}], [\text{N/m}]$
$K_{vf}$	torsional constant of fibre	$[\text{m}^4]$
$L_i$	side-length of network along axis $i$ , $i = x, y, z$	$[\text{m}]$
$M_{ult}$	ultimate moment in bond	$[\text{Nm}]$
$N_x$	probability distribution function for parameter $x$	$[-]$
$RBA$	relative bonded area	$[-]$
$V_h$	degree of heterogeneity, see Section 3.3	$[\text{m}^2], [\text{m}^3]$

### Roman lower-case letters

$b_f$	width of rectangular fibre cross-section	$[\text{m}]$
$c$	curl index, see Figure 3.1	$[-]$
$e$	maximum fibre centre-line distance for bond to occur	$[\text{m}]$
$\mathbf{f}$	force vector	$[\text{N}], [\text{Nm}]$
$h_f$	depth of rectangular fibre cross-section	$[\text{m}]$
$k_i$	stiffness of spring in direction $i$ , $i = x, y, \phi$	$[\text{N/m}], [\text{Nm/rad}]$
$k_n$	stiffness of normal spring in bond	$[\text{N/m}^3]$
$k_t$	stiffness of shear spring in bond	$[\text{N/m}^3]$
$l_{ch}$	characteristic length	$[\text{m}]$
$l_f$	fibre length	$[\text{m}]$
$l_s$	free fibre segment length	$[\text{m}]$
$n_c$	number of fibre crossings	$[-]$

$n_f$	number of fibres	[-]
$n_s$	number of slips before complete bond failure	[-]
$p$	approximate active part of network	[-]
$r$	radius of curvature of fibre	[m]
$s$	probability of bond at a fibre crossing	[-]
$\mathbf{u}$	displacement vector in node, element or structure	[m],[rad]
$w_e$	external work	[Nm]
$w_i$	internal elastic strain energy	[Nm]
$\mathbf{x}$	$(x, y, z)$ , rectangular Cartesian coordinates	[m]

### Greek letters

$\alpha$	angle of fibre relative to the $x$ -axis	[rad]
$\beta$	angle of fibre relative to the $xy$ -plane	[rad]
$\gamma$	angle of fibre around its own axis	[rad]
$\boldsymbol{\epsilon}$	strain vector, 3D: $(\epsilon_x, \epsilon_y, \epsilon_z, \gamma_{xy}, \gamma_{xz}, \gamma_{yz})$ 2D: $(\epsilon_x, \epsilon_y, \gamma_{xy})$	[-]
$\epsilon_{lim}$	strain in network at maximum stress	[-]
$\epsilon_{ult}$	ultimate strain in network	[-]
$\kappa$	fibre curvature	[m <sup>-1</sup> ]
$\lambda_1$	reduction of bond stiffness at slip	[-]
$\lambda_2, \lambda_3$	reduction of bond strength at slip	[-]
$\mu$	shear strength factor of bond	[-]
$\nu$	homogenized Poisson's ratio for a network	[-]
$\rho$	network density; total fibre length per unit area or volume	[m <sup>-1</sup> ],[m <sup>-2</sup> ]
$\rho_s$	sheet density	[kg/m <sup>2</sup> ]
$\rho_f$	fibre density	[kg/m <sup>3</sup> ]
$\boldsymbol{\sigma}$	stress vector, 3D: $(\sigma_x, \sigma_y, \sigma_z, \tau_{xy}, \tau_{xz}, \tau_{yz})$ 2D: $(\sigma_x, \sigma_y, \tau_{xy})$	[Pa],[N/m]
$\sigma_{adh}$	adhesion strength of bond	[Pa]
$\sigma_{max}$	maximum stress in network	[Pa],[N/m]
$\sigma_n$	normal stress	[Pa]
$\sigma_{ult}$	ultimate normal stress in fibre	[Pa]
$\tau$	shear stress	[Pa]
$\tau_{ult}$	ultimate shear stress in fibre	[Pa]
$\theta$	angle along circle arc fibre	[rad]



## 2. EARLIER CELLULOSE FIBRE NETWORK MECHANICS MODELLING

The development of models aimed at improving our understanding of the mechanical behaviour of fibre networks started with analytical models assuming uniform strain. Being analytical, the earliest models were confined to rather simple, uniform networks. Nevertheless, they produced results of great interest and value. During the 1970s and 1980s the arrival of computers with considerable computation capacity resulted in the first computer simulations of network behaviour. The evolution has continued, and in the 1990s several new models appeared, taking more and more variables into account. The variables included in the models are naturally those which are believed to be of importance. Experimental progress, i.e. the possibility of measuring new properties in a network, has also been an important factor in choosing which parameters to study.

Most references cited in this chapter deal with paper, and this reflects the fact that not much is to be found in the literature on the geometry and mechanics of dry-shaped cellulose fibre materials. There are, however, obvious similarities between the two types of material, the main differences being the density, the more three-dimensional character and weaker fibre-to-fibre bonding of a fibre fluff.

### 2.1. Geometry models

A very often cited paper dealing with the geometry of fibre networks was presented by Kallmes and Corte in 1960 [23]. They stated that the structure of paper, i.e. the geometric arrangement of fibres and inter-fibre spaces, is an effect of the paper-making process, as well as the cause of the paper's properties. In their article, relations are presented between various geometrical properties of the network such as number of fibre crossings and average segment length between crossings, and basic properties of the fibres and the sheet, such as the mean fibre length and number of fibres.

They considered a two-dimensional sheet, which was defined as a sheet where the area which is covered by more than two fibres is negligible. Probability theory was used, and the fibres were assumed to be deposited independently of each other. Further, it was assumed that the fibres were randomly distributed over the area and had a uniform orientation distribution. Among the results, the following equations are cited for  $\bar{n}_c$ , the average number of fibre crossings in a square of side length  $L$ , occupied by  $n_f$  fibres of average length  $\bar{l}_f$ , and  $\bar{l}_s$ , the average free segment length

on a fibre.  $\bar{c}$  denotes the average curl index, that is the distance between fibre end points divided by fibre length, see Figure 3.1.

$$\bar{n}_c = \frac{(n_f \bar{l}_f)^2 \bar{c}^2}{L^2 \pi} \quad (2.1)$$

$$\bar{l}_s = \frac{\bar{l}_f n_f \bar{c}}{2 \bar{n}_c} \quad (2.2)$$

The influence of  $\bar{c}$  was, however, not found to agree with simulation results, as is further discussed in Section 5.2. In addition to average values of geometrical and topological properties of the model network, distributions of various properties were also given, and the analytical results compared with experimental results.

In 1977, Komori and Makishima [31] presented the equations corresponding to (2.1) and (2.2) for a three-dimensional fibre assembly, where the fibres had an arbitrary orientation distribution. If the fibres are not straight, however, the orientation distribution function must be interpreted as the orientation distribution of the infinitesimal fibre segments. For the case of a two-dimensional network with a uniform orientation distribution, the equations as expected reduce to those of Kallmes and Corte [23].

In a book presented by Deng and Dodson in 1994 [12], various aspects of the stochastic geometry of paper are compiled.

## 2.2. Uniform strain models

The relation between basic fibre and bond parameters and the mechanical properties of a network has been investigated by means of several network theories. Many network theories rely on the assumption of uniform strain, that is, that the strain is equal everywhere in a sheet and thus equal to the average strain. In a heterogeneous material there is generally not a state of uniform strain since areas of less stiffness elongate more than stiffer areas when a sheet is subjected to extension. Uniform strain is, however, a better approximation, the more homogeneous the material.

A typical uniform strain theory is formulated by first making basic assumptions regarding the geometry of the network, e.g. straight identical fibres positioned uniformly in the sheet and oriented according to some arbitrary distribution. The homogeneous strain assumption implies that each bond centre is displaced according to the mean strain field. The rotation of the bond centres can be assumed to be for example, zero or related to the rotation of the neighbouring fibre segments. The displacement and rotation of the fibre segment end points are then calculated as a function of fibre orientation angle and global strain. Assumptions are made regarding the types of deformation a fibre can sustain, e.g. axial elongation, bending and shear. By means of this and assuming constitutive behaviour of the fibre, for example, linear elastic, the forces in the fibre segments as a function of fibre orientation angle and global strain can be calculated. The number of fibres of a certain angle crossing a line of unit length parallel to the  $x$ - and  $y$ -axes, which depends on

the total fibre length per unit area and the orientation distribution, is calculated. Finally, the stresses in the  $x$ - and  $y$ -directions can be integrated and from the relation between the applied strain and resulting stress the elastic coefficients can be calculated.

Some uniform strain theories which, in principle, follow the outline above are described in the following. Cox [11] presented a network model in 1952 in which the fibres were assumed to extend from one side of the network to the other, carry only axial load and not interact with each other. The elastic coefficients were derived as a function of the fibre orientation distribution. Due to its simplicity, the Cox model is of special interest and the main concepts are described here as an example of a uniform-strain theory. Cox assumed the long straight thin fibres to be oriented according to the distribution function:

$$f(\alpha) = \frac{1}{\pi}(1 + a_1 \cos 2\alpha + a_2 \cos 4\alpha + \dots + b_1 \sin 2\alpha + b_2 \sin 4\alpha + \dots) , \quad (2.3)$$

where  $\alpha$  is the angle of the fibre relative to the  $x$ -axis,  $a_i$  and  $b_i$  constants and

$$\int_0^\pi f(\alpha) d\alpha = 1 . \quad (2.4)$$

Each fibre was assumed to extend from one edge of the network to the other, see Figure 2.1; its bending stiffness assumed to be negligible and there is no interaction between the fibres. These assumptions imply that the strain field is homogeneous

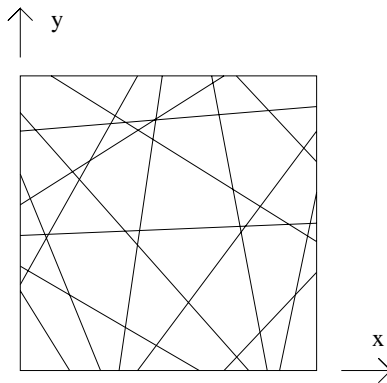


Figure 2.1: A Cox network.

throughout the network, and the approximation is thus not concerned with the uniformity of the strain field, but rather with whether the analysed network is similar to the real material which is being modelled. If the network is subjected to a strain

$$\boldsymbol{\epsilon} = (\epsilon_x, \epsilon_y, \gamma_{xy}) ,$$

the axial strain in a fibre inclined at an angle  $\alpha$  to the  $x$ -axis is:

$$\epsilon = \epsilon_x \cos^2 \alpha + \epsilon_y \sin^2 \alpha + \gamma_{xy} \cos \alpha \sin \alpha \quad (2.5)$$

The fibres were assumed to resist only axial stress and to be linearly elastic with an elastic modulus  $E_f$  and cross-sectional area  $A_f$ . From Hooke's law we can derive the force,  $F$ , in a fibre:

$$F = E_f A_f (\epsilon_x \cos^2 \alpha + \epsilon_y \sin^2 \alpha + \gamma_{xy} \cos \alpha \sin \alpha) \quad (2.6)$$

The numbers of fibres at an angle  $\alpha$  which intersect a line of unit length perpendicular to the  $x$ - and  $y$ -directions are  $\rho f(\alpha) \cos \alpha$  and  $\rho f(\alpha) \sin \alpha$ , respectively, where  $\rho$  denotes the total fibre length per unit area. By integrating over  $\alpha$ , the forces per unit length in the  $x$ - and  $y$ -directions as a function of the strain are obtained. From this, the elements of the constitutive matrix  $\mathbf{D}$  can be obtained:

$$\begin{aligned} D_{11} &= \frac{K}{16}(6 + 4a_1 + a_2) \\ D_{22} &= \frac{K}{16}(6 - 4a_1 + a_2) \\ D_{13} &= \frac{K}{16}(2b_1 + b_2) \\ D_{23} &= \frac{K}{16}(2b_1 - b_2) \\ D_{12} = D_{33} &= \frac{K}{16}(2 - a_2) \end{aligned} \quad (2.7)$$

where

$$K = A_f E_f \rho = \frac{\rho_s}{\rho_f} E_f, \quad (2.8)$$

$\rho_s$  is the sheet density and  $\rho_f$  is the density of the fibre. Note that the higher order terms in the expansion of  $f(\alpha)$  disappear in the integration. For an isotropic network, where  $f(\alpha) = 1/\pi$ , (2.7) reduces to

$$E = \frac{K}{3} \quad (2.9)$$

$$G = \frac{K}{8} \quad (2.10)$$

$$\nu = \frac{1}{3}, \quad (2.11)$$

$E$ ,  $G$  and  $\nu$  denoting elastic modulus, shear modulus and Poisson's ratio of the network. The stiffness values predicted by Cox's model are not reached in real cellulose fibre networks, but they could be viewed as an upper limit. Several authors [24, 45] have reported stiffness values approaching those calculated by Cox for well-bonded networks made of long fibres. To approach the homogeneous strain field situation

in a network where the fibres do not extend from edge to edge, an alternative mechanism for transferring forces across the network must be provided. This could be completely rigid bonds between the fibres and sufficiently high network density to suppress the effect of bending of the fibres.

Cox also introduced the idea that the effect of short fibres can be approximated by reducing the fibre modulus by an amount corresponding to the average stress in a short fibre compared with the stress in an infinite fibre. The stress distribution in a fibre depends on the transfer of stress between the single fibre and the medium to which it is bonded. This method of calculation of the stress along a fibre is often called shear-lag theory.

A strength criterion for uniaxial tension can also be deduced from Cox's article. The most severely stressed fibre is oriented in the direction of the strain. When the stress in this fibre reaches the fibre strength the maximum sheet stress is reached.

Campbell [10] presented a similar long-fibre model, but in a less general manner, and obtained the same results for the elastic modulus and Poisson's ratio as Cox.

Van den Akker [61] assumed that apart from axial strain the unbonded parts of the fibres can also sustain bending and shear. When bending and shear are considered an assumption has to be made regarding the rotation of the bonds. Van den Akker assumed the bonds to be rigid and to rotate an amount equal to the average of the rotations of the two bonded fibres.

Kallmes et al. [24] repeated the calculations of Campbell and Van den Akker, emphasizing the contributions of the free and bonded parts of the fibre segments. They also suggested some minor changes in Van den Akker's theory regarding fibre curl and the penetration of bending from the unbonded into the bonded fibre regions. Kallmes and Perez [25] also introduced a theory for the entire load-elongation behaviour of paper relying on the assumption of uniform strain. The total force in the fibres crossing a line is considered to depend on three factors. The first is the force in a fibre of orientation  $\theta$ . This is determined from the uniform strain assumption and assumed linear elastic-brittle material behaviour. The second is the number of fibres crossing the line. This is obtained as in the previously mentioned theories, uniform orientation distribution is assumed and only the fibres subjected to tension are considered. The third factor is the probability that a fibre crossing the line is carrying a load. This probability is divided into two parts, one taking account of non-straight fibres not carrying any load, and one taking account of fibres not carrying any load due to bond failure at their ends. The latter is a function of relative bonded area,  $RBA$ . Failure is assumed to result from either the fibre strength being exceeded, or from progressive bond failure.

In 1969, Page [44] proposed the following equation for paper strength,  $T$ , under uniaxial tension:

$$\frac{1}{T} = \frac{9}{8Z} + \frac{12A_f\rho_f9.81}{bPl_fRBA} \quad (2.12)$$

where  $Z$  denotes zero-span tensile strength,  $\rho_f$  fibre density,  $b$  shear bond strength per unit area,  $P$  the perimeter of the fibre cross-section and  $RBA$  the relative bonded area of the sheet. Despite the non-rigorous derivation, this equation which

emphasizes the relative importance of fibre and bond properties for sheet failure, showed good agreement with experimental results.

Perkins and Mark [46] assumed that the entire fibre segments acted in the same way and could sustain axial load and bending. In addition, the effect of relative deformation between the fibres in a bond was taken into account when the elastic stiffness was calculated. The axial stiffness also includes the effect of out-of-plane curl.

Kallmes et al. [26] considered only tension in the fibres. They stated that not all the fibres in the network were active, due to initial slack etc., and that only the active fibres could carry load.

Page and Seth [45] argued that the elastic modulus of paper is controlled by three factors, the first being the fibre modulus. For networks of long, straight, well-bonded fibres the modulus is that derived by Cox. The two factors that cause the paper modulus to fall short of this value are limitations in the load transfer between the fibres and defects in the fibres such as micro compressions, curl and kinks. The elastic moduli resulting from these models are all given in [5], from which Table 2.1 is taken.

Cox [11] also derived the elastic constants for a three-dimensional isotropic network, using the same assumptions as in the 2D case of long fibres carrying only axial force. The result is

$$E = \frac{K}{6} \quad (2.13)$$

$$G = \frac{K}{15} \quad (2.14)$$

$$\nu = \frac{1}{4} \quad , \quad (2.15)$$

where  $K$  is given in (2.8).

Qi [49] used the same assumptions regarding the fibre properties but gave an angular distribution function suitable for describing the three-dimensional fibre orientation distribution in paper. A  $z$ -directional ordering parameter defining the degree of out-of-plane orientation of the fibres was given, and the elastic parameters were calculated for different values of the ordering parameter, both for isotropic handsheets and machine-made papers showing a non-isotropic in-plane orientation distribution. The model was further developed [50] to include the effects of transversal fibre stiffness.

Toll and Månson [59] studied a planar fibre network under transverse compression. The fibres were assumed to be long, lie in one plane and have an arbitrary orientation distribution in that plane. When the network is compressed more fibre contact points are created and the beam segments providing resistance to compression become shorter and stiffer. The stress needed for compressing the network was found to be proportional to the volume fraction of fibres raised to the power of five. The results showed good agreement with experiments performed on glass-fibre networks.

Table 2.1: *Elastic modulus resulting from different uniform strain models. From Baum [5].*

Author	Elastic Modulus	Ref.
Cox (1952)	$\frac{1}{3} \frac{\rho_s}{\rho_f} E_f$	[11]
Campbell (1963)	$\frac{1}{3} \frac{\rho_s}{\rho_f} E_f$	[10]
Van den Akker (1962)	$\frac{1}{3} \left(1 + \frac{4I_f G_f}{A_f G_f b^2 + 12E_f I_f + 2G_f I_f}\right) \frac{\rho_s}{\rho_f} E_f$	[61]
Kallmes et al. (1963)	$\frac{1}{3} \left(1 + \frac{16I_f G_f}{3A_f G_f b^2 + 36E_f I_f + 8G_f I_f}\right) \frac{\rho_s}{\rho_f c} E_f$	[24]
Perkins and Mark (1976)	$\frac{1 + 2\beta}{3 + 2\beta} \frac{1}{1 + 1.5(2a_0/t_f)^2} \frac{\rho_s}{\rho_f} E_f$	[46]
Kallmes et al. (1977)	$\frac{1}{3} (1 - f_i) \frac{\rho_s}{\rho_f} E_f$	[26]
Page and Seth (1979)	$\frac{1}{3} \left(1 - \frac{w}{gRBA} (E_f/2G_f)^{1/2}\right) \frac{\rho_s}{\rho_f} E_f$	[45]
<b>Notations differing from those in Section 1.4</b>		
$a_0$	Measure of slackness in unstrained network	
$b$	Unbonded fibre segment length	
$f_i$	Initial fraction of inactive fibres	
$g$	Fibre segment length	
$t_f$	Fibre thickness	
$w$	Fibre width	
$\beta$	Dimensionless parameter which is a function of fibre geometry and elastic properties and $a_0$	

### 2.3. Semi-analytical models

As the theory becomes more complicated, the integrations necessary in the analytical models become difficult. An alternative approach is to calculate the stress distribution in a single fibre by analytical methods and to use a computer to solve the resulting equations by numerical methods.

Ramasubramanian and Perkins [53] considered elements consisting of a fibre connected to a homogeneously strained medium by crossing fibre segments. The work done on the element was derived assuming axial elastic-plastic behaviour of the fibre, and taking into account the flexibility of the crossing fibres and the elastic-plastic behaviour of the bonds. The stress-strain behaviour of a strip of paper was

obtained by means of computer simulations using the above model. For each level of global external strain the total work done on the system was numerically calculated, and the corresponding global stress was obtained as the derivative of the work with respect to the strain. Poisson's ratio was treated as a constant during the elastic part of the straining, and was obtained by a minimum work criterion during the plastic part.

Kärenlampi studied the effect of distributions of fibre properties on the tensile strength [27, 28]. An analytical expression was derived for the force across a scan line at a certain global strain. The expression consisted of integrals of the distribution functions. The equation was solved numerically for the cases of all fibres parallel to the direction of strain and uniform orientation distribution. Discrete and continuous distributions of fibre axial stiffness and maximum external strain without dramatic fibre or bond failure were considered.

The approach used by Feldman et al. [14] was to generate many fibres crossing a scan line, using distribution functions for the fibre and bond properties. Integration was replaced by summation over all the generated fibres. The fibres were assumed to be straight and lying in one plane. Using a bi-linear stress-strain curve for the single fibre the stress distribution in a fibre and its bonds was calculated using shear-lag theory. The strain was increased in small increments and for each strain level all fibres and bonds were checked against a fracture criterion, maximum axial load for fibres and maximum shear stress for bonds. When a fibre failed, the load it was carrying was assumed to be evenly distributed to the 30 closest fibres. The values for sheet strength obtained agreed quite well with those obtained from the strength theories [26, 44] and, in addition, the entire stress-strain curve was obtained. The benefit of this line-simulation approach is that it is not as numerically cumbersome as the 2D and 3D simulations discussed in the next section, and networks consisting of very many fibres can be dealt with. On the other hand, more assumptions have to be made regarding for example the stress distribution in fibres and the redistribution of load following fibre or bond failure.

## 2.4. Computer simulations

Since the mid 1970s, much of the work carried out in the area of geometrical and mechanical properties of random fibre networks has been based on computer simulations. An early example of computer simulation of cellulose fibre structures was presented by Yang in 1975 [64]. He modelled paper with a two-dimensional network of randomly distributed fibres with prescribed distributions of length and orientation. He generated network geometries and compared the number of fibre crossings and average free fibre segment length with the values predicted by Kallmes and Corte [23]. The fibres were ribbon-like with non-zero width, and the part of the fibre area which is in contact with other fibres, the relative bonded area, was computed. Among the geometrical output was also "percentage of free fibre ends", which is closely related to what in this work is called the "approximate active part", see Section 5.3. The linear elastic stiffness was calculated by means of the finite

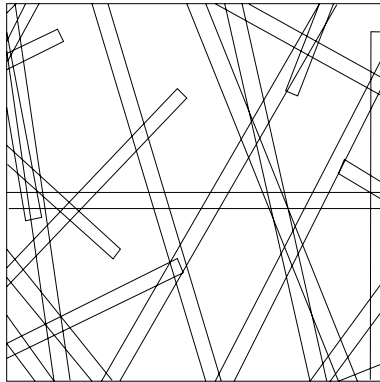


Figure 2.2: *Example of a base element [64].*

element method. The fibres were represented by orthotropic quadrilateral elements, and the areas where fibres overlap were treated as a composite consisting of two layers of orthotropic material. The concept of sub-structuring was used to overcome the problem of poor computer capacity, i.e., several small base elements, see e.g. Figure 2.2, were analysed. These elements were then condensed into quadrilateral elements with two degrees of freedom at each corner. The condensed base elements, which have statistical variations in properties, were then used to model the paper sheet. The results of the simulation showed good agreement with experiments performed on kraft paper.

In 1984, Rigdahl et al. [54] investigated the axial stress distribution in the fibres of a network by means of finite element simulations. Figure 2.3a shows a simplified sketch of the network geometry considered. It consists of parallel fibres of finite length bonded together through fibres crossing at right angles. The fibres were modelled by linearly elastic straight beam elements, and the fibre-to-fibre bonds were rigid. It was observed that the axial strain in the fibres was smaller than the global strain of the network. The strain in a fibre was zero at the fibre end, rose quite quickly to a plateau value, and, moreover, where the neighbouring fibre ends, there was a peak in the strain (see Figure 2.3b). This is because the force transmitted in the neighboring fibre row has to find another way when there is suddenly a discontinuity in the path. The influence of the stiffness of the inter-fibre bond was also investigated. This was done by considering two parallel fibres connected by crossing fibres, fibre-to-fibre bonding not being rigid. One of the fibres was subjected to a strain corresponding to the result of one of the previously mentioned analyses, and the transfer of strain to the other fibre as a function of bond stiffness was studied. It was found that the bond stiffness was of little importance, unless it is below a certain critical value, in which case the transfer of strain deteriorates rapidly.

In his thesis of 1991, [19], Hamlen considered mechanical properties as well as the

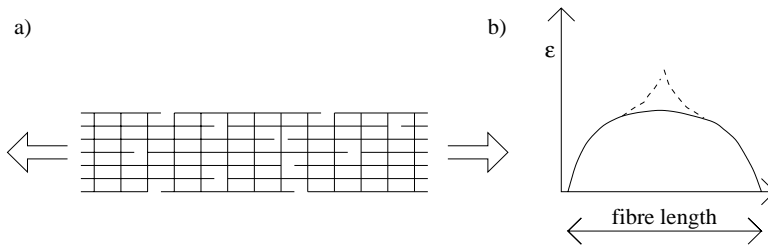


Figure 2.3: a) *Illustration of network geometry.* b) *Strain as a function of position in a fibre, adapted from [54].*

permeability of paper by means of network modelling. He examined the properties of several regular (triangular, square, hexagonal) and perturbed regular networks, and concluded that the regular networks needed to give satisfactory results when modelling paper were not less computationally demanding than random networks. He therefore chose to study random networks, in two and three dimensions. His two-dimensional model was composed of linearly elastic straight beams of random distribution and orientation, connected rigidly at crossings. The network geometry was periodic, but the loading conditions were not. The fibres were assigned a breaking stress in simple tension, adjusted in size to reflect the breaking of bonds. The results indicated that tensile extension of fibres was the dominant mechanism of force transfer in a fibre network. He also studied the influence of fibre curl by assigning a non-linear elastic modulus to the fibres. The elastic modulus was initially set to zero, and when the network had been strained enough to completely straighten out a fibre, its modulus was reset to a value representative of a straight fibre. Hamlen also proposed a three-dimensional network model for paper, called the "sequential deposition model". A network was generated by allowing the projection of a fibre on the  $xy$ -plane to fall down on the already deposited fibres. Initially, it lands on two points where it first meets previously deposited fibres. Then the fibre continues to descend between the supports to an extent determined by the fibre stiffness through a 'limit angle', possibly making contact with more fibres. In this model the fibre-to-fibre bonds are represented by beam elements. The computations proved to be extremely numerically demanding, in spite of the use of a CRAY-2/512. It was concluded that here too the dominant mode of deformation was tension in fibres, followed by shear in bonds. To facilitate further 3D simulations, it was proposed that the modes of deformation of less importance be neglected, and that alternative numerical methods of dealing with the non-linearity due to the breaking of elements be considered.

Åström and Niskanen reported simulations of fracture in random fibre networks [2, 3]. They examined 2D random fibre networks of uniform spatial and orientation distribution; the fibres being straight and the fibre-to-fibre bonds rigid. The mechanical properties of the networks were evaluated as functions of the width-

to-length ratio of a fibre segment and the ratio of network density to percolation network density. They suggested that the specific modulus of elasticity ( $E$  of the network relative to  $E_f$  of a fibre) at low densities is a linear function of network density, and that at high densities it deviates from Cox's homogeneous field value by an amount inversely proportional to the network density. Fracture calculations were performed by introducing fracture criteria for fibres and bonds in terms of axial strain, and by performing successive linear calculations where the fractured elements were removed from the structure. The simulations indicated that, in the case of bond breaking, the strength was equal to the product of the elastic modulus of the network and the maximum shear strain that a bond can carry. The character of the stress strain-curve was discussed in terms of comparisons with predictions from the homogeneous field approximation. Åström et al. [4] performed further simulations with the model. The distribution of axial stress along the fibres was examined and was found to agree with the shape derived by Cox using a shear-lag approach. This distribution is qualitatively similar to the one illustrated in Figure 2.3b. The stress distribution in the fibre segments was found to be exponential. Niskanen also provides a review of the the knowledge about strength and fracture of paper [40].

Jangmalm [22] modelled paper with a two-dimensional network composed of curled fibres. The circle arc fibres were randomly distributed, and length, width, curl and orientation were described by statistical distributions. The fibre-to-fibre bonds, which occur at a prescribed percentage of the crossings, were rigid. Although the fibres were assumed to be curled, they were modelled by straight, linearly elastic beam elements, but if the free fibre segments were considered to be too long they were divided into several shorter straight elements. The main objective was to investigate the influence of fibre curl on the linear elastic stiffness of a network. This is due to the possibility of measuring fibre curl in pulp with the STFI-FiberMaster, referred to in [22]. The influence of fibre length and percentage of bonds in the crossings on the elastic stiffness was also investigated, and some calculations were made using large-strain theory. The latter showed that the non-linear effect of large strain is rather small. Comparisons of the results of simulation were made with those from experiments performed on laboratory sheets made from commercial pulp. It was found that the effect of curl was stronger in the laboratory sheets than that predicted by the model. Several possible reasons for the discrepancies were discussed, among which were the two-dimensional character of the model and the fact that out-of-plane curl was not taken into account. Further simulations using this model have been presented [58].

Räisänen et al. [51] developed the model of Åström [4] and simulated fracture in a 2D network made of rigidly bonded, elastic-plastic fibres showing a bilinear stress-strain relationship. It was concluded that the stress-strain curve for the network, with the stress divided by network elastic modulus, is similar to the stress-strain curve of the fibres, irrespective of network density or degree of bonding. Yielding occurred mainly in the fibres oriented in the straining direction, and occurred uniformly over the entire network.

KCL-PAKKA [39] is a model which simulates the 3D geometry of paper by sequentially depositing fibres on a square lattice. The fibres are flexible and thus conform to each other according to the input value of fibre flexibility. Geometrical and optical properties of the sheet can be calculated from the sheet geometry structure. Sheet stiffness can be estimated using a derived formula containing geometrical parameters, such as the relative bonded area.

A 3D network model for application to cement excelsior board was presented by Stahl and Cramer [57]. The cement-coated wood strands were assumed to be straight and continuous across the modelled volume and connected by rigid bonds where the strand volumes interfere. The strands were modelled as 3D linear elastic beams and fracture of strands were considered through an axial stress fracture criterion. Comparisons with experimental measurements showed reasonable accuracy of the model.

The Division of Structural Mechanics in Lund has a tradition of studying the fracture of heterogeneous materials. This has led to a number of computer simulation studies in network mechanics, [6], [55], [17], [20], [21] and [52].

## 3. THE MODEL

The modelling includes an in-plane, two-dimensional network model and a three-dimensional network model. The 2D and 3D models have many features in common and are both defined in this chapter. The definition of the models is divided into three parts; Fibres, Section 3.1, Inter-fibre bonds, Section 3.2.1, and Network cell geometry, Section 3.3. Section 3.4 discusses some aspects of modelling of heterogeneity. Assumptions and modelling with regard to boundary conditions and loading are discussed in Chapter 6.

### 3.1. Fibres

A wood fibre is a complex composite structure made up of layers of different orthotropic materials with different principal directions. It also contains pores, which are essential for the tree, but which can be regarded as defects when mechanical modelling of a single fibre is considered. The pulping process further complicates the situation by introducing curl and kinks and generally treating the fibre harshly.

As this work deals with micro-mechanical modelling, from the fibre level, to the homogenized network level, the objective is to devise a simple model of the fibre which does not explicitly take into account the variables mentioned above. The model should, however, still be realistic enough to be able to make use of existing experimental knowledge about fibres and results from micro-mechanical modelling on the sub-fibre to fibre level.

In this work, the fibre is modelled as a Bernoulli beam of circle-arc shape. The cross-section is constant along the beam and arbitrary with respect to stiffness properties since the cross-sectional area and moments of inertia are given as input. The detection of bonds in the 3D model is based on a circular cross-section, and the implementation of the fracture criterion used in the analysis of 2D network failure is based on a rectangular cross-section.

The fibres are assumed to be made of a homogeneous isotropic linearly elastic material. A fibre is assumed to fail in a brittle manner when

$$f(\sigma_n, \tau) = 0 \quad . \quad (3.1)$$

Fibre fracture is implemented in the 2D model, and  $f$  is then set to

$$f(\sigma_n, \tau) = \max \begin{cases} \frac{|\sigma_n|}{\sigma_{ult}} - 1 \\ \frac{|\tau|}{\tau_{ult}} - 1 \end{cases} . \quad (3.2)$$

Here  $|\sigma_n|$  is the maximum absolute value of normal stress in the fibre,  $\sigma_{ult}$  is the ultimate normal stress,  $|\tau|$  is the absolute value of shear stress in the fibre, and  $\tau_{ult}$  is the ultimate shear stress. Denoting the axial force  $N$ , the bending moment  $M$ , the shear force  $V$  and the area and moment of inertia of the beam cross-section  $A_f$  and  $I_f$ , gives for a rectangular cross-section

$$\sigma_n = \pm \frac{N}{A_f} \pm \frac{M}{I_f} \sqrt{\frac{3I_f}{A_f}} , \quad (3.3)$$

$$\tau = \frac{1.5V}{A_f} . \quad (3.4)$$

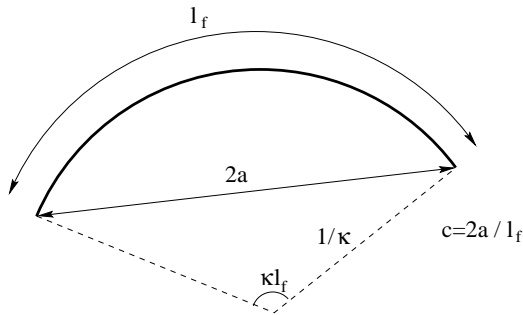
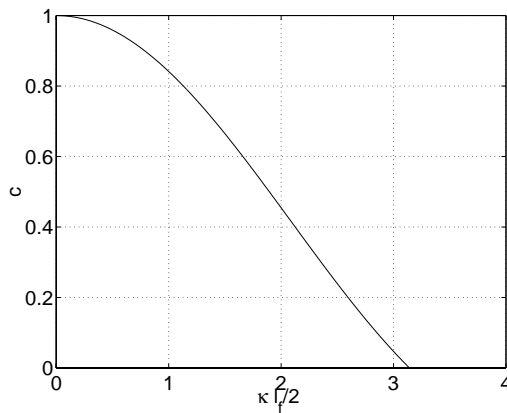
Second-order effects are not taken into account; that is, the decrease in stiffness due to a compressive normal force in a fibre, and possible buckling, are disregarded.

Table 3.1 lists the parameters defining a fibre. In a two-dimensional analysis only the in-plane deformation modes are considered, and thus fewer parameters are needed. Moments of inertia of the fibre are denoted by  $J$  in Table 3.1, which is the modified bending stiffness used for curved beams. For the fibre geometries used in this work the difference between  $J$  and  $I$  is, however, negligible.  $N$  represents

Table 3.1: *Parameters defining a fibre.*

Parameter	Notation	
	2D	3D
Length	$l_f \in N_{l_f}$	$l_f \in N_{l_f}$
Curvature	$\kappa \in N_\kappa$	
Curl index		$c \in N_c$
Area of cross section	$A_f \in N_{A_f}$	$A_f \in N_{A_f}$
Moment of inertia, in-plane	$J_{z_f} \in N_{J_{z_f}}$	$J_{z_f} \in N_{J_{z_f}}$
Moment of inertia, out-of-plane		$J_{y_f} \in N_{J_{y_f}}$
Torsional constant		$K_{v_f} \in N_{K_{v_f}}$
Modulus of elasticity	$E_f \in N_{E_f}$	$E_f \in N_{E_f}$
Shear modulus		$G_f \in N_{G_f}$
Ultimate normal stress	$\sigma_{ult} \in N_{\sigma_{ult}}$	
Ultimate shear stress	$\tau_{ult} \in N_{\tau_{ult}}$	

a distribution of the parameter in question. If a parameter is assumed to be of constant value,  $N$  is the Dirac delta distribution. The implementation of other distributions is discussed in Section 4.1.

Figure 3.1: Definition of curl index,  $c$ , and curvature,  $\kappa$ .Figure 3.2: Curl index,  $c$ , versus normalized curvature,  $\kappa l_f / 2$ .

A special case is zero fibre curvature corresponding to  $\kappa = 0$ , that is, straight fibres. In experimental situations fibre curl is often quantified by the curl index,  $c$ , defined as the distance between the end-points of a fibre divided by the fibre length, see Figure 3.1. Assuming constant curvature, the relation between curl index and curvature is:

$$c = \frac{2}{\kappa l_f} \sin\left(\frac{\kappa l_f}{2}\right) \quad (3.5)$$

Since it is not possible to solve this equation analytically for  $\kappa$  a graphical representation of (3.5) is given in Figure 3.2.  $\kappa$  is chosen as input in the 2D model while  $c$  is used in the 3D model. In simulations where all the fibres are of the same length there is no difference between the resulting networks. For a network of varying fibre length, however, a constant  $c$  gives varying fibre curvature depending on fibre length, and this was found to agree better with experimental results of fibre curvature.

## 3.2. Inter-fibre bonds

### 3.2.1. Bond model consisting of coupled springs

The mechanisms of fibre-fibre interactions in fluffed dry-shaped cellulose fibre materials are not completely understood; in all probability, several mechanisms are acting together. One mechanism is that in which kinked fibres hook onto each other, another is fibre-to-fibre friction. Chemical attraction may also play a role. When an adhesive aerosol is added during the dry-forming process a different type of material is obtained. The adhesive provides a much stronger fibre-fibre connection than the mechanisms suggested above. The inter-fibre bonds are not modelled by trying to imitate any of the above mechanisms explicitly, but rather through introducing a fictive bond element which enables a wide range of bond behaviour.

A bond is modelled as two circular plates of area  $A_b$  connected by distributed normal and shear springs of stiffnesses  $k_n$  and  $k_t$ . The dimension of the spring stiffnesses is stress/length and they are symbolically illustrated in Figure 3.3. Note that there are shear springs in two perpendicular directions on the bond area even though only one direction is illustrated in the figure. The circular areas are perpendicular to the line connecting the two fibre centre lines at the bond site, they are assumed to be at zero distance from each other and are rigidly connected to the fibre centre lines. The mode of deformation which separates the circular areas is not relevant in the 2D model, and thus only the shear springs are present in this case. The stiffness relation resulting from this model is presented in Section 6.1.2.

The bonds show non-linear stick-slip fracture behaviour. A slip criterion is defined, and when this is fulfilled a slip occurs which implies degradation of stiffness and strength properties of the bond. The number of slips occurring before complete failure of a bond is denoted  $n_s$ . The special case of  $n_s = 1$  corresponds to brittle failure. The criterion for a fracture event, a slip, to occur in a bond is

$$g(\sigma_n, \tau) = 0 \quad , \quad (3.6)$$

where  $\sigma_n$  and  $\tau$  are average normal and shear stresses over the bond area. In the

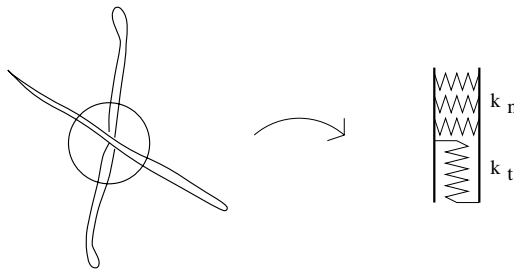
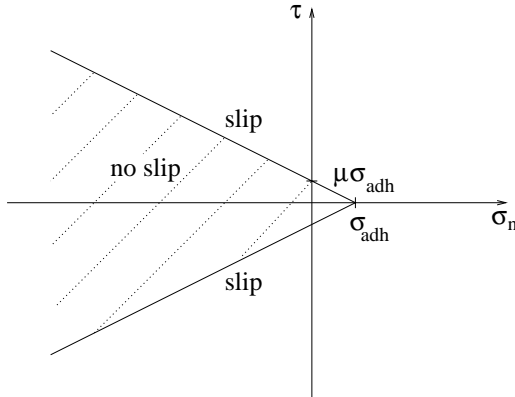


Figure 3.3: A bond is modelled as two circular areas connected by springs.

Figure 3.4: *Slip criterion for bond.*

2D model,  $\sigma_n$  is always zero.  $g$  is set to

$$g(\sigma_n, \tau) = \frac{|\tau|}{\mu\sigma_{adh} - \mu\sigma_n} - 1, \quad (3.7)$$

where  $\sigma_{adh}$  represents adhesion strength and  $\mu$  is a shear strength factor. The slip criterion is illustrated in Figure 3.4, by indicating the area in the  $\sigma_n$ - $\tau$  plane for which no slip occurs. In the 2D model, the only possible stress states are situated on the  $\tau$ -axis. In [1], friction between two pulp fibres was examined, and the results support a relationship between normal and friction force, or normal and shear stress, at the initiation of a slip according to Figure 3.4. Tests were, however, only made for compressive normal forces. The results of [1] are further commented in Section 8.1.

When the slip criterion is fulfilled for a bond its properties are changed, depending on whether the normal stress is compressive or tensile, as can be seen in Table 3.2. That is, if a bond under tensile normal stress fulfils the slip criterion

Table 3.2: *Change in bond parameters at slip.*

Variable	New value after slip	
	$\sigma_n > 0$	$\sigma_n < 0$
$A_b$	$A_b$	$A_b$
$k_n$	0	$k_n$
$k_t$	0	$\lambda_1 k_t$
$\mu$	0	$\lambda_2 \mu$
$\sigma_{adh}$	0	$\lambda_3 \sigma_{adh}$

there is complete fracture of the bond. If, on the other hand, a slip occurs during

compression,  $k_n$  is unchanged and  $k_t$ ,  $\mu$  and  $\sigma_{adh}$  are reduced by factors  $\lambda_1$ ,  $\lambda_2$  and  $\lambda_3$  respectively. The reduction in  $k_t$ ,  $\mu$  and  $\sigma_{adh}$  can occur at most  $n_s - 1$  times, the  $n_s$ th time a slip occurs there is complete fracture. Figure 3.5 shows some examples of how the slip criterion is changed in different cases. Table 3.3 lists the parameters defining a bond.

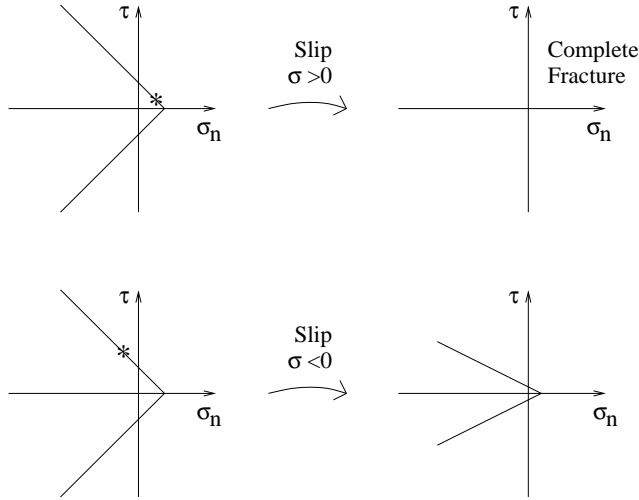


Figure 3.5: *Change in slip criterion at slip.*

Table 3.3: *Parameters defining a bond.*

Parameter	Notation	
	2D	3D
Area	$A_b \in N_{A_b}$	$A_b \in N_{A_b}$
Normal stiffness		$k_n \in N_{k_n}$
Initial shear stiffness	$k_t \in N_{k_t}$	$k_t \in N_{k_t}$
Initial adhesion strength	$\sigma_{adh} \in N_{\sigma_{adh}}$	$\sigma_{adh} \in N_{\sigma_{adh}}$
Initial shear strength factor	$\mu \in N_{\mu}$	$\mu \in N_{\mu}$
Reduction of shear stiffness at slip	$\lambda_1 \in N_{\lambda_1}$	$\lambda_1 \in N_{\lambda_1}$
Reduction of shear strength factor at slip	$\lambda_2 \in N_{\lambda_2}$	$\lambda_2 \in N_{\lambda_2}$
Reduction of adhesion strength at slip	$\lambda_3 \in N_{\lambda_3}$	$\lambda_3 \in N_{\lambda_3}$
Number of slips before complete failure	$n_s \in N_{n_s}$	$n_s \in N_{n_s}$

### 3.2.2. Bond model consisting of uncoupled springs

In the previous section the resistance to relative translational motion and to relative rotation in the plane of the bond are coupled. In 2D, however, simulations were made where the translational and rotational stiffnesses were assumed to be independent of each other. Figure 3.6 shows an illustration of this bond model, where the spring stiffnesses are denoted  $k_x$ ,  $k_y$  and  $k_\phi$ .

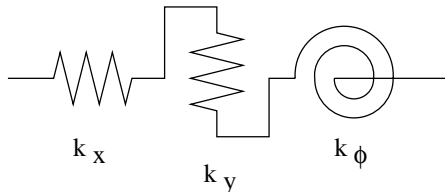


Figure 3.6: *Illustration of a bond consisting of uncoupled springs.*

For this case, shear stresses due to forces and moments are considered separately in the slip criterion, and  $g$  is set to

$$g(F, M) = \frac{|F|}{F_{ult}} + \frac{|M|}{M_{ult}} - 1, \quad (3.8)$$

where  $|F|$  is the absolute value of the vector sum of the forces in the  $x$  and  $y$  springs,  $F_{ult}$  is the ultimate force of the bond,  $|M|$  is the absolute value of the moment in the  $\phi$  spring and  $M_{ult}$  is the ultimate moment of the bond.

Figure 3.7 shows the fracture behaviour of a bond, in this case an  $x$  spring, but the same parameters apply to all springs in a bond. Initially, the spring is defined by its stiffness  $k_1$ , and strength  $F_{ult1}$ . When the situation  $g(F, M) = 0$  occurs, the stiffness is reduced by a factor  $\lambda_1$  and the strength is reduced by a factor  $\lambda_2$ . This is repeated  $n_s - 1$  times, and when  $g(F, M) = 0$  the  $n_s$ th time the connection fails completely. Table 3.4 lists the parameters defining a bond made of uncoupled springs.

### 3.3. Network cell geometry

The three-dimensional geometry of a cellulose fibre network is dependent on the constituent fibres, as well as the process which has generated it. Examples of important fibre properties are length distribution, flexibility of fibres and the tendency to form bonds with neighbouring fibres. Examples of two different classes of processes are the wet-forming process, producing paper, and the dry blowing of fibres producing fluff. In paper production, a dilute suspension of fibres is spread over a wire mesh. Dewatering leads to a fibre web which has a strong preference for fibre orientation in the wire plane and also a certain preference for fibre orientation in the machine direction due to the speed of the wire relative to that of the fibre suspension flow.

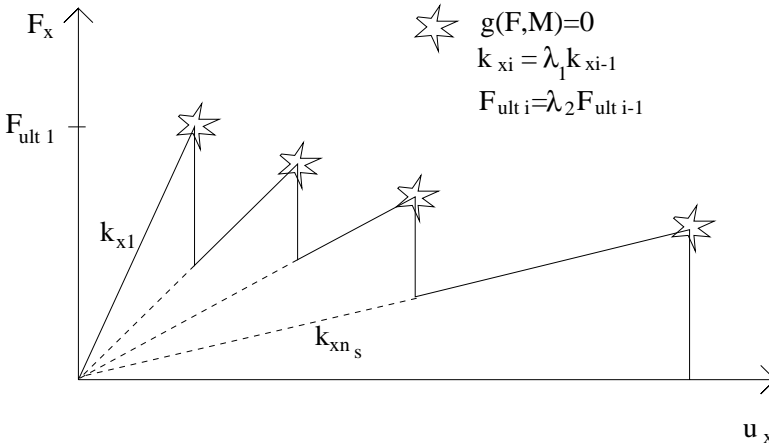


Figure 3.7: *Stick-slip fracture performance of a bond consisting of uncoupled springs.*

Table 3.4: *Parameters defining a bond made of uncoupled springs, used in 2D.*

Parameter	Notation 2D
Initial translational spring stiffness	$k_x = k_y \in N_{k_x}$
Initial rotational spring stiffness	$k_\phi \in N_{k_\phi}$
Initial ultimate force	$F_{ult} \in N_{F_{ult}}$
Initial ultimate moment	$M_{ult} \in N_{M_{ult}}$
Reduction of stiffness at slip	$\lambda_1 \in N_{\lambda_1}$
Reduction of strength at slip	$\lambda_2 \in N_{\lambda_2}$
Number of slips before complete failure	$n_s$

When fibres in an air stream are blown towards a permeable wire the result is a much more three-dimensional structure, where the fibres are not in such good contact with each other as in the case of paper, and where there is inter-fibre contact the bonds are much weaker.

To model this kind of network geometry is a complicated issue. Modelling of the full dynamic process of fibres flowing turbulently in the air and landing on the wire and connecting to other fibres lies well in the future when even more efficient computational methods and computers will be available. Today, it is necessary to use a simplified approach. One reasonably simple approach is to place fibres at random, independent of each other, in space. This method has the benefit of being relatively fast and easy to implement, but it also has drawbacks. One problem is the non-physical assumption of the fibres' positions being independent of each other, which is obviously not the truth considering the production process. This

assumption probably also leads to fewer bonds than in a real network, a drawback which can be compensated for by forming bonds, even if the distance between fibre centre lines is slightly greater than the fibre extension. A 2D network is a further simplification, but many fundamental characteristics of a heterogeneous structure can probably still be captured in this kind of model.

In this work, the network structure was obtained by successively placing fibres in the studied cell, which in the 3D case is a box of dimensions  $L_x$ ,  $L_y$  and  $L_z$ , and in the 2D case, a rectangle of dimensions  $L_x$  and  $L_y$ . The fibres are positioned independently of each other in the cell. The location of a fibre centre in the cell is random and the fibre orientation is decided according to an arbitrary orientation distribution. Fibre orientation is defined by the distributions of the angles  $\alpha$ ,  $\beta$  and  $\gamma$ .  $\alpha$  is the angle of the fibre relative to the  $x$ -axis, or in 3D, the angle of the fibre's projection onto the  $xy$ -plane relative to the  $x$ -axis.  $\beta$  and  $\gamma$  apply only to 3D networks and denote the angle between the line between the fibre end-points and the  $xy$ -plane and the position of a curled fibre around its own axis, respectively. It should be noted that in order to obtain a nominally isotropic network, a non-uniform distribution of  $\beta$  must be used. For an isotropic orientation distribution, the number of fibres having a certain orientation should be proportional to the corresponding part of the area of a sphere. Since the part of a sphere of radius  $r_s$  which is defined by the interval  $\beta_1 < \beta < \beta_2$  is

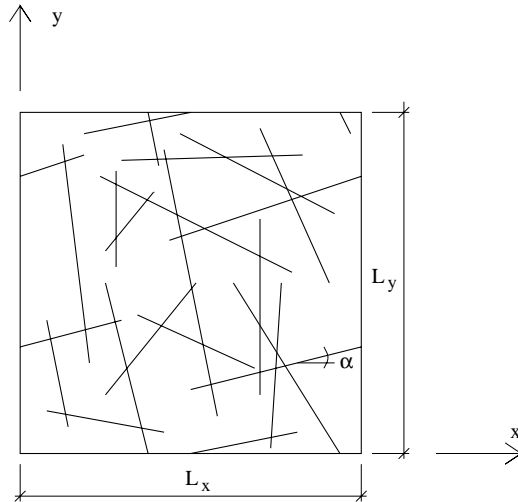
$$\frac{1}{2\pi r_s^2} 2\pi r_s^2 \int_{\beta_1}^{\beta_2} \cos \beta d\beta = \sin \beta_2 - \sin \beta_1 \quad , \quad (3.9)$$

this is the part of the fibres which should have an angle  $\beta$  in the interval  $\beta_1 < \beta < \beta_2$  in a nominally isotropic network. The number of fibres in a cell is determined from the network density,  $\rho$ , defined as the total fibre length per unit volume or unit area, and the degree of heterogeneity which is discussed later in this section.

The network geometry is periodic, such that opposite sides of the area or volume studied match, as shown in Figure 3.8. This allows the cell under observation to be regarded as one of many identical cells making up a global structure. It also allows periodic boundary conditions to be specified. These are discussed in Chapter 6.

When two fibres intersect, there is the possibility of interaction between the fibres. In the 3D model a possible bond site is assumed to exist when the distance between two fibre centre lines is shorter than an arbitrary interaction distance,  $e$ . This assumption implicitly assumes a circular fibre cross-section of diameter  $e$  when detection of bonds is considered, even though the fibre cross-section is not assumed to be circular when stiffness is concerned. In 2D analysis there is a possible bond site at each fibre crossing and it is not necessary to define the diameter of the fibre. At each possible bond site, the probability of a bond is denoted  $s$ .  $s$  can be used to simulate a 3D effect in a 2D network, in which a fibre crossing in the  $xy$ -plane does not automatically imply a bond.

The degree of heterogeneity of a network is an interesting issue. The heterogeneity of paper is often quantified by a formation spectrum which describes the mass variation between different areas of the paper as a function of area size. The

Figure 3.8: *2D network cell of periodic geometry.*

rather complicated expression for the formation spectrum of a 2D random sheet is given in [34]. A formation spectrum is one way of quantifying the heterogeneity of a given network. In the method used to generate a network here, a simpler one-parameter definition of heterogeneity is used. The heterogeneity is defined as the volume (area),  $V_h$ , for which the number of fibres per unit volume (area) is given as an exact number. The distribution of the fibres within  $V_h$  is random.  $V_h$  can be infinite, larger than, equal to or smaller than the network volume (area)  $V_0$  which is to be generated. The implementation supports values of  $V_h \geq V_0$ . A high value of  $V_h$  implies a comparatively high heterogeneity while a low value of  $V_h$  implies a more homogeneous material. For the case  $V_h > V_0$  the number of fibres,  $n_f$ , in  $V_0$  is binomially distributed, [23]. If a large number of fibres,  $n_h$ , is deposited independently and randomly in  $V_h$ , the probability that there are  $n_f$  fibres,  $P(n_f)$ , in a cell of size  $V_0$  is

$$P(n_f) = \binom{n_h}{n_f} \left(\frac{V_0}{V_h}\right)^{n_f} \left(1 - \frac{V_0}{V_h}\right)^{n_h - n_f} . \quad (3.10)$$

If  $n_h$  and  $V_h/V_0$  are large and  $\bar{n}_h = n_h/V_h$  is of moderate size, this reduces to the Poisson approximation to the Binomial distribution:

$$P(n_f) = \frac{e^{-\bar{n}_h} \bar{n}_h^{n_f}}{n_f!} \quad (3.11)$$

The number of fibres in  $V_0$  is thus different in different simulations of nominally identical networks. That is, if  $V_h = \infty$  and a cell of size  $V_0$  is to be analysed, the number of fibres in the cell should be chosen from the Poisson distribution  $\text{Po}(\bar{n}_h) = \text{Po}(\rho V_0)$ .

The parameter  $V_h$  gives the possibility to change the size of the simulated volume  $V_0$  without changing the nominal heterogeneity of the network. However, this one-parameter description does not allow the generation of a network with an arbitrary formation spectrum; this would require a more complex generation strategy. Most simulations presented in this thesis were made with  $V_h = V_0$ .

The parameters defining the network cell geometry are given in Table 3.5.

Table 3.5: *Parameters defining network cell geometry.*

Parameter	Notation	
	2D	3D
Size of cell	$L_x, L_y$	$L_x, L_y, L_z$
Network density	$\rho$	$\rho$
Orientation of fibre	$\alpha \in N_\alpha$	$\alpha \in N_\alpha, \beta \in N_\beta, \gamma \in N_\gamma$
Maximum interaction distance		$e$
Probability of bond at crossing	$s$	$s$
Degree of heterogeneity	$V_h$	$V_h$

### 3.4. Remarks on heterogeneity and periodic geometry

The concept of periodic geometry and the degree of heterogeneity parameter opens up several possibilities for performing stiffness simulations and interpreting the results. One straightforward approach is to set  $V_h = V_0$  and simulate an infinite network made up of identical cells. The resulting homogenized properties, e.g. elastic modulus,  $E$ , vary if several simulations are performed on nominally identical networks. This is illustrated in Figure 3.9 for the case  $V_h = V_0$ , as different values of  $E$  for the same number of fibres in the cell,  $n_f$ . The variation is due to differences in the structure and element properties of the different unit cells. If each simulation is assumed to represent an infinite network made up of identical cells, the arithmetic mean value of  $E$  is taken to represent the average of several networks.

If, however,  $V_h$  is set to infinity, the situation becomes more complicated, but perhaps more realistic. The task is then to simulate the stiffnesses of several cells, where the number of fibres in each cell is chosen from the Poisson distribution. The stiffness of one of these cells is then obtained by assuming that it forms part of an infinite network made up of identical cells. This is in contradiction to what was stated above about the varying number of fibres in the different cells, but it probably provides a fair approximation of the stiffness of a certain cell in the varied-cell network. The results of this kind of simulation series are illustrated in Figure 3.9 for the case  $V_h \gg V_0$ . The evaluation of the stiffness of the infinite network from the distribution of stiffnesses of the individual cells in principle require its own micro-

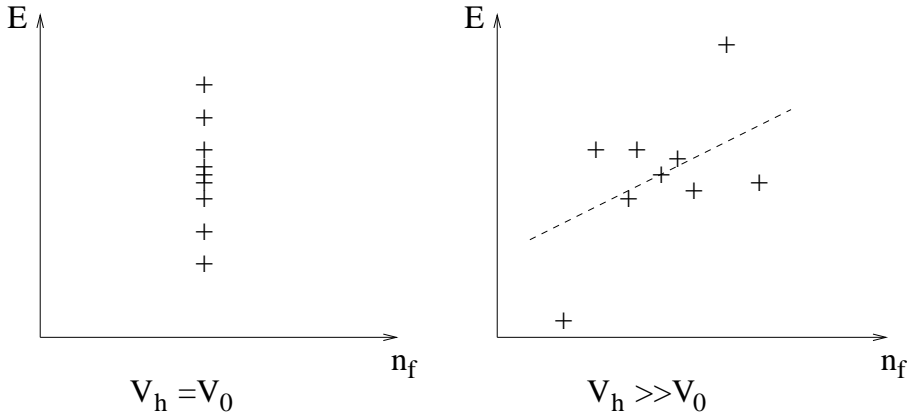


Figure 3.9: *Illustration of stiffness results for different values of  $V_h$ .*

mechanical study. An estimate of the global stiffness can be obtained from [13]:

$$E = (\sum(V_i E_i)^n)^{1/n} \quad (3.12)$$

This equation assumes that the Poisson ratio,  $\nu$ , equals zero.  $E_i$  denotes the elastic modulus of a single cell and  $V_i$  denotes the part of the total volume occupied by the cell.  $n=1$  corresponds to parallel coupling of all the cells and  $n = -1$  corresponds to serial coupling. Serial and parallel coupling are the extreme cases and  $n$  should be chosen such that

$$-1 \leq n \leq 1 \quad . \quad (3.13)$$

If  $E$  is assumed to be a linear function of  $n_f$ , which according to results in Section 7.3 could be realistic for higher network densities, and  $n$  is chosen to be 1, the resulting value of  $E$  is the same as that obtained for  $V_h = V_0$ . The spread in the results for the same number of simulations is however larger, as is illustrated in Figure 3.9. This is consistent with the higher degree of heterogeneity.

The above discussion applies mainly to elastic stiffness where size effects are not very strong. In determining the strength of a heterogeneous material, the effect of sample size can never be avoided. This is further discussed in Chapter 8.

## 4. GENERATION AND ANALYSIS OF GEOMETRY

The analysis of a fibre network can be divided into two main parts: generation and analysis of the network geometry, and analysis of the mechanical properties of the network structure. The first part, which is described in this chapter, consists of reading in input, generating a network, processing it as is described below and preparing the necessary input data for the subsequent analysis of the mechanical properties. The main structure of the geometry generation code is illustrated by Figure 4.1.

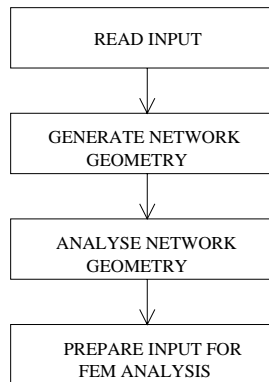


Figure 4.1: *Main structure of the geometry generation code.*

### 4.1. Input data

Input parameters related to the network are listed in Chapter 3. Many of the input parameters are given in terms of a statistical distribution. The statistical distribution is quantified by a cumulative distribution function composed of straight line segments. In Figure 4.2 an example is given of a hypothetical experimental distribution and an approximation of this curve made up of three straight lines. The input to the program is the two vectors of interval boundaries of probability and values of the variable:  $(0, p_1, p_2, p_3)$  and  $(0, v_1, v_2, v_3)$ . If the variable was constant at value  $v$ , the vectors would be  $(0, 1)$  and  $(v, v)$ . If a random number  $p$

is obtained from a random number generator, the variable is given the value  $v$ , as indicated by the dotted line in Figure 4.2.

For each variable given in the form of a statistical distribution, a random seed is given. This implies that identical networks are reproduced if the same seeds are given in two simulations.

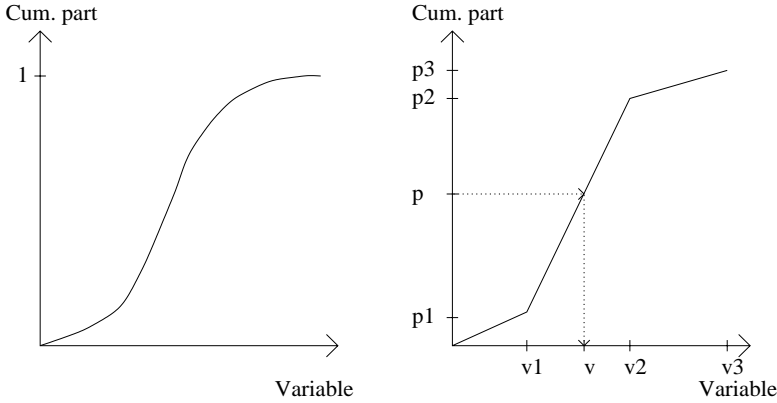


Figure 4.2: *Statistical distribution and approximation consisting of straight lines.*

## 4.2. Generation of network geometry

Network geometry generation is here mainly discussed in relation to 3D networks. The generation of 2D networks is, in many respects analogous, but simpler, and is discussed in detail in [20].

A fibre network is generated by sequentially placing fibres in a cell of dimensions  $L_x, L_y$  and  $L_z$ , until the desired number of fibres, determined by the network density and degree of heterogeneity, is reached. That is, since the number of fibres is an integer, the network density may not be exactly as specified. The steps through which one fibre is added to the network are illustrated in Figure 4.3.

A fibre is generated by assigning to it values of all the parameters given in Table 3.1, as well as the orientation angles  $\alpha, \beta$  and  $\gamma$ . The values of these parameters are calculated from the statistical distributions according to the principles described in Section 4.1. The input variables relevant for defining the position and orientation of a fibre are  $l_f, c, \alpha, \beta$  and  $\gamma$ .

The fibre is deposited by placing its mid-point inside the cell; for a curved fibre the mid-point is defined as  $\mathbf{m}$  in Figure 4.4. The distribution of fibre mid-points in the cell is such that there is equal probability of a fibre mid-point being placed anywhere in the cell, and the placement of one fibre is independent of the position of the other fibres.

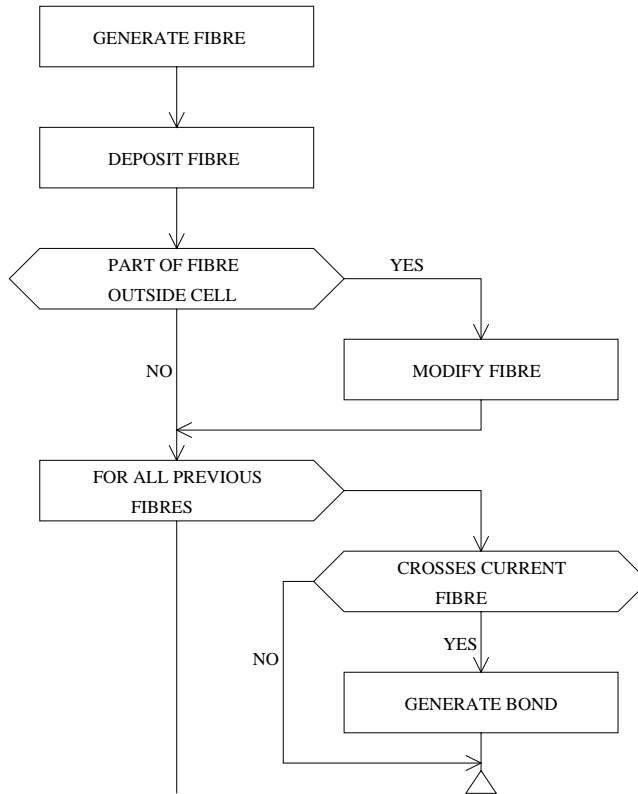


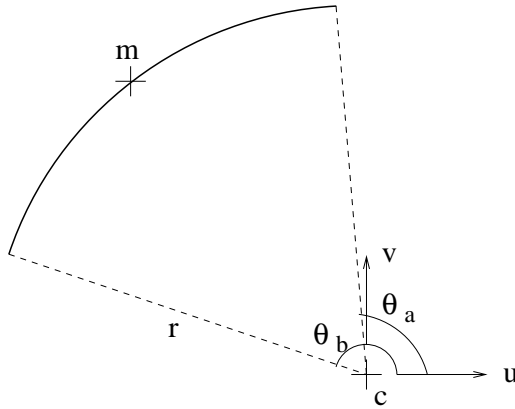
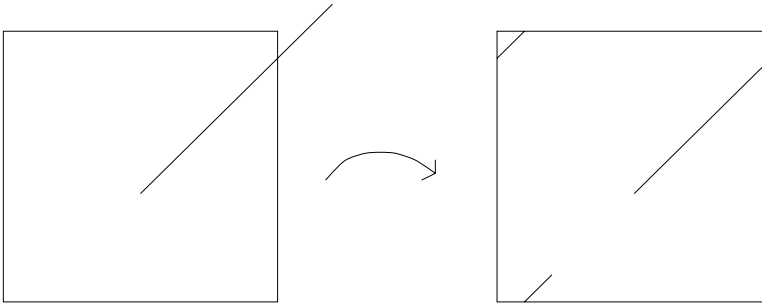
Figure 4.3: Steps through which one fibre is added to the network.

The parameters suitable for defining the geometry and location of a fibre for computational purposes are the centre point,  $\mathbf{c}$ , the radius of curvature  $r$ , two unit vectors in the plane of the fibre which constitute a positively oriented orthonormal coordinate system,  $\mathbf{u}$  and  $\mathbf{v}$ , and angles relative to  $\mathbf{u}$  between which the fibre extends,  $\theta_a, \theta_b$ .  $\mathbf{u}$  is chosen as the unit vector in a fibre plane whose projection on the  $xy$ -plane is parallel to the  $x$ -axis. These parameters are illustrated in Figure 4.4, and are calculated from the input parameters mentioned above, as is shown in Appendix A. Thus, a point on the fibre,  $\mathbf{x}$ , is defined by

$$\mathbf{x} = \mathbf{c} + r \cos \theta \mathbf{u} + r \sin \theta \mathbf{v} \quad , \quad \theta_a \leq \theta \leq \theta_b \quad . \quad (4.1)$$

In the case of 2D modelling,  $\mathbf{u}$  and  $\mathbf{v}$  are unit vectors parallel to the  $x$ - and  $y$ -axes, respectively, for all the fibres and this reduces the amount of information that must be stored in the computer.

Since the geometry is assumed to be periodic, a fibre must be modified if part of it extends outside the cell under investigation; the principle for this modification is illustrated for the 2D model in Figure 4.5.

Figure 4.4: *Definition of circle arc fibre.*Figure 4.5: *Modification of fibre that extends outside the cell.*

When a fibre has been deposited, it is checked for crossing points with all previous fibres. In a 3D simulation, a crossing is assumed to occur if the distance between two fibre centre lines is shorter than  $e$ . The essence of detecting crossings is thus to determine the shortest distance between two fibres; Two fibres are described by (4.1):

$$\begin{aligned} \mathbf{x}_1 &= \mathbf{c}_1 + r_1 \cos \theta_1 \mathbf{u}_1 + r_1 \sin \theta_1 \mathbf{v}_1 \\ \mathbf{x}_2 &= \mathbf{c}_2 + r_2 \cos \theta_2 \mathbf{u}_2 + r_2 \sin \theta_2 \mathbf{v}_2 \end{aligned} \quad (4.2)$$

The distance,  $d$ , between two points on the fibres defined by angles  $(\theta_1, \theta_2)$  is then

$$\begin{aligned}
d(\theta_1, \theta_2) = & ((\mathbf{x}_1 - \mathbf{x}_2)(\mathbf{x}_1 - \mathbf{x}_2)^T)^{\frac{1}{2}} = \\
& \mathbf{c}_1 \mathbf{c}_1^T - 2\mathbf{c}_1 \mathbf{c}_2^T + \mathbf{c}_2 \mathbf{c}_2^T + r_1^2 + r_2^2 \\
& + (\mathbf{c}_1 \mathbf{u}_1^T - \mathbf{c}_2 \mathbf{u}_1^T) 2r_1 \cos \theta_1 \\
& + (\mathbf{c}_1 \mathbf{v}_1^T - \mathbf{c}_2 \mathbf{v}_1^T) 2r_1 \sin \theta_1 \\
& + (\mathbf{c}_2 - \mathbf{c}_1) \mathbf{u}_2^T 2r_2 \cos \theta_2 \\
& + (\mathbf{c}_2 - \mathbf{c}_1) \mathbf{v}_2^T 2r_2 \sin \theta_2 \\
& - 2\mathbf{u}_1 \mathbf{u}_2^T r_1 r_2 \cos \theta_1 \cos \theta_2 \\
& - 2\mathbf{u}_1 \mathbf{v}_2^T r_1 r_2 \cos \theta_1 \sin \theta_2 \\
& - 2\mathbf{v}_1 \mathbf{u}_2^T r_1 r_2 \sin \theta_1 \cos \theta_2 \\
& - 2\mathbf{v}_1 \mathbf{v}_2^T r_1 r_2 \sin \theta_1 \sin \theta_2 .
\end{aligned} \tag{4.3}$$

The minimum value of  $d$  can be determined by differentiating  $d$  with respect to  $\theta_1$  and  $\theta_2$ , setting the derivatives equal to zero and solving the resulting system of two non-linear equations in two unknowns. The two non-linear equations can also be obtained by using the condition that if the two points on the fibres which are closest to each other are joined by a line, this line is perpendicular to the tangents of the fibres at both points. It is, however, not easy to calculate the minimum value of  $d$  analytically. Therefore, it was decided to use a numerical approach. The method used is simply to calculate  $d$  for a large number of points  $(\theta_1, \theta_2)$ , and to refine the search in the area where  $d$  is smallest. This is a very time-consuming part of the network generation. A steepest-descent scheme was also tested, but this strategy was not always stable and was no faster. In 2D simulations, there is possibility of a bond occurring wherever two fibres cross. The problem of finding crossings of circle arcs on a plane is simpler, and an algorithm can be found in [20].

If a crossing is found, a bond is created with the probability  $s$ . A bond is created by assigning to it the properties listed in Section 3.2.1 and assigning the coordinates of the bond to the fibres involved. Topological information concerning the bond is also stored.

### 4.3. Analysis of network geometry

The network geometry is treated and analysed as indicated in Figure 4.6. In order to analyse the mechanical properties of a network by means of the finite element method (FEM) the fibres must first be divided into beam elements. Each fibre segment between two bonds, between a boundary and a bond or between two boundaries of the network is made into one beam element. To do this, the coordinates of the bonds on a certain fibre must be sorted in their order along the fibre, since these points are also the end-points of the beam elements. The fibre segments which are free ends of fibres with only one, or possibly no end, situated on the boundary or bonded to another fibre are not made into beam elements. This is because they would be zero-stress elements that have no influence on the network's behaviour.

Before the network structure can be analysed by FEM it must be established that the network is indeed a connected structure, and not composed of several separate

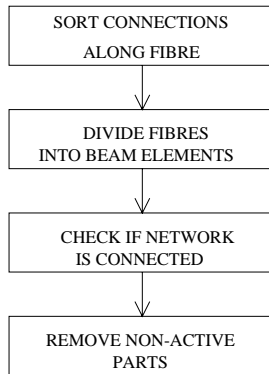


Figure 4.6: *Analysis of network geometry.*

clusters of fibres, since this results in a degenerate system of equations. This is usually only a real issue in the case of network densities close to the percolation threshold. For 3D simulations there is, theoretically, even the possibility of several separate connected structures. The algorithm used for verifying connectedness is discussed and presented in Appendix B.

An interesting geometrical property is the active part of a network. Non-active parts, are those parts which are in a state of zero stress regardless of loading at the boundary of the network. In Figure 4.7 the non-active parts of a 2D network are shown by dashed lines. Most of the zero-stress fibres are removed from the network

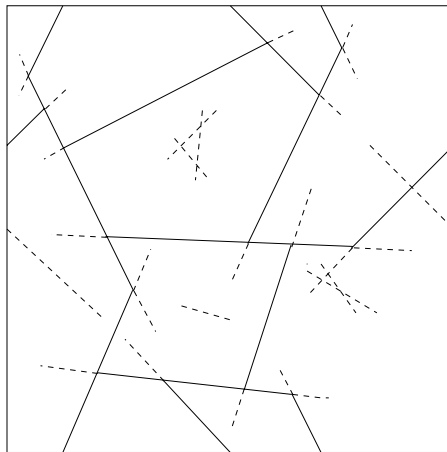


Figure 4.7: *A fibre network with non-active parts shown dashed.*

by not making free fibre ends into beam elements, but there may still be small

clusters of fibres not in contact with the rest of the network. These must also be removed in order to provide a positive definite system stiffness matrix. In addition to isolated clusters of fibres, there may be clusters of fibres in contact with the rest of the network by only one fibre. These are also zero-stress elements, and could be removed in order to save degrees of freedom, and to yield the exact percentage of the fibres that take an active part in the load-carrying structure. If the aim is to obtain the network stiffness, it is, however, doubtful if it is worthwhile to remove clusters connected to the rest of the structure by only one fibre, since they are uncommon in fairly dense networks and detecting them is an extremely time-consuming task. The detection of zero-stress fibres is carried out in connection with the verification of the connectedness of the network, and the method is briefly described in Appendix B.

#### 4.4. Output from geometry unit

A number of output parameters are obtained from the analysis of the network geometry. These are

- the number of beam elements and total beam length,
- the number of fibre crossings (2D)/possible bond sites (3D)
- the number of bond elements,
- whether the structure is connected or not,
- the active part of the network, for 2D,
- the number of degrees of freedom in the FEM model.

When the final network structure has been obtained, all necessary data defining the FEM model are formatted according to the standards of the FEM code used for the analysis of mechanical properties.

In order to visualize the network, geometry data are prepared for the visualisation package specially developed for this purpose by Olsson, [42]. This consists of Matlab routines, [37], which produce a VRML file, [63], representing the network, which can be viewed on a computer with a standard Internet browser. The images of 3D networks in the report were further processed in the program 3D Studio, [62], to obtain better printing quality. Figure 9.46 was produced using the program Fibre-Scope, [33], which was written for real-time visualisation of fibre networks under deformation. In 2D simulations the visualization process is simpler and in this case, the Moviestar pre- and post-processing package was used.



## 5. RESULTS OF GEOMETRY ANALYSIS

### 5.1. Basic example networks

Figures 5.3 and 5.4 show examples of 2D and 3D network structures. Unless indicated otherwise the results cited in Chapters 5 and 7 refer to networks with the same nominal properties as those defined in the basic example networks of Figures 5.3, 5.4 and Table 5.1. The values in Table 5.1 correspond roughly to mean values of what is known and believed to be true about dry-shaped cellulose fibre materials, although some simplifications have been made to facilitate the simulations.

An example of a fibre length distribution, from [56], of a CTMP fluff (prepared using a chemical-thermo-mechanical process) is shown in Figure 5.1. The two curves are the cumulative population distribution of fibre length (the percentage of the number of fibres that is shorter than a predefined length) and the cumulative weighted distribution of fibre length (the percentage of the total fibre length that consists of fibres shorter than a predefined length). The arithmetic mean fibre length is  $\bar{l}_f^a = 1.34$  mm, and the weighted mean fibre length is  $\bar{l}_f^w = 2.18$  mm, where

$$\bar{l}_f^a = \frac{\sum_{i=1}^{n_f} l_{fi}}{n_f} \quad (5.1)$$

and

$$\bar{l}_f^w = \frac{\sum_{i=1}^{n_f} l_{fi}^2}{\sum_{i=1}^{n_f} l_{fi}}. \quad (5.2)$$

The mean fibre lengths given above were calculated ignoring fibres shorter than 0.11 mm; the extremely short fibres are, however, included in the figure. The arithmetic mean fibre length of all fibres is approximately 1.0 mm; the weighted mean fibre length is less affected by ignoring short fibres. For the basic example networks we chose to use a constant fibre length equal to the arithmetic mean value of the fibre length for all the fibres, i.e. 1.0 mm.

The fibres in the 2D network are straight, while a curl index of 0.91 was chosen for the 3D network.

The cross section of a cellulose fibre varies between different tree species as well as between earlywood and latewood fibres. Figure 5.2 shows a typical fibre cross section and the simplified cross section used in the calculations. When a suitable cross section has been chosen, the problem of deciding in what direction the bending occurs remains. We chose to study a spirally shaped fibre which has an effective

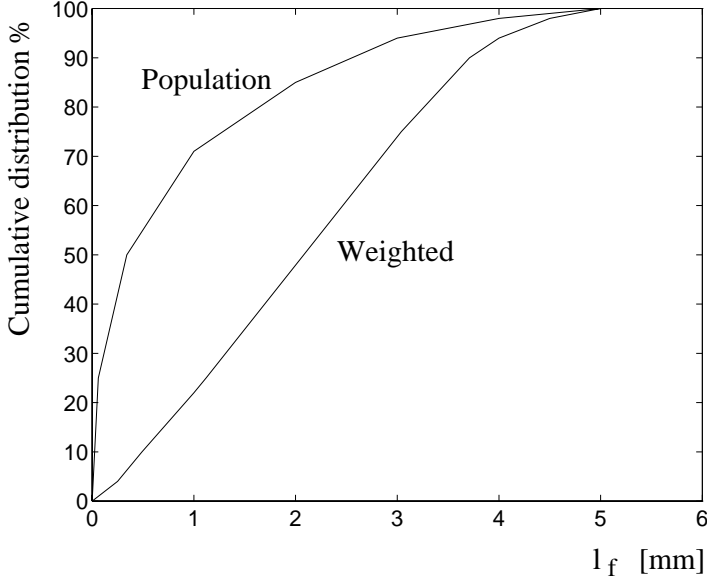


Figure 5.1: *Cumulative distributions of fibre length.*

bending stiffness,  $I_f^e$ ,

$$I_f^e = \frac{b_f^3 h_f^3}{6(b_f^2 + h_f^2)} , \quad (5.3)$$

$b_f$  denoting width and  $h_f$  the depth of cross section, see Appendix C. As discussed in Section 6.1.1, a modified bending stiffness,  $J$ , is used instead of  $I$  for curved beams. For the 3D basic example network, however, the ratio  $(h_f/2r)^2$  is much less than 1, and the difference between  $I$  and  $J$ , can be neglected. For the basic example networks we thus used a cross-sectional area of

$$A_f = 7 \cdot 10^{-6} \cdot 35 \cdot 10^{-6} = 2.5 \cdot 10^{-10} \text{ m}^2 ,$$

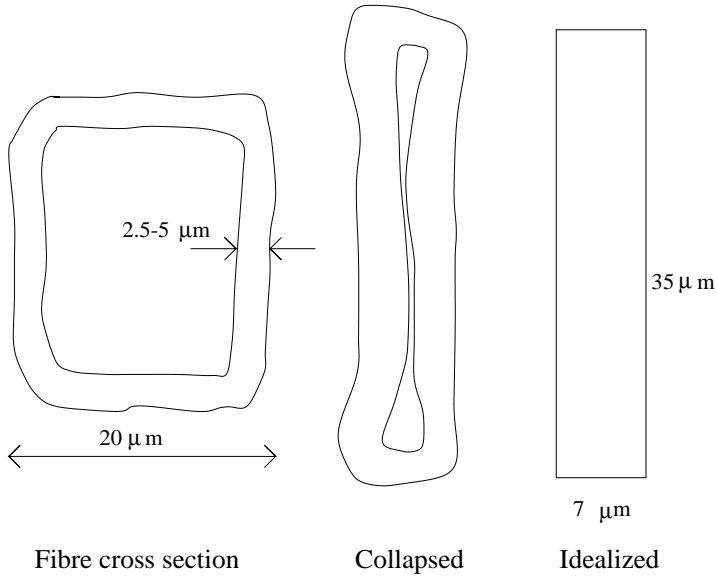
and moments of inertia

$$I_f = J_{zf} = J_{yf} = \frac{(7 \cdot 10^{-6})^3 \cdot (35 \cdot 10^{-6})^3}{6((7 \cdot 10^{-6})^2 + (35 \cdot 10^{-6})^2)} = 20 \cdot 10^{-22} \text{ m}^4 .$$

These values of  $A_f$  and  $I_f$  define a new rectangular effective cross section of

$$h_f^e = \sqrt{\frac{12I_f}{A_f}} = 9.8 \cdot 10^{-6} \text{ m} , \quad (5.4)$$

$$b_f^e = \frac{A_f}{h_f^e} = 25.5 \cdot 10^{-6} \text{ m} , \quad (5.5)$$

Figure 5.2: *Idealization of fibre cross section.*

which is used in 2D fracture simulations where the depth of the cross section enters the calculations. The torsional constant,  $K_{vf}$ , for a solid rectangular fibre cross section is, [48],

$$K_{vf} = \eta h_f b_f^3 = 0.288 h_f b_f^3 = 35 \cdot 10^{-22} \text{ m}^4, \quad (5.6)$$

where the value of the constant  $\eta$  depends on the ratio  $b_f/h_f$ .

The elastic modulus for a cellulose fibre also varies between different species and earlywood and latewood, but we chose 35 GPa as a typical value, [29]. The shear modulus,  $G_f$ , was set to 2.6 GPa, see [30].

There is a lack in knowledge regarding inter-fibre bond properties, due to experimental difficulties. For the 2D basic example network we therefore estimated the stiffness  $k_x$  to be  $E_f A_f / l_f$ , and  $k_\phi$  to be  $4E_f I_f / l_f$  for a 1 mm fibre. These values correspond to the axial and bending stiffness of a 1 mm fibre. For 3D simulations, we chose a bond area of radius  $1 \cdot 10^{-5}$  m. A value of  $k_n$  of  $3 \cdot 10^{13}$  Pa/m then gives approximately the same axial and bending stiffness as a 1 mm fibre.  $k_t$  was chosen to be 1/10 of this value, i.e.  $3 \cdot 10^{12}$  Pa/m.

We assumed a bond in every fibre crossing point and a uniform orientation distribution. The minimum distance for a bond to occur in a 3D network,  $e$ , was set to  $20 \cdot 10^{-6}$  m.  $\rho$  was set to  $60 \text{ mm}^{-1}$  for the 2D network. This means that the mean number of bonds per fibre, obtained as the total number of bonds from (2.1) divided by the number of fibres and multiplied by two, is 37. This value is probably rather high for a dry-shaped cellulose fibre fluff. For the 3D network,  $\rho$  was set to  $145 \text{ mm}^{-2}$ , which corresponds to about 5 bonds per fibre. The side-length of the

studied cell was 1.2 mm and the heterogeneity parameter  $V_h$  was set equal to the size of the studied cell.

The input parameters of the basic example networks are listed in Table 5.1. Tables 5.2 and 5.3 give some geometry output parameters for the basic example networks as well as the mean values from ten different networks that have the same nominal properties as the basic example networks. For the definition of the active part, see Section 5.3.

Table 5.1: *Input parameters for the basic example networks.*

Parameter	Value and unit-2D	Value and unit-3D
$l_f$	1 mm	1 mm
$\kappa$	$0 \text{ mm}^{-1}$	-
$c$	-	0.91
$A_f$	$2.5 \cdot 10^{-10} \text{ m}^2$	$2.5 \cdot 10^{-10} \text{ m}^2$
$I_f, J_{zf}$	$2.0 \cdot 10^{-21} \text{ m}^4$	$2.0 \cdot 10^{-21} \text{ m}^4$
$J_{yf}$	-	$2.0 \cdot 10^{-21} \text{ m}^4$
$K_{vf}$	-	$3.5 \cdot 10^{-21} \text{ m}^4$
$E_f$	$35 \cdot 10^9 \text{ Pa}$	$35 \cdot 10^9 \text{ Pa}$
$G_f$	-	$2.6 \cdot 10^9 \text{ Pa}$
$A_b$	-	$3.1 \cdot 10^{-10} \text{ m}^2$
$k_n$	-	$3.0 \cdot 10^{13} \text{ Pa/m}$
$k_t$	-	$3.0 \cdot 10^{12} \text{ Pa/m}$
$k_{x1} = k_{y1}$	$8750 \text{ N/m}$	-
$k_{\phi 1}$	$2.8 \cdot 10^{-7} \text{ Nm/rad}$	-
$L_x, L_y, L_z$	1.2 mm	1.2 mm
$\rho$	$60 \text{ mm}^{-1}$	$145 \text{ mm}^{-2}$
$N_\alpha$	$\frac{1}{\pi}, \quad 0 < \alpha < \pi$	$\frac{1}{\pi}, \quad 0 < \alpha < \pi$
$N_\beta$	-	$\cos \beta, \quad 0 < \beta < \pi/2$
$N_\gamma$	-	$\frac{1}{\pi}, \quad 0 < \gamma < \pi$
$e$	-	$20 \cdot 10^{-6} \text{ m}$
$s$	1.0	1.0
$V_h$	$1.44 \text{ mm}^2$	$1.73 \text{ mm}^3$

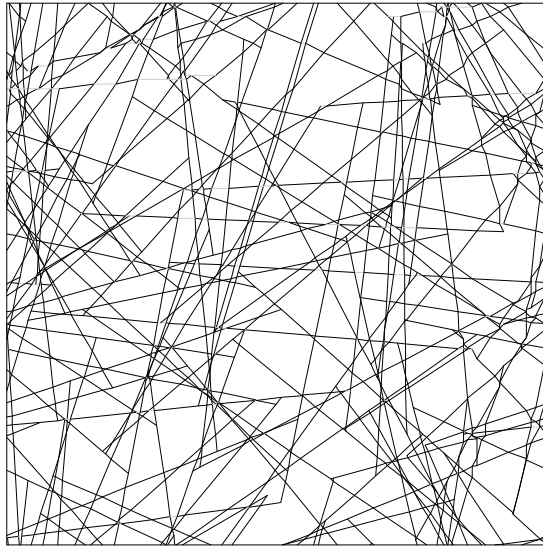
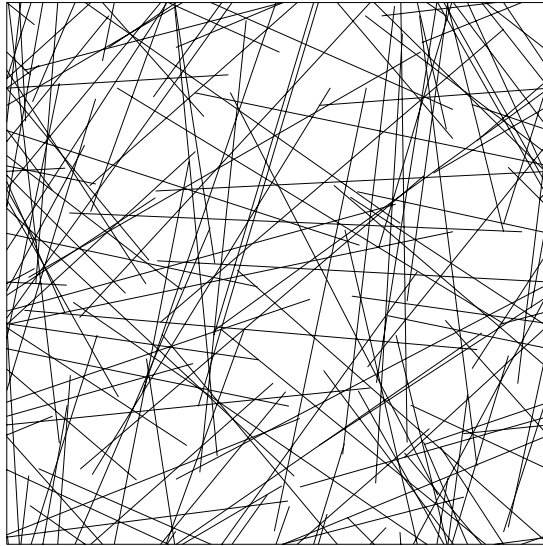


Figure 5.3: *a) 2D basic example network geometry. b) 2D basic example network with non-active parts removed.*

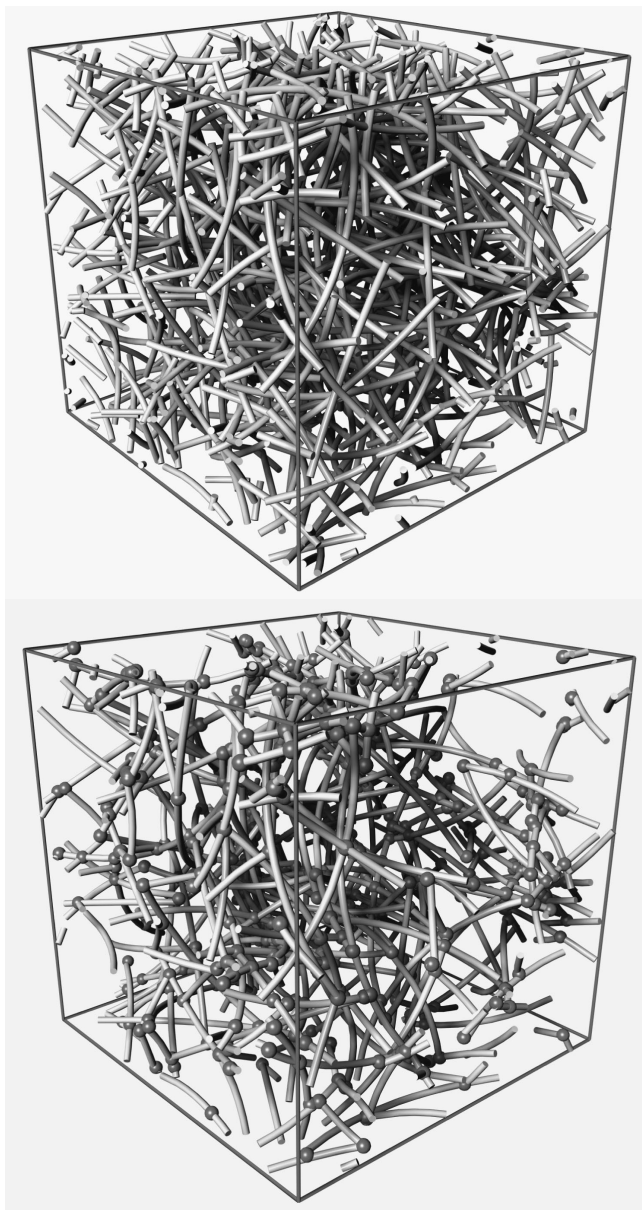


Figure 5.4: a) 3D basic example network geometry. b) 3D basic example network, FEM model of active part.

Table 5.2: *Geometry output for the 2D basic example network and for ten other nominally identical networks generated by other random number seeds.*

Parameter	Result for basic example network	Result for ten nominally identical networks	
		Average value	Standard deviation
Number of fibres	86	86	0
Total fibre length	86 mm	86 mm	0 mm
Number of fibre segments	3213	3228	25
Number of fibre crossings	1603	1612	14
Mean no. of crossings/fibre	37	37	0.3
Structure connected	yes	yes, all	-
Active part	95.3%	94.8%	0.6%
Number of beams in FEM model	3211	3223	25
Number of bonds in FEM model	1603	1611	13
Degrees of freedom in FEM model	10164	10181	64

Table 5.3: *Geometry output for the 3D basic example network and for ten other nominally identical networks generated by other random number seeds.*

Parameter	Result for basic example network	Result for ten nominally identical networks	
		Average value	Standard deviation
Number of fibres	250	250	0
Total fibre length	250 mm	250 mm	0 mm
Number of possible bond sites	564	566	13
Mean no. of bond sites/fibre	4.5	4.5	0.1
Structure connected	yes	yes, all	-
Number of beams in FEM model	1052	1044	43
Number of bonds in FEM model	555	560	15
Degrees of freedom in FEM model	8856	8723	368

## 5.2. Number of fibre crossings

The average number of fibre crossings,  $\bar{n}_c$ , in a 2D random assembly of fibres with a uniform orientation distribution is, according to Kallmes and Corte [23],

$$\bar{n}_c^{2D} = \frac{(n_f \bar{l}_f)^2 \bar{c}^2}{L^2 \pi} . \quad (5.7)$$

The corresponding relation for 3D networks of straight fibres is, [31],

$$\bar{n}_c^{3D} = \frac{(n_f \bar{l}_f)^2 \pi d}{4L^3} , \quad (5.8)$$

where  $d$  is the fibre diameter. Generally, there is a much stronger tendency for fibres to cross when they are located in a plane than when they are distributed in space. To have any crossings at all in a 3D network it is necessary to define the diameter,  $d$ , of the fibres. The parameter corresponding to fibre diameter in the model in Chapter 3 is  $e$ . By means of (5.7) and (5.8) the degree of bonding,  $s$ , in a 2D network of straight fibres which gives the same number of crossings as in a 3D network for the same amount of fibres, can be calculated:

$$s = \frac{\pi^2 d}{4L} \quad (5.9)$$

For  $d = 0.02$  mm and  $L = 1.2$  mm this yields  $s = 0.04$ . This emphasizes the fact that many more fibres are required to obtain a connected network in 3D.

For the basic 2D example network, (5.7) gives 1635 crossings, and this agrees well with the value of 1612 crossings obtained as the mean value for ten simulated networks, see Table 5.2. The standard deviation, as obtained by the numerical simulations, is equal to 14 crossings. For the basic 3D example network, (5.8) gives 568 crossings and the mean value from ten simulated networks is 566. The standard deviation is 13 crossings.

According to (5.7) and (5.8) the number of fibre crossings in a network of straight fibres with a uniform orientation distribution depends only on the total fibre length,  $n_f \bar{l}_f$ . This agrees well with results from simulations, see Figure 5.5. This diagram shows the number of crossings in a 2D network relative to the number of crossings predicted by (5.7). The network density is  $20 \text{ mm}^{-1}$ , and the orientation distribution is uniform. The variable on the  $x$ -axis is fibre length  $l_f$ , i.e. all networks have the same network density, but the networks on the left are made up of many short fibres and those on the right are made of fewer but longer fibres. The  $L/l_f$  ratio is 1.2, except for fibre lengths 10 and 12 mm where it is only 1.0 and 0.8, respectively. This is to avoid an unreasonably large number of crossings. Ten simulations were performed for each fibre length considered; the mean value of these is shown as a dashed line. The values are slightly more scattered for the smallest values of  $l_f$ , and for  $l_f = 12$  mm there is a decrease to  $n_c/n_{c_{eq.(5.7)}} = 0.97$ . This is probably because there are so few fibres that the orientation distribution is no longer uniform, the latter being an assumption made in the derivation of (5.7). This assumption of

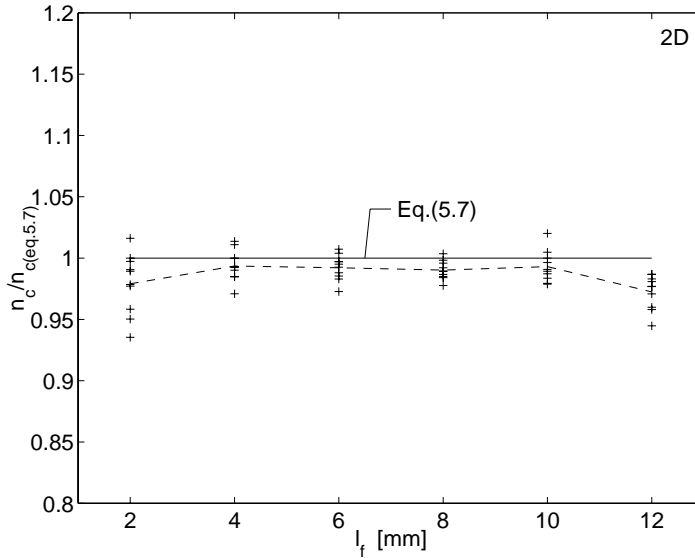


Figure 5.5: Normalized value of  $n_c$  plotted against fibre length,  $l_f$ .

ideal uniformity may also be the reason why  $\bar{n}_c$  from (5.7) in general seems to be slightly larger than that obtained with the numerical simulations.

The fibre diameter,  $d$ , enters the equation for  $\bar{n}_c^{3D}$ . Figure 5.6 shows a comparison between the results obtained with (5.8) and those from a 3D simulation. In the 3D simulations,  $\rho=60 \text{ mm}^{-2}$ ,  $l_f=1 \text{ mm}$ ,  $L=1.5 \text{ mm}$  and the fibres were assumed to be straight and of uniform orientation. The values of  $e$ , which correspond to  $d$ , simulated were 0.005, 0.01, 0.02, 0.04, 0.06 and 0.08 mm and for each value of  $e$  ten simulations were performed. The results from the individual simulations are shown as '+', and the average is shown as a dotted line. It can be seen that the results are slightly more scattered than in the 2D simulations, especially for low values of  $e$ , which also implies a low absolute number of crossings. The normalized number of crossings is also somewhat more below unity, down to 0.91 for  $e=0.02 \text{ mm}$ , compared with 0.97 for the 2D case.

The average curl index,  $\bar{c}$ , appears in (5.7), but this equation is not believed to be accurate in estimating number of fibre crossings in an assembly of curled fibres, since in the derivation of the equation in [23], the fact that two curled fibres may cross each other twice is disregarded. For the case of circular arc shaped fibres of constant length, it is shown in [20], that the number of crossings in a 2D network is independent of fibre curvature:

$$\bar{n}_c^{2D} = \frac{(n_f \bar{l}_f)^2}{L^2 \pi} \quad (5.10)$$

The relation for the 3D case, (5.8), is based on the assumption of straight fibres,

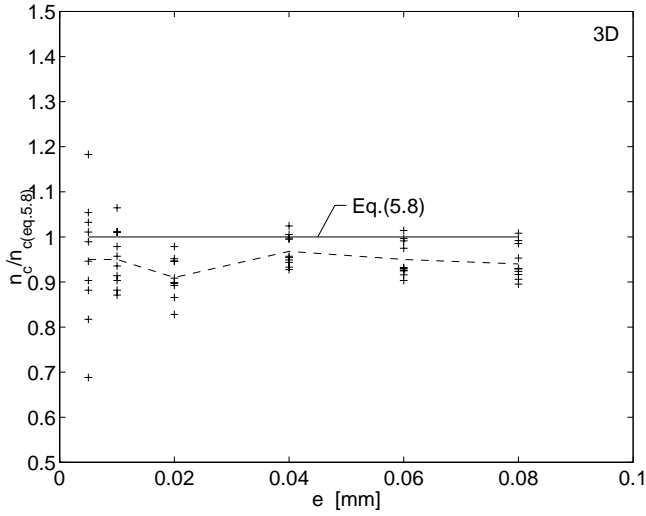


Figure 5.6: Normalized value of  $n_c$  plotted against fibre diameter,  $e$ .

but it is said in the article, [31], that provided the orientation distribution of small fibre segments is uniform the same equation applies to curled fibres.

A comparison between the two equations (5.7) and (5.10) as well as results from numerical simulations are shown in Figure 5.7. The simulations employed the 2D basic example network as a starting point, and the curvature and the length of the square,  $L$ , were varied. Four different values of curvature were simulated, 0, 1000, 2000 and 3000  $\text{mm}^{-1}$ ; 0  $\text{mm}^{-1}$  representing a straight fibre and 3000  $\text{mm}^{-1}$  being close to a semi-circle. The transition from curvature to curl index can be seen in Figure 3.2. Three different values of  $L$  were considered, representing  $L/l_f$  ratios of 0.6, 1.2 and 2.4. The variation of  $L$  means that the assumptions of  $L^2$  and  $n_f$  being large are violated to different degrees. In the figure the number of crossings relative to the number of crossings predicted by (5.10) is plotted against the curl index. The relative standard deviations of the simulation results, which are averages of ten simulations, are 4-9% for  $L/l_f=0.6$  and 1-2% for  $L/l_f=1.2$  and 2.4. (5.7) predicts a pronounced decrease in the number of crossings as the fibres become more curled, while (5.10) suggests the number of crossings to be independent of the curl index. The simulations agree well with (5.10), but as the  $L/l_f$  ratio decreases, the results deviate more from the prediction of (5.10), especially for low curl indices. Like for the case in Figure 5.5, this deviation probably occurs because a lower  $L/l_f$  ratio means fewer fibres, and fewer fibres means that the orientation distribution tends to be less uniform. Another assumption which is not fulfilled when the  $L/l_f$  ratio decreases is that of  $L^2$  being large. In the derivation of  $n_c$ , a large value of  $L^2$  is assumed. We can say that  $L^2$  in the simulations is also large by considering many cells, but there will then be a periodicity in position and orientation of the fibres

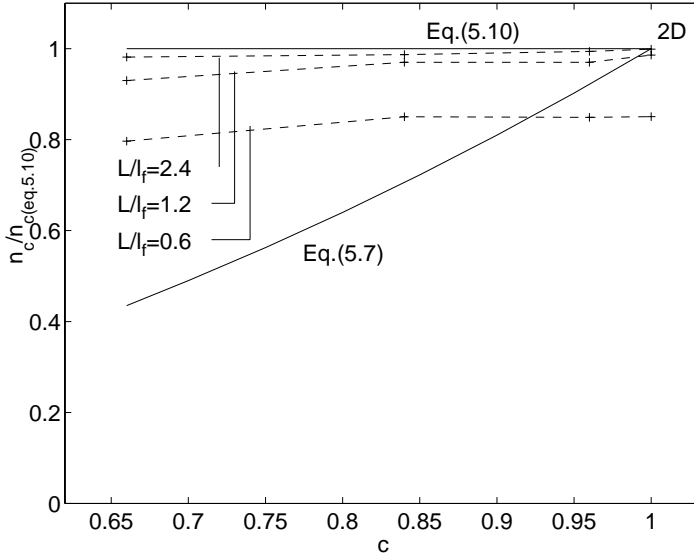


Figure 5.7: Normalized value of  $n_c$  plotted against curl index,  $\bar{c}$ .

which does not agree with the assumptions of random fibre position and orientation in the entire area.

Simulations of number of bonds were made on 3D networks with non-uniform orientation distribution. The series of simulations was made on cells ranging from a cube where  $L_x=L_y=L_z$  towards a cell that is compacted in the  $z$ -direction and thus approaching a 2D network. Figure 7.29 shows the five examined network cell sizes. The number of fibres was 173 in all the cells. The in-plane orientation distribution was uniform while the out-of-plane angle was smaller as the cell height decreased, see Section 7.5.

The simulation results, average from ten simulations, are shown in Figure 5.8 as 'o' signs. The theoretical value of number of bonds for a 2D network,  $\bar{n}_c^{2D}$ , is shown as an 'x' at  $L_z/L_x = 0$ . The values of  $\bar{n}_c^{3D}$  obtained from (5.8) are shown by a dashed line. The dashed line follows the simulation results quite closely down to  $L_z/L_x = 0.2$ , but then it tends to infinity since  $L_z$  is in the denominator of (5.8). This implies that the assumption of uniform orientation distribution of the fibres in (5.8) is not very important in this case.

### 5.3. Percolation and the active part of a network

Non-active parts are those parts of a network which are in a state of zero stress regardless of loading at the boundary of the network. In Figure 5.3a the 2D basic example network is shown as it appears when first generated, while Figure 5.3b

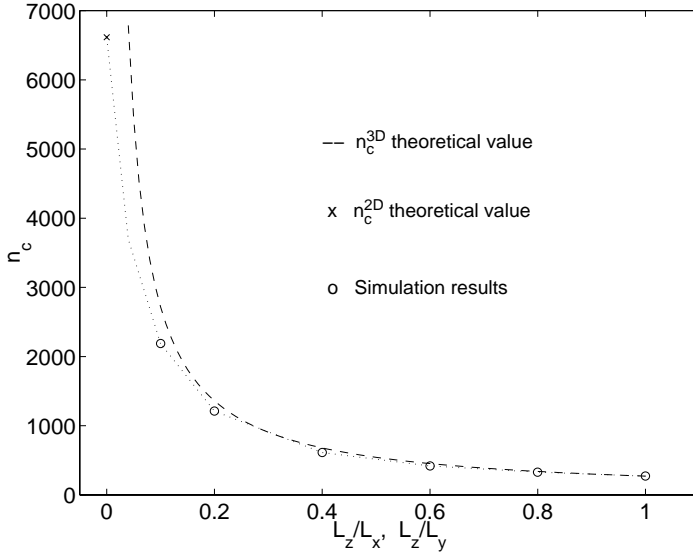


Figure 5.8:  $n_c$  plotted against  $L_z/L_x$  and  $L_z/L_y$ .

shows the active part of the network.

As was seen in Section 5.2, for a reasonably large network the mean number of fibre crossings in an area depends on the total fibre length only. The active part of the network, however, depends also on the length distribution of the fibres. Figure 5.9 shows the percentage of a 2D network which is active as a function of fibre length for network densities of 2 and 4  $\text{mm}^{-1}$ . The values for  $\rho = 2 \text{ mm}^{-1}$  are averages from three simulations and the values for  $\rho = 4 \text{ mm}^{-1}$  represent one single simulation. The straight fibres have a uniform orientation distribution and interact at all crossings. In each simulation all fibres are of the same length. As the diagram shows, for a given network density a small number of long fibres yields a higher active percentage than a large number of short fibres. The symbols on the  $x$ -axis of Figure 5.9 refer to  $\rho = 2 \text{ mm}^{-1}$ , and represent non-continuous networks, that is networks that are not connected and hence have no load-bearing function. The fibre length at which a network of given density theoretically reaches the percolation threshold, that is, becomes unconnected, is given in [3] as being

$$l_f \approx 5.7/\rho, \quad (5.11)$$

which yields  $l_f = 2.85 \text{ mm}$  in the case of  $\rho = 2 \text{ mm}^{-1}$ . Despite this the simulated networks are not connected until  $l_f = 5 \text{ mm}$ . This is probably because the results are widely scattered as the percolation threshold is approached. Figure 5.9 shows both the active part and the part of the network that is left when only the free fibre ends have been removed. It should be noted that a fibre that is not in contact with

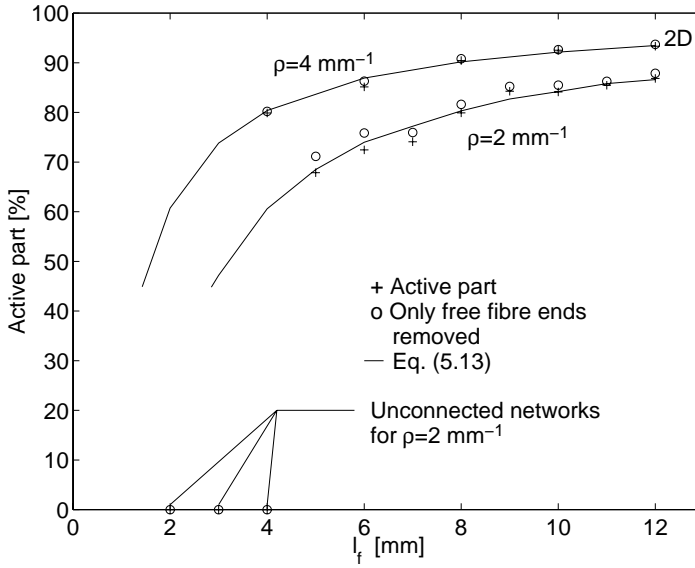


Figure 5.9: Active part of network plotted against fibre length,  $l_f$ .

any other fibre, as well as clusters composed of only two fibres, are included in free fibre ends in this case, although they can also be viewed as ‘isolated clusters’.

Even at this low density there is little difference between the two parameters. This indicates that an approximate expression for the active part of a network,  $p$ , is given by the fibre length minus the length of the two free end segments, divided by fibre length:

$$p = \frac{\bar{l}_f - 2\bar{l}_s}{\bar{l}_f} \quad (5.12)$$

Employing (2.2), (5.7) and (5.8) this yields, for 2D networks:

$$p_{2D} = 1 - \frac{n_f}{\bar{n}_c} = 1 - \frac{\pi}{\rho \bar{l}_f} \quad , \quad (5.13)$$

and for 3D networks

$$p_{3D} = 1 - \frac{n_f}{\bar{n}_c} = 1 - \frac{4}{\rho \bar{l}_f \pi d} \quad . \quad (5.14)$$

The approximate value  $p_{2D}$  is shown as a solid line in Figure 5.9, and is supposed to fit to values denoted by open circles (o), indicating the corresponding numerical results.

When the probability of interaction  $s \neq 1$  the equation is modified to

$$p = 1 - \frac{n_f}{s \bar{n}_c} \quad . \quad (5.15)$$

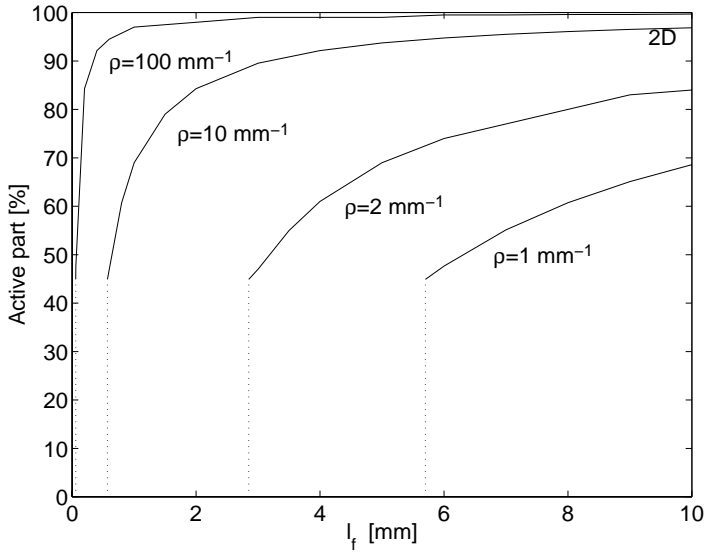


Figure 5.10: Approximate active part of a 2D network plotted against fibre length,  $l_f$ .

In Figure 5.10 the approximate active part,  $p$ , predicted by (5.13) is given for different network densities. At the percolation threshold,  $\rho l_f = 5.7$ , from (5.11), and this gives  $p = 0.45$ . That is, at the percolation threshold fibre length,  $p$  is the same for all densities, which can also be seen from the figure. For higher network densities the active part increases rapidly towards 1.0, but for  $\rho = 1 \text{ mm}^{-1}$  the increase is slower.

## 6. FEM MODEL AND ANALYSIS OF INITIAL STIFFNESS

In order to describe the pre-fracture global constitutive properties of a network, which is a heterogeneous structure, the terminology of elasticity of continuous media is employed. In linear elasticity of continuous materials, the constitutive properties are contained in the coefficients describing stress,  $\boldsymbol{\sigma}$ , as a linear function of strain,  $\boldsymbol{\epsilon}$ , i.e. the matrix  $\mathbf{D}$  in Hooke's law, [35]:

$$\boldsymbol{\sigma} = \mathbf{D}\boldsymbol{\epsilon} \quad (6.1)$$

$\mathbf{D}$  is symmetric when a strain-energy function exists, [35], and this is assumed to be the case here.

The stiffness properties of a fibre network are here characterized by the  $\mathbf{D}$  matrix of a continuous medium which yields the same resultant forces on the boundaries as the network when subjected to the same strain.

The finite element method (FEM), see [43], [65], was used to obtain the stiffness properties. This is done by dividing the network into beam and bond elements (fibre segments and inter-fibre bonds), computing the element stiffness matrix for each element and assembling all element stiffness matrices into a global system stiffness matrix. The element stiffness matrices for beam and bond elements are given in the next section. The next step is to prescribe the load on the structure. In this case the network was loaded by prescribing a global strain, i.e. boundary displacements. This was done according to the principles in Section 6.2. The system of equations was then solved, Section 6.3, and the resultant forces and  $\mathbf{D}$  evaluated as described in Section 6.4.

The  $\mathbf{D}$  matrix obtained from a 3D simulation contains 36 constants, of which only 21 are independent due to the symmetry of  $\mathbf{D}$ . To reduce the number of constants, a method of estimating the two independent elastic constants of an isotropic material is employed, see Section 6.6. The corresponding method for orthotropic material is given in Section 6.7.

### 6.1. Element stiffness matrices

The element stiffness matrix,  $\mathbf{K}_e$ , gives the reaction forces,  $\mathbf{f}$ , when the element is subjected to displacements,  $\mathbf{u}$ , that is

$$\mathbf{K}_e \mathbf{u} = \mathbf{f} \quad , \quad (6.2)$$

where  $\mathbf{u}$  is the vector of displacements in the directions of the degrees of freedom of the element, see Figure 6.1, and  $\mathbf{f}$  is the corresponding force vector.

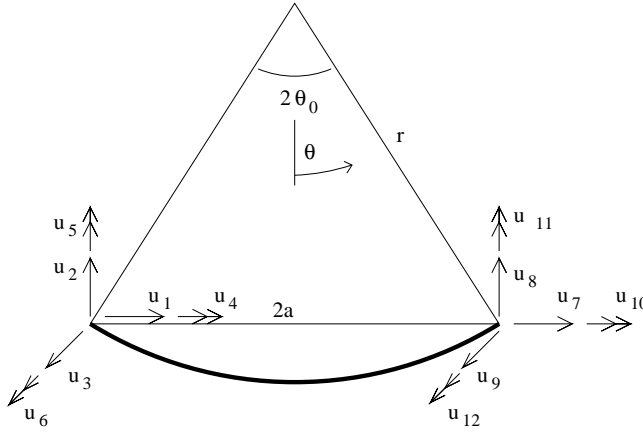


Figure 6.1: Definition of curved beam element geometry and degrees of freedom.

### 6.1.1. Beam elements

The stiffness matrices used here for beams rely on the assumptions of small strain and that plane sections perpendicular to the beam axis remain plane during deformation. In [32], Krenk presents a method of deriving stiffness matrices for beam elements. The method makes use of the stationary nature of the complementary energy and a set of homogeneous equilibrium states. A few examples of two-dimensional beam elements, among which one is of constant curvature, are given in the article. Here, the method is used to obtain the stiffness matrix of a three-dimensional beam element of constant curvature, for small strains. The derivation, which is not repeated here, leads to the equation

$$\mathbf{K}_e = \mathbf{G}^T \mathbf{H}^{-1} \mathbf{G} . \tag{6.3}$$

In the 3D case,  $\mathbf{G}$  is a 6x12 matrix where each row contains the 12 nodal element forces for the corresponding equilibrium state, and  $\mathbf{H}$  is a 6x6 matrix representing the homogeneous part of the internal energy. From the definition of the six homogeneous equilibrium states in Figure 6.2 and the definition of positive directions of nodal forces in Figure 6.1,  $\mathbf{G}$  can be established.

$$\mathbf{G} = \begin{bmatrix} -1 & 0 & 0 & 0 & 0 & 0 & 1 & 0 & 0 & 0 & 0 & 0 \\ 0 & 0 & 0 & 0 & 0 & -a & 0 & 0 & 0 & 0 & 0 & a \\ 0 & 0 & 0 & 0 & -a & 0 & 0 & 0 & 0 & 0 & a & 0 \\ 0 & 0 & 0 & -a & 0 & 0 & 0 & 0 & 0 & a & 0 & 0 \\ 0 & 1 & 0 & 0 & 0 & a & 0 & -1 & 0 & 0 & 0 & a \\ 0 & 0 & -1 & 0 & a & 0 & 0 & 0 & 1 & 0 & a & 0 \end{bmatrix} \tag{6.4}$$

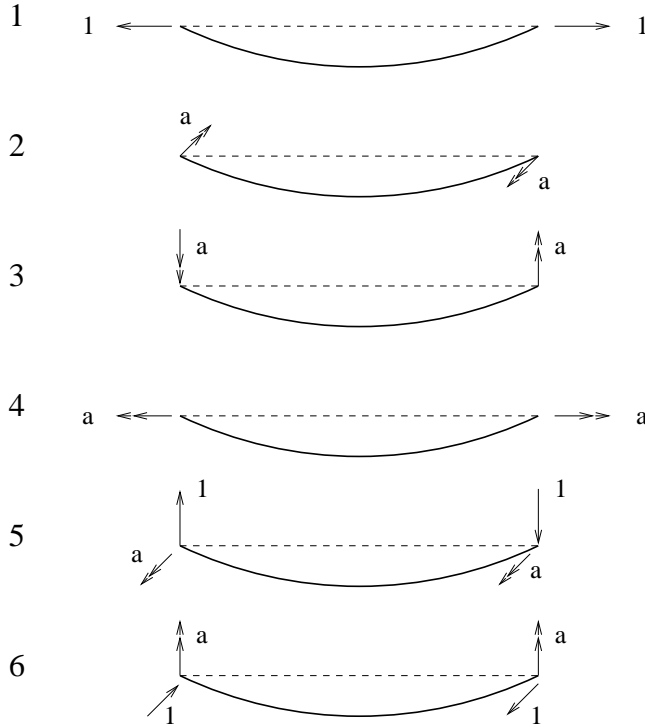


Figure 6.2: Definition of the six homogeneous equilibrium states.

Before  $\mathbf{H}$  is given, some cross-section constants and the elastic energy for a curved beam are introduced. For a curved beam, a modified bending stiffness parameter,  $J$ , is used instead of moment of inertia,  $I$ . Figure 6.3 defines a local coordinate system, with the origin in the cross-section centroid, and the sign convention for sectional forces. Denoting the cross-sectional area  $A$  and the radius of curvature  $r$ , we have:

$$J_z = \int_A \frac{y^2}{1 - y/r} dA \quad (6.5)$$

$$J_y = \int_A \frac{z^2}{1 - y/r} dA \quad (6.6)$$

For a rectangular cross section this gives:

$$J_z = r^3 b \ln \left( \frac{2r+h}{2r-h} \right) - r^2 b h = I_z \left( 1 + \frac{3}{5} \left( \frac{h}{2r} \right)^2 + \frac{3}{7} \left( \frac{h}{2r} \right)^4 + \dots \right), \quad (6.7)$$

$$J_y = \frac{r b^3}{12} \ln \left( \frac{2r+h}{2r-h} \right) = I_y \left( 1 + \frac{1}{3} \left( \frac{h}{2r} \right)^2 + \frac{1}{5} \left( \frac{h}{2r} \right)^4 + \dots \right),$$

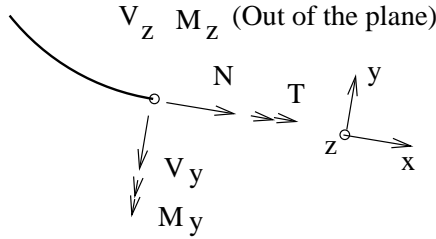


Figure 6.3: Sign convention for sectional forces and local coordinate system in the cross-section centroid.

where  $I$  is the moment of inertia of the cross-section and  $b$  and  $h$  denote width and depth. For moderate values of the ratio section size to radius of curvature, the higher order terms of the serial expansion are small, and only the first few terms need to be considered.

The axial stress in a section of a curved beam, symmetrical about the  $y$ -axis, as a function of the sectional forces is, [41],

$$\sigma_n = \frac{N}{A} + \frac{M_z}{rA} - \frac{M_z}{J_z} \frac{y}{1 - y/r} - \frac{M_y}{J_y} \frac{z}{1 - y/r} . \quad (6.8)$$

The elastic strain energy per unit length,  $E_{\sigma_n}$ , caused by axial stress, is for a curved beam

$$E_{\sigma_n} = \int_A \sigma_n \epsilon \frac{r - y}{r} dA = \int_A \frac{\sigma_n^2}{E} \frac{r - y}{r} dA . \quad (6.9)$$

Using (6.8) and including the effect of torsion this yields the total elastic strain energy per unit length,  $E_e$ ,

$$E_e = E_{\sigma_n} + \frac{T^2}{2GK_v} = \frac{1}{2} \left( \frac{1}{EA} \left( N + \frac{M_z}{r} \right)^2 + \frac{M_z^2}{EJ_z} + \frac{M_y^2}{EJ_y} + \frac{T^2}{GK_v} \right) , \quad (6.10)$$

where  $E$  denotes elastic modulus,  $G$  the shear modulus and  $K_v$  the torsional constant of the beam. The effect of shear strains due to shear forces has been neglected in the calculation of  $E_e$ .

$\mathbf{H}$  is defined as:

$$H_{ij} = r \int_{-\theta_0}^{\theta_0} \left( \left( N_i + \frac{M_{zi}}{r} \right) \frac{1}{EA} \left( N_j + \frac{M_{zj}}{r} \right) + M_{zi} \frac{1}{EJ_z} M_{zj} + M_{yi} \frac{1}{EJ_y} M_{yj} + T_i \frac{1}{GK_v} T_j \right) d\theta \quad (6.11)$$

The indices  $i, j$  refer to equilibrium state number, and by comparison with (6.10) it can be seen how  $\mathbf{H}$  is related to the strain energy of the beam.

In order to evaluate  $\mathbf{H}$  the section forces along the beam must be known. The relation between the nodal element forces and the sectional forces along the beam for

the different equilibrium states can be obtained from equilibrium. These relations are summarized in Table 6.1.

Table 6.1: *Sectional forces along the beam for the six equilibrium states.*

no	$\mathbf{N}$	$\mathbf{V}_y$	$\mathbf{V}_z$	$\mathbf{T}$	$\mathbf{M}_y$	$\mathbf{M}_z$
1	$\cos \theta$	$\sin \theta$	0	0	0	$r(\cos \theta_0 - \cos \theta)$
2	0	0	0	0	0	$r \sin \theta_0$
3	0	0	0	$r \sin \theta_0 \sin \theta$	$-r \sin \theta_0 \cos \theta$	0
4	0	0	0	$r \sin \theta_0 \cos \theta$	$r \sin \theta_0 \sin \theta$	0
5	$-\sin \theta$	$\cos \theta$	0	0	0	$r \sin \theta$
6	0	0	1	$r \sin \theta_0 \sin \theta +$ $r(1 - \cos(\theta_0 - \theta))$	$-r \sin \theta_0 \cos \theta +$ $r(\sin(\theta_0 - \theta))$	0

Now the components of  $\mathbf{H}$  can be calculated. The non-zero components are:

$$\begin{aligned}
 H_{11} &= 2 \left( \frac{r}{EA} + \frac{r^3}{EJ_z} \right) \theta_0 \cos^2 \theta_0 + \frac{r^3}{EJ_z} (\theta_0 - 3 \sin \theta_0 \cos \theta_0) \\
 H_{12} = H_{21} &= 2 \left( \frac{r}{EA} + \frac{r^3}{EJ_z} \right) \theta_0 \sin \theta \cos \theta_0 - 2 \frac{r^3}{EJ_z} \sin^2 \theta_0 \\
 H_{22} &= 2 \left( \frac{r}{EA} + \frac{r^3}{EJ_z} \right) \theta_0 \sin^2 \theta_0 \\
 H_{33} &= \frac{r^3}{EJ_y} \sin^2 \theta_0 (\theta_0 + \sin \theta_0 \cos \theta_0) + \frac{r^3}{GK_v} \sin^2 \theta_0 (\theta_0 - \sin \theta_0 \cos \theta_0) \\
 H_{44} &= \frac{r^3}{EJ_y} \sin^2 \theta_0 (\theta_0 - \sin \theta_0 \cos \theta_0) + \frac{r^3}{GK_v} \sin^2 \theta_0 (\theta_0 + \sin \theta_0 \cos \theta_0) \\
 H_{46} = H_{64} &= \frac{r^3}{EJ_y} \sin \theta_0 (\sin \theta_0 \cos^2 \theta_0 - \theta_0 \cos \theta_0) + \\
 &\quad \frac{r^3}{GK_v} \sin \theta_0 (-\sin \theta_0 \cos^2 \theta_0 - \theta_0 \cos \theta_0 + 2 \sin \theta_0) \\
 H_{55} &= \frac{r^3}{EJ_z} (\theta_0 - \sin \theta_0 \cos \theta_0)
 \end{aligned} \tag{6.12}$$

$$H_{66} = \frac{r^3}{EJ_y}(-\sin\theta_0\cos^3\theta_0 + \theta_0\cos^2\theta_0) + \frac{r^3}{GK_v}(2\theta_0 - 4\sin\theta_0\cos\theta_0 + \sin\theta_0\cos^3\theta_0 + \theta_0\cos^2\theta_0)$$

Since  $\mathbf{H}$  is close to diagonal,  $\mathbf{H}^{-1}$  can be calculated explicitly,

$$\mathbf{H}^{-1} = \begin{bmatrix} H_{22}/H_a & -H_{12}/H_a & 0 & 0 & 0 & 0 \\ -H_{12}/H_a & H_{11}/H_a & 0 & 0 & 0 & 0 \\ 0 & 0 & 1/H_{33} & 0 & 0 & 0 \\ 0 & 0 & 0 & H_{66}/H_b & 0 & -H_{46}/H_b \\ 0 & 0 & 0 & 0 & 1/H_{55} & 0 \\ 0 & 0 & 0 & -H_{46}/H_b & 0 & H_{44}/H_b \end{bmatrix}, \quad (6.13)$$

where

$$H_a = H_{11}H_{22} - H_{12}^2 \quad (6.14)$$

and

$$H_b = H_{44}H_{66} - H_{46}^2. \quad (6.15)$$

Only the multiplication of (6.2), repeated here, remains to obtain  $\mathbf{K}_e$ .

$$\mathbf{K}_e = \mathbf{G}^T \mathbf{H}^{-1} \mathbf{G} \quad (6.16)$$

The stiffness matrix of a two-dimensional curved beam element is obtained analogously, by only considering the in-plane degrees of freedom and equilibrium states. This gives

$$\mathbf{G} = \begin{bmatrix} -1 & 0 & 0 & 1 & 0 & 0 \\ 0 & 0 & -a & 0 & 0 & a \\ 0 & 1 & a & 0 & -1 & a \end{bmatrix}, \quad (6.17)$$

$$\mathbf{H}^{-1} = \begin{bmatrix} H_{22}/H_a & -H_{12}/H_a & 0 \\ -H_{12}/H_a & H_{11}/H_a & 0 \\ 0 & 0 & 1/H_{55} \end{bmatrix}. \quad (6.18)$$

The stiffness matrix for a plane straight beam element of length  $l$  can be found, for example, in [43]:

$$\mathbf{K}_e = \begin{bmatrix} \frac{EA}{l} & 0 & 0 & -\frac{EA}{l} & 0 & 0 \\ 0 & \frac{12EI}{l^3} & \frac{6EI}{l^2} & 0 & -\frac{12EI}{l^3} & \frac{6EI}{l^2} \\ 0 & \frac{6EI}{l^2} & \frac{4EI}{l} & 0 & -\frac{6EI}{l^2} & \frac{2EI}{l} \\ -\frac{EA}{l} & 0 & 0 & \frac{EA}{l} & 0 & 0 \\ 0 & -\frac{12EI}{l^3} & -\frac{6EI}{l^2} & 0 & \frac{12EI}{l^3} & -\frac{6EI}{l^2} \\ 0 & \frac{6EI}{l^2} & \frac{2EI}{l} & 0 & -\frac{6EI}{l^2} & \frac{4EI}{l} \end{bmatrix} \quad (6.19)$$

An alternative to using the curved beam elements here is to divide a curved fibre into several short straight beam elements. This approach is, however, only applicable when the ratio of beam depth to radius of curvature is small. If this method is used only the simple standard straight beam element is needed, but on the other hand, it entails an excessive number of degrees of freedom. The redundant degrees of freedom can be eliminated by static condensation before the final system of equations is solved, but extra computational work is still required to generate the stiffness matrix. In addition, if the sectional forces are to be determined, the eliminated degrees of freedom will be needed again. In order to estimate the accuracy of the approximate method a comparison was made between a curved fibre segment and a corresponding structure consisting of a number of straight elements. The properties of the 3D fibre segment were as in the basic example network, and the sector angle,  $2\theta_0$ , was 0.2 rad. Table 6.2 shows the maximum error in a single coefficient of  $\mathbf{K}_e$  for different numbers of straight beam elements used to approximate the curved fibre segment. For most of the coefficients of  $\mathbf{K}_e$  the error is considerably smaller than the maximum error.

Table 6.2: *Maximum error for a single component in  $\mathbf{K}_e$  for different numbers of straight elements used in the approximation.*

Number of elements	Max. error [%]
2	146
3	64
4	38
6	15
8	7
10	4.8
20	1.4

6.1.2. Bond elements

The derivation of the stiffness matrix for a 3D bond element consisting of circular plates connected by distributed normal and shear springs, which was defined in Section 3.2.1, is performed in two steps. First the behaviour of the two circular areas connected with springs is studied, then the effect of the rigid coupling to the fibre centre lines is included.

Figure 6.4 shows the circular plates with the corresponding degrees of freedom. With the  $x$ -axis in the centre of the plates the following stiffness matrix is obtained by integrating the stresses resulting from the different modes of deformation.

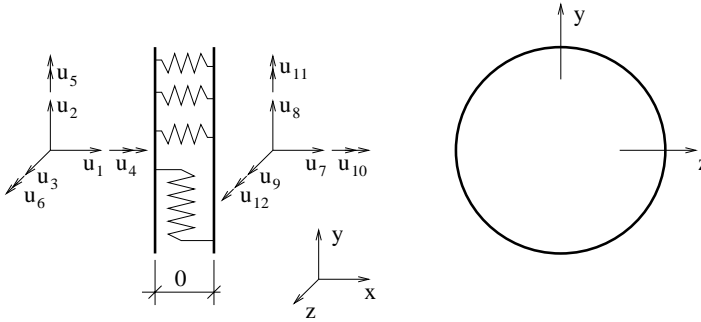


Figure 6.4: Section and plane view of circular areas with degrees of freedom indicated on the section.

$$\mathbf{K}_e^2 = \begin{bmatrix} \mathbf{K}_e^1 & -\mathbf{K}_e^1 \\ -\mathbf{K}_e^1 & \mathbf{K}_e^1 \end{bmatrix}, \tag{6.20}$$

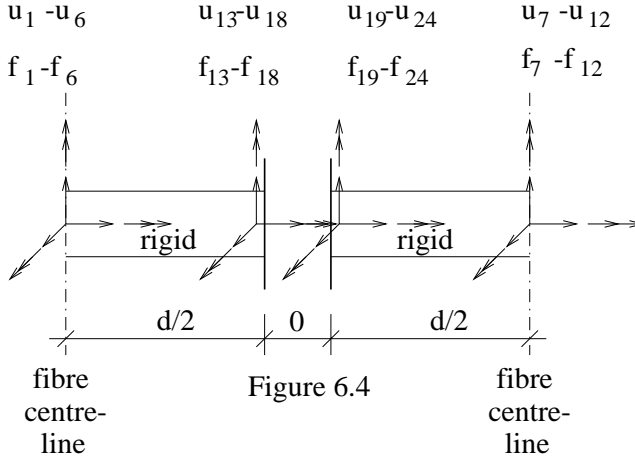
where

$$\mathbf{K}_e^1 = \begin{bmatrix} k_n A_b & 0 & 0 & 0 & 0 & 0 \\ 0 & k_t A_b & 0 & 0 & 0 & 0 \\ 0 & 0 & k_t A_b & 0 & 0 & 0 \\ 0 & 0 & 0 & k_t I_p & 0 & 0 \\ 0 & 0 & 0 & 0 & k_n I & 0 \\ 0 & 0 & 0 & 0 & 0 & k_n I \end{bmatrix} \tag{6.21}$$

and  $A_b$ ,  $I_p$  and  $I$  denote the area, the polar moment of inertia and the moment of inertia of the circular cross-section, respectively.

The next task is to include the effect of the rigid coupling to the fibre centre lines, where the fibre nodes are located. Figure 6.5 shows the bond element, from fibre centre line to fibre centre line. Degrees of freedom  $u_1 - u_{12}$  in Figure 6.4 correspond to degrees of freedom  $u_{13} - u_{24}$  in Figure 6.5. The relation between  $[f_{13}..f_{24}]$  and  $[u_{13}..u_{24}]$  is thus known from (6.2) and (6.20):

$$[f_{13-24}] = \mathbf{K}_e^2 [u_{13-24}] \tag{6.22}$$

Figure 6.5: *Bond element.*

We now require the relation between  $[f_1..f_{12}]$  and  $[u_1..u_{12}]$  in Figure 6.5. Let us start by considering the left part of the element. From equilibrium it follows that:

$$\begin{bmatrix} f_1 \\ f_2 \\ f_3 \\ f_4 \\ f_5 \\ f_6 \end{bmatrix} = \begin{bmatrix} 1 & 0 & 0 & 0 & 0 & 0 \\ 0 & 1 & 0 & 0 & 0 & 0 \\ 0 & 0 & 1 & 0 & 0 & 0 \\ 0 & 0 & 0 & 1 & 0 & 0 \\ 0 & 0 & -d/2 & 0 & 1 & 0 \\ 0 & d/2 & 0 & 0 & 0 & 1 \end{bmatrix} \begin{bmatrix} f_{13} \\ f_{14} \\ f_{15} \\ f_{16} \\ f_{17} \\ f_{18} \end{bmatrix} = \mathbf{G}_1 \begin{bmatrix} f_{13} \\ f_{14} \\ f_{15} \\ f_{16} \\ f_{17} \\ f_{18} \end{bmatrix} \quad (6.23)$$

Kinematic reasoning gives, for the corresponding displacements:

$$\begin{bmatrix} u_{13-18} \end{bmatrix} = \mathbf{G}_1^T \begin{bmatrix} u_{1-6} \end{bmatrix} \quad (6.24)$$

These relations can be expanded into

$$\begin{bmatrix} f_{1-6} \\ f_{19-24} \end{bmatrix} = \begin{bmatrix} \mathbf{G}_1 & \mathbf{0} \\ \mathbf{0} & \mathbf{I} \end{bmatrix} \begin{bmatrix} f_{13-18} \\ f_{19-24} \end{bmatrix} = \mathbf{A}_1 \begin{bmatrix} f_{13-18} \\ f_{19-24} \end{bmatrix}, \quad (6.25)$$

$$\begin{bmatrix} u_{13-18} \\ u_{19-24} \end{bmatrix} = \begin{bmatrix} \mathbf{G}_1^T & \mathbf{0} \\ \mathbf{0} & \mathbf{I} \end{bmatrix} \begin{bmatrix} u_{1-6} \\ u_{19-24} \end{bmatrix} = \mathbf{A}_1^T \begin{bmatrix} u_{1-6} \\ u_{19-24} \end{bmatrix}. \quad (6.26)$$

By combining (6.25), (6.22) and (6.26) we obtain

$$\begin{bmatrix} f_{1-6} \\ f_{19-24} \end{bmatrix} = \mathbf{A}_1 \mathbf{K}_e^2 \mathbf{A}_1^T \begin{bmatrix} u_{1-6} \\ u_{19-24} \end{bmatrix}. \quad (6.27)$$

Considering the right side of the element we have

$$\begin{bmatrix} f_7 \\ f_8 \\ f_9 \\ f_{10} \\ f_{11} \\ f_{12} \end{bmatrix} = \begin{bmatrix} 1 & 0 & 0 & 0 & 0 & 0 \\ 0 & 1 & 0 & 0 & 0 & 0 \\ 0 & 0 & 1 & 0 & 0 & 0 \\ 0 & 0 & 0 & 1 & 0 & 0 \\ 0 & 0 & d/2 & 0 & 1 & 0 \\ 0 & -d/2 & 0 & 0 & 0 & 1 \end{bmatrix} \begin{bmatrix} f_{19} \\ f_{20} \\ f_{21} \\ f_{22} \\ f_{23} \\ f_{24} \end{bmatrix} = \mathbf{G}_2 \begin{bmatrix} f_{19} \\ f_{20} \\ f_{21} \\ f_{22} \\ f_{23} \\ f_{24} \end{bmatrix}. \quad (6.28)$$

Equivalently, for the corresponding displacements, we have

$$\begin{bmatrix} u_{19-24} \end{bmatrix} = \mathbf{G}_2^T \begin{bmatrix} u_{7-12} \end{bmatrix}. \quad (6.29)$$

Defining

$$\mathbf{A}_2 = \begin{bmatrix} \mathbf{I} & \mathbf{0} \\ \mathbf{0} & \mathbf{G}_2 \end{bmatrix}, \quad (6.30)$$

finally leads to:

$$\begin{bmatrix} f_{1-6} \\ f_{7-12} \end{bmatrix} = \mathbf{A}_2 \mathbf{A}_1 \mathbf{K}_e^2 \mathbf{A}_1^T \mathbf{A}_2^T \begin{bmatrix} u_{1-6} \\ u_{7-12} \end{bmatrix} \quad (6.31)$$

That is,

$$\mathbf{K}_e = \mathbf{A}_2 \mathbf{A}_1 \mathbf{K}_e^2 \mathbf{A}_1^T \mathbf{A}_2^T. \quad (6.32)$$

In a 2D analysis only the degrees of freedom associated with  $k_t$  are relevant. This means that  $\mathbf{K}_e^2$  is only a 6x6 matrix. Furthermore, the distance  $d/2$  in Figure 6.5 is zero, implying that

$$\mathbf{K}_e = \mathbf{K}_e^2 = \begin{bmatrix} k_t A_b & 0 & 0 & -k_t A_b & 0 & 0 \\ 0 & k_t A_b & 0 & 0 & -k_t A_b & 0 \\ 0 & 0 & k_t I_p & 0 & 0 & -k_t I_p \\ -k_t A_b & 0 & 0 & k_t A_b & 0 & 0 \\ 0 & -k_t A_b & 0 & 0 & k_t A_b & 0 \\ 0 & 0 & -k_t I_p & 0 & 0 & k_t I_p \end{bmatrix}. \quad (6.33)$$

When the transversal and rotational stiffnesses are regarded as independent, as in the alternative 2D model of Section 3.2.2, we simply have

$$\mathbf{K}_e = \begin{bmatrix} k_x & 0 & 0 & -k_x & 0 & 0 \\ 0 & k_y & 0 & 0 & -k_y & 0 \\ 0 & 0 & k_\phi & 0 & 0 & -k_\phi \\ -k_x & 0 & 0 & k_x & 0 & 0 \\ 0 & -k_y & 0 & 0 & k_y & 0 \\ 0 & 0 & -k_\phi & 0 & 0 & k_\phi \end{bmatrix}. \quad (6.34)$$

### 6.1.3. Transformation to global coordinates

The element stiffness matrices given above refer to a local coordinate system with axes parallel to the element's degrees of freedom. In the fibre network, the elements have, in general, an orientation that differs from the global coordinate axes. When this is the case, the element stiffness matrix must be transformed, see [43]:

$$\mathbf{K}_e^g = \mathbf{A}^T \mathbf{K}_e^l \mathbf{A} , \quad (6.35)$$

where the superscript  $g$  denotes global, and the superscript  $l$  denotes local.

In the 3D case  $\mathbf{A}$  is given by

$$\mathbf{A} = \begin{bmatrix} \mathbf{A}_n & \mathbf{0} & \mathbf{0} & \mathbf{0} \\ \mathbf{0} & \mathbf{A}_n & \mathbf{0} & \mathbf{0} \\ \mathbf{0} & \mathbf{0} & \mathbf{A}_n & \mathbf{0} \\ \mathbf{0} & \mathbf{0} & \mathbf{0} & \mathbf{A}_n \end{bmatrix} , \quad (6.36)$$

where  $\mathbf{0}$  is a 3x3 zero matrix and

$$\mathbf{A}_n = \begin{bmatrix} n_{x\bar{x}} & n_{y\bar{x}} & n_{z\bar{x}} \\ n_{x\bar{y}} & n_{y\bar{y}} & n_{z\bar{y}} \\ n_{x\bar{z}} & n_{y\bar{z}} & n_{z\bar{z}} \end{bmatrix} , \quad (6.37)$$

$n_{i\bar{j}}$  denoting the cosine of the angle between the global  $i$ - and local  $\bar{j}$ -axes.

In the 2D case  $\mathbf{A}$  is given by

$$\mathbf{A} = \begin{bmatrix} n_{x\bar{x}} & n_{y\bar{x}} & 0 & 0 & 0 & 0 \\ n_{x\bar{y}} & n_{y\bar{y}} & 0 & 0 & 0 & 0 \\ 0 & 0 & 1 & 0 & 0 & 0 \\ 0 & 0 & 0 & n_{x\bar{x}} & n_{y\bar{x}} & 0 \\ 0 & 0 & 0 & n_{x\bar{y}} & n_{y\bar{y}} & 0 \\ 0 & 0 & 0 & 0 & 0 & 1 \end{bmatrix} . \quad (6.38)$$

In two dimensions, the direction of a bond element is not defined, and if  $k_x = k_y$ , the bond element is unaffected by the transformation.

When all elements have been transformed into global coordinates, each element stiffness matrix is assembled into the global stiffness matrix,  $\mathbf{K}$ .

## 6.2. Methods of applying strain

To obtain the response of a network, it is subjected to deformations corresponding to various modes of strain, and the resulting forces on the boundaries of the network are registered. A deformation to which the network is subjected, reflects a certain global mean strain,  $\boldsymbol{\epsilon} = (\epsilon_x, \epsilon_y, \epsilon_z, \gamma_{xy}, \gamma_{xz}, \gamma_{yz})$ , of the cell. There are several different methods of applying such a mean strain. A natural concept would be to imitate the situation when testing a fibre material in the laboratory. This could be a strip

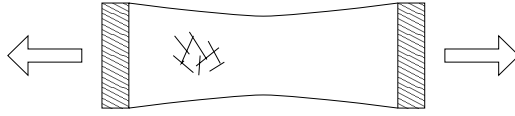


Figure 6.6: Fibre network in simple tension test.

of material clamped at the ends and otherwise free, see Figure 6.6. This method would facilitate a direct comparison between the results obtained from tests and simulations. One problem is, however, that with today's computer performance it is not feasible to carry out simulations on a piece of material as large as a test specimen. The stiffness parameters are also complicated to evaluate in this deformation mode: for example, how large is the contraction in this case when contraction is prevented at the edges and becomes gradually more free towards the centre?

To avoid these problems a concept of cyclic geometry and boundary conditions is employed. The essence of these is that the network cell under observation is regarded as one of many identical cells making up a global network structure of infinite size. This leads to certain continuity requirements, namely that the cells must also match in a deformed condition.

The boundary conditions that have been used in most of the simulations allow the boundaries of the cell to deform, but only in such a way that the continuity requirements are fulfilled. These are defined in (6.39).  $u_1..u_6$  are the displacements defined, for example, in Figure 6.1, and superscripts indicate on which side of the unit cell a certain node is located. The sides of a unit cell are defined in Figure 6.7 and  $L_x, L_y, L_z$  denote the cell lengths along the coordinate axes.

$$\begin{bmatrix} u_1^{s2} - u_1^{s1} \\ u_2^{s2} - u_2^{s1} \\ u_3^{s2} - u_3^{s1} \\ u_4^{s2} - u_4^{s1} \\ u_5^{s2} - u_5^{s1} \\ u_6^{s2} - u_6^{s1} \\ u_1^{s4} - u_1^{s3} \\ u_2^{s4} - u_2^{s3} \\ u_3^{s4} - u_3^{s3} \\ u_4^{s4} - u_4^{s3} \\ u_5^{s4} - u_5^{s3} \\ u_6^{s4} - u_6^{s3} \\ u_1^{s6} - u_1^{s5} \\ u_2^{s6} - u_2^{s5} \\ u_3^{s6} - u_3^{s5} \\ u_4^{s6} - u_4^{s5} \\ u_5^{s6} - u_5^{s5} \\ u_6^{s6} - u_6^{s5} \end{bmatrix} = \begin{bmatrix} L_x & 0 & 0 & 0 & 0 & 0 \\ 0 & 0 & 0 & 0 & 0 & 0 \\ 0 & 0 & 0 & 0 & 0 & 0 \\ 0 & 0 & 0 & 0 & 0 & 0 \\ 0 & 0 & 0 & 0 & 0 & 0 \\ 0 & 0 & 0 & 0 & 0 & 0 \\ 0 & 0 & 0 & L_y & 0 & 0 \\ 0 & L_y & 0 & 0 & 0 & 0 \\ 0 & 0 & 0 & 0 & 0 & 0 \\ 0 & 0 & 0 & 0 & 0 & 0 \\ 0 & 0 & 0 & 0 & 0 & 0 \\ 0 & 0 & 0 & 0 & 0 & 0 \\ 0 & 0 & 0 & 0 & 0 & 0 \\ 0 & 0 & 0 & 0 & L_z & 0 \\ 0 & 0 & 0 & 0 & 0 & L_z \\ 0 & 0 & L_z & 0 & 0 & 0 \\ 0 & 0 & 0 & 0 & 0 & 0 \\ 0 & 0 & 0 & 0 & 0 & 0 \\ 0 & 0 & 0 & 0 & 0 & 0 \\ 0 & 0 & 0 & 0 & 0 & 0 \end{bmatrix} \begin{bmatrix} \epsilon_x \\ \epsilon_y \\ \epsilon_z \\ \gamma_{xy} \\ \gamma_{xz} \\ \gamma_{yz} \end{bmatrix} \quad (6.39)$$

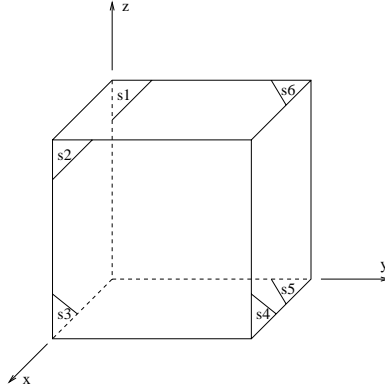


Figure 6.7: Labelling of the sides of a unit cell.

In two dimensions, this reduces to:

$$\begin{bmatrix} u_1^{s2} - u_1^{s1} \\ u_2^{s2} - u_1^{s1} \\ u_3^{s2} - u_1^{s1} \\ u_1^{s4} - u_3^{s3} \\ u_2^{s4} - u_3^{s3} \\ u_3^{s4} - u_3^{s3} \end{bmatrix} = \begin{bmatrix} L_x & 0 & 0 \\ 0 & 0 & 0 \\ 0 & 0 & 0 \\ 0 & 0 & L_y \\ 0 & L_y & 0 \\ 0 & 0 & 0 \end{bmatrix} \begin{bmatrix} \epsilon_x \\ \epsilon_y \\ \gamma_{xy} \end{bmatrix} \quad (6.40)$$

Some 2D simulations were also performed with boundary conditions where the boundaries were forced to remain straight during deformation. This leads to the following prescribed displacements of each node on the boundary:

$$\begin{bmatrix} u_1 \\ u_2 \\ u_3 \end{bmatrix} = \begin{bmatrix} x & 0 & 0 \\ 0 & y & 0 \\ 0 & 0 & -\sin^2 \alpha \end{bmatrix} \begin{bmatrix} \epsilon_x \\ \epsilon_y \\ \gamma_{xy} \end{bmatrix} \quad (6.41)$$

Here,  $(x, y)$  are the coordinates of the node, with the origin in the lower left corner of the network, and  $\alpha$  is the inclination of the fibre. The considerations that lead to the factor  $-\sin^2 \alpha$  can be found in [20].

The two different kinds of boundary conditions, which in the following are denoted S for straight boundaries and C for curved boundaries, are compared in Figure 6.8. One important consequence of boundary conditions C is that they entail equilibrium for each node along the boundary. Conditions S only give equilibrium in a mean sense. The consequences of the different boundary conditions are further discussed in Section 6.4.

### 6.3. Solution of the system of equations

The solution of the system of equations for the boundary conditions S, requiring straight boundaries, is straightforward. All boundary nodes have prescribed values

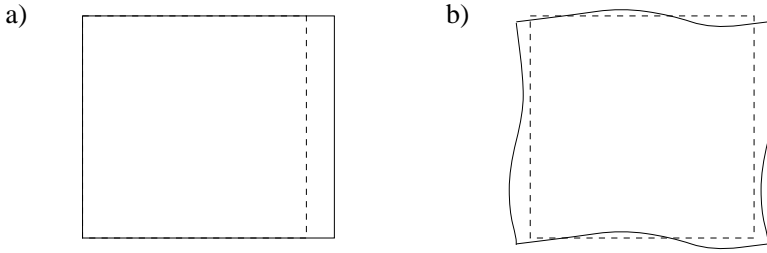


Figure 6.8: 2D cell subjected to  $\epsilon = (\epsilon_0, 0, 0)$  for a) boundary conditions  $S$ , according to (6.41), b) boundary conditions  $C$ , according to (6.40).

of displacement, and thus there are reaction forces on all the boundary nodes and no reaction forces occur on any interior node.

For boundary conditions  $C$ , allowing curving of the boundaries, the prescribed displacements are specified in terms of relations between different degrees of freedom, i.e. constraints. The constrained degrees of freedom are removed from the system of equations, see [55]. The original system of equations is:

$$K\mathbf{u} = \mathbf{f} \tag{6.42}$$

The constraints can be formulated as relations between a full and a reduced displacement vector  $\mathbf{u}$  and  $\mathbf{u}_{red}$ ,

$$\mathbf{u} = \mathbf{B}\mathbf{u}_{red} + \mathbf{C} . \tag{6.43}$$

For the nodes located along the boundaries, (6.39) rewritten in the form of (6.43) is

$$\begin{bmatrix} u_1^{s1} \\ u_1^{s2} \\ u_2^{s1} \\ u_2^{s2} \\ u_3^{s1} \\ u_3^{s2} \\ u_1^{s3} \\ u_1^{s4} \\ u_2^{s3} \\ u_2^{s4} \\ u_3^{s3} \\ u_3^{s4} \end{bmatrix} = \begin{bmatrix} 1 & 0 & 0 & 0 & 0 & 0 \\ 1 & 0 & 0 & 0 & 0 & 0 \\ 0 & 1 & 0 & 0 & 0 & 0 \\ 0 & 1 & 0 & 0 & 0 & 0 \\ 0 & 0 & 1 & 0 & 0 & 0 \\ 0 & 0 & 1 & 0 & 0 & 0 \\ 0 & 0 & 0 & 1 & 0 & 0 \\ 0 & 0 & 0 & 1 & 0 & 0 \\ 0 & 0 & 0 & 0 & 1 & 0 \\ 0 & 0 & 0 & 0 & 1 & 0 \\ 0 & 0 & 0 & 0 & 0 & 1 \\ 0 & 0 & 0 & 0 & 0 & 1 \end{bmatrix} \begin{bmatrix} u_1^{s1} \\ u_2^{s1} \\ u_3^{s1} \\ u_1^{s3} \\ u_2^{s3} \\ u_3^{s3} \end{bmatrix} + \begin{bmatrix} 0 \\ L_x \epsilon_x \\ 0 \\ 0 \\ 0 \\ 0 \\ 0 \\ L_y \gamma_{xy} \\ 0 \\ L_y \epsilon_y \\ 0 \\ 0 \end{bmatrix} . \tag{6.44}$$

In order to save space this is only given for the 2D case, but the 3D version is completely analogous. Insertion of (6.43) into (6.42) gives:

$$K\mathbf{B}\mathbf{u}_{red} + K\mathbf{C} = \mathbf{f} \tag{6.45}$$

In order to obtain a symmetric stiffness matrix, all terms are multiplied by  $\mathbf{B}^T$ :

$$\mathbf{B}^T \mathbf{K} \mathbf{B} \mathbf{u}_{red} = \mathbf{B}^T \mathbf{f} - \mathbf{B}^T \mathbf{K} \mathbf{C} \quad (6.46)$$

Defining

$$\mathbf{K}_{red} = \mathbf{B}^T \mathbf{K} \mathbf{B} , \quad (6.47)$$

$$\mathbf{f}_{red} = \mathbf{B}^T \mathbf{f} - \mathbf{B}^T \mathbf{K} \mathbf{C} , \quad (6.48)$$

we now have

$$\mathbf{K}_{red} \mathbf{u}_{red} = \mathbf{f}_{red} . \quad (6.49)$$

This system of equations is solved for  $\mathbf{u}_{red}$ ,  $\mathbf{u}$  is obtained from (6.43) and the reaction forces are obtained from (6.42).

In (6.49) rigid-body translation must be prevented, by e.g. prescribing zero displacement in the  $x$ -,  $y$ - and  $z$ -directions in an interior node. Rigid-body rotation is prevented automatically by the constraints. For example, since  $u_2^{s1}$  and  $u_2^{s2}$  must always be the same, the cell is not able to rotate.

As in the case of boundary conditions S, (6.41), for boundary conditions C there are also reaction forces on all boundary nodes, and none on the interior nodes. Moreover, for boundary conditions C the reaction forces in two opposite nodes are always equal in magnitude and opposite in direction. Should reaction forces occur in the interior node prescribed zero translation, this indicates lack of equilibrium due to numerical problems or some other error.

## 6.4. Evaluation of resultant forces and D matrix

To obtain the  $\mathbf{D}$  matrix of the equivalent continuous material, the network is successively subjected to six modes of deformation, corresponding to the six components of strain. First the strain  $\boldsymbol{\epsilon} = (1, 0, 0, 0, 0, 0)$  is applied, representing extension in the  $x$ -direction, without strain in the  $y$ - or  $z$ -directions or shear strains. The resultant forces on the sides of the network are calculated and are divided by the area of the side to obtain the stress. In two dimensions there are only three modes of deformation, and the procedure of obtaining the stresses is illustrated in Figure 6.9. Note that moments in the boundary nodes are omitted in the figure.

From (6.1) it follows that for  $\boldsymbol{\epsilon} = (1, 0, 0, 0, 0, 0)$ ,

$$\begin{bmatrix} \sigma_x \\ \sigma_y \\ \sigma_z \\ \tau_{xy} \\ \tau_{xz} \\ \tau_{yz} \end{bmatrix} = \begin{bmatrix} D_{11} & D_{12} & D_{13} & D_{14} & D_{15} & D_{16} \\ D_{12} & D_{22} & D_{23} & D_{24} & D_{25} & D_{26} \\ D_{13} & D_{23} & D_{33} & D_{34} & D_{35} & D_{36} \\ D_{14} & D_{24} & D_{34} & D_{44} & D_{45} & D_{46} \\ D_{15} & D_{25} & D_{35} & D_{45} & D_{55} & D_{56} \\ D_{16} & D_{26} & D_{36} & D_{46} & D_{56} & D_{66} \end{bmatrix} \begin{bmatrix} 1 \\ 0 \\ 0 \\ 0 \\ 0 \\ 0 \end{bmatrix} = \begin{bmatrix} D_{11} \\ D_{12} \\ D_{13} \\ D_{14} \\ D_{15} \\ D_{16} \end{bmatrix} . \quad (6.50)$$

Thus, the first column of  $\mathbf{D}$  is equal to the calculated stress vector. The remaining columns of  $\mathbf{D}$  are obtained analogously through applying  $\boldsymbol{\epsilon} = (0, 1, 0, 0, 0, 0)$  and so on.

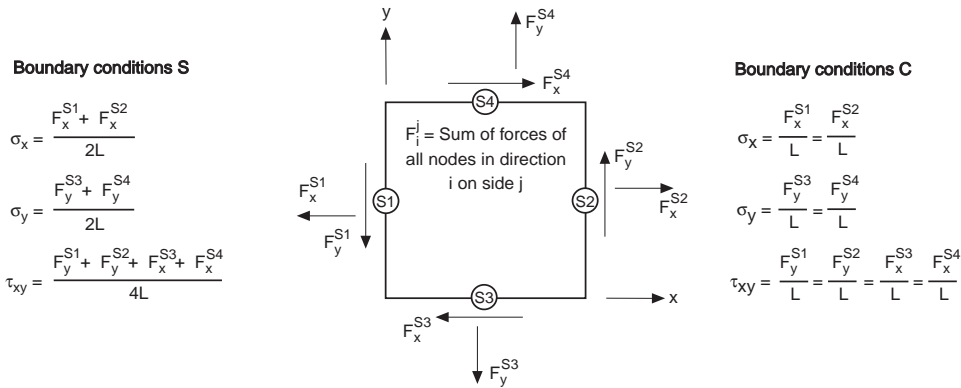


Figure 6.9: Evaluation of stresses.

For the case of boundary conditions C, the reaction forces in two opposite boundary nodes are equal in magnitude, and opposite in direction. This means that the sums of normal forces on opposite boundaries are equal, and the resultants are situated exactly opposite each other. In Figure 6.9 this means that  $F_x^{s1}$  and  $F_x^{s2}$  as well as  $F_y^{s3}$  and  $F_y^{s4}$  are collinear. Since the moments in opposite boundary nodes are also equal in size and opposite in direction, the total moment on the network from moments at the boundary nodes is zero. For the global moment equilibrium to be satisfied it is then necessary that the forces  $F_y^{s1}, F_y^{s2}$  and  $F_x^{s3}, F_x^{s4}$  are of equal magnitude. The  $D$  matrix obtained from boundary conditions C is automatically symmetric.

When boundary conditions S are employed the forces in opposite nodes are not equal, and thus  $F_x^{s1}$  and  $F_x^{s2}$  are not collinear, and  $F_y^{s1}, F_y^{s2}, F_x^{s3}$  and  $F_x^{s4}$  need not have the same values. Despite this, the global equilibrium of the cell is of course satisfied. The somewhat absurd consequence of forces in opposite nodes not being equal, is that if one imagines two neighbouring cells, the forces are not the same in the two fibre ends that are assumed to be attached to each other in the global network. The matrix  $D$  obtained from boundary conditions S is not symmetric. Since we want a symmetric  $D$  matrix, the mean values across the diagonal are taken as  $D$ . When requiring that the boundaries remain straight, the network is not allowed to deform in the way that is most natural to it. One may imagine a rigid frame being attached onto the network, which transfers the forces needed for the prescribed deformation to be possible. Intuitively this stiffens up the structure.

### 6.5. Anisotropic, orthotropic and isotropic materials

A linear elastic continuous material can be classified into different categories with respect to the symmetries of the material. If there are no preferred directions the

material is isotropic, otherwise it is anisotropic and, in the most general case,  $\mathbf{D}$  contains 21 independent constants:

$$\mathbf{D} = \begin{bmatrix} D_{11} & D_{12} & D_{13} & D_{14} & D_{15} & D_{16} \\ D_{12} & D_{22} & D_{23} & D_{24} & D_{25} & D_{26} \\ D_{13} & D_{23} & D_{33} & D_{34} & D_{35} & D_{36} \\ D_{14} & D_{24} & D_{34} & D_{44} & D_{45} & D_{46} \\ D_{15} & D_{25} & D_{35} & D_{45} & D_{55} & D_{56} \\ D_{16} & D_{26} & D_{36} & D_{46} & D_{56} & D_{66} \end{bmatrix} \quad (6.51)$$

In the case of symmetry with respect to three perpendicular axes, the material is orthotropic and the number of independent constants is reduced to nine.

$$\mathbf{D}^{ort} = \begin{bmatrix} \frac{E_x}{F}(1 - \nu_{zy}\nu_{yz}) & \frac{E_x}{F}(\nu_{yx} + \nu_{zx}\nu_{yz}) & \frac{E_x}{F}(\nu_{zx} + \nu_{yx}\nu_{zy}) & 0 & 0 & 0 \\ \frac{E_y}{F}(\nu_{xy} + \nu_{zy}\nu_{xz}) & \frac{E_y}{F}(1 - \nu_{zx}\nu_{xz}) & \frac{E_y}{F}(\nu_{zy} + \nu_{xy}\nu_{zx}) & 0 & 0 & 0 \\ \frac{E_z}{F}(\nu_{xz} + \nu_{xy}\nu_{yz}) & \frac{E_z}{F}(\nu_{yz} + \nu_{xz}\nu_{yx}) & \frac{E_z}{F}(1 - \nu_{xy}\nu_{yx}) & 0 & 0 & 0 \\ 0 & 0 & 0 & G_{xy} & 0 & 0 \\ 0 & 0 & 0 & 0 & G_{xz} & 0 \\ 0 & 0 & 0 & 0 & 0 & G_{yz} \end{bmatrix} \quad (6.52)$$

where

$$F = 1 - \nu_{zx}\nu_{xz} - \nu_{yx}\nu_{xy} - \nu_{zy}\nu_{yz} - \nu_{zx}\nu_{xy}\nu_{yz} - \nu_{yx}\nu_{zy}\nu_{xz} \quad (6.53)$$

and

$$\begin{aligned} E_x\nu_{yx} &= E_y\nu_{xy} \\ E_x\nu_{zx} &= E_z\nu_{xz} \\ E_y\nu_{zy} &= E_z\nu_{yz} . \end{aligned} \quad (6.54)$$

When the properties are the same in one plane and have different values in the out-of-plane direction the material is denoted transversely isotropic and the number of independent constants is five. Prime denoting out-of-plane properties, we have:

$$\mathbf{D}^{trans} = \begin{bmatrix} \frac{E(\nu'^2 E - E')}{F_1 F_2} & -\frac{E(\nu E' + \nu'^2 E)}{F_1 F_2} & -\frac{E E' \nu'}{F_2} & 0 & 0 & 0 \\ \frac{E(\nu E' + \nu'^2 E)}{F_1 F_2} & \frac{E(\nu'^2 E - E')}{F_1 F_2} & -\frac{E E' \nu'}{F_2} & 0 & 0 & 0 \\ -\frac{E E' \nu'}{F_2} & -\frac{E E' \nu'}{F_2} & \frac{E'^2(\nu - 1)}{F_2} & 0 & 0 & 0 \\ 0 & 0 & 0 & G & 0 & 0 \\ 0 & 0 & 0 & 0 & G' & 0 \\ 0 & 0 & 0 & 0 & 0 & G' \end{bmatrix} , \quad (6.55)$$

where

$$F_1 = (1 + \nu) , \quad (6.56)$$

$$F_2 = \nu E' - E' + 2\nu'^2 E \quad (6.57)$$

and

$$G = \frac{E}{2(1 + \nu)} . \quad (6.58)$$

The simplest possible material is isotropic, meaning that it has the same properties in every direction. In this case, the  $\mathbf{D}$  matrix contains only two independent constants, namely the modulus of elasticity,  $E$ , and Poisson's ratio,  $\nu$ :

$$\mathbf{D}^{iso} = \frac{E}{(1 + \nu)(1 - 2\nu)} \begin{bmatrix} 1 - \nu & \nu & \nu & 0 & 0 & 0 \\ \nu & 1 - \nu & \nu & 0 & 0 & 0 \\ \nu & \nu & 1 - \nu & 0 & 0 & 0 \\ 0 & 0 & 0 & \frac{1 - 2\nu}{2} & 0 & 0 \\ 0 & 0 & 0 & 0 & \frac{1 - 2\nu}{2} & 0 \\ 0 & 0 & 0 & 0 & 0 & \frac{1 - 2\nu}{2} \end{bmatrix} \quad (6.59)$$

In two dimensions, the corresponding anisotropic  $\mathbf{D}$  matrix contains 6 independent constants:

$$\mathbf{D} = \begin{bmatrix} D_{11} & D_{12} & D_{13} \\ D_{12} & D_{22} & D_{23} \\ D_{13} & D_{23} & D_{33} \end{bmatrix} \quad (6.60)$$

For orthotropic material the number of independent constants is reduced to four, and on assuming plane stress we obtain

$$\mathbf{D}^{ort} = \frac{1}{1 - \nu_{xy}\nu_{yx}} \begin{bmatrix} E_x & E_x\nu_{yx} & 0 \\ E_y\nu_{xy} & E_y & 0 \\ 0 & 0 & G_{xy}(1 - \nu_{xy}\nu_{yx}) \end{bmatrix}, \quad E_x\nu_{yx} = E_y\nu_{xy} . \quad (6.61)$$

For an isotropic material, the elastic parameters are  $E$  and  $\nu$ , as in the 3D case.

$$\mathbf{D}^{iso} = \frac{E}{1 - \nu^2} \begin{bmatrix} 1 & \nu & 0 \\ \nu & 1 & 0 \\ 0 & 0 & \frac{1 - \nu}{2} \end{bmatrix} \quad (6.62)$$

For an isotropic material,  $\mathbf{D}$  is the same for every material orientation, while for anisotropic materials  $\mathbf{D}$  depends on the orientation of the material. The orthotropic  $\mathbf{D}$  matrices given above refer to the case when the coordinate axes coincide with the principal directions of the material. The inverse of  $\mathbf{D}$  is generally of a simpler form, but since it is strain that is prescribed in the simulations it is despite this natural to use  $\mathbf{D}$ .

For a three-dimensional isotropic material, it is known that certain restrictions can be imposed on the elastic moduli. Assuming positive definiteness of the strain energy, see [35], leads to the conditions

$$E > 0 \quad \text{and} \quad -1 < \nu < \frac{1}{2} . \quad (6.63)$$

Even if a two-dimensional network is approximately isotropic in its own plane, there is no reason to believe that it has the same properties in the out-of-plane direction. Because of this, the restrictions given above are not generally applicable to the moduli of two-dimensional networks.

Although a network is in general anisotropic, one would expect nearly isotropic or transversely isotropic behaviour for fairly dense networks, if the fibres have a uniform orientation distribution. If the orientation distribution  $N_\alpha$  is symmetric with respect to three/two perpendicular axes, nearly orthotropic network properties can be expected.

If the network is to be represented as an anisotropic material, the  $\mathbf{D}$  matrix obtained from the simulations requires no further processing, except for symmetrization for boundary conditions S. For boundary conditions C, the anisotropic representation describes *exactly* how the simulated network responds when subjected to strain, but it has the drawback of a difficult intuitive physical interpretation of the constants and requires as many as 21 (6 in two dimensions) constants to characterize the material.

In cases where the network is nearly isotropic it would be advantageous to characterize the material with the two well-known parameters  $E$  and  $\nu$  instead.

## 6.6. Approximation of a near isotropic $\mathbf{D}$ matrix

It is desirable to have a method of finding the parameters that describe an isotropic material that is, in some sense, as close as possible to the simulated material. In order to obtain this isotropic approximation of the anisotropic  $\mathbf{D}$  matrix resulting from a simulation, a least-squares procedure is applied.

The heterogeneous network material is assumed to be subject to uniaxial tensile strain,  $\epsilon_0$ , in every direction. This results, in general, in different stresses for tensile strain in different directions. For a homogeneous isotropic material the stresses are, however, independent of the direction of the applied strain. The idea is to minimize the square of the difference between the stresses obtained for a homogeneous isotropic material and those obtained for the simulated anisotropic network material, summed over every direction of the applied strain, and for each strain direction summed over the six stress components for all material rotations about the strain direction.

The orientation of a coordinate system  $(x', y', z')$  relative to the original system can be defined by three angles  $(\alpha_x, \alpha_y, \alpha_z)$ , representing successive rotations about the  $x$ -,  $y$ - and  $z$ -axes.

From (6.1) and (6.59) we have, for an isotropic material

$$\begin{bmatrix} \sigma_x^{iso}(\alpha_x, \alpha_y, \alpha_z) \\ \sigma_y^{iso}(\alpha_x, \alpha_y, \alpha_z) \\ \sigma_z^{iso}(\alpha_x, \alpha_y, \alpha_z) \\ \tau_{xy}^{iso}(\alpha_x, \alpha_y, \alpha_z) \\ \tau_{xz}^{iso}(\alpha_x, \alpha_y, \alpha_z) \\ \tau_{yz}^{iso}(\alpha_x, \alpha_y, \alpha_z) \end{bmatrix} = \mathbf{D}^{iso} \begin{bmatrix} \epsilon_0 \\ 0 \\ 0 \\ 0 \\ 0 \\ 0 \end{bmatrix} = \begin{bmatrix} \frac{E(1-\nu)}{(1+\nu)(1-2\nu)}\epsilon_0 \\ \frac{\nu E}{(1+\nu)(1-2\nu)}\epsilon_0 \\ \frac{\nu E}{(1+\nu)(1-2\nu)}\epsilon_0 \\ 0 \\ 0 \\ 0 \end{bmatrix}, \quad (6.64)$$

where the superscript *iso* denotes isotropic material. That is,  $\sigma_x$ ,  $\sigma_y$  and  $\sigma_z$  are constant with respect to material orientation angles  $(\alpha_x, \alpha_y, \alpha_z)$ , and  $\tau_{xy}$ ,  $\tau_{xz}$  and  $\tau_{yz}$  are identically equal to zero for every value of  $(\alpha_x, \alpha_y, \alpha_z)$ .

For an anisotropic material all stress components vary with  $(\alpha_x, \alpha_y, \alpha_z)$ . Since it is not practically possible to simulate tension in a network in all directions,  $\boldsymbol{\sigma}^s$  is obtained by transforming  $\mathbf{D}$  from one simulation to all material orientations. The superscript *s* here denotes simulated network material.

If the coordinate frame is rotated through an angle  $\alpha_x$  about the *x*-axis,  $\mathbf{D}$  is transformed into

$$\mathbf{D}'(\alpha_x) = \mathbf{T}_1(\alpha_x)\mathbf{D}\mathbf{T}_1^T(\alpha_x), \quad (6.65)$$

where the matrix  $\mathbf{T}_1$  is derived in Appendix D. The equivalent relations for rotation about the *y*- and *z*-axes are

$$\mathbf{D}'(\alpha_y) = \mathbf{T}_2(\alpha_y)\mathbf{D}\mathbf{T}_2^T(\alpha_y), \quad (6.66)$$

$$\mathbf{D}'(\alpha_z) = \mathbf{T}_3(\alpha_z)\mathbf{D}\mathbf{T}_3^T(\alpha_z). \quad (6.67)$$

An arbitrary orientation of the *x'*-axis can be obtained by rotating the coordinate system through an angle  $\alpha_y$ ,  $0 \leq \alpha_y \leq 2\pi$ , followed by rotation through an angle  $\alpha_z$ ,  $-\pi/2 \leq \alpha_z \leq \pi/2$ . For every direction of the *x'*-axis the *y'*- and *z'*-axes are rotated through an angle  $\alpha_x$ ,  $0 \leq \alpha_x \leq 2\pi$  in order to cover every possible material orientation. This leads to

$$\mathbf{D}'(\alpha_x, \alpha_y, \alpha_z) = \mathbf{T}_1\mathbf{T}_3\mathbf{T}_2\mathbf{D}\mathbf{T}_2^T\mathbf{T}_3^T\mathbf{T}_1^T. \quad (6.68)$$

It should be noted that the order of finite rotations is not arbitrary. In connection with the integration limits that are chosen here only the rotation sequences  $(\mathbf{T}_2\mathbf{T}_3\mathbf{T}_1)$  and  $(\mathbf{T}_1\mathbf{T}_3\mathbf{T}_2)$ , counted from the inside, represent uniquely all possible orientations of the coordinate frame. Even those two sequences give different values of  $\mathbf{D}'$  for the same set of angles  $(\alpha_x, \alpha_y, \alpha_z)$ , but the integrals over all orientations are the same.

This gives the following expression for  $\boldsymbol{\sigma}^s$ :

$$\begin{bmatrix} \sigma_x^s(\alpha_x, \alpha_y, \alpha_z) \\ \sigma_y^s(\alpha_x, \alpha_y, \alpha_z) \\ \sigma_z^s(\alpha_x, \alpha_y, \alpha_z) \\ \tau_{xy}^s(\alpha_x, \alpha_y, \alpha_z) \\ \tau_{xz}^s(\alpha_x, \alpha_y, \alpha_z) \\ \tau_{yz}^s(\alpha_x, \alpha_y, \alpha_z) \end{bmatrix} = \mathbf{D}'(\alpha_x, \alpha_y, \alpha_z) \begin{bmatrix} \epsilon_0 \\ 0 \\ 0 \\ 0 \\ 0 \\ 0 \end{bmatrix} = \begin{bmatrix} D'_{11}(\alpha_x, \alpha_y, \alpha_z)\epsilon_0 \\ D'_{21}(\alpha_x, \alpha_y, \alpha_z)\epsilon_0 \\ D'_{31}(\alpha_x, \alpha_y, \alpha_z)\epsilon_0 \\ D'_{41}(\alpha_x, \alpha_y, \alpha_z)\epsilon_0 \\ D'_{51}(\alpha_x, \alpha_y, \alpha_z)\epsilon_0 \\ D'_{61}(\alpha_x, \alpha_y, \alpha_z)\epsilon_0 \end{bmatrix} \quad (6.69)$$

This expression is too long to present in an explicit form, but it can readily be calculated using Maple [36].

Now we can give an expression for the square of the difference between the components of  $\boldsymbol{\sigma}^{iso}$  and  $\boldsymbol{\sigma}^s$ , integrated over all possible material orientations. The objective is to find the values of  $E$  and  $\nu$  that minimize this functional  $Q$ :

$$Q = \int_{sphere} \int_0^{2\pi} (\sigma_x^s - \sigma_x^{iso})^2 + (\sigma_y^s - \sigma_y^{iso})^2 + (\sigma_z^s - \sigma_z^{iso})^2 + (\tau_{xy}^s - \tau_{xy}^{iso})^2 + (\tau_{xz}^s - \tau_{xz}^{iso})^2 + (\tau_{yz}^s - \tau_{yz}^{iso})^2 d\alpha_x dA_{sphere} \quad (6.70)$$

On inserting (6.64) and noting that  $dA_{sphere} = \cos\alpha_z d\alpha_y d\alpha_z$  we obtain

$$Q = \int_{-\frac{\pi}{2}}^{\frac{\pi}{2}} \int_0^{2\pi} \int_0^{2\pi} \left( \left( \sigma_x^s - \frac{E(1-\nu)}{(1+\nu)(1-2\nu)}\epsilon_0 \right)^2 + \left( \sigma_y^s - \frac{\nu E}{(1+\nu)(1-2\nu)}\epsilon_0 \right)^2 + \left( \sigma_z^s - \frac{\nu E}{(1+\nu)(1-2\nu)}\epsilon_0 \right)^2 + (\tau_{xy}^s)^2 + (\tau_{xz}^s)^2 + (\tau_{yz}^s)^2 \right) \cos\alpha_z d\alpha_x d\alpha_y d\alpha_z . \quad (6.71)$$

Minimize  $Q$  with respect to  $\frac{E}{(1+\nu)(1-2\nu)}$  and  $\frac{\nu E}{(1+\nu)(1-2\nu)}$ :

$$\begin{aligned} \frac{\partial Q}{\partial \frac{E}{(1+\nu)(1-2\nu)}} &= \int_{-\frac{\pi}{2}}^{\frac{\pi}{2}} \int_0^{2\pi} \int_0^{2\pi} -2\epsilon_0 \cos\alpha_z \left( \sigma_x^s - \frac{E(1-\nu)}{(1+\nu)(1-2\nu)}\epsilon_0 \right) d\alpha_x d\alpha_y d\alpha_z = 0 \\ \frac{\partial Q}{\partial \frac{\nu E}{(1+\nu)(1-2\nu)}} &= \int_{-\frac{\pi}{2}}^{\frac{\pi}{2}} \int_0^{2\pi} \int_0^{2\pi} -2\epsilon_0 \cos\alpha_z \left( \sigma_y^s - \frac{\nu E}{(1+\nu)(1-2\nu)}\epsilon_0 \right) - \\ &\quad 2\epsilon_0 \left( \sigma_z^s - \frac{\nu E}{(1+\nu)(1-2\nu)}\epsilon_0 \right) d\alpha_x d\alpha_y d\alpha_z = 0 \end{aligned} \quad (6.72)$$

Integrating the terms representing  $\sigma^{iso}$  and rearranging the equations gives

$$\int_{-\frac{\pi}{2}}^{\frac{\pi}{2}} \int_0^{2\pi} \int_0^{2\pi} \sigma_x^s \cos \alpha_z d\alpha_x d\alpha_y d\alpha_z = \frac{E(1-\nu)}{(1+\nu)(1-2\nu)} 8\pi^2$$

$$\int_{-\frac{\pi}{2}}^{\frac{\pi}{2}} \int_0^{2\pi} \int_0^{2\pi} (\sigma_y^s + \sigma_z^s) \cos \alpha_z d\alpha_x d\alpha_y d\alpha_z = \frac{2E\nu}{(1+\nu)(1-2\nu)} 8\pi^2 .$$
(6.73)

It now remains to evaluate the integrals of the stresses for a simulated material.

$$\int_{-\frac{\pi}{2}}^{\frac{\pi}{2}} \int_0^{2\pi} \int_0^{2\pi} \sigma_x^s \cos \alpha_z d\alpha_x d\alpha_y d\alpha_z = \frac{\pi^2}{15} (24(D_{11} + D_{22} + D_{33}) + 16(D_{12} + D_{13} + D_{23})$$

$$+ 32(D_{44} + D_{55} + D_{66}))$$

$$\int_{-\frac{\pi}{2}}^{\frac{\pi}{2}} \int_0^{2\pi} \int_0^{2\pi} \sigma_y^s \cos \alpha_z d\alpha_x d\alpha_y d\alpha_z = \frac{\pi^2}{15} (8(D_{11} + D_{22} + D_{33}) + 32(D_{12} + D_{13} + D_{23}) +$$

$$- 16(D_{44} + D_{55} + D_{66}))$$

$$\int_{-\frac{\pi}{2}}^{\frac{\pi}{2}} \int_0^{2\pi} \int_0^{2\pi} \sigma_z^s \cos \alpha_z d\alpha_x d\alpha_y d\alpha_z = \frac{\pi^2}{15} (8(D_{11} + D_{22} + D_{33}) + 32(D_{12} + D_{13} + D_{23}) +$$

$$- 16(D_{44} + D_{55} + D_{66}))$$

$$\int_{-\frac{\pi}{2}}^{\frac{\pi}{2}} \int_0^{2\pi} \int_0^{2\pi} \tau_{xy}^s \cos \alpha_z d\alpha_x d\alpha_y d\alpha_z = 0$$

$$\int_{-\frac{\pi}{2}}^{\frac{\pi}{2}} \int_0^{2\pi} \int_0^{2\pi} \tau_{xz}^s \cos \alpha_z d\alpha_x d\alpha_y d\alpha_z = 0$$

$$\int_{-\frac{\pi}{2}}^{\frac{\pi}{2}} \int_0^{2\pi} \int_0^{2\pi} \tau_{yz}^s \cos \alpha_z d\alpha_x d\alpha_y d\alpha_z = 0$$
(6.74)

The latter three integrals do not enter into the equations, but it is still of interest that the shear stresses integrated over all orientations equals zero, as in an isotropic material.

From (6.73) and (6.74) we can now calculate the values of  $\nu$  and  $E$  that minimize

$Q$  in 3D analysis:

$$\nu = \frac{\int_{-\frac{\pi}{2}}^{\frac{\pi}{2}} \int_0^{2\pi} \int_0^{2\pi} (\sigma_y^s + \sigma_z^s) d\alpha_x d\alpha_y d\alpha_z}{2 \int_{-\frac{\pi}{2}}^{\frac{\pi}{2}} \int_0^{2\pi} \int_0^{2\pi} \sigma_x^s d\alpha_x d\alpha_y d\alpha_z + \int_{-\frac{\pi}{2}}^{\frac{\pi}{2}} \int_0^{2\pi} \int_0^{2\pi} (\sigma_y^s + \sigma_z^s) d\alpha_x d\alpha_y d\alpha_z} =$$

$$\frac{D_{11} + D_{22} + D_{33} + 4(D_{12} + D_{13} + D_{23}) - 2(D_{44} + D_{55} + D_{66})}{4(D_{11} + D_{22} + D_{33}) + 6(D_{12} + D_{13} + D_{23}) + 2(D_{44} + D_{55} + D_{66})}$$

$$E = \frac{(1 + \nu)(1 - 2\nu)}{8\pi^2(1 - \nu)} \int_{-\frac{\pi}{2}}^{\frac{\pi}{2}} \int_0^{2\pi} \int_0^{2\pi} \sigma_x^s d\alpha_x d\alpha_y d\alpha_z =$$

$$\frac{(1 + \nu)(1 - 2\nu)}{15(1 - \nu)} (3(D_{11} + D_{22} + D_{33}) + 2(D_{12} + D_{13} + D_{23}) + 4(D_{44} + D_{55} + D_{66})) \quad (6.75)$$

An analogous approach is used in 2 dimensions. This gives for  $\boldsymbol{\sigma}^{iso}$  as a function of material orientation angle  $\alpha_z$ :

$$\begin{bmatrix} \sigma_x^{iso}(\alpha_z) \\ \sigma_y^{iso}(\alpha_z) \\ \tau_{xy}^{iso}(\alpha_z) \end{bmatrix} = \frac{E}{1 - \nu^2} \begin{bmatrix} 1 & \nu & 0 \\ \nu & 1 & 0 \\ 0 & 0 & \frac{1 - \nu}{2} \end{bmatrix} \begin{bmatrix} \epsilon_0 \\ 0 \\ 0 \end{bmatrix} = \begin{bmatrix} \frac{E}{1 - \nu^2} \epsilon_0 \\ \frac{\nu E}{1 - \nu^2} \epsilon_0 \\ 0 \end{bmatrix} \quad (6.76)$$

If the coordinate frame is rotated an angle  $\alpha_z$ ,  $\mathbf{D}$  is transformed into, see [65],

$$\mathbf{D}'(\alpha_z) = \mathbf{T} \mathbf{D} \mathbf{T}^T, \quad (6.77)$$

where

$$\mathbf{T} = \begin{bmatrix} \cos^2 \alpha_z & \sin^2 \alpha_z & 2 \sin \alpha_z \cos \alpha_z \\ \sin^2 \alpha_z & \cos^2 \alpha_z & -2 \sin \alpha_z \cos \alpha_z \\ -\sin \alpha_z \cos \alpha_z & \sin \alpha_z \cos \alpha_z & \cos^2 \alpha_z - \sin^2 \alpha_z \end{bmatrix}. \quad (6.78)$$

This gives

$$\begin{bmatrix} \sigma_x^s(\alpha_z) \\ \sigma_y^s(\alpha_z) \\ \tau_{xy}^s(\alpha_z) \end{bmatrix} = \mathbf{D}'(\alpha_z) \begin{bmatrix} \epsilon_0 \\ 0 \\ 0 \end{bmatrix} = \begin{bmatrix} D'_{11}(\alpha_z) \epsilon_0 \\ D'_{21}(\alpha_z) \epsilon_0 \\ D'_{31}(\alpha_z) \epsilon_0 \end{bmatrix}. \quad (6.79)$$

Denoting  $\cos \alpha_z$  by  $c$  and  $\sin \alpha_z$  by  $s$  yields:

$$\begin{aligned}
 \sigma_x^s(\alpha_z) &= (c^4 D_{11} + 2c^2 s^2 D_{12} + 4sc^3 D_{13} + s^4 D_{22} + 4s^3 c D_{23} + 4s^2 c^2 D_{33}) \epsilon_0 \\
 \sigma_y^s(\alpha_z) &= (s^2 c^2 D_{11} + (s^4 + c^4) D_{12} + 2sc(s^2 - c^2) D_{13} + s^2 c^2 D_{22} + \\
 &\quad 2sc(c^2 - s^2) D_{23} - 4s^2 c^2 D_{33}) \epsilon_0 \\
 \tau_{xy}^s(\alpha_z) &= (-sc^3 D_{11} + sc(c^2 - s^2) D_{12} + ((c^2 - s^2)c^2 - 2s^2 c^2) D_{13} + s^3 c D_{22} + \\
 &\quad ((c^2 - s^2)s^2 + 2s^2 c^2) D_{23} + 2sc(c^2 - s^2) D_{33}) \epsilon_0
 \end{aligned} \tag{6.80}$$

In Figure 6.10 the stresses  $\sigma^s$  and  $\sigma^{iso}$  are plotted as a function of  $\alpha_z$ . The compo-

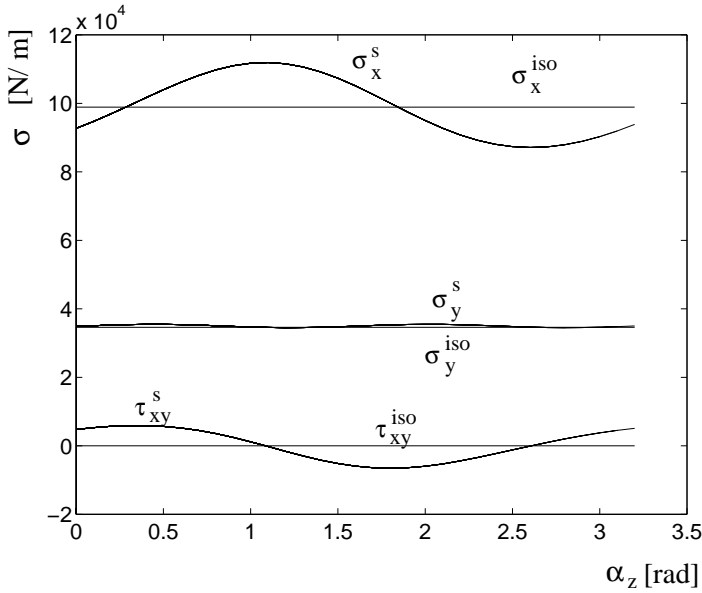


Figure 6.10: Stresses  $\sigma^s$  and  $\sigma^{iso}$  as a function of the angle  $\alpha_z$ .

nents of  $\sigma^s$  plotted are those of the 2D basic example network. The components of  $\sigma^{iso}$  are plotted in the position that the calculations will finally give.

The functional  $Q$  now takes the form:

$$Q = \int_0^\pi (\sigma_x^s - \sigma_x^e)^2 + (\sigma_y^s - \sigma_y^e)^2 + (\tau_{xy}^s - \tau_{xy}^e)^2 d\alpha_z \tag{6.81}$$

On inserting (6.76) we have

$$Q = \int_0^\pi \left( \sigma_x^s - \frac{E}{1-\nu^2} \epsilon_0 \right)^2 + \left( \sigma_y^s - \frac{\nu E}{1-\nu^2} \epsilon_0 \right)^2 + \tau_{xy}^{s^2} d\alpha_z . \tag{6.82}$$

Minimize  $Q$  with respect to  $\frac{E}{1-\nu^2}$  and  $\frac{\nu E}{1-\nu^2}$ :

$$\begin{aligned}\frac{\partial Q}{\partial \frac{E}{1-\nu^2}} &= \int_0^\pi -2\epsilon_0\left(\sigma_x^s - \frac{E}{1-\nu^2}\epsilon_0\right)d\alpha_z = 0 \\ \frac{\partial Q}{\partial \frac{\nu E}{1-\nu^2}} &= \int_0^\pi -2\epsilon_0\left(\sigma_y^s - \frac{\nu E}{1-\nu^2}\epsilon_0\right)d\alpha_z = 0\end{aligned}\tag{6.83}$$

Integrating the last term and rearranging the equations gives

$$\begin{aligned}\int_0^\pi \sigma_x^s d\alpha_z &= \frac{E}{1-\nu^2}\epsilon_0\pi \\ \int_0^\pi \sigma_y^s d\alpha_z &= \frac{E\nu}{1-\nu^2}\epsilon_0\pi .\end{aligned}\tag{6.84}$$

The equations imply that the areas under the curves for isotropic and simulated material should be the same.

Integrating (6.80) gives

$$\begin{aligned}\int_0^\pi \sigma_x^s d\alpha_z &= \frac{\pi}{8}(3D_{11} + 2D_{12} + 3D_{22} + 4D_{33}) \\ \int_0^\pi \sigma_y^s d\alpha_z &= \frac{\pi}{8}(D_{11} + 6D_{12} + D_{22} - 4D_{33}) \\ \int_0^\pi \tau_{xy}^s d\alpha_z &= 0 .\end{aligned}\tag{6.85}$$

From (6.84) and (6.85) we can now calculate the values of  $\nu$  and  $E$  that minimize  $Q$  for 2D analysis:

$$\begin{aligned}\nu &= \frac{\int_0^\pi \sigma_y^s d\alpha_z}{\int_0^\pi \sigma_x^s d\alpha_z} = \frac{(D_{11} + 6D_{12} + D_{22} - 4D_{33})}{(3D_{11} + 2D_{12} + 3D_{22} + 4D_{33})} \\ E &= \frac{1-\nu^2}{\epsilon_0\pi} \int_0^\pi \sigma_x^s d\alpha_z = \frac{1-\nu^2}{8\epsilon_0}(3D_{11} + 2D_{12} + 3D_{22} + 4D_{33})\end{aligned}$$

## 6.7. Approximation of a near orthotropic D matrix

If the orientation distribution of the fibres is not uniform, but still symmetric with respect to perpendicular axes, there is no longer any reason to believe that the material is isotropic, but rather orthotropic. We thus, want to know which is the best estimation of orthotropic material parameters.

One problem that arises is that of finding the principal directions of the simulated material. The simplest solution would be to assume that the principal directions are coincident with the symmetry axes of the fibre orientation distribution, which they should be on taking the average of many networks. A second way is to transform the  $\mathbf{D}$  matrix obtained from simulations to different material orientations and check where a principal direction criterion is best fulfilled. This criterion could be the maximum value of  $D_{11}$ ,  $D_{22}$  or  $D_{33}$  and a close to zero value for the components which are identically equal to zero for an orthotropic material. We chose to use the first approach since this seems to be a reasonable approximation in the cases where it is used, see Section 7.5.

We thus assumed that the principal directions are known to coincide with the coordinate axes. For simplicity, the calculations are shown for two dimensions, but the 3D case is completely analogous. We use the same approach as for isotropic material, that is minimize the expression

$$Q = \int_0^\pi [(\sigma_x^s - \sigma_x^{ort})^2 + (\sigma_y^s - \sigma_y^{ort})^2 + (\tau_{xy}^s - \tau_{xy}^{ort})^2] d\alpha_z, \quad (6.86)$$

with respect to the four independent components of  $\mathbf{D}^{ort}$ , see (6.61).

$\sigma^s$  is the same as in the preceding section, that is

$$\begin{aligned} \int_0^\pi \sigma_x^s d\alpha_z &= \frac{\pi}{8}(3D_{11}^s + 2D_{12}^s + 3D_{22}^s + 4D_{33}^s) \\ \int_0^\pi \sigma_y^s d\alpha_z &= \frac{\pi}{8}(D_{11}^s + 6D_{12}^s + D_{22}^s - 4D_{33}^s) \\ \int_0^\pi \tau_{xy}^s d\alpha_z &= 0, \end{aligned} \quad (6.87)$$

where the superscript  $s$  has been added to emphasize that we are referring to the components of  $\mathbf{D}$  obtained from simulations.  $\sigma^{ort}$  is not as simple as in the isotropic case, the superscript  $ort$  here denoting orthotropic material, since it is dependent on the material orientation angle  $\alpha_z$ . That is:

$$\begin{bmatrix} \sigma_x^{ort}(\alpha_z) \\ \sigma_y^{ort}(\alpha_z) \\ \tau_{xy}^{ort}(\alpha_z) \end{bmatrix} = \mathbf{D}^{ort'}(\alpha_z) \begin{bmatrix} \epsilon_0 \\ 0 \\ 0 \end{bmatrix} = \begin{bmatrix} D_{11}^{ort'}(\alpha_z)\epsilon_0 \\ D_{21}^{ort'}(\alpha_z)\epsilon_0 \\ D_{31}^{ort'}(\alpha_z)\epsilon_0 \end{bmatrix} \quad (6.88)$$

In analogy with  $\sigma^s$ , this yields

$$\begin{aligned} \int_0^\pi \sigma_x^{ort} d\alpha_z &= \frac{\pi}{8}(3D_{11}^{ort} + 2D_{12}^{ort} + 3D_{22}^{ort} + 4D_{33}^{ort}) \\ \int_0^\pi \sigma_y^{ort} d\alpha_z &= \frac{\pi}{8}(D_{11}^{ort} + 6D_{12}^{ort} + D_{22}^{ort} - 4D_{33}^{ort}) \\ \int_0^\pi \tau_{xy}^{ort} d\alpha_z &= 0. \end{aligned} \quad (6.89)$$

On inserting the expressions for  $\sigma^{ort}$  and  $\sigma^s$  into (6.86), it is found that the best estimate is to take the coefficients directly from the simulated  $\mathbf{D}$  matrix, that is:

$$\begin{aligned} D_{11}^{ort} &= D_{11}^s \\ D_{12}^{ort} &= D_{12}^s \\ D_{22}^{ort} &= D_{22}^s \\ D_{33}^{ort} &= D_{33}^s \end{aligned} \tag{6.90}$$

The components  $D_{31}^s$  and  $D_{32}^s$  provide a measure of the correctness of the approximation to orthotropic material, since they should be identically equal to zero in a truly orthotropic material.

The step from components of  $\mathbf{D}^{ort}$  to the individual physical constants  $E_x$ ,  $E_y$ ,  $G_{xy}$ ,  $\nu_{xy}$  and  $\nu_{yx}$  consists of solving the non-linear system of equations

$$\left\{ \begin{array}{l} \frac{E_x}{1 - \nu_{xy}\nu_{yx}} = D_{11}^{ort} \\ \frac{E_y}{1 - \nu_{xy}\nu_{yx}} = D_{22}^{ort} \\ \frac{E_x\nu_{yx}}{1 - \nu_{xy}\nu_{yx}} = D_{12}^{ort} \\ \frac{E_y\nu_{xy}}{1 - \nu_{xy}\nu_{yx}} = D_{12}^{ort} \\ G_{xy} = D_{33}^{ort} \end{array} \right. . \tag{6.91}$$

The solution to this is:

$$\left\{ \begin{array}{l} E_x = D_{11}^{ort} \left( 1 - \frac{(D_{12}^{ort})^2}{D_{11}^{ort} D_{22}^{ort}} \right) \\ E_y = D_{22}^{ort} \left( 1 - \frac{(D_{12}^{ort})^2}{D_{11}^{ort} D_{22}^{ort}} \right) \\ \nu_{yx} = \frac{D_{12}^{ort}}{D_{11}^{ort}} \\ \nu_{xy} = \frac{D_{12}^{ort}}{D_{22}^{ort}} \\ G_{xy} = D_{33}^{ort} \end{array} \right. , \tag{6.92}$$

providing the parameters used to describe an orthotropic network in the next chapter.

The corresponding solution for three dimensions is obtained using Maple, [36]:

$$\left\{ \begin{array}{l}
 E_x = \frac{D_{11}^{ort} D_{22}^{ort} D_{33}^{ort} - D_{11}^{ort} (D_{23}^{ort})^2 - D_{22}^{ort} (D_{13}^{ort})^2 - D_{33}^{ort} (D_{12}^{ort})^2 + 2D_{12}^{ort} D_{13}^{ort} D_{23}^{ort}}{D_{11}^{ort} D_{33}^{ort} - (D_{13}^{ort})^2} \\
 E_y = \frac{D_{11}^{ort} D_{22}^{ort} D_{33}^{ort} - D_{11}^{ort} (D_{23}^{ort})^2 - D_{22}^{ort} (D_{13}^{ort})^2 - D_{33}^{ort} (D_{12}^{ort})^2 + 2D_{12}^{ort} D_{13}^{ort} D_{23}^{ort}}{D_{11}^{ort} D_{33}^{ort} - (D_{13}^{ort})^2} \\
 E_z = \frac{(D_{11}^{ort} D_{22}^{ort} D_{33}^{ort} - D_{11}^{ort} (D_{23}^{ort})^2 - D_{22}^{ort} (D_{13}^{ort})^2 - D_{33}^{ort} (D_{12}^{ort})^2 + 2D_{12}^{ort} D_{13}^{ort} D_{23}^{ort})}{D_{11}^{ort} D_{22}^{ort} - (D_{12}^{ort})^2} \\
 \nu_{yx} = \frac{-D_{13}^{ort} D_{23}^{ort} + D_{33}^{ort} D_{12}^{ort}}{D_{11}^{ort} D_{33}^{ort} - (D_{13}^{ort})^2} \\
 \nu_{xy} = \frac{-D_{13}^{ort} D_{23}^{ort} + D_{33}^{ort} D_{12}^{ort}}{D_{22}^{ort} D_{33}^{ort} - (D_{23}^{ort})^2} \\
 \nu_{xz} = \frac{D_{13}^{ort} D_{22}^{ort} - D_{23}^{ort} D_{12}^{ort}}{D_{22}^{ort} D_{33}^{ort} - (D_{23}^{ort})^2} \\
 \nu_{zx} = \frac{D_{13}^{ort} D_{22}^{ort} - D_{23}^{ort} D_{12}^{ort}}{D_{11}^{ort} D_{22}^{ort} - (D_{12}^{ort})^2} \\
 \nu_{yz} = \frac{D_{11}^{ort} D_{23}^{ort} - D_{12}^{ort} D_{13}^{ort}}{D_{11}^{ort} D_{33}^{ort} - (D_{13}^{ort})^2} \\
 \nu_{zy} = \frac{D_{11}^{ort} D_{23}^{ort} - D_{12}^{ort} D_{13}^{ort}}{D_{11}^{ort} D_{22}^{ort} - (D_{12}^{ort})^2} \\
 G_{xy} = D_{44}^{ort} \\
 G_{xz} = D_{55}^{ort} \\
 G_{yz} = D_{66}^{ort}
 \end{array} \right. \quad (6.93)$$

When a material that is close to transversely isotropic is expected, we want a method to find the transversely isotropic parameters that correspond to the  $\mathbf{D}$  obtained from the simulations. Transverse isotropy is viewed as a special case of orthotropy. The difference between  $\mathbf{D}$  for a transversely isotropic and an orthotropic material is that for a transversely isotropic material  $D_{11} = D_{22}$  and  $D_{13} = D_{23}$ . The coefficients of the transversely isotropic  $\mathbf{D}$  are obtained through taking the mean values as follows:

$$D_{11}^{trans} = D_{22}^{trans} = \frac{D_{11}^{ort} + D_{22}^{ort}}{2}, \quad (6.94)$$

$$D_{13}^{trans} = D_{23}^{trans} = \frac{D_{13}^{ort} + D_{23}^{ort}}{2}. \quad (6.95)$$

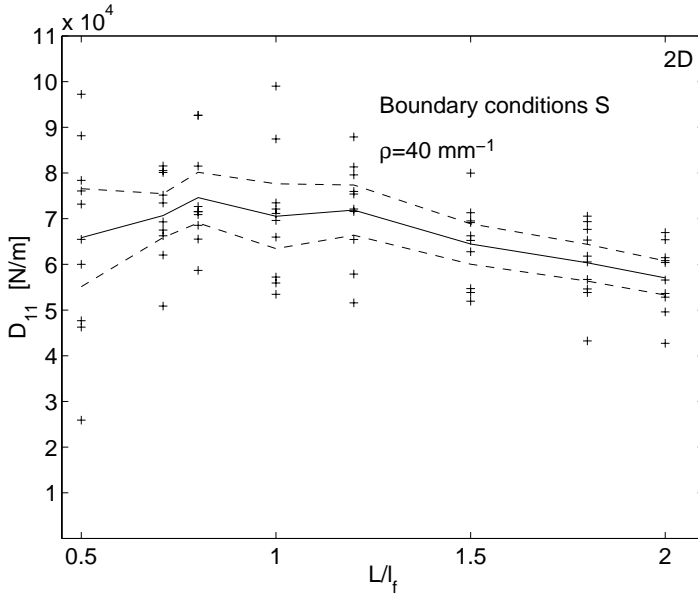
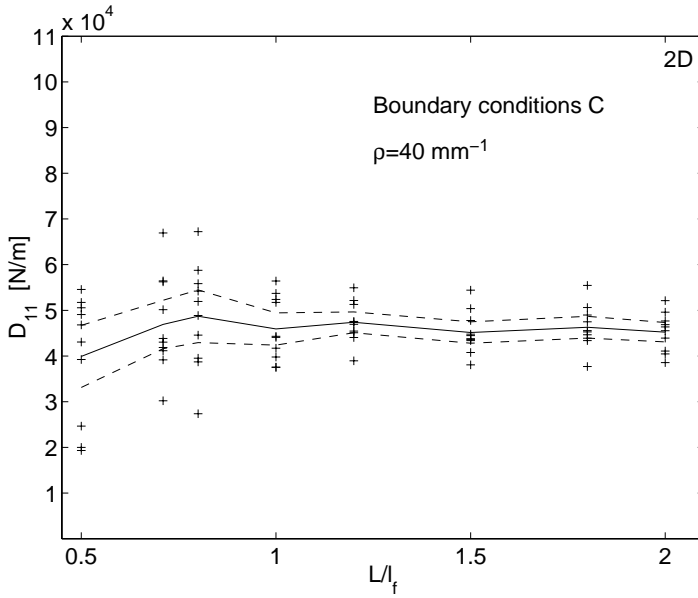
## 7. RESULTS FROM THE ANALYSIS OF INITIAL GLOBAL STIFFNESS PROPERTIES

This chapter presents results concerning the initial global stiffness of a network as a function of various micro-level parameters. The simulation and representation of the initial global stiffness properties were discussed in detail in the preceding chapter. If isotropy is assumed, the elastic modulus,  $E$ , and the Poisson ratio,  $\nu$ , represent the initial stiffness. These are obtained from the results of three or six simulations corresponding to the different modes of unit strain in 2D and 3D modelling respectively. In Section 7.1, however, stiffness is in some cases given in terms of a single component of  $\mathbf{D}$ . These results are based on simulations of only one mode of strain. In Section 7.1 the relative variation in the stiffness, rather than the absolute value, is the primary concern. Because of this, the simpler method of evaluating stiffness is considered to be sufficient.

### 7.1. Effect of boundary conditions and sample size

Since computer resources are limited, it is preferable to analyse as small a cell as possible. At some point, however, the results are affected if the cell is too small compared with the fibre length. To determine the smallest possible cell size, numerical simulations were carried out to examine the dependence of the calculated stiffness on the sample size and the modelling of boundary conditions. The networks that were simulated had material properties equal to those specified for the basic example networks, Section 5.1. In Figures 7.1-7.4 and 7.8, the relationship between components of  $\mathbf{D}$  and cell size to fibre length ratio  $L/l_f$  is plotted.

Figures 7.1 and 7.2 show the results from 2D simulations of networks for which  $\rho = 40 \text{ mm}^{-1}$ . For every value of  $L/l_f$  considered, ten different geometries were simulated, each geometry being subjected to the two sets of boundary conditions discussed in Section 6.2: S in Figure 7.1 and C in Figure 7.2. It can be seen from the figures that the scattering of the points is considerable for low values of  $L/l_f$ , and that the scattering gradually decreases as  $L/l_f$  increases. It is also noted that the scattering is greater for boundary conditions S. The solid line indicates the average of the ten simulations, while the dashed lines denote the standard deviation. For boundary conditions S the average stiffness initially increases and decreases, but from  $L/l_f = 1.2$  it decreases. Boundary conditions C, on the other hand, produce a

Figure 7.1:  $D_{11}$  plotted against  $L/l_f$ : Boundary conditions S.Figure 7.2:  $D_{11}$  plotted against  $L/l_f$ : Boundary conditions C.

rather constant stiffness from  $L/l_f \approx 1.0$ . This suggests that the stiffness is dependent on sample size for boundary conditions S at these values of  $L/l_f$  and  $\rho$ , but not when boundary conditions C are imposed.

Figure 7.3 shows the average value of  $D_{11}$  from ten calculations, as a function of  $L/l_f$  for three different densities,  $\rho = 30, 40$  and  $50 \text{ mm}^{-1}$ . The results of calculations using both boundary conditions are shown for each density. These results also indicate that when using boundary conditions S, one must analyse a much larger network in order to obtain a correct value of the stiffness than is the case for boundary conditions C. It is concluded that for boundary conditions C,  $L/l_f \geq 1$  is a minimum requirement for obtaining reliable stiffness values. For the conventional boundary conditions S, the corresponding minimum requirement can be estimated to be  $L/l_f > 3$ . This crude estimate is based on the results shown in Figure 7.3, which shows that S still gives much higher calculated stiffness than C at  $L/l_f = 2.0$  and  $2.5$ .

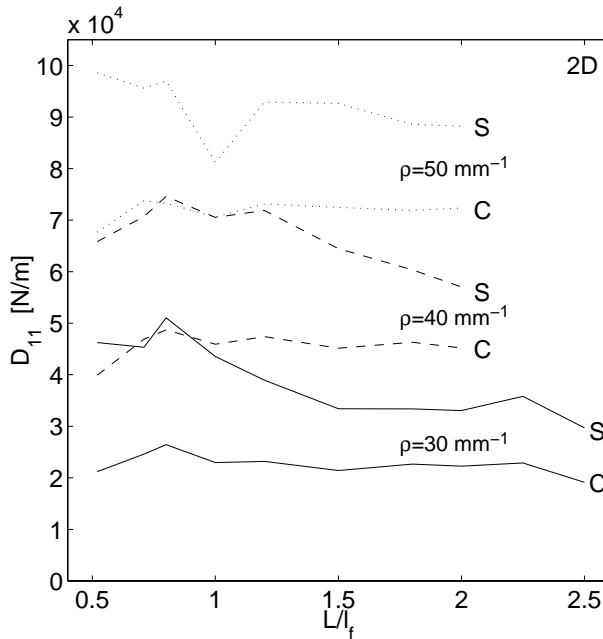


Figure 7.3:  $D_{11}$  plotted against  $L/l_f$ .

Figure 7.4 shows results from 3D simulations. Boundary conditions C were used and the components  $D_{11}$  to  $D_{66}$  are plotted against  $L/l_f$ . For each value of  $L/l_f$  ten different geometries were simulated and the points represent the average of these.  $D_{11}$ ,  $D_{22}$  and  $D_{33}$  are related to the stiffness in the  $x$ -,  $y$ - and  $z$ -directions, respectively. The network has approximately the same stiffness in the three different directions, which is expected as the orientation distribution of the fibres is uniform.

As for 2D simulations, there is a tendency for the stiffness to increase for small values of  $L/l_f$ . These results suggest that a slightly larger ratio of  $L/l_f$  must be used than in 2D to achieve size independence.  $D_{44}$ ,  $D_{55}$  and  $D_{66}$  are approximately equivalent to the three different shear moduli of the network. The variation in shear moduli for a given value of  $L/l_f$  is smaller than that of  $D_{11}$ - $D_{33}$ , and the size dependence is also less pronounced.

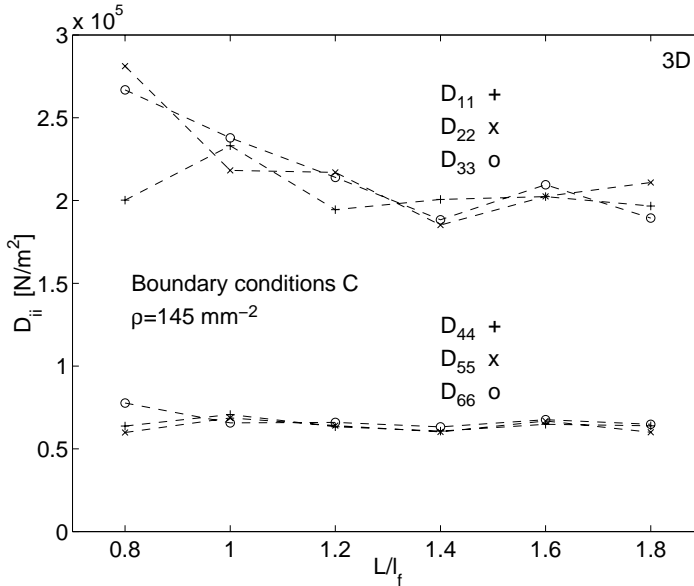
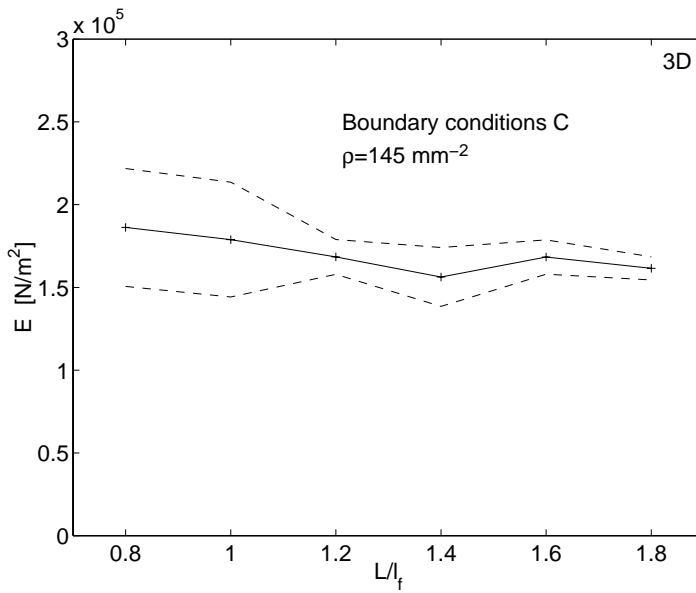
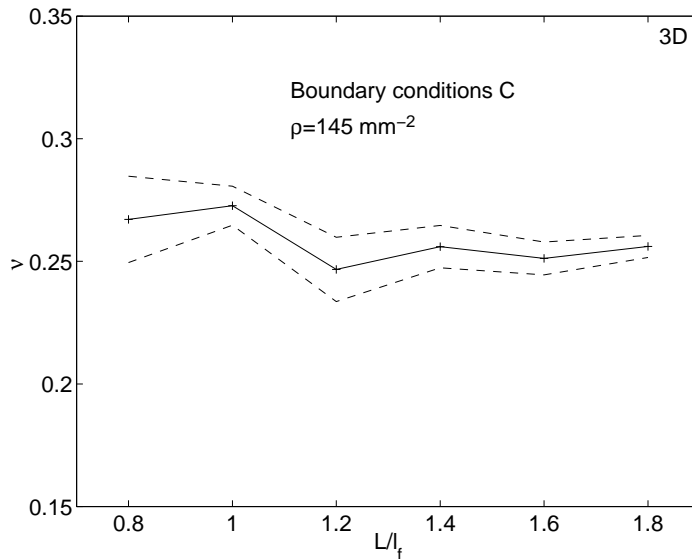


Figure 7.4: Diagonal components of  $\mathbf{D}$  plotted against  $L/l_f$ .

Figures 7.5 and 7.6 show the results corresponding to Figure 7.4, but now represented by the approximated isotropic elastic parameters  $E$  and  $\nu$ . The solid line represents the average value and the dotted lines the standard deviation. As in the 2D case, there is a greater scattering of the results for the smallest values of  $L/l_f$ , and a constant value of  $E$  is reached at approximately  $L/l_f=1.2$ .  $\nu$  is quite constant, around 0.25, except for the smallest values of  $L/l_f$ , where it is somewhat higher.

Since boundary conditions C allow smaller cells, it is concluded that the use of these conditions is by far the more economic alternative. The gain is not quite as large, however, as one might at first expect. This is because conditions C involve the use of constraints, which makes the solution of the system of equations more time-consuming and requires more memory. The next issue is to determine what value of  $L/l_f$  is optimal. The standard deviation decreases moderately with increasing  $L/l_f$ , which means that the number of simulations can be decreased for larger values of  $L/l_f$ . Since the computational time increases dramatically, however, as  $L/l_f$  increases, from a computational point of view it is best to select a minimal value of

Figure 7.5:  $E$  plotted against  $L/l_f$ .Figure 7.6: Poisson's ratio,  $\nu$ , plotted against  $L/l_f$ .

$L/l_f$ . Unless otherwise stated, boundary conditions C and  $L/l_f = 1.2$  are used in all the initial stiffness simulations discussed in the following. In the networks simulated in this section all fibres are assumed to be of the same length. For the case of a statistical distribution of fibre length, the requirement  $L/l_f \geq 1.2$  may have to be modified depending on the distribution.

In the above, it has been implicitly assumed that the stiffness of a network is size independent, and that size dependencies in the results are caused by boundary effects in the simulations. This assumption may, however, not be correct for all networks. There may be a real size dependence of the stiffness due to the effects of scattering in stiffness values in different areas of a heterogeneous material. The influence of increased cell size on stiffness lies somewhere between the influences of the extreme cases of coupling more and more material cells in series or in parallel. In parallel coupling, the total stiffness is not affected by scattering in the values of the components, while a structure coupled in series is weakened by scattering. This effect is illustrated by a simple example of springs coupled in series and parallel in Figure 7.7. The average spring stiffness is the same in all four cases. As a growing cell could be viewed as a combination of serial and parallel coupling, the weakening effect of scattering on global stiffness may be of significance if the scattering is large enough. As the scattering in stiffness results increases for decreasing network density, this would be important in particular for low network densities. Figure 7.8 shows results from 2D simulations of  $\rho = 15$  and  $20 \text{ mm}^{-1}$ , with boundary conditions C. The solid lines denote the averages of ten calculations, while the dotted lines denote the standard deviation. There is a weak tendency towards increasing slope of the curves as  $\rho$  decreases, but the large standard deviation makes definite conclusions difficult. This issue is further discussed in Section 9.1.1.

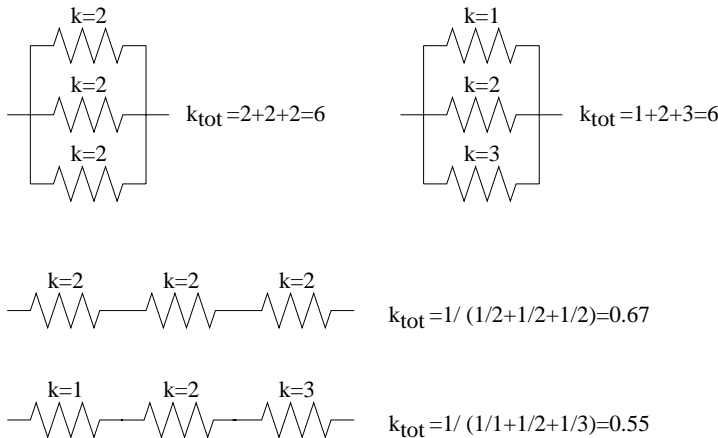
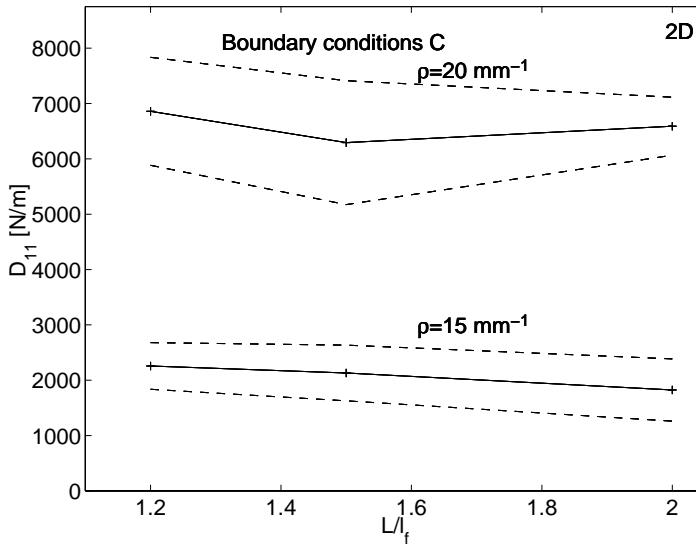


Figure 7.7: Example showing the effect of scattering in stiffness properties for spring couplings.

Figure 7.8:  $D_{11}$  plotted against  $L/l_f$ .

## 7.2. Global elastic stiffness vs stiffness of components

The global elastic stiffness of a network depends on the relative stiffness properties of the components. Depending on the relation between fibre stiffness and bond stiffness, different modes of deformation may dominate the network. The relations between axial and bending stiffness of the fibres and normal and shear stiffness of the bonds cause the same kind of effects. To examine the effect of the stiffness of the components on the global elastic stiffness, simulations were performed using the basic example networks. Several stiffness parameters were varied over a wide range. The parameters considered for 2D networks were stiffness of bonds,  $k_x = k_y$  and  $k_\phi$ , and moment of inertia,  $I_f$ , cross-sectional area,  $A_f$ , and elastic modulus,  $E_f$ , of fibres, and for 3D networks elastic modulus,  $E_f$ , and shear modulus,  $G_f$ , of fibres and normal and shear stiffnesses,  $k_n$  and  $k_t$ , of bonds.

Each point in the diagrams of Figures 7.9-7.12 shows the average of three simulations. For 2D simulations, the coefficient of variation for  $E$  was  $< 1\%$ , except for the  $I_f$ -curve in Figure 7.10 where it was 1-5%. For  $\nu$  the coefficient of variation was 1-5% except for a few values in the lower ranges of  $I_f$ , Figure 7.10, where it rose to at most 11%. For 3D simulations the coefficient of variation was 15-20% for  $E$  and 1-5% for  $\nu$ . The higher standard deviation for 3D simulations was caused by a less dense 3D example network.

In Figure 7.9 the influence of the stiffness of the bonds in a 2D network is shown. The variable on the  $x$ -axis is  $\log(k_x/k_x^0)$ , where  $k_x^0$  denotes  $k_x$  for the basic example network. Analogous notation is used in Figures 7.10 to 7.12. Since it was found

that the rotational stiffness has very little influence on  $E$ , two curves showing the variation of  $k_x$  and  $k_y$  are plotted, one with an extremely high and one with an extremely low value of  $k_\phi$ . When  $k_x = k_y$  approaches zero, the global stiffness obviously also approaches zero. When the value of  $k_x = k_y$  increases, a plateau is reached where the bonds are rigid compared with the fibres. One can compare this plateau value with the value predicted by Cox' homogeneous field approximation, (2.9).

For the basic example network, (2.9) gives  $E = 17.5 \cdot 10^4$  N/m and the plateau value obtained from the simulations is  $E = 13.2 \cdot 10^4$  N/m. Accordingly, the homogeneous field assumption predicts a significantly stiffer network, even when assuming the bonds to be rigid. This is probably due to bending of the fibres, as discussed in Section 2.1.

Poisson's ratio, in contrast to the elastic modulus, is affected by  $k_\phi$ , as can be seen in Figure 7.9. For a weak  $\phi$  spring  $\nu$  is approximately constant, whereas it is strongly dependent on  $k_x$  and  $k_y$  in the case of stiffer  $\phi$  springs. For the stiffer  $x$  and  $y$  springs  $\nu$  is close to the value of  $1/3$  predicted by (2.9) for a 2D network experiencing homogeneous strain.

$E$  and  $\nu$  for a 2D network as a function of  $\log(I_f/I_f^0)$ ,  $\log(A_f/A_f^0)$  and  $\log(E_f/E_f^0)$  are shown in Figure 7.10. It can be seen that  $A_f$  is the most important variable and that  $I_f$  has less influence on  $E$ , when varying the parameters around the values of the basic example network. Changing the ratio  $A_f/I_f$  means primarily distorting the cross section, and this is not very realistic over the wide ranges considered here. In Figure 7.10 it can also be seen that  $\nu$  shows moderate variations, except for very small values of  $A_f$ . Here,  $\nu$  suddenly decreases, and even attains negative values. For small values of  $A_f$  the fibre elongation deformation mode is much weaker than the other deformation modes. This means that the length of the fibres changes, but no angles change, through bending of the fibres, or through deformation in the bonds. When this is the case, the deformation resulting from uniaxial tension is close to a simple rescaling of the network, which then becomes wider as well as longer, corresponding to a negative value of  $\nu$ . Negative values of  $\nu$  have also been found experimentally in paper, see [47], which is a dense cellulose fibre network.

Figure 7.11 shows  $E$  and  $\nu$  for a 3D network as a function of bond stiffness. The three curves represent variation of  $k_n$ ,  $k_t$  and  $k_n$  and  $k_t$  together. The results show that  $k_t$ , which represents a deformation mode of fibres sliding relative to each other, has a stronger influence on network stiffness than  $k_n$ , which represents fibre separation. Network stiffness does not tend as strongly to zero when  $k_n$  is decreased, as when the resistance to the sliding mode is weakened. When  $k_n$  and  $k_t$  are varied together a plateau is reached where the bonds are rigid compared with the fibres, as for 2D networks. Cox' homogeneous strain prediction for 3D networks is given in (2.13). This gives a value of  $E$  as high as  $E = 210 \cdot 10^6$  N/m<sup>2</sup> for the basic example network compared with  $E = 5.1 \cdot 10^5$  N/m<sup>2</sup> which is the plateau value obtained from the diagram. That is, the 3D basic example network is 400 times weaker than a homogeneous strain network would be. This is because fibre curl and bending and torsion of fibres has a considerable influence on the network at this low density.

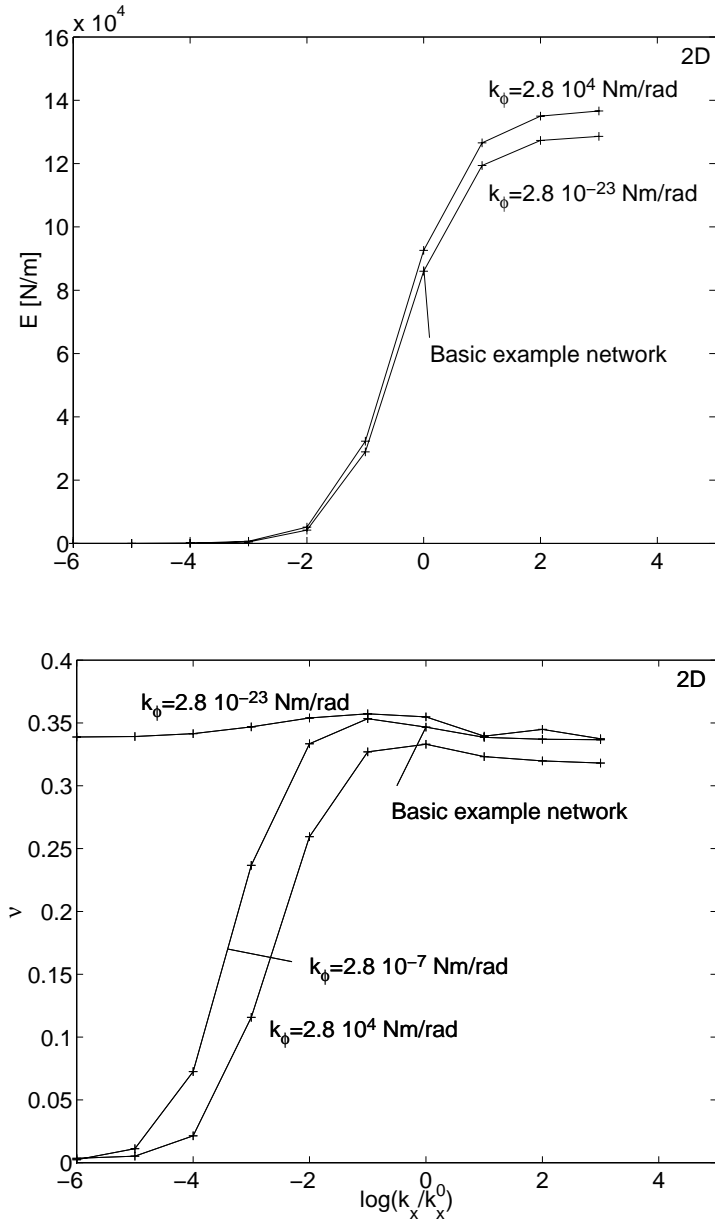


Figure 7.9:  $E$  and  $\nu$  plotted against  $\log(k_x/k_x^0)$ .

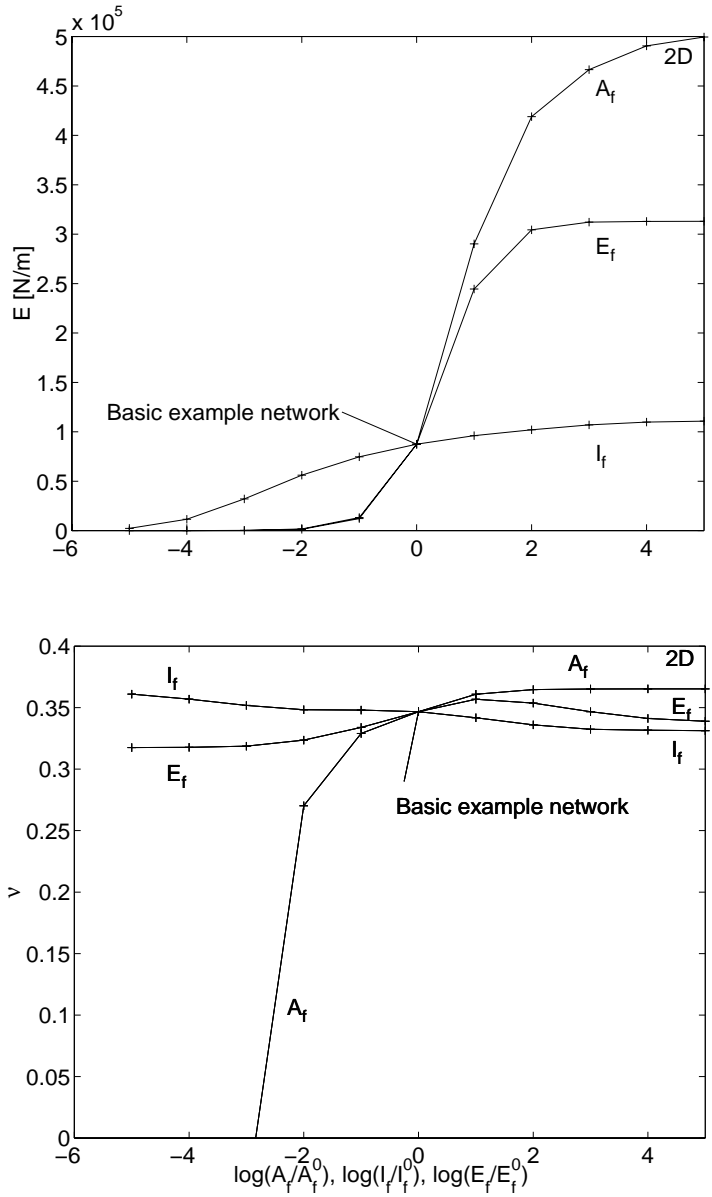


Figure 7.10:  $E$  and  $\nu$  plotted against  $\log(A_f/A_f^0)$ ,  $\log(I_f/I_f^0)$  and  $\log(E_f/E_f^0)$ .

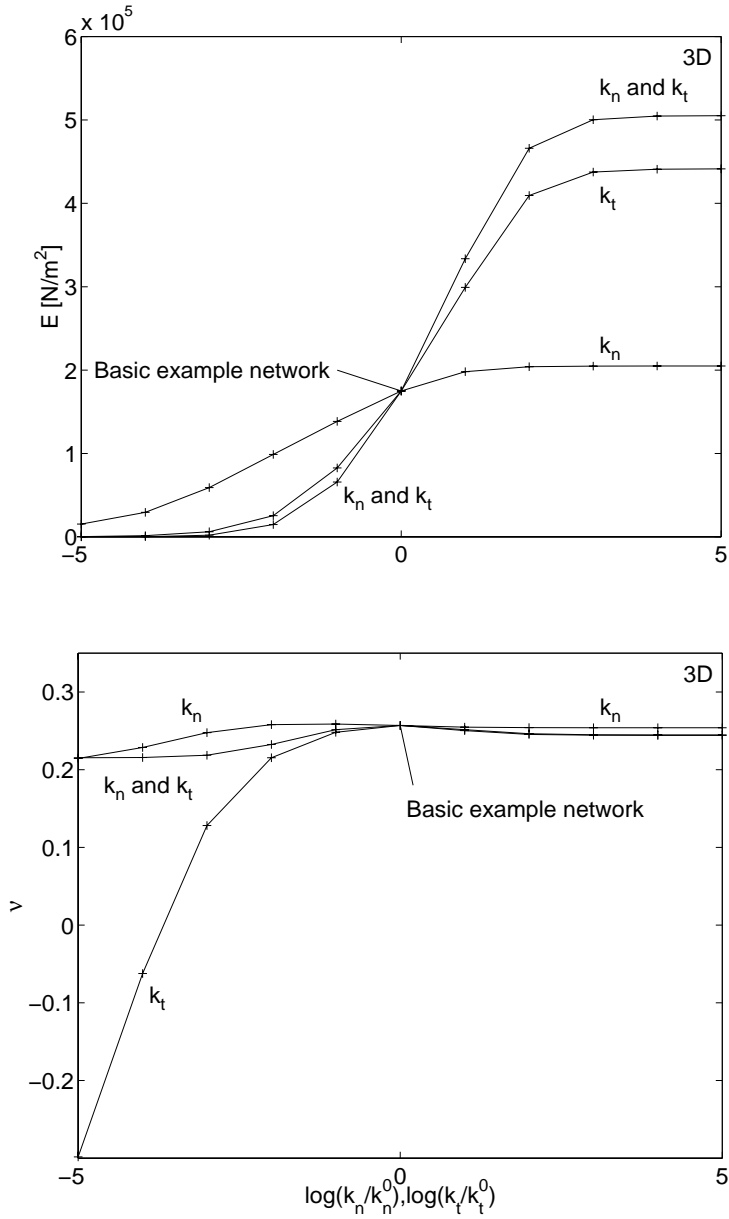


Figure 7.11:  $E$  and  $\nu$  plotted against  $\log(k_n/k_n^0)$  and  $\log(k_t/k_t^0)$ .

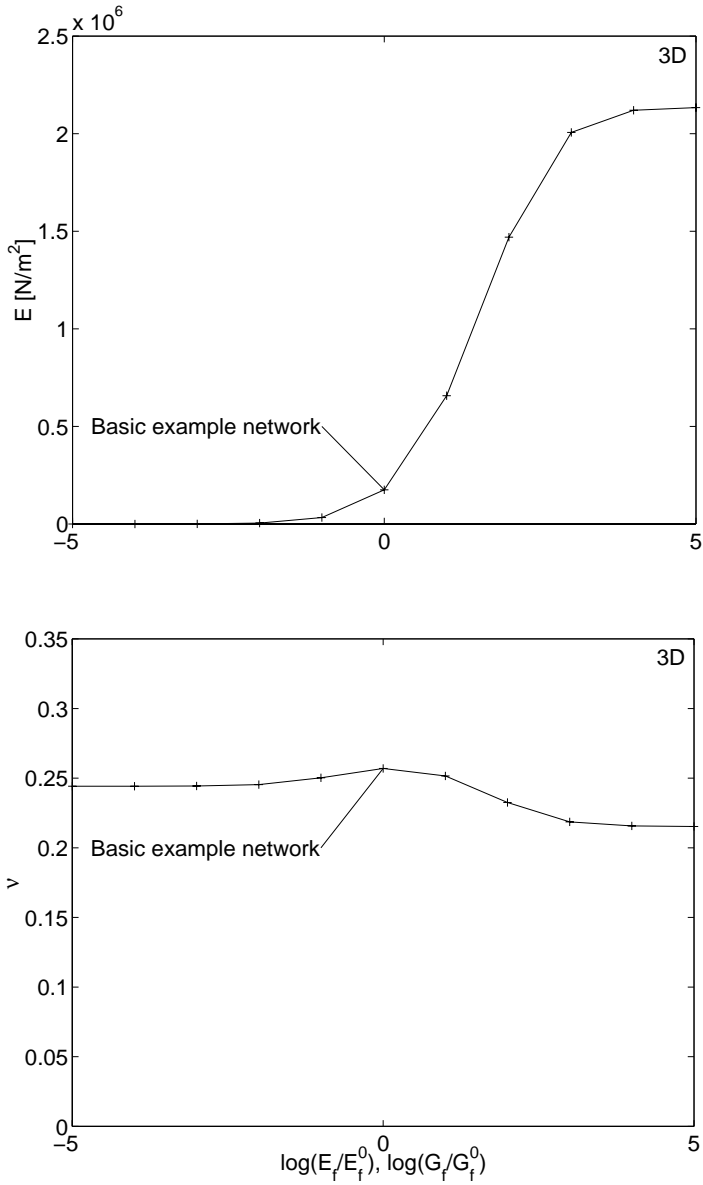


Figure 7.12:  $E$  and  $\nu$  plotted against  $\log(E_f/E_f^0)$  and  $\log(G_f/G_f^0)$ .

Poisson's ratio,  $\nu$ , on the other hand, is not significantly affected by the deviation from homogeneous strain. The value of  $\nu$  is quite close to 0.25, irrespective of the values of  $k_n$  and  $k_t$ , except for extremely low values of  $k_t$  where  $\nu$  decreases and even attains negative values.

Figure 7.12 shows  $E$  and  $\nu$  for a 3D network as a function of fibre stiffness. Both  $E_f$  and  $G_f$  were varied by the same amount. As expected,  $E$  approaches zero as fibre stiffness vanishes and reaches a plateau when the fibres become rigid compared with the bonds. The value of  $\nu$  is quite stable around 0.22-0.25.

### 7.3. Global elastic stiffness vs network density and degree of fibre-to-fibre interaction

The network density was found to have a strong influence on the elastic stiffness of the network structure. Simulations were performed for six different densities for 2D and 3D networks.

In Figures 7.13 and 7.14  $E$  and  $\nu$  for a 2D network are plotted against network density  $\rho$ . The five curves represent different probabilities of interaction at a fibre crossing,  $s=1.0$ ,  $s=0.8$ ,  $s=0.6$ ,  $s=0.4$  and  $s=0.2$ . For densities of  $\rho=30-60 \text{ mm}^{-1}$  ten simulations were performed for each value of  $\rho$ , but for  $\rho=70$  and  $80 \text{ mm}^{-1}$  it was deemed sufficient to perform seven and three simulations, respectively, due to the small standard deviation at the higher values of  $\rho$ . Vertical lines indicate the standard deviation in  $E$  in Figure 7.13. The lower densities are omitted for  $s=0.4$  and  $s=0.2$ , since the results showed too much scattering to be relevant. The value of Poisson's ratio,  $\nu$ , is rather stable at around 0.34; it is only due to the scale of the diagram that one can detect any differences, irrespective of changes in  $\rho$  and  $s$ , except for  $s = 0.2$ , which yields a somewhat higher value of  $\nu$ . The standard deviation is not plotted since the curves are often so close that the error bars would interfere.

Figures 7.15 and 7.16 show  $E$  and  $\nu$  as a function of network density for 3D networks. The same five values of probability of interaction at a fibre crossing were simulated, but for  $s = 0.2$   $E$  was too small to plot in Figure 7.15. Ten simulations were performed for each value of  $\rho$  and  $s$ , and the vertical lines denote standard deviation in Figure 7.15.  $E$  as a function of  $\rho$  is more linear in the 2D case than in the 3D case, where the dependence of  $E$  becomes greater than linear for the lower density values. One reason for this difference between 2D and 3D networks is probably that the simulated 3D networks are closer to the percolation threshold. Poisson's ratio increases slightly, from just below 0.25 to just over 0.25. For the lower values of  $s$  and  $\rho$ ,  $\nu$  is not plotted due to the networks being unconnected or the spread in the results being too great. As in the 2D results, the curve for  $s = 0.2$  differs from the other curves.

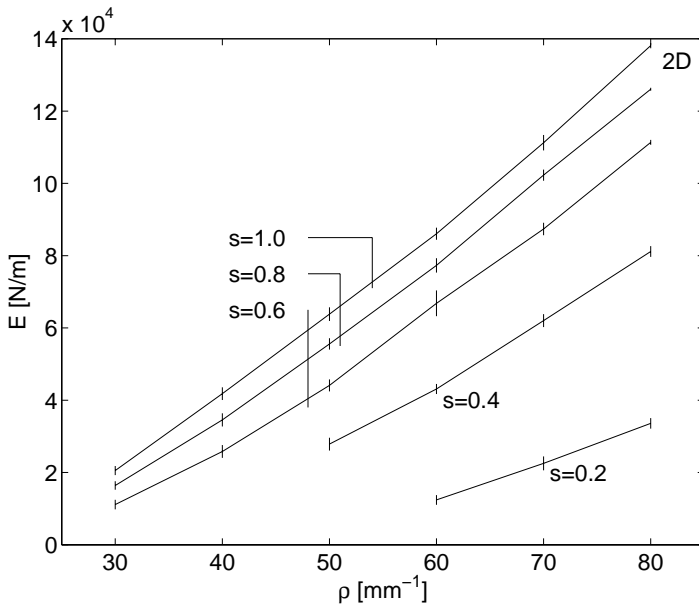


Figure 7.13:  $E$  plotted against  $\rho$  and  $s$ .

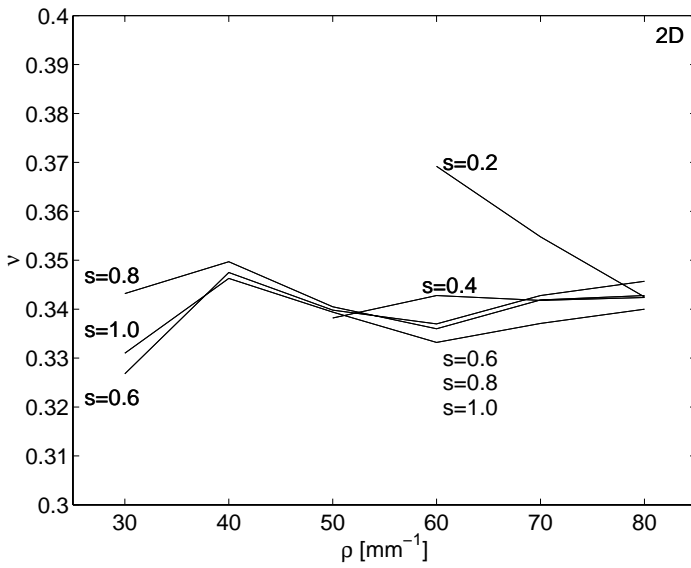
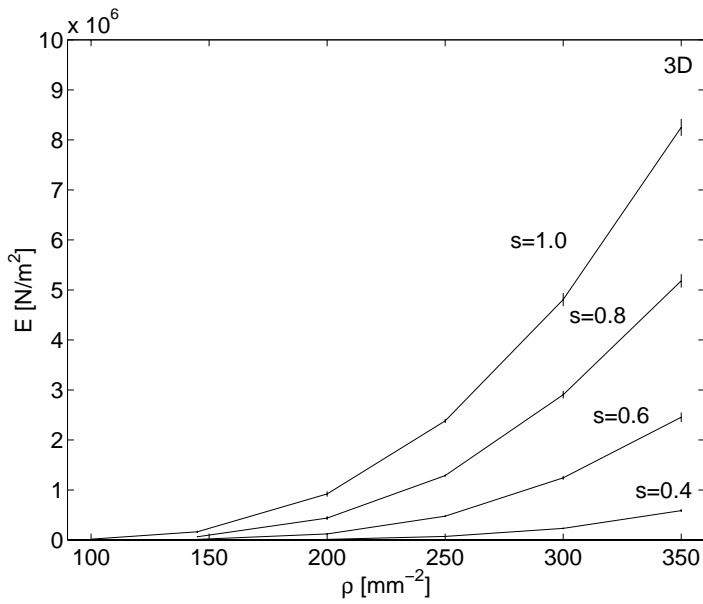
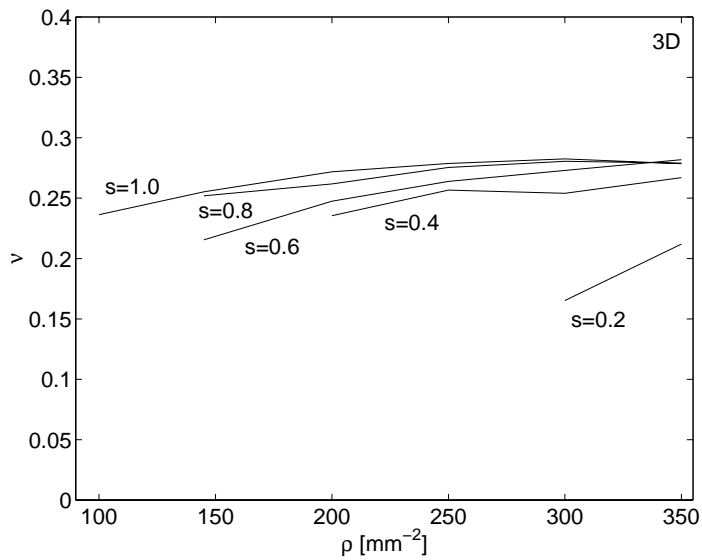


Figure 7.14:  $\nu$  plotted against  $\rho$  and  $s$ .

Figure 7.15:  $E$  plotted against  $\rho$  and  $s$ .Figure 7.16:  $\nu$  plotted against  $\rho$  and  $s$ .

### 7.4. Global elastic stiffness vs fibre curl

Fibre curl is found to have a strong influence on the global elastic stiffness of a network. This is because curled fibres have lower values of axial stiffness, and also because the geometry of the network becomes different. The load-bearing lines no longer extend as straight lines, but take a curved path.

Simulations have been carried out in 2 and 3 dimensions to evaluate the dependence of  $E$  and  $\nu$  on the degree of curl of the fibres. The curl indices considered were 0.7, which is close to a semi-circle, 0.8, 0.9 and 1.0, which corresponds to a straight fibre.

2D simulations were performed for two different network densities and the results are shown in Figures 7.17 and 7.19. Each point is the average of two or three simulations; standard deviations are indicated by vertical lines. It can be seen that  $E$  increases with increasing curl index for both  $\rho=40 \text{ mm}^{-1}$  and  $\rho=60 \text{ mm}^{-1}$ , but  $c$  has a greater influence on the less dense network. Here, the ratio between  $E$  for straight fibres and  $E$  for  $c=0.7$  is equal to 3.6, while the same ratio for  $\rho=60 \text{ mm}^{-1}$  is only 1.9. Poisson's ratio does not differ much between the two densities, but shows a clear tendency to increase as the fibres become more curled, as can be seen in Figure 7.19. Poisson's ratio does even increase above 0.5, a fact that is discussed in Section 6.5.

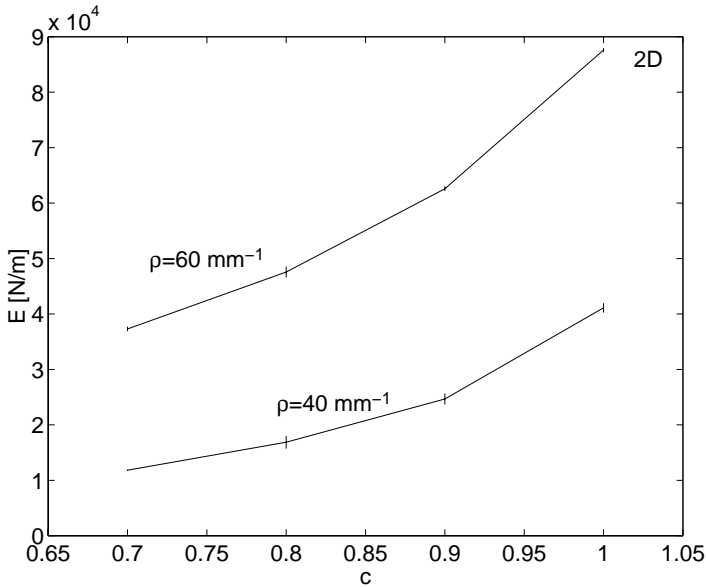


Figure 7.17:  $E$  plotted against the curl index,  $c$ .

3D simulations were performed for three different network densities and the results are shown in Figures 7.18 and 7.19. Each point is the average of ten simu-

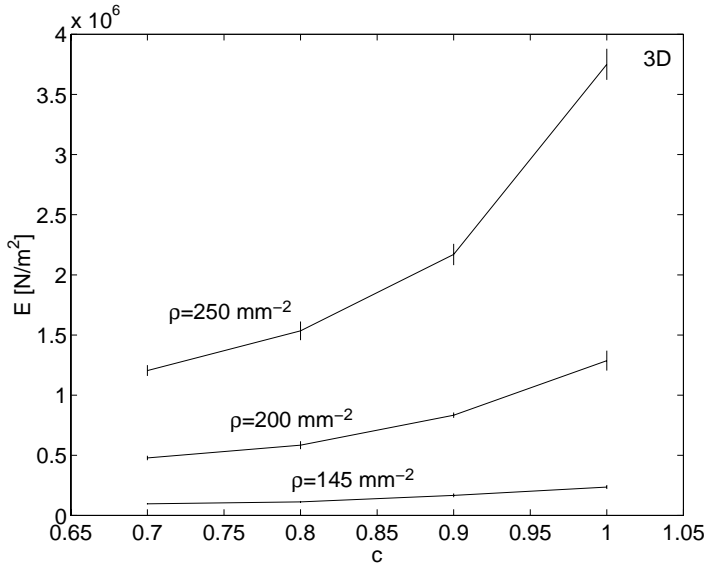


Figure 7.18:  $E$  plotted against the curl index,  $c$ .

lations, and the standard deviations are indicated by vertical lines. As for the 2D case,  $E$  increases as the fibres become straighter. The ratios between  $E$  for  $c = 1$  and  $c = 0.7$  are 2.4, 2.7 and 3.1 for the three densities 145, 200 and  $250 \text{ mm}^{-2}$ , respectively. That is, in contrast to the 2D network, the influence of fibre curl is greater for higher densities. Fibre curl does not have much influence on  $\nu$ , but there is a weak tendency for  $\nu$  to decrease as the fibres become straighter.

The effect of fibre curl can be imagined as consisting of two interactive effects. One is that the whole fibre does not extend straight across the network, but describes a curved path. The other is that the fibre segment between two neighbouring bonds is curved, and is thus weaker in the axial direction. The two different effects will be of differing importance depending on the average free fibre segment length. The free fibre segment lengths have different sizes for 2D and 3D networks, (5-8 bonds/fibre for 3D and 27-37 for 2D), and this could provide the explanation of the contradictory results concerning the effect of curl for different densities. The effect of axial stiffness is large when the free fibre segments are long, and should vanish as the free fibre segment length approaches zero. The curved path effect is probably small in the somewhat undefined limiting case of the longest possible fibre segments since then only one or few fibre segments extend from one border of the network to the other. The observation that the curved path effect increases for medium segment lengths and decreases or vanishes again as the free fibre segment length approaches zero would be consistent with the simulation results obtained.

The relative importance of the two effects has been investigated for the 2D case.

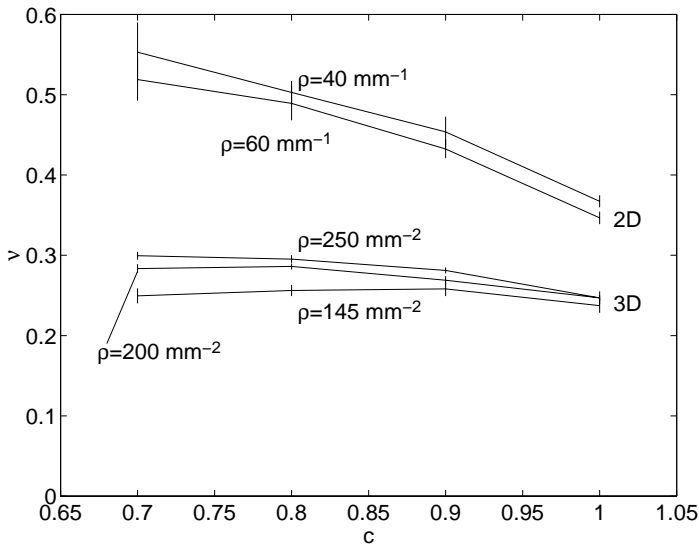


Figure 7.19:  $\nu$  plotted against the curl index,  $c$ .

In addition to the simulations with curled fibres, simulations have been performed in which the beam elements were replaced by straight ones in the curled global geometry. A network of straight fibres was also generated, with the same nominal properties as the network of curled fibres, but the beam elements were replaced by curved ones, with the curl indices that were considered above. A sketch of the networks and notations used is presented in Figure 7.20. Figure 7.21 shows  $E$  as a function of the curl index for the different types of networks.  $E$  for a network of curled fibres, Figure 7.17, is illustrated by solid lines. The dotted lines marked CS and SC represent networks according to Figure 7.20, and the dash-dotted lines indicate the value of  $E$  for a network of straight fibres. It is concluded that the effect of fibres not extending straight across the network is more important than that of the axial stiffness being lower for this case. Moreover, in the cases shown in the figure the two effects seem to be additive.

Figure 7.22 shows the corresponding curves for  $\nu$ . It can be seen that a network of type SC gives a value of  $\nu$  that is practically identical to that of a network of straight fibres. Somewhat surprisingly, a network of type CS exhibits even higher values of  $\nu$  than the network consisting of curled fibres. Obviously,  $\nu$  is not very dependent on the axial stiffness of the fibres, which is also consistent with the results shown in Figure 7.10, in the range close to the basic example network. A geometry made up of curled fibres, on the other hand, has a rather strong increasing effect on  $\nu$ .

An approximate method of accounting for curled fibres might be to reduce the axial stiffness of the beam elements. The results presented here indicate, however

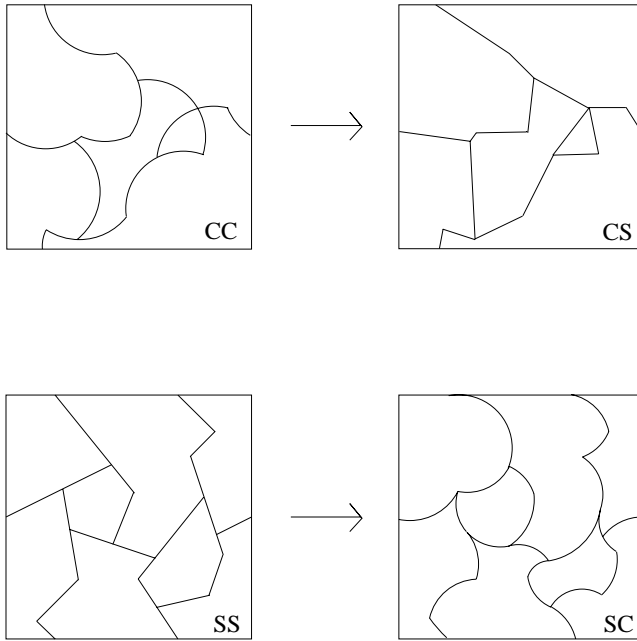


Figure 7.20: Different combinations of straight and curled fibres.

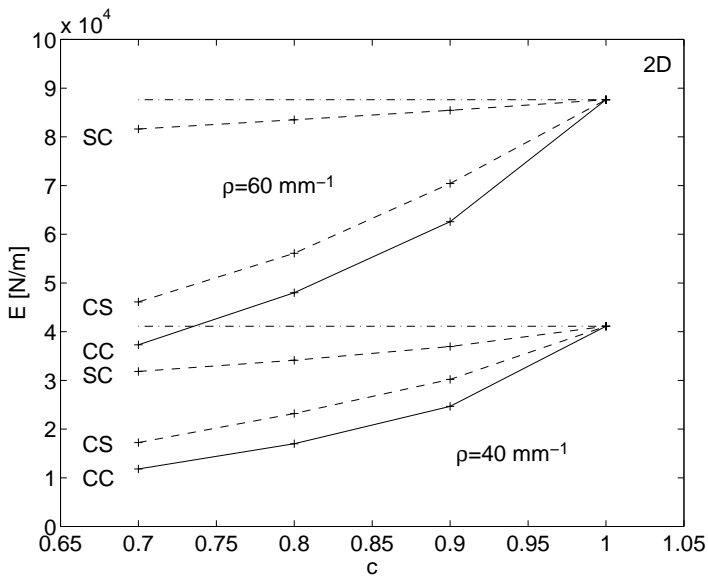


Figure 7.21:  $E$  plotted against the curl index,  $c$ .

that, at least for high network densities, this approach would not give satisfactory results.

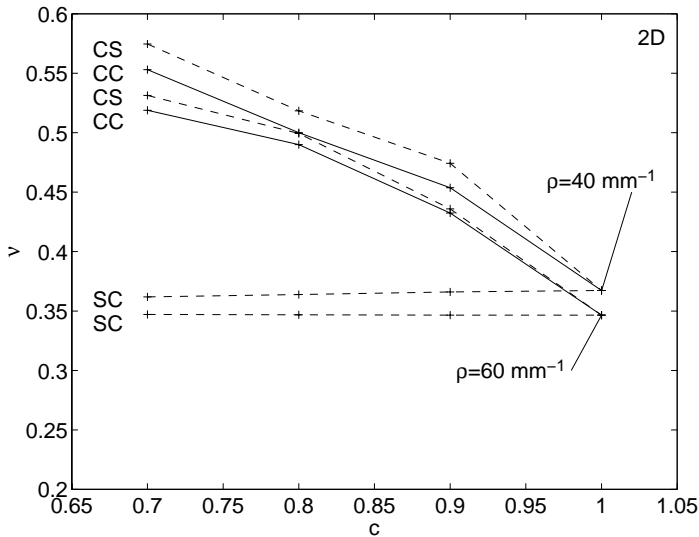


Figure 7.22:  $\nu$  plotted against the curl index,  $c$ .

## 7.5. Global elastic stiffness vs orientation distribution

In the preceding sections results have been presented in terms of the elastic modulus and the Poisson ratio for the isotropic continuous material which most closely resembles the simulated network material in mechanical behaviour. This was done as when the fibres have a nominally uniform orientation distribution, the network is expected to be close to isotropic, at least at sufficiently high network densities. Now we shall investigate the influence on the elastic stiffness of a non-uniform orientation distribution of the fibres. Two different kinds of non-uniform orientation distributions were investigated; 2D networks where there is a preference for one fibre direction in the plane, and 3D networks where the fibres tend to lie in one plane.

For a 2D network with a non-uniform orientation distribution there is no longer any reason to believe that the network's performance will be the same in each direction. If, however, the orientation distribution is symmetric with respect to two perpendicular directions, we can expect nearly orthotropic behaviour. Some 2D networks with orientation distributions satisfying this condition are examined, and the results are given as orthotropic material parameters, according to the principles presented in Section 6.7.

One way of defining an orientation distribution is [64],

$$f(\alpha) = \frac{1}{\pi} - a \cos 2\alpha . \quad (7.1)$$

This distribution function satisfies the criterion

$$\int_0^\pi f(\alpha) d\alpha = 1 , \quad (7.2)$$

for all values of the constant  $a$ , but to avoid negative probabilities should only be used for  $-1/\pi \leq a \leq 1/\pi$ . Simulations have been performed for the cases of  $a = 0$ ,  $1/(2\pi)$  and  $1/\pi$ , giving the distribution functions shown in Figure 7.23. The curves in the figure have been approximated by ten straight line segments, and this is also the input to the program which generates the network. For comparison, Figure 7.24 shows an example of the fibre orientation distribution of a commercial kraft paper [64]. The network with  $a = 0$  is the 2D basic example network, and for the other values of  $a$  all properties except the orientation distribution are the same as for the 2D basic example network. Figure 7.25 shows examples of network geometries for the three different values of  $a$ . For each value of  $a$ , 10 simulations were performed of nominally identical networks.

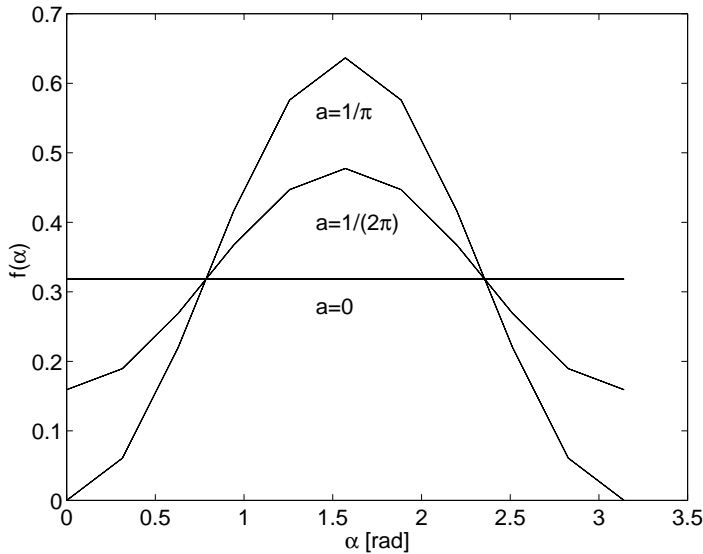


Figure 7.23: *Fibre orientation distributions for different values of  $a$ .*

The simulations for  $a = 0$  are the same as those performed for the basic example network, but they have been evaluated as for an orthotropic material. Ideally,  $E_x$  and  $E_y$ , as well as  $\nu_{yx}$  and  $\nu_{xy}$ , should be identical. That they are not, implies that the networks which have nominally uniform orientation distribution are not

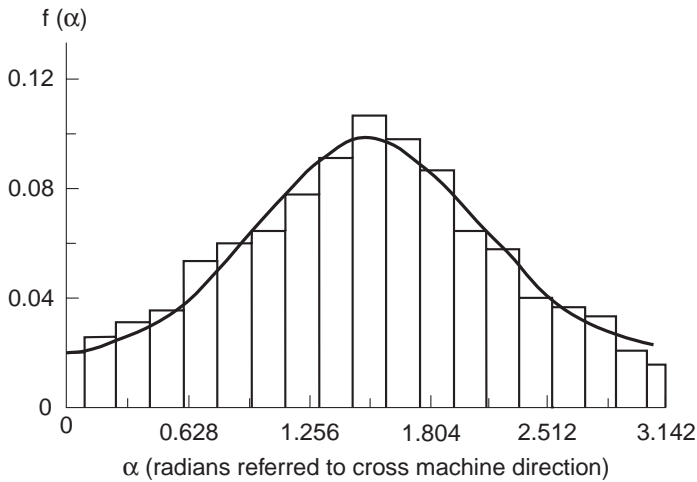


Figure 7.24: *Fibre orientation distribution of commercial kraft paper*, [64].

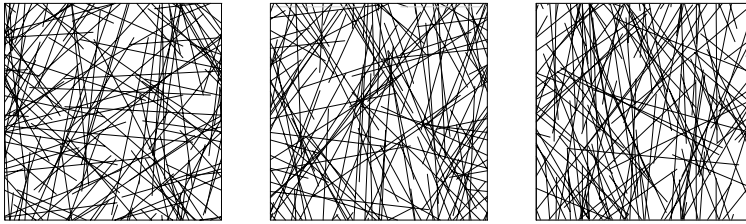


Figure 7.25: *Examples of network geometries for the cases  $a=0$ ,  $a = 1/(2\pi)$  and  $a = 1/\pi$ .*

exactly isotropic, but they are still quite close. As  $a$  increases there is a stronger tendency for the fibres to be oriented vertically, as can be seen from Figures 7.23 and 7.25. This results in an increasing modulus  $E_y$  and decreasing  $E_x$ , as can be seen in Figure 7.26, where the mean values and standard deviation of  $E_x$ ,  $E_y$  and  $G_{xy}$  are indicated. The shear modulus,  $G_{xy}$ , decreases only slightly as  $a$  increases. In Figure 7.27 Poisson's ratios,  $\nu_{yx}$  and  $\nu_{xy}$ , are shown against  $a$ . At  $a=0$  they are almost the same, but as  $a$  increases,  $\nu_{yx}$  increases considerably while  $\nu_{xy}$  decreases moderately. A comparison can be made with (2.7), which predicts the coefficients of  $\mathbf{D}$  for the case of uniform strain and an orientation distribution of the form of (2.3). Disregarding the absolute values, (2.7) predicts  $D_{12}$  and  $D_{33}$  to be constant and  $D_{11}$  and  $D_{22}$  to vary linearly. This agrees quite well for  $D_{33}$  which is equal to  $G_{xy}$ . That it agrees equally well for the other components of  $\mathbf{D}$  can be seen by the

use of (6.91).

Finally, Figure 7.28 shows a typical example of the difference between  $\mathbf{D}$  from a simulation, denoted  $\mathbf{D}^s$ , and the corresponding estimated value of orthotropic  $\mathbf{D}$ , denoted  $\mathbf{D}^e$ , as a function of  $\theta$ . The figure is based on a simulation where  $a = 1/(2\pi)$  and  $\mathbf{D}^s$  is

$$\mathbf{D}^s = \begin{bmatrix} 0.6130 & 0.3340 & 0.0273 \\ 0.3340 & 1.3236 & 0.0328 \\ 0.0273 & 0.0328 & 0.3146 \end{bmatrix} \cdot 10^5 ,$$

and the estimated value of orthotropic  $\mathbf{D}^e$  is, from Section 6.7,

$$\mathbf{D}^e = \begin{bmatrix} 0.6130 & 0.3340 & 0 \\ 0.3340 & 1.3236 & 0 \\ 0 & 0 & 0.3146 \end{bmatrix} \cdot 10^5 .$$

The difference between the solid lines, which represent  $\mathbf{D}^s$ , and the dotted lines, which are  $\mathbf{D}^e$ , is rather small. This indicates that the assumption discussed in Section 6.7, i.e. assuming the principal directions of the simulated material to be coincident with the symmetry axes of the orientation distribution, is acceptable.

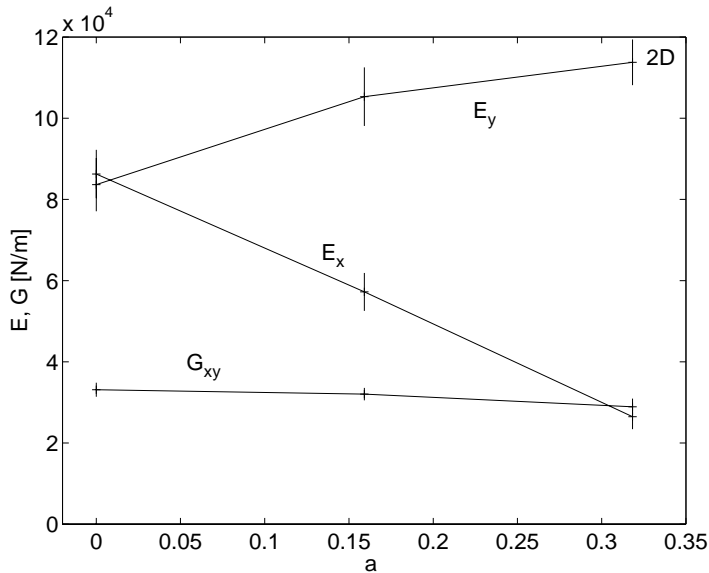


Figure 7.26: *Elastic moduli plotted against orientation distribution parameter,  $a$ .*

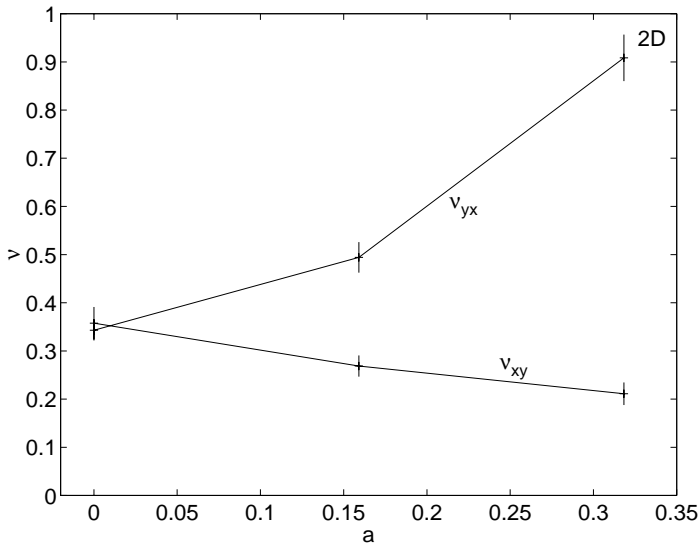


Figure 7.27: Poisson's ratios plotted against orientation distribution parameter,  $a$ .

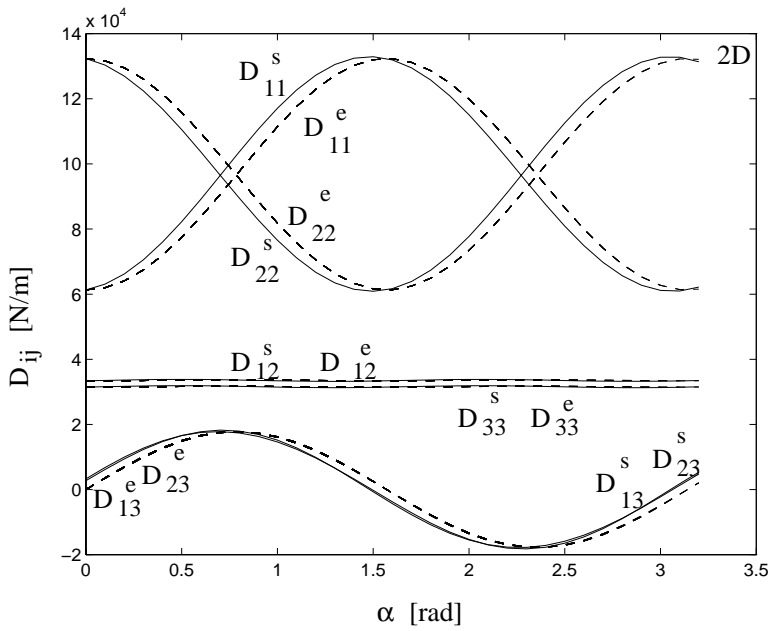


Figure 7.28: Components  $D_{ij}$  plotted against  $\alpha$ .

Simulations were also performed on 3D networks with a non-uniform orientation distribution. A series of simulations was performed on cells ranging from a cube, where  $L_x=L_y=L_z$ , to a cell that is compacted in the  $z$ -direction and thus approaching a 2D network. Figure 7.29 shows the five network cells investigated. The number of fibres was 173 in all the cells. This corresponds to a network density of  $100 \text{ mm}^{-2}$  for the case of  $L_z/L_x = 1.0$ , and a density of  $500 \text{ mm}^{-2}$  when  $L_z/L_x = 0.2$ . The simulations can be viewed as an illustration of how the network properties change when a fixed number of fibres form a network which ranges from a full 3D network to close to a 2D network. The orientation distribution in the  $xy$ -plane, which is quantified by the angle  $\alpha$ , is uniform. The out-of-plane angle  $\beta$  is distributed as

$$f(\beta) = \frac{L_x}{L_z} \cos \beta \quad 0 \leq \beta \leq \arcsin \frac{L_z}{L_x} . \quad (7.3)$$

Except for cell size, the distribution of  $\beta$  and the network density, all other parameters are as in the 3D basic example network.

The material properties were evaluated as for a transversely isotropic material, see Section 6.7. The parameters given in the figures are in-plane and out-of-plane elastic modulus and Poisson's ratio, showing the average of ten simulations. Figure 7.30 shows in-plane and out-of-plane elastic modulus multiplied by  $L_z$  as a function of  $L_z/L_x$ . As the network is compacted the fibres become more oriented in the  $xy$ -plane giving an increased stiffness in this plane. The number of inter-fibre bonds also increases, making the fibre segments shorter and thus decreasing the influence of bending and torsion. These two effects result in an extremely high increase in in-plane stiffness. The out-of-plane stiffness also shows an increase as the ratio  $L_z/L_x$  decreases. This implies that the effect of shorter fibre segments is more important than that of fewer fibres being oriented in the  $z$ -direction. The ratio  $E_{in-plane}$  to  $E_{out-of-plane}$  is 0.8 at  $L_z/L_x = 1.0$  and 44 at  $L_z/L_x = 0.2$ . At  $L_z/L_x = 1.0$  the ratio should ideally be equal to 1.0; this was not so, due to the considerable spread in the results at this low density. The coefficients of variation from the simulations range from approximately 0.35 for  $L_z/L_x = 1.0$  down to 0.10 for  $L_z/L_x = 0.2$ . Figure 7.31 shows in-plane and out-of-plane Poisson ratio as a function of  $L_z/L_x$ . Here the coefficients of variation range from approximately 0.45 down to 0.1.  $\nu_{in-plane}$  can be interpreted as the strain in the  $y$ -direction relative to that in the  $x$ -direction when the network is stressed in the  $x$ -direction. Correspondingly,

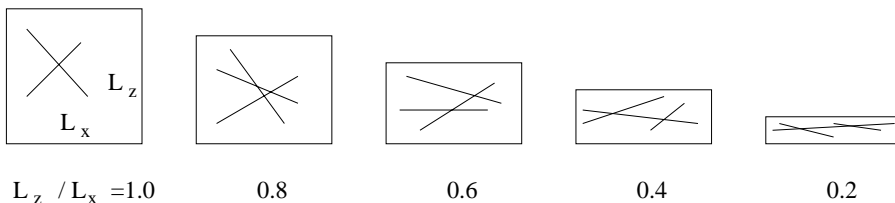


Figure 7.29: Investigated 3D cell shapes.  $L_x = L_y$  for all cells.

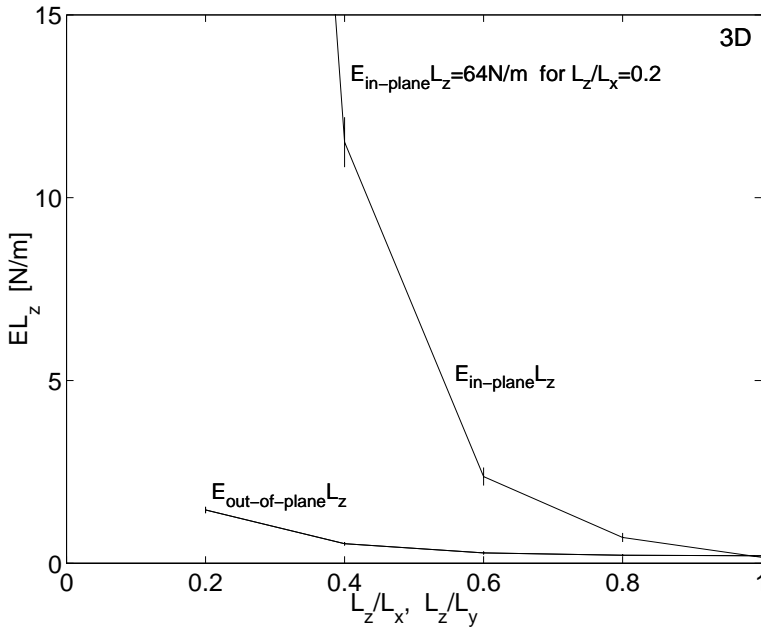


Figure 7.30:  $EL_z$  plotted against  $L_z/L_x=L_z/L_y$ .

$\nu_{out-of-plane}$  is the strain in the  $z$ -direction relative to that in the  $x$ -direction when the network is stressed in the  $x$ -direction.  $\nu_{out-of-plane}$  decreases as the network becomes more two-dimensional.  $\nu_{in-plane}$  fluctuates but overall decreases somewhat as  $L_z/L_x$  decreases. For 2D networks  $\nu$  is typically around 0.34, see Section 7.3. The difference between an ideal 2D network and one in which  $L_z/L_x = 0.2$  can be expected to be rather large, but the fact that  $\nu_{in-plane}$  for  $L_z/L_x = 0.2$  is only around 0.15 indicates that the phenomena which are included only in the 3D model, such as torsion and separation of fibres at the bonds, have an appreciable influence on the shear contraction.

## 7.6. Global elastic stiffness vs length distribution

The length of the fibres has a considerable influence on the stiffness properties of a network. Extremely short fibres can be likened to dust and do not constitute a connected structure. As the fibres become longer, the structure gradually becomes more like a real network and becomes stiffer. This effect has been studied for 2D networks. Figure 7.33 shows  $E$  plotted against fibre length for networks which are all of constant fibre length and network density  $40 \text{ mm}^{-1}$ . The solid line in the diagram connects points which show averages of ten calculations. Vertical lines denote standard deviation. The elastic modulus increases considerably as the fibre

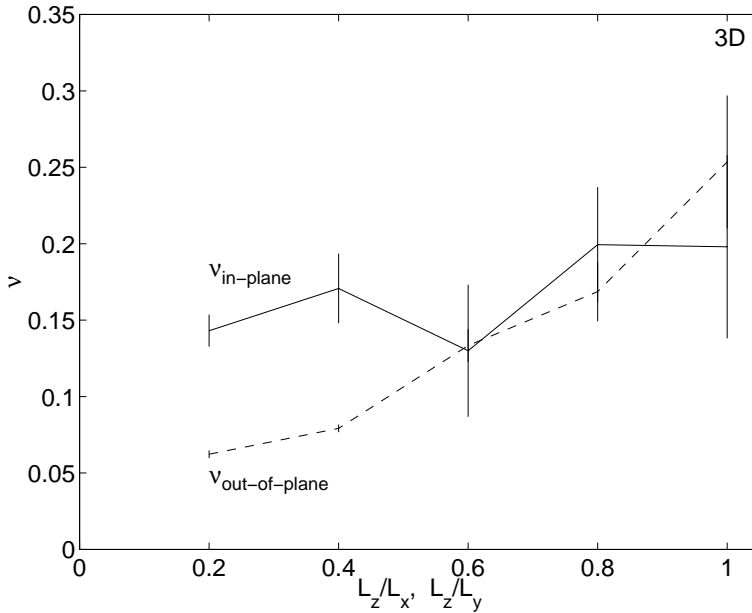


Figure 7.31:  $\nu$  plotted against  $L_z/L_x=L_z/L_y$ .

length is increased at constant network density. Poisson's ratio, on the other hand, is stable around 0.33-0.34 for all fibre lengths investigated, which can be seen from Figure 7.34.

When all the fibres are of the same length, the simulations show quite clearly that longer fibres lead to a stiffer network and that Poisson's ratio is not affected much. In order to investigate the case where the fibre length is given by a statistical distribution, networks with the same network density,  $40 \text{ mm}^{-1}$ , but a length distribution similar to that of the CTMP fluff of Figure 5.1 were simulated. The population distribution in length, the weighted length distribution and the cumulative population distribution in length of the fibres are given in Figure 7.32. It should be noted that in the last bar of the population distribution there is an over-representation of 4 mm fibres, since from the cumulative population distribution 2% of the fibres are exactly 4 mm. The arithmetic mean fibre length is 0.85 mm and the weighted mean fibre length 1.77 mm. The mean value of  $E$  from ten simulations is  $6.48 \cdot 10^4 \text{ N/m}$ ; this value is indicated by the dashed line in Figure 7.33. If the network with varying fibre length can be described by some characteristic fibre length with regard to the initial elastic modulus, the arithmetic mean fibre length does not seem to be the appropriate value. For the case investigated, the constant fibre length which gives the same value of  $E$  is approximately 1.55 mm, which is closer to the weighted mean fibre length. More simulations are needed to confirm this hypothesis, but it seems probable that this tendency holds, since longer fibres contribute more to the stiff-

ness of the network. The average Poisson ratio for networks of varying fibre length, shown as a dashed line in Figure 7.34, is 0.336. That is, Poisson's ratio does not seem to be affected by either mean fibre length or length distribution.

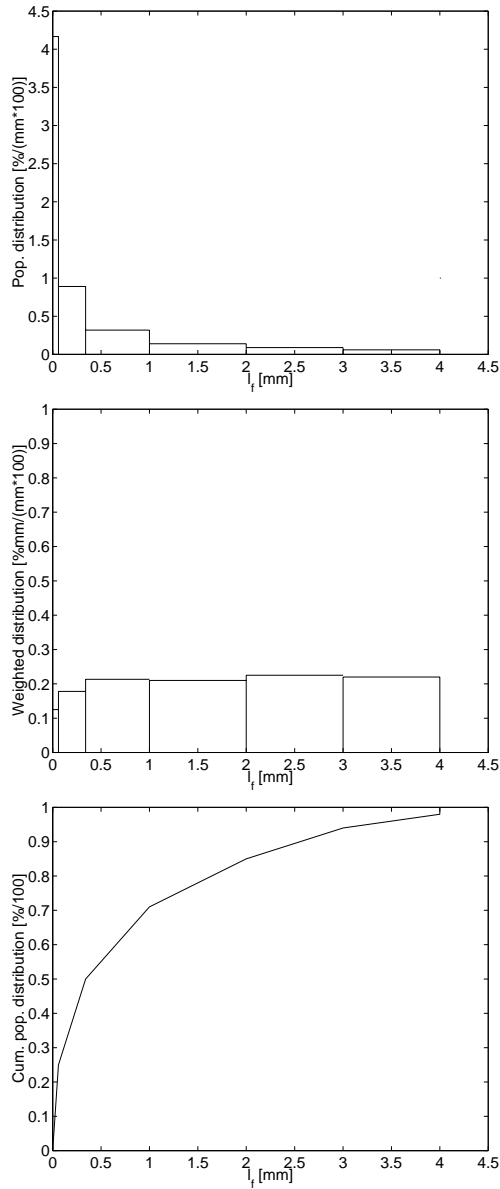


Figure 7.32: Population distribution, weighted distribution and cumulative population distribution of fibre length.

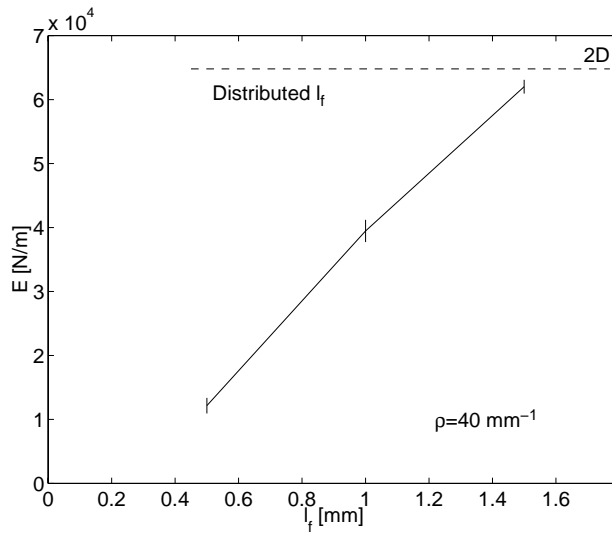


Figure 7.33: Elastic modulus plotted against fibre length.

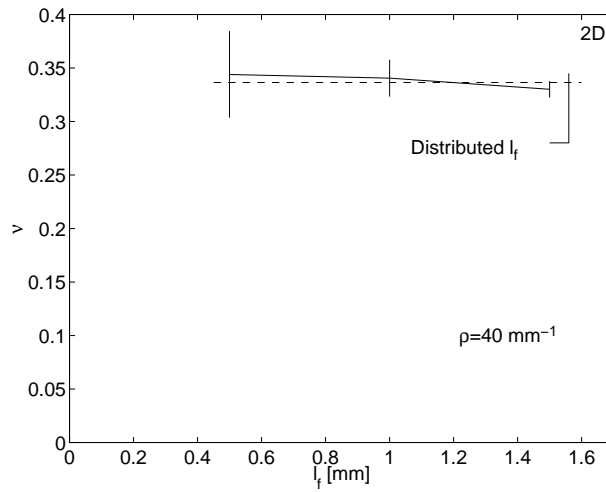


Figure 7.34: Poisson's ratio plotted against fibre length.



## 8. ANALYSIS OF THE FRACTURE PROCESS

The fracture of a heterogeneous structure is a non-linear process; the properties of the structure changing as failure progresses in the material. The analysis of non-linear fracture can, however, be performed as a series of linear steps, if it is assumed that the behaviour of each component of the structure is step-wise linear. This approach has been used, and it is further described in Section 8.2. The fracture criteria and behaviour of the components of the network are defined in Chapter 3, and the numerical values used are given in the next section. It is more complex to quantify the fracture process of a material than the initial stiffness properties. The output parameters used to characterize fracture in this study are discussed in Section 8.3.

### 8.1. Input parameters for fracture analysis

The input parameters for the fracture analysis are given in the form of 2D and 3D example networks. In the next chapter different parameters from these basic fracture example networks are varied, and their influence on the fracture behaviour of the network is investigated. The input parameters required for the basic fracture example networks are much the same as those in the basic example networks of Section 5.1. Some parameters must, however, be changed, and the fracture-related variables are included.

When the initial stiffness was considered, it was concluded in Section 7.1 that a cell length of 1.2 times the fibre length is sufficient. When fracture localization phenomena are studied, results in the next chapter indicate that the cell length must be about twice the fibre length. The size of the cell has considerable influence on the number of degrees of freedom in the simulation. For example, for the same fibre length and network density a cell side length twice the fibre length implies  $2^3/1.2^3 = 4.6$  times more degrees of freedom than in a 3D elastic simulation where  $L = 1.2l_f$ . In addition, the larger system of equations must be solved many times. This makes the choice of long fibres very expensive in terms of computational time.

Since the results from Section 7.6 indicate that the weighted mean fibre length is more relevant for the mechanical properties of a network than is the arithmetic mean, the 2D fracture simulations were performed with a fibre length of 2 mm. For the 2D basic fracture example a side-length  $L=4$  mm was chosen. To compensate for the longer fibre length, it was decided to assume a lower network density in the 2D basic fracture example network;  $\rho=8.7 \text{ mm}^{-1}$  instead of  $60 \text{ mm}^{-1}$  which was used in the elastic simulations. In relation to a typical fluff material of the kind

used in disposable nappies,  $\rho=8.7 \text{ mm}^{-1}$  is estimated to be more realistic in terms of the corresponding number of fibre-to-fibre bonds per fibre, which is about 5.5 in this case.

For the 3D case, however, the effect of longer fibres is even greater and the fibre length was chosen to be 1 mm, as in the 3D basic example network. The network density was set to  $100 \text{ mm}^{-2}$ , corresponding to about 3 bonds per fibre.

The ultimate tensile stress of softwoods such as spruce or pine, containing no faults, is about 100 MPa in the direction of the fibres. The cross-section of wood, however, consists partly of pore space, indicating a higher value of ultimate stress for the material in a single fibre. Yet the fibre is weakened by the defibration process, and the ultimate normal stress for a fibre was therefore set to 100 MPa in the 2D basic fracture example network. The ultimate shear stress was set to a lower value, 50 MPa.

The strength parameters of the fibre-to-fibre bonds can, at present only be estimated in a rough manner. It is known that in a dry-shaped cellulose fibre material to which no adhesive has been added, it is the bonds that break, and not the fibres. Bearing this in mind, and the assumption that the parts of degree of utilization originating from translation and rotation are of the same order of magnitude, the strength values for the 2D network were chosen to be  $F_{ult}=3.5 \cdot 10^{-3} \text{ N}$  and  $M_{ult}=5.6 \cdot 10^{-9} \text{ Nm}$ . For the 2D basic fracture example network, completely brittle failure of bonds was assumed, and  $n_s$  was thus set to 1.

For the 3D basic fracture example network guidance can be found in [1], where friction between pulp fibres was investigated by Andersson and Rasmuson. One fibre was fixed in a horizontal position and another fibre, loaded by a small weight, was slid upwards against it, and the lifting force was recorded. The friction forces obtained from the measured values were fitted to three different friction models. One of the two models that showed the best fit is:

$$F = \mu_{F_0} N + F_0 \quad , \quad (8.1)$$

where  $F$  denotes the friction force and  $N$  denotes the normal force. The values of the constants  $\mu_{F_0}$  and  $F_0$  obtained for friction under dry conditions fitted to this friction model are given in Table 8.1. The three pulps investigated were a kraft pulp and two TMP pulps with the high freeness values of 514 and 700 mL CSF, respectively. (8.1) and Table 8.1 are also illustrated in Figure 8.1. Considering the

Table 8.1: Values of  $F_0$  and  $\mu_{F_0}$  obtained for friction under dry conditions, [1].

Pulp	$F_0$ [mN]	$\mu_{F_0}$
Kraft	0.06	0.56
TMP 514CSF	0.17	0.66
TMP 700CSF	0.53	0.44

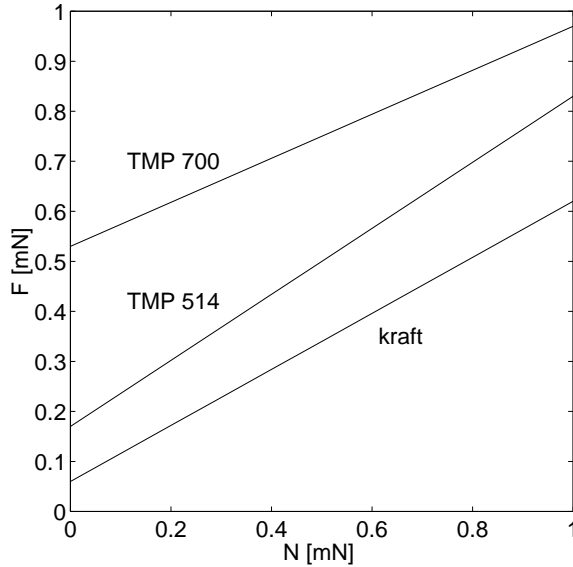


Figure 8.1: Frictional force as a function of normal force for three different pulps, according to (8.1) and Table 8.1.

results in [1], the values of  $\sigma_{adh}$  and  $\mu$  were set to  $5 \cdot 10^5$  Pa and 0.5 respectively.  $5 \cdot 10^5$  Pa corresponds to a value of  $F_0$  of 0.15 mN. Several stick-slips do not change the values of  $\mu_{F_0}$  and  $F_0$ , according to [1]. This implies values of  $\lambda_2$  and  $\lambda_3$  of unity. For the 3D basic fracture example network,  $n_s$  was, however, set to 1, making  $\lambda_2$  and  $\lambda_3$  unnecessary. The stiffness of a bond element, which can be seen as governing the small-scale deformation of a bond before a slip occurs, is assumed to be the same as in the 3D elastic example network.

The input parameters for the basic fracture example networks are summarized in Tables 8.2 and 8.3, which also indicate in which section the variation of a certain parameter is discussed. Unless otherwise stated, the simulations in Chapter 9 refer to networks with the properties listed in Tables 8.2 and 8.3.

## 8.2. Method of analysis

A non-linear fracture analysis can be performed as a series of linear steps, assuming that the behaviour of each component of the structure is step-wise linear. Using this method of non-linear analysis, the equilibrium conditions are fulfilled during the entire course of loading and fracture, apart from effects of round-off errors. The drift from the equilibrium path that may occur in conventional incremental analysis is avoided, and there is no need for iterations, as in methods of the Newton-Raphson kind.

Table 8.2: *Input parameters for the 2D basic fracture example network.*

Parameter	Value and unit	Varied in Section
$l_f$	2 mm	9.1.5
$\kappa$	0 mm <sup>-1</sup>	9.1.5
$A_f$	$2.5 \cdot 10^{-10}$ m <sup>2</sup>	
$I_f$	$2.0 \cdot 10^{-21}$ m <sup>4</sup>	
$E_f$	$35 \cdot 10^9$ Pa	
$\sigma_{ult}$	100 MPa	9.1.2
$\tau_{ult}$	50 MPa	9.1.2
$k_{x1} = k_{y1}$	8750 N/m	9.1.3
$k_{\phi 1}$	$2.8 \cdot 10^{-7}$ Nm/rad	9.1.3
$F_{ult1}$	$3.5 \cdot 10^{-3}$ N	9.1.2, 9.1.3
$M_{ult1}$	$5.6 \cdot 10^{-9}$ Nm	9.1.2, 9.1.3
$n_s$	1	9.1.3, 9.1.5
$\lambda_1$	1.0	9.1.3, 9.1.5
$\lambda_2$	1.0	
$L_x, L_y$	4 mm	9.1.1, 9.1.5
$\rho$	8.7 mm <sup>-1</sup>	9.1.4, 9.1.5
$N_\alpha$	$\frac{1}{\pi}, \quad 0 < \alpha < \pi$	
$s$	1.0	9.1.5
$V_h$	16.0 mm <sup>2</sup>	

In the present analysis, a unit strain is first applied to the structure in each step. The degree of utilization is then calculated for the elements which have a fracture criterion. In 2D networks, both fibre segments and bonds can fail, but in 3D networks fracture is considered for bonds only. The element that is utilized the most is detected and the applied strain is proportioned so that the degree of utilization is exactly unity in the most severely stressed element. The reaction forces obtained are proportioned to the same degree, and thus we obtain corresponding values of stress and strain for the situation when the first element is about to break, or more generally, a change in properties is about to take place, giving new linear characteristics. Next, the global stiffness matrix is adjusted according to the new properties of the partly broken element, and a new linear step is performed. This process can continue until the structure collapses completely and can no longer sustain any load.

Each linear step is performed according to the principles described in Chapter 6, using cyclic boundary and loading conditions. The procedure of finding and removing the most severely loaded element between two successive steps is described below. The element forces are calculated from (6.2), which is repeated here:

$$\mathbf{K}_e \mathbf{u} = \mathbf{f} \quad (8.2)$$

Table 8.3: *Input parameters for the 3D basic fracture example network.*

Parameter	Value and unit	Varied in Section
$l_f$	1 mm	9.2.4, 9.2.5
$c$	0.91	9.2.3, 9.2.5
$A_f$	$2.5 \cdot 10^{-10} \text{ m}^2$	
$I_f, J_{zf}$	$2.0 \cdot 10^{-21} \text{ m}^4$	
$J_{yf}$	$2.0 \cdot 10^{-21} \text{ m}^4$	
$K_{vf}$	$3.5 \cdot 10^{-20} \text{ m}^4$	
$E_f$	$35 \cdot 10^9 \text{ Pa}$	
$G_f$	$2.6 \cdot 10^9 \text{ Pa}$	
$A_b$	$3.1 \cdot 10^{-10} \text{ m}^2$	
$k_n$	$3.0 \cdot 10^{13} \text{ Pa/m}$	9.2.3, 9.2.5
$k_t$	$3.0 \cdot 10^{12} \text{ Pa/m}$	9.2.3, 9.2.5
$\sigma_{adh}$	$5 \cdot 10^5 \text{ Pa}$	9.2.5
$\mu$	0.5	
$n_s$	1	
$\lambda_1$	1.0	
$\lambda_2$	1.0	
$\lambda_3$	1.0	
$L_x, L_y, L_z$	2 mm	9.2.2
$\rho$	$100 \text{ mm}^{-2}$	9.2.1, 9.2.3, 9.2.5
$N_\alpha$	$\frac{1}{\pi}, \quad 0 < \alpha < \pi$	
$N_\beta$	$\cos \beta, \quad 0 < \beta < \frac{\pi}{2}$	9.2.2
$N_\gamma$	$\frac{1}{\pi}, \quad 0 < \gamma < \pi$	
$e$	$20 \cdot 10^{-6} \text{ m}$	
$s$	1.0	
$V_h$	$8.0 \text{ mm}^3$	

$\mathbf{K}_e$  is the element stiffness matrix, in global coordinates, and  $\mathbf{u}$  is the vector of displacements in the directions of the global degrees of freedom of the element.  $\mathbf{f}$  is also in global coordinates, and must be transformed into local element directions before it can be used in a fracture criterion. This is valid for the 2D beam elements and the bond elements used in 3D modelling. The 2D bond elements have the same local and global directions and these need not be transformed. From the fracture criterion (3.2) we can see that the degree of utilization,  $m$ , for a beam element is

$$m = \max \left\{ \begin{array}{l} \frac{|\sigma_n|}{\sigma_{ult}} \\ \frac{|\tau|}{\tau_{ult}} \end{array} \right. , \quad (8.3)$$

where, according to (3.3) and (3.4), for a straight beam of rectangular cross-section

$$\sigma_n = \pm \frac{N}{A_f} \pm \frac{M}{I_f} \sqrt{\frac{3I_f}{A_f}},$$

and

$$\tau = \frac{1.5V}{A_f}.$$

$N$ ,  $M$  and  $V$  denote normal force, bending moment and shear force, respectively in the most stressed section of the beam. Since there is no load on the beams between the bond elements,  $N$  and  $V$  are constant throughout the element.  $M$  varies linearly and thus reaches its maximum value at one of the ends of the element.

The degree of utilization for a 2D bond element of uncoupled springs is, from (3.8),

$$m = \frac{\sqrt{F_x^2 + F_y^2}}{F_{ult}} + \frac{|M|}{M_{ult}}. \quad (8.4)$$

For the 3D bond element the scale factor for the stress,  $c_\sigma$ , for which the fracture criterion, (3.7), is exactly fulfilled is:

$$c_\sigma = \frac{\mu\sigma_{adh}}{|\tau| + \mu\sigma_n} \quad (8.5)$$

The most stressed element is the one that has the smallest positive value of  $c_\sigma$ .

When an element of the structure reaches a degree of utilization of unity it breaks, and the properties of the network structure change. When a beam element breaks, it does so in a brittle manner. This is taken into consideration by assembling the negative value of the broken element's stiffness matrix into the system stiffness matrix, i.e. by removing this element from the system. When the fracture criterion for a bond is fulfilled, the system stiffness matrix is adjusted in a similar way, except that the bond element is not removed altogether. If we have the reduction coefficient for bond stiffness,  $\lambda_1$ , the negative element stiffness matrix multiplied by  $(1 - \lambda_1)$  is assembled into the system stiffness matrix, except when the bond reaches final failure and is removed altogether.

Loading of a network is defined in terms of global straining of the network. A 2D strain state is described by the strain vector  $\epsilon = (\epsilon_x, \epsilon_y, \gamma_{xy})$ , which has three components. A strain state can thus be viewed as a point in a three-dimensional strain space, and the loading of a structure can be represented by a path in strain space. The situation for a 3D simulation is analogous, the difference being that the strain space is six-dimensional. When using the method outlined above the path must be composed of piece-wise straight lines.

The simplest case is to follow a straight line from the origin. This means that the ratios between the single strain components are fixed, and only one calculation needs to be performed during each step. All simulations reported on in the next chapter are of this type, and the line followed from the origin is the  $\epsilon_x$ -  $\epsilon_y$ - or  $\epsilon_z$ -axis. Typically, the path from original structure to complete failure consists of a 'two-steps-forward

one-step-back' walk on the  $\epsilon_x$ -axis. It is equally simple to follow one line from the origin to a certain extent and thereafter change into another one. An example of this is to strain the material in the  $x$ -direction until it is partly broken, unload the structure and then subject it to pure tension in the  $y$ -direction until complete failure. A more complex situation arises if one wants to study a strain path that does not pass the origin, for example constant strain in the  $x$ -direction under increasing strain in the  $y$ -direction. Under these circumstances three or six calculations have to be performed in each step, corresponding to the different modes of strain. This is because, since the strain components do not increase proportionally, the effect of each strain component on each element of the structure must be obtained.

If one wishes to use the results obtained from simulations on small cells for analysis of a larger structure made of the same material, the effect of heterogeneity and size must be taken into account. One way is to build up the large object of finite elements of the same size as the simulated cells. The finite elements should have material properties according to the stress-strain curves obtained from the simulations. The variation in material properties for the finite elements should be according to the spread in simulation results. If the studied structure is much larger than the simulated cells it might be necessary to apply the above process in two steps.

It should be noted that all simulations in this study are based on small displacement theory. Most of the results in the next chapter are within the small displacement range, the few which are not might be unreliable.

### 8.3. Output parameters from fracture analysis

An example of important output from fracture analysis is the set of points in the  $\sigma_x \epsilon_x$  plane representing global force in the direction of strain versus global strain. By definition,

$$\sigma_x = F_x/L_y \text{ for 2D,} \quad (8.6)$$

$$\sigma_x = F_x/L_y L_z \text{ for 3D and} \quad (8.7)$$

$$\epsilon_x = \Delta u_x/L_x . \quad (8.8)$$

Each  $\sigma_x \epsilon_x$  point corresponds to the fracture, partial or complete, of one component of the structure. Each linear step can be represented by a line extending from the origin to the point at which the first element fails in that step. Since the stiffness of a structure decreases as more components fail, the chronological order of the failure points is defined by a successively smaller inclination of the lines from the origin to the point.

A great deal of information can be extracted from these points. The inclination of the line from the origin to the first point gives the initial stiffness of the network, denoted  $(\sigma_x/\epsilon_x)_0$ . The highest value of the global mean stress attained is denoted the maximum stress,  $\sigma_{max}$ , and the corresponding value of strain is denoted the limit strain,  $\epsilon_{lim}$ . The ultimate strain,  $\epsilon_{ult}$ , that is, the strain at which the last component

fails rendering the network completely separated, was not used to characterize the material in this study, since there is a considerable scatter in this value between nominally identical networks. The last few points may also be unreliable due to numerical problems arising when the structure approaches zero stiffness. An integrated measure of the straining capacity which is not so sensitive to the variations in single points is preferable. Fracture energy is such a measure. The various output parameters, excluding fracture energy, obtained from the global  $\sigma_x \varepsilon_x$  response are summarized in Figure 8.2, where the points have been joined together by straight lines. Fracture energy and its coupling to internal elastic energy is discussed in more detail below.

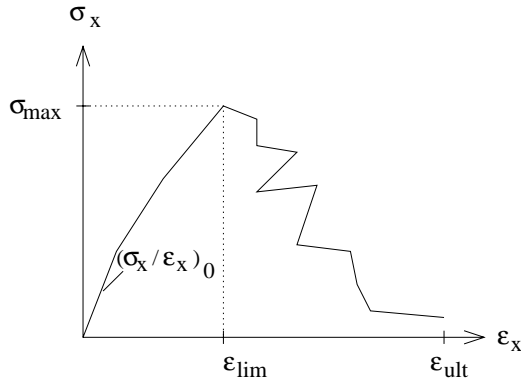


Figure 8.2: *Illustration of some fracture output parameters.*

The amount of energy that has to be supplied to a network to cause its complete failure is an important parameter. A low fracture energy implies a sudden, brittle mode of failure, while a higher value indicates fracture in a more ductile manner.

In each linear step, the external energy that has been supplied to the system is equal to the internal energy stored in the structure. Since the work  $w$  of a force  $F$  and a moment  $M$  is

$$w = \int (F d(\Delta u) + M d(\Delta \theta)) , \quad (8.9)$$

the internal elastic strain energy stored in a bond element,  $w_i^b$ , is

$$w_i^b = \frac{k_n A_b (\Delta u_x)^2}{2} + \frac{k_t A_b ((\Delta u_y)^2 + (\Delta u_z)^2)}{2} + \frac{k_t I_p (\Delta \theta_x)^2}{2} + \frac{k_n I ((\Delta \theta_y)^2 + (\Delta \theta_z)^2)}{2} . \quad (8.10)$$

For a bond element consisting of uncoupled springs the elastic strain energy is,

$$w_i^b = \frac{k_x (\Delta u_x)^2}{2} + \frac{k_y (\Delta u_y)^2}{2} + \frac{k_\phi (\Delta \theta)^2}{2} . \quad (8.11)$$

$\Delta u$  denotes the extension of a spring, and  $\Delta \theta$  is the rotation. The internal elastic strain energy for a fibre segment modelled as a 3D Bernoulli beam,  $w_i^f$ , was given

in (6.10):

$$w_i^f = \int \frac{1}{2} \left( \frac{1}{EA} \left( N + \frac{M_z}{r} \right)^2 + \frac{M_z^2}{EJ_z} + \frac{M_y^2}{EJ_y} + \frac{T^2}{GK_v} \right) dx, \quad (8.12)$$

where  $N$ ,  $M$  and  $T$  denote normal force, bending moment and torque in the fibre segment, and the integration is performed along the axis of the beam. For 2D beams the out-of-plane quantities are excluded.

Fracture was defined in (3.6) to occur in a bond element when

$$g(\mathbf{F}) = 0,$$

where  $g$  is defined in (3.8). The path from the point where the fracture criterion is reached, down to zero force in the spring, has been defined to be a vertical line in Figure 3.7. This means that the fracture of a single bond is assumed to be a stable process, without any dynamic effects. An alternative assumption could be a fracture curve as shown in Figure 8.3, where the difference between the strain energy in the spring at the onset of fracture and the fracture energy consumed by the spring material, is transformed into kinetic energy during unstable fracture, resulting in dynamic effects.

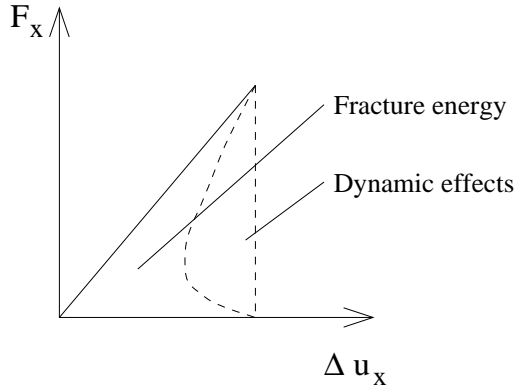


Figure 8.3: *Force-extension diagram for a spring. Alternative where part of the elastic energy gives dynamic effects at failure.*

The external energy supplied to a network,  $w_e^n$ , is the integral of force multiplied by the displacement of the boundary nodes. When cyclic boundary and loading conditions are used, the reaction forces in two opposite nodes are always equal in magnitude and opposite in direction. This means that if a network is subjected to a strain  $\epsilon = (\epsilon_x, 0, 0, 0, 0, 0)$  the external energy supplied to the network in a linear step,  $w_e^n$ , is simply

$$w_e^n = \frac{F_x \epsilon_x L_x}{2}, \quad (8.13)$$

$F_x$  denoting the resultant force in the  $x$ -direction on the faces of the network that are perpendicular to the  $x$ -axis,  $L_x$  being the length of the cell in the  $x$ -direction.

In a linear step,  $w_e^n$ , which is equal to the area under the  $F_x$ - $\Delta u_x$  graph for the network is equal to the sum of the internal strain energies of all the elements of the network, see Figure 8.4,

$$w_e^n = \Sigma w_i^b + \Sigma w_i^f . \quad (8.14)$$

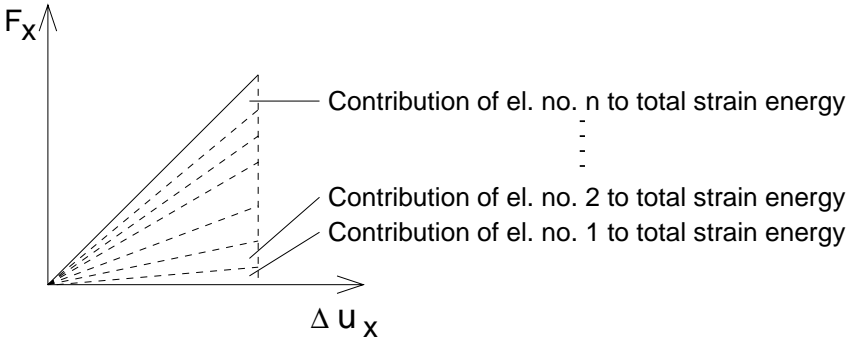


Figure 8.4: *The external energy is equal to the sum of the internal elastic strain energies of the components of the network.*

Within each linear step there is thus equality between external and internal energy. We now compare the internal elastic energy stored in the structure in two successive steps. A network is assumed to be loaded to the extent of failure of the most severely stressed element; this element fails and the new structure obtained when the failed element is removed, or assigned new stiffness properties, is loaded to the same strain. The value of  $F_x$  will now be lower for the same value of  $\Delta u_x$ , since the structure has lost some stiffness due to the removal or change of the fractured element. Thus, the internal strain energy is now smaller, and the difference between the total internal strain energies before and after element failure consists of the fracture energy of the failed element plus the energy lost due to load redistribution within the network; see Figure 8.5, for a simple symbolic example, and Figure 8.6.

The fracture energy of a network,  $w^n$ , is thus larger than the sum of the fracture energies of the failed components,  $\Sigma w^{fc}$ .

$$w^n \geq \Sigma w^{fc} , \quad (8.15)$$

$$w^n = \int_0^{\epsilon_{ult}} F_x L_x d\epsilon_x . \quad (8.16)$$

The total fracture energy of a network is the area under a curve joining the points in some way. Figure 8.7 shows two different ways of joining the points, representing different fracture mechanisms, the second of which is used when fracture energy is evaluated.

The total fracture energy,  $w^n$ , is divided into two parts, the part before maximum load is reached,  $w_1^n$ , and the part after maximum load,  $w_2^n$ , see Figure 8.8.  $w_1^n$

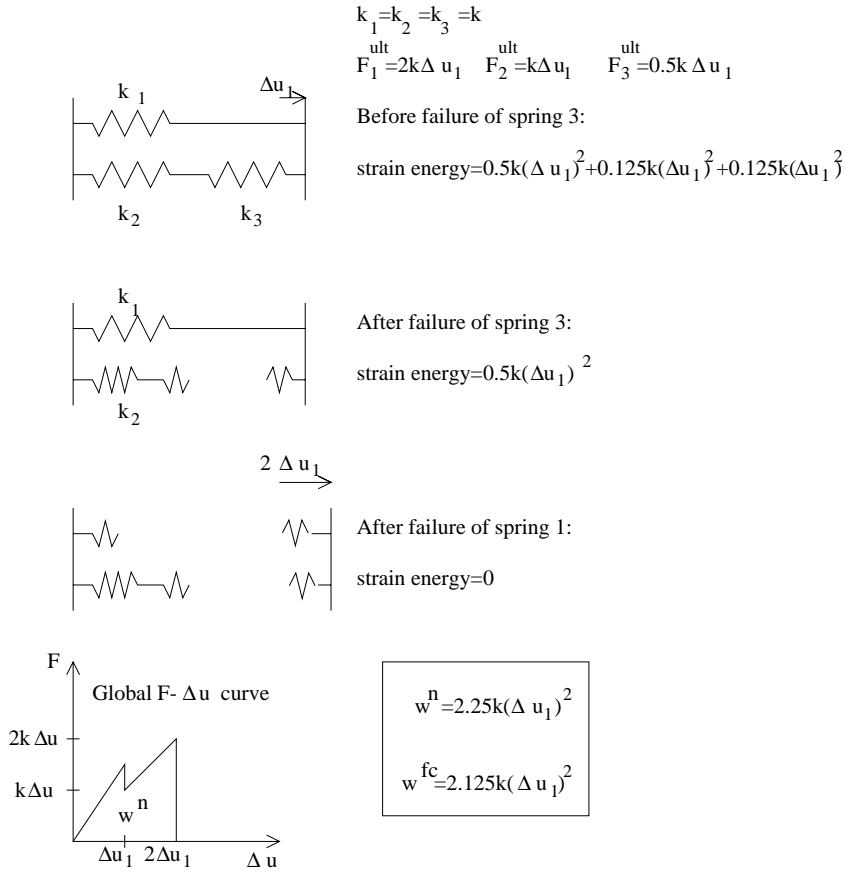


Figure 8.5: Strain energy at different stages of failure.

represents the loss of energy, or dissipation, when a structure is loaded to maximum load and then unloaded. This energy is related to the more or less evenly distributed damage to the material as the global load increases. If the network is reasonably homogeneous one may, as a first approximation, assume  $w_1^n$  to be proportional to the volume, or in 2D, the area of the network.

$w_2^n$  represents the dissipation when the global load  $F_x$  decreases, as  $\Delta u_x$  increases. When  $F_x$  decreases the parts of the structure outside a localized fracturing region are unloaded and contract elastically without any dissipation. The dissipation  $w_2^n$  is instead due to the increasing strain and fracture taking place in the localized fracture process region. Since the fracture events after peak global load can be assumed to be localized to one section, one may, as a first approximation, assume  $w_2^n$  to be proportional to  $L_y L_z$  in 3D and  $L_y$  in 2D. The ratio  $w_2^n / L_y$  corresponds directly to the material parameter "critical energy release rate,  $G_c$ ", used in linear

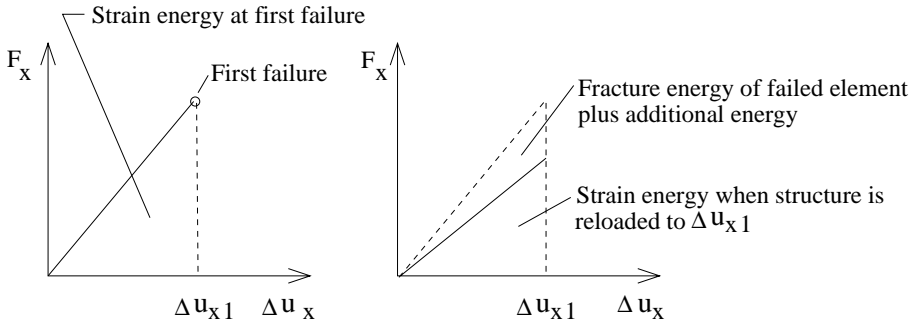


Figure 8.6: *Strain energy in system before and after element failure.*

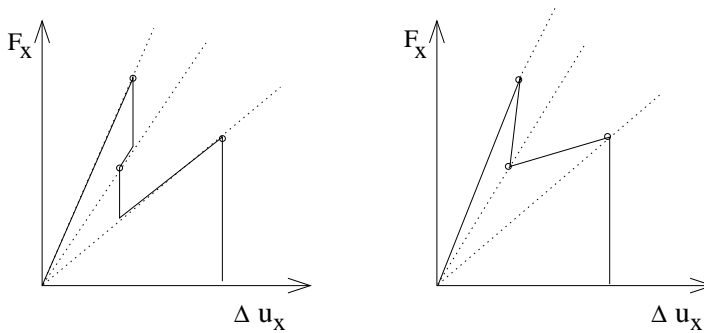


Figure 8.7: *Different ways of calculating the fracture energy.*

elastic fracture mechanics, and to the fracture energy,  $G_F$ , used in non-linear fracture mechanics. Here the notations

$$G_F = w_2^n / L_y \quad \text{and} \quad (8.17)$$

$$G_F = w_2^n / L_y L_z \quad (8.18)$$

will be used for 2D and 3D modelling respectively.

From the fracture energy,  $G_F$ , the strength,  $\sigma_{max}$ , and the stiffness  $(\sigma_x / \epsilon_x)_0$ , an absolute length scale characteristic of the material, can be defined as

$$l_{ch} = (\sigma_x / \epsilon_x)_0 G_F / \sigma_{max}^2 \quad . \quad (8.19)$$

When analysing fracture, such an intrinsic length is needed due to size effects during fracture, even for homogeneous materials.  $l_{ch}$  is also a measure of the brittleness of the material, a low value indicating a brittle material, and corresponding directly to the ratio  $(K_c / \sigma_{max})^2$  used in linear elastic fracture mechanics,  $K_c$  being the fracture toughness of the material. Empirically, it has been found that  $l_{ch}$  is usually

related to the geometrical size of the particles and pores, etc. in a material. In the present calculation of  $l_{ch}$ ,  $(\sigma_x/\epsilon_x)_0$  was used as a measure of the elastic stiffness of the material. For some applications,  $E$  or  $\sigma_{max}/\epsilon_{lim}$  may be more relevant alternative measures of the elastic stiffness. Values of  $l_{ch}$  for various materials have been reported by Gustafsson [16].

The  $\sigma_x\epsilon_x$  curves obtained from simulations show pronounced saw-tooth behaviour. This kind of fracture behaviour is usually not seen in experimental curves. This is because very fast unloading of the material would be required to be able to follow a curve that exposes snap-back performance, faster than is possible in practice. In deformation-controlled experiments, the strain is not allowed to decrease at all, making it impossible to record the snap-back behaviour of the sample, see Figure 8.9. Although difficult to record experimentally, this saw-tooth kind of behaviour may not be unrealistic: when testing a sample as small as those studied in numerical simulations, each individual fracture event within the micro-structure of the material might very well give a noticeable saw-tooth in the global  $\sigma_x\epsilon_x$  curve.

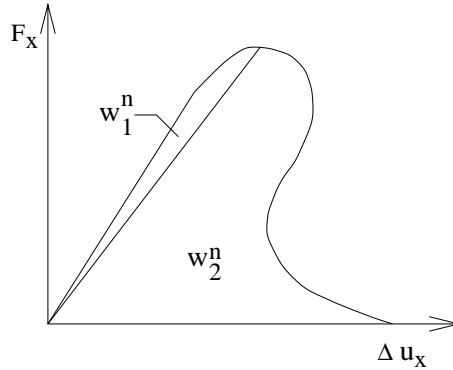


Figure 8.8: Definition of  $w_1^n$  and  $w_2^n$ .

In addition to the stress-strain relationship of the network, it is also interesting to study the localization of the fracture. This is done by plotting the positions of the failed bonds, the zero-stress beams or the remaining active structure of the network as fracture progresses.

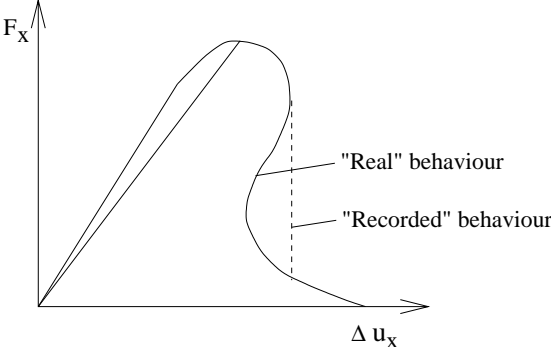


Figure 8.9: Snap-back behaviour.

## 9. RESULTS FROM THE ANALYSIS OF THE FRACTURE PROCESS

### 9.1. Fracture in 2D networks

#### 9.1.1. Effect of sample size

The results obtained from a fracture test or simulation of a heterogeneous material are dependent on the sample size. This effect can be seen in a series of simulations where the shape and size of the sample have been varied. The 2D cells shown in Figure 9.1 were subjected to uniaxial tension in the  $x$ -direction,  $\epsilon = (\epsilon_x, 0, 0)$ , and maximum stress, initial stiffness, fracture energy and localization were evaluated. Apart from the cell size and degree of heterogeneity, all other properties of the networks are as given in Table 8.2. Only the fracture of bonds was considered. For each cell size, five simulations were made, and the averages of the results are given in the following figures.

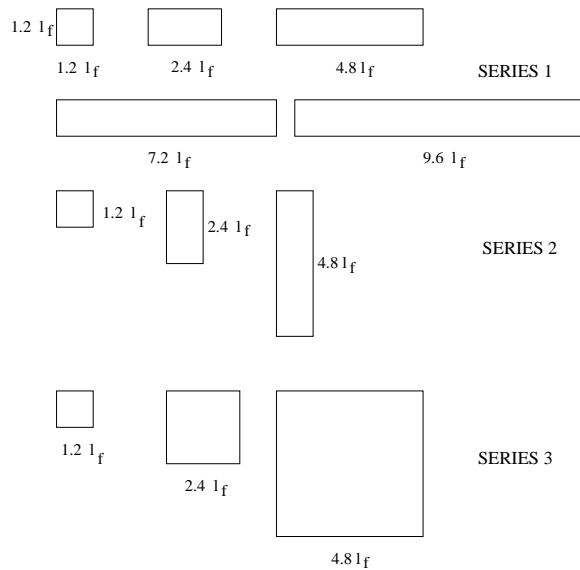


Figure 9.1: *Shape and size of investigated 2D cells.*

If we regard a square with sides of length  $L=1.2 l_f$  as a basic unit cell, the

following samples in series 1 are 2, 4, 6 and 8 times longer than the basic cell. These longer samples should, however, not be regarded as a number of statistically equal unit cells coupled in series. In general the weakest link will determine the strength of a serial system. This phenomenon is described by Weibull theory for certain serial systems, cf. [7]. As the number of cells coupled in series increases, the probability of a really weak cell increases, and therefore it is expected that the strength will decrease as the length of the sample increases in the loading direction. This is indeed the case for the computational results; see Figure 9.2, where maximum stress is plotted against  $L/l_f$  for series 1.

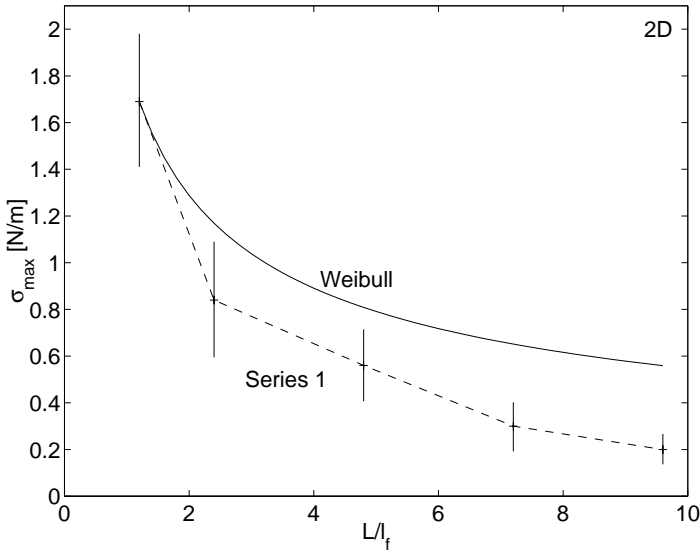


Figure 9.2: Maximum stress plotted against  $L/l_f$  for series 1.

The dashed line connects the average of the simulation results with vertical lines denoting the standard deviation. The solid line shows the size effect prediction of Weibull theory, which is

$$\frac{\sigma_{max}^a}{\sigma_{max}^b} = \left(\frac{l_s^a}{l_s^b}\right)^{1/m}, \quad (9.1)$$

where  $l_s^a$  and  $l_s^b$  are the lengths of two samples  $a$  and  $b$ , and  $m$  is a function of the coefficient of variation, cf. [16]. In Figure 9.2,  $m$ , which is 1.88, is based on the average coefficient of variation of the different cell sizes, 0.56. The simulation results show a greater decrease in strength than that predicted by Weibull theory. This is because a basic assumption of Weibull theory is not fulfilled in the present case. In Weibull theory, cells coupled in series are assumed to have the same strength distribution as a sample consisting of a single cell. This condition would have been fulfilled if the network had been generated in such a way that the density in each of

the square cells coupled in series had been the same. In the present case, however, the network is generated with a prescribed average network density for the whole sample, and due to the random positioning of the fibres there are variations in the average network density from one region of the basic cell to another. Since the weakest link determines the strength, fracture will usually occur in a region of low density. The average of the network density in the fracture zone, taken as a strip of width equal to the fibre length across the sample, is shown in Figure 9.3, vertical lines denoting standard deviation.

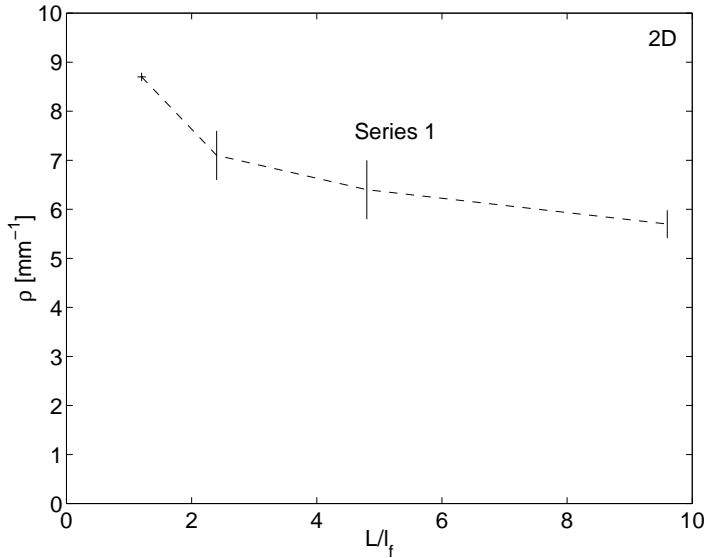


Figure 9.3: Average network density in the fracture zone plotted against  $L/l_f$  for series 1.

While the strength of a sample of length  $9.6l_f$  is determined by a zone of density  $5.7 \text{ mm}^{-1}$ , the strength of a sample of length  $1.2l_f$  is determined by a fracture zone extending over almost the whole sample, and hence of density  $8.7 \text{ mm}^{-1}$ . Figure 9.4 shows examples of the networks of series 1, with fracture zones indicated. It is also clear from this figure that the density in the fracture area decreases as sample length increases.

Series 2 can be compared to unit cells coupled in parallel, although this is not strictly the case. In this case fracture in the weakest cell does not imply global failure, since the forces can be redistributed to other paths where the material is stronger. Because of this, Weibull theory is no longer applicable. Instead, one may as a first approximation expect that the maximum stress remains at an almost constant level as the sample height increases. The computational results are shown in Figure 9.5 and Table 9.1.

Series 3 is a combination of the former two, and the results should be somewhere between the extreme cases of series 1 and series 2. The maximum stress is shown as a function of the the characteristic  $L/l_f$  ratios of the different series in Figure 9.5.

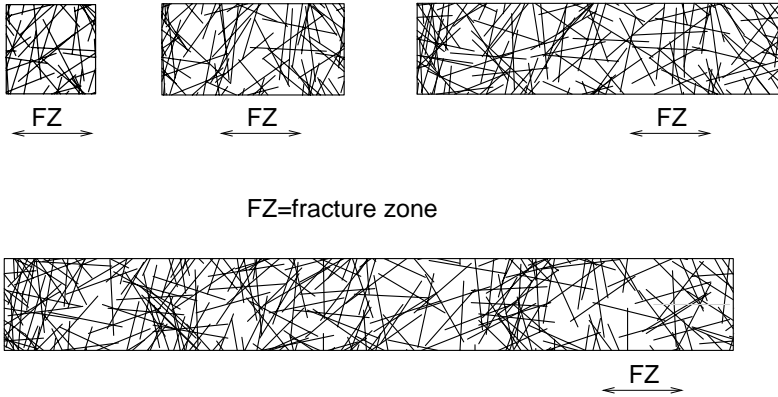


Figure 9.4: *Examples of networks and fracture zones from series 1.*

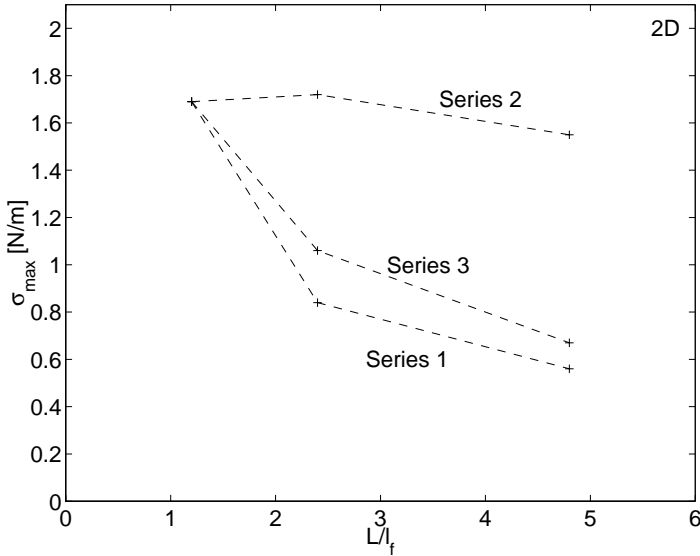


Figure 9.5: *Maximum stress plotted against  $L/l_f$  for series 1, 2 and 3.*

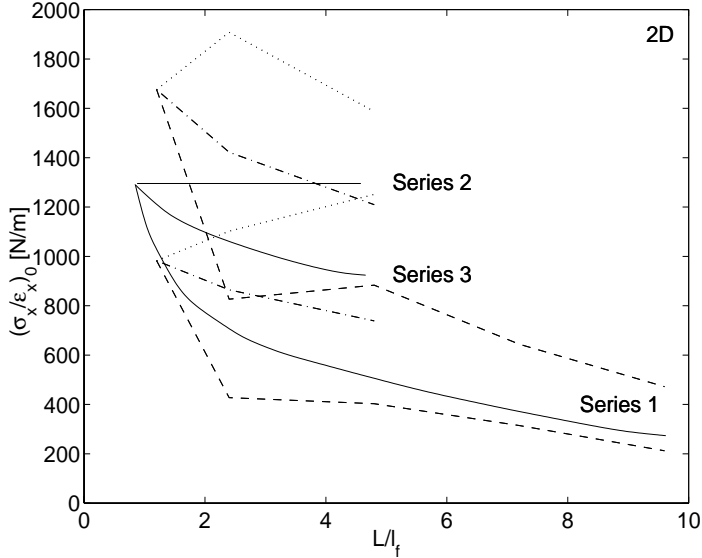


Figure 9.6: Normalized initial stiffness plotted against  $L/l_f$ .

In series 2 the maximum stress remained rather constant, and in series 3 it decreased, but not as strongly as in series 1. In Table 9.1, mean values and coefficients of variation for the calculated strengths as well as the other parameters studied with respect to sample size are given.

In Figure 9.6 the initial stiffness is plotted against  $L/l_f$  for the three series. The heavy lines are estimations made within the 90% confidence interval, the limits of which are also indicated in the figure. As far as strength is concerned, the weakest part of the material is decisive, and it is then obvious to expect a dependence on heterogeneity and sample size. The initial stiffness, on the other hand, is an integrated measure of the properties of the whole sample. As discussed in Section 7.1, the resulting global stiffness in serial coupling is, despite this, dependent on variations in stiffness in a sample, since a weak part weakens the structure more than a stiff part stiffens it. As expected from this, the serial coupling of series 1 shows a pronounced decrease in initial stiffness as the sample length increases. For series 2 the initial stiffness remains constant, as is expected in parallel coupling. Series 3 shows a moderate decrease, although much more obvious than that in Figure 7.8. It seems that the density here is low enough to render the effect of heterogeneity significant.

Another interesting property of a network is the fracture energy, see Section 8.3 for definition. The fracture energies,  $G_F$ , for the different series are plotted against  $L/l_f$  in Figure 9.7. The heavy lines are estimates made within the 90% confidence interval, as in Figure 9.6. For series 1,  $G_F$  decreases as  $L/l_f$  increases, although not as strongly as in the case of maximum stress. This means that the elongation of the fracture zone before complete fracture increases as  $L/l_f$  increases, as could be expected when the network density decreases. For series 2 both the maximum stress

and  $G_F$  are approximately constant, which means that the elongation of the fracture zone is also approximately constant. The curve of series 3 is, as usual, situated between the two extreme cases. The fracture energy,  $G_F$ , shown in Figure 9.7 corresponds to the localized fracture dissipation. The part of the fracture energy corresponding to the pre-fracture distributed dissipation is almost negligible in this case. This result is, however, not thought to be general. Very different results might be obtained if a network with, for instance, bonds with other properties is analysed.

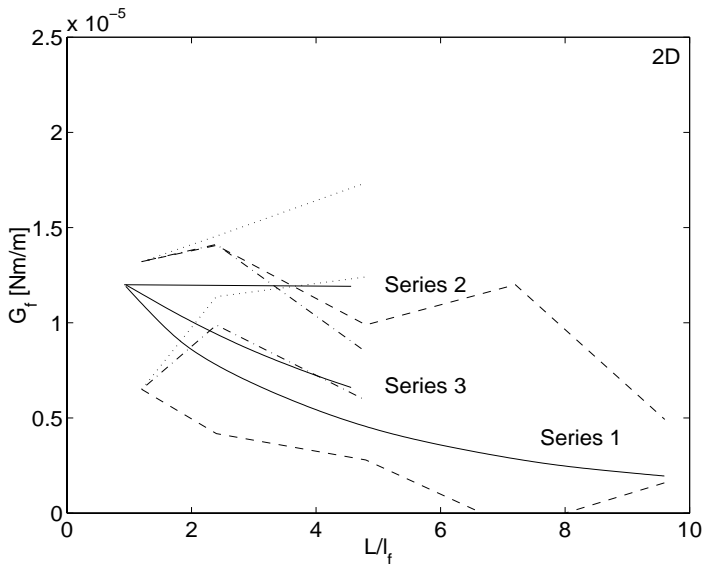


Figure 9.7: Fracture energy plotted against  $L/l_f$ .

Figure 9.8 shows examples of networks and locations of the fractured bonds for the three sample sizes of series 3. As indicated before, it can be seen from the figure that the fracture process zone is of the same order of magnitude as the fibre length. Hence, in the smallest network in which  $L/l_f = 1.2$ , one cannot distinguish a localized fracture zone since the entire area under observation represents a fracture zone. If one wishes to study localization phenomena, the dimensions of the cell studied should therefore be well over one fibre length; twice the fibre length was used in the following.

The final conclusion is that the results of a 2D or 3D fracture simulation of a heterogeneous material must always be considered in relation to the size and shape of the sample. The phenomenon of sample-size dependence cannot be avoided in either experiments or simulations.

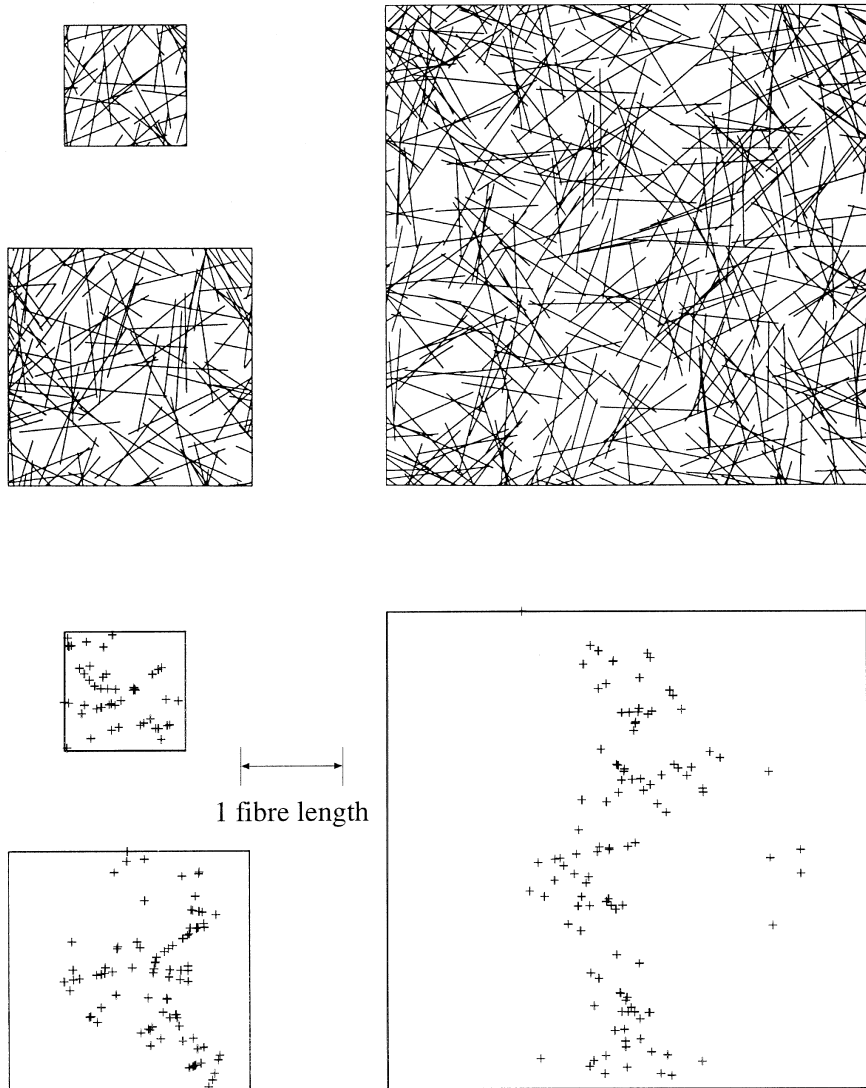


Figure 9.8: *Networks and locations of fractured bonds.*

Table 9.1: Average and coefficient of variation, (c.o.v.), of  $F_x/(E_f L_y l_f \epsilon_x)$ ,  $\sigma_{max}$  and  $G_F$  versus sample size.

$L_x L_y / l_f^2$	$(\sigma_x / \epsilon_x)_0$ [N/m]		$\sigma_{max}$ [N/m]		$G_F$ [Nm/m]	
	Average	c.o.v.	Average	c.o.v.	Average	c.o.v.
Series 1						
$1.2 \times 1.2$	1300	0.50	1.70	0.34	$0.99 \cdot 10^{-5}$	0.46
$2.4 \times 1.2$	630	0.61	0.84	0.58	$0.91 \cdot 10^{-5}$	0.74
$4.8 \times 1.2$	640	0.72	0.56	0.55	$0.63 \cdot 10^{-5}$	0.76
$7.2 \times 1.2$	480	0.66	0.30	0.71	$0.56 \cdot 10^{-5}$	1.55
$9.6 \times 1.2$	340	0.73	0.20	0.64	$0.33 \cdot 10^{-5}$	0.69
Series 2						
$1.2 \times 1.2$	1300	0.50	1.70	0.34	$0.99 \cdot 10^{-5}$	0.46
$1.2 \times 2.4$	1500	0.52	1.72	0.19	$1.30 \cdot 10^{-5}$	0.17
$1.2 \times 4.8$	1400	0.23	1.55	0.30	$1.49 \cdot 10^{-5}$	0.23
Series 3						
$1.2 \times 1.2$	1300	0.50	1.70	0.34	$0.99 \cdot 10^{-5}$	0.46
$2.4 \times 2.4$	1100	0.47	1.06	0.13	$1.20 \cdot 10^{-5}$	0.24
$4.8 \times 4.8$	970	0.47	0.67	0.25	$0.72 \cdot 10^{-5}$	0.24

### 9.1.2. Fracture of an example network

The 2D basic fracture example network of Section 8.1, shown in Figure 9.9, will be used to demonstrate the character of different kinds of network failure: failure of bonds only, failure of fibre segments only, and simultaneous failure of bonds and fibres.

Figure 9.1.2 shows the progression of network failure for the case of failure in bonds only. This mode of failure is accomplished by giving the beam elements a much higher strength, or by only evaluating the degree of utilization in the bond elements. The three columns show active structure, zero-stress fibre segments and fractured bonds, initially and after 12, 50, 75 and 96 bonds have failed. Final failure occurs after the 97th bond has failed, and after this step the entire structure is stressless. The corresponding  $\sigma_x \epsilon_x$ -curve is given in Figure 9.11, with indications of which points on the curve correspond to the states shown in Figure 9.1.2. The corresponding results from the case of beam failure only are shown in Figures 9.12 and 9.13.

Finally, Figure 9.14 shows the  $\sigma_x \epsilon_x$ -curve for the case when both strength of beams and bonds are as described in Section 8.1, and both degrees of utilization are evaluated. For the strength parameters chosen here, almost only bonds fail; of the 88 failed elements at complete fracture only 5 are beam elements. The domination of bond failure reflects the performance of a dry-shaped material. If the strength

parameters for the bonds were adjusted to reflect the strength of bonds of a wet-shaped material, such as paper, the occurrence of beam failure, i.e. fibre failure, would be more frequent.

With respect to strength, Figures 9.11 and 9.14 show that prevention of beam failure does not lead to any increase at all for the present network. Comparing Figures 9.14 and 9.13, it can be seen that the prevention of bond failure gave an approximately 60% increase in strength. For a real network, bond failure can be avoided by using an adhesive aerosol, as discussed in Chapter 1.

The character of the fracture process is somewhat different depending on whether bond or beam failure is considered. When a beam has failed a load-bearing path has been completely destroyed, whereas when a bond fails load may still be transmitted. There is more of a pull-out fracture phenomenon when bonds fail; only when a fibre end has been completely pulled out of the structure is the load-bearing path entirely destroyed. This explains why it takes fewer element failures to reach complete failure when only beam failure is considered. The curves of Figures 9.11 and 9.14 are similar, since both show fracture when bond failures are dominant.

To give a numerical example and an illustration to (8.15), which states that the fracture energy  $w^n$  of a network is greater than the sum of the fracture energies of the failed components,  $w^{fc}$ , the network with only bond failures is considered. For this network  $w^n$  is  $7.2 \cdot 10^{-8}$  Nm, while the sum of the fracture energies of the failed bonds is only  $0.6 \cdot 10^{-8}$  Nm. The difference between the fracture energy of a material and the sum of the fracture energies of the failing micro-components of the material, even when there is no plastic dissipation, is in principle quite important and can also be of significant magnitude. In the present example less than 10% of the total energy corresponds to fracture energy of the failing components. The other part, more than 90%, can be attributed to the heterogeneity of the material. This major part of the fracture energy can be regarded as a result of instabilities within the micro-structure of the material.

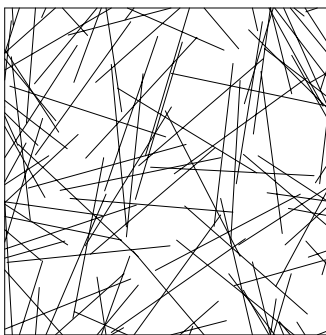


Figure 9.9: *2D basic fracture example network.*

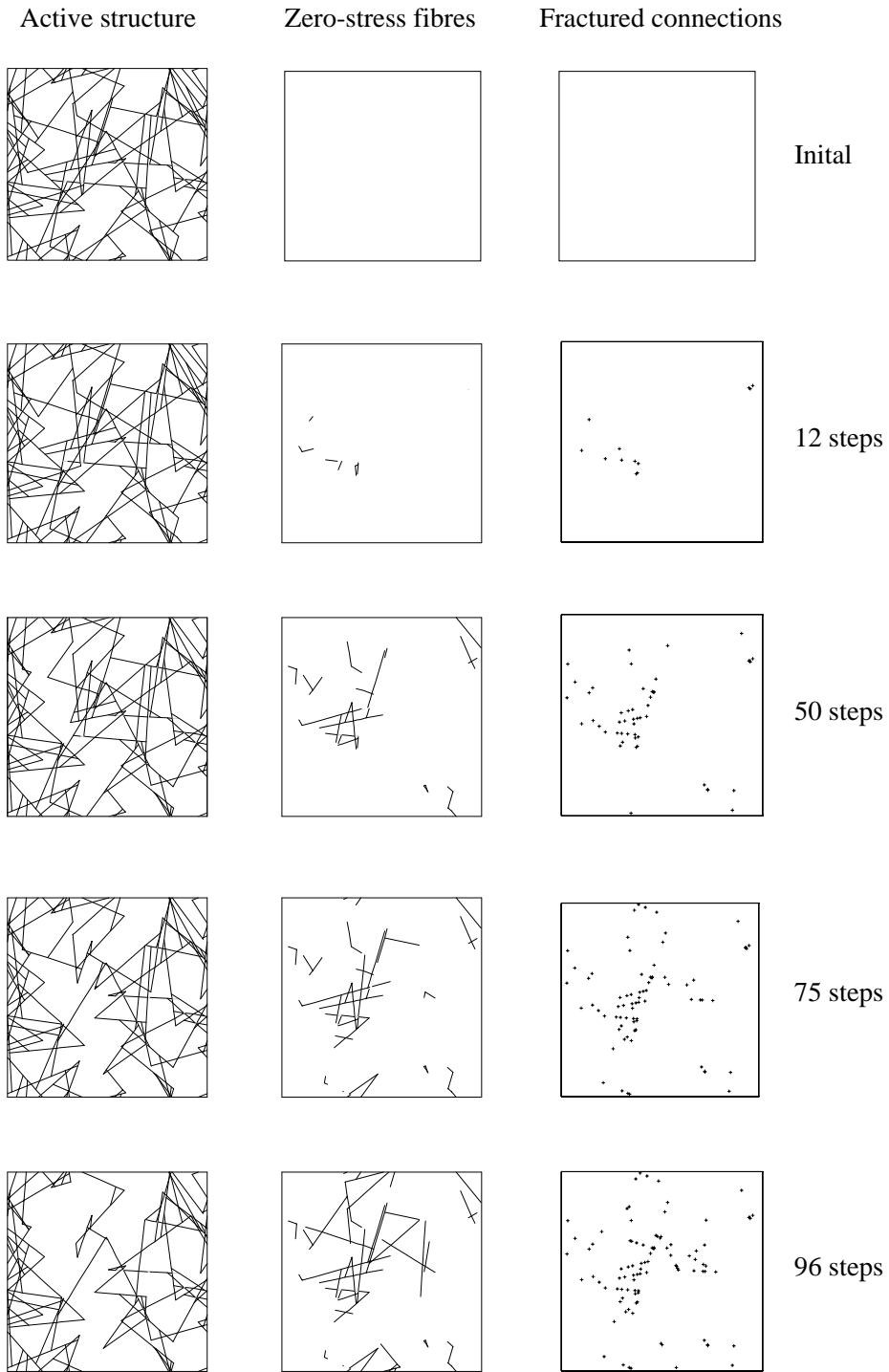


Figure 9.10: *Fracture process of example network, fracture of bonds only considered, i.e. fracture of fibres prevented.*

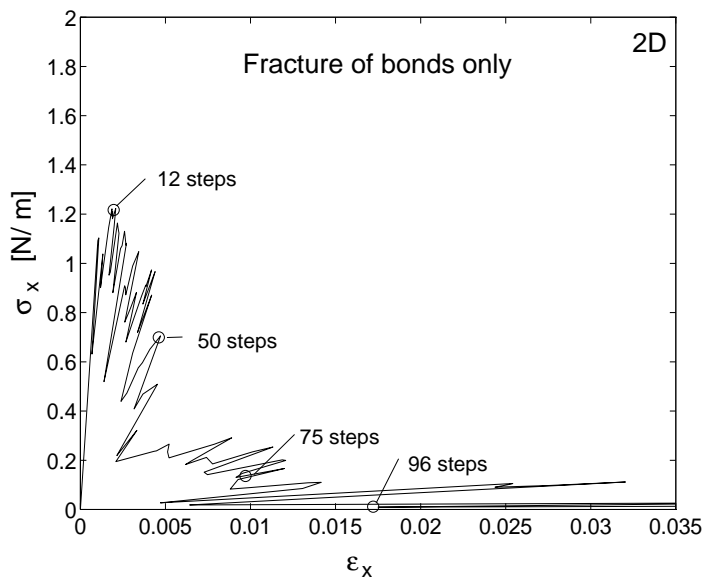


Figure 9.11: *Stress-strain relationship of example network, fracture of bonds only considered, i.e. fracture of fibres prevented.*

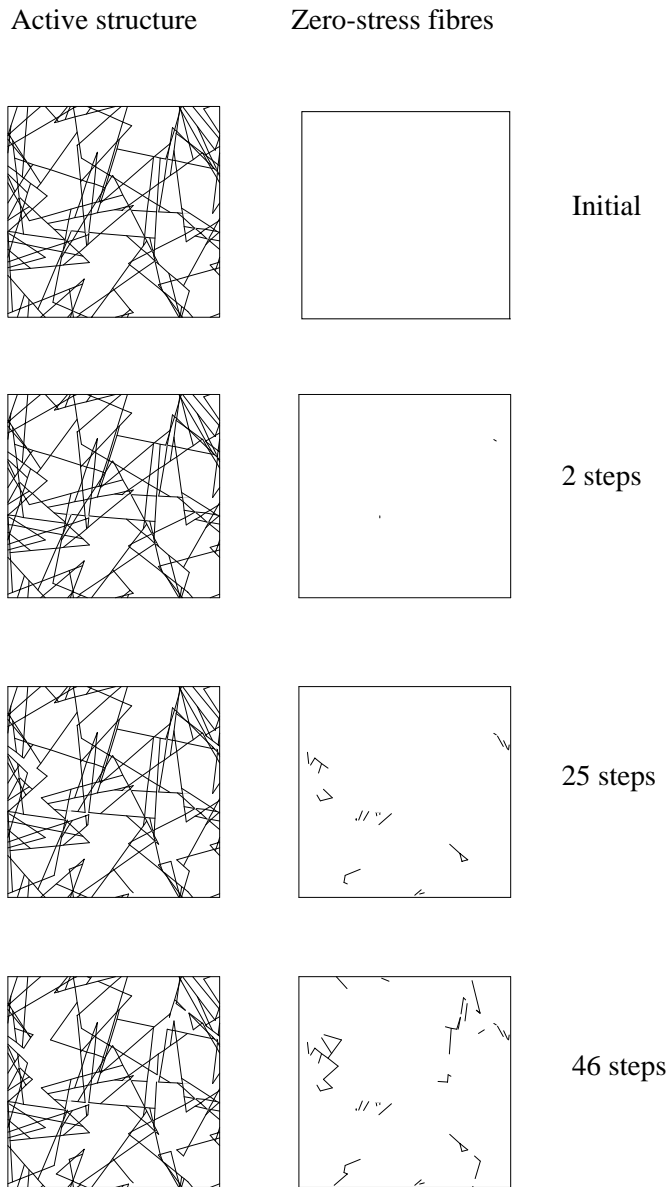


Figure 9.12: *Fracture process of example network, fracture of fibres only considered, i.e. fracture of bonds prevented.*

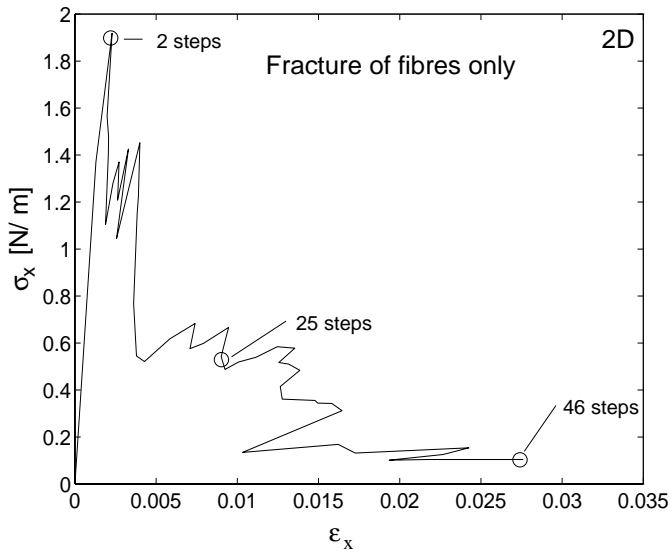


Figure 9.13: *Stress-strain relationship of example network, fracture of fibres only considered, i.e. fracture of bonds prevented.*

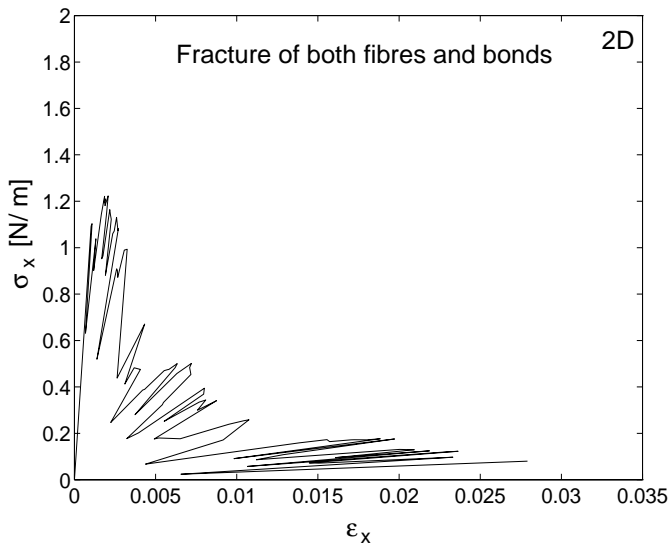


Figure 9.14: *Stress-strain relationship of example network, both fracture of bonds and of fibres considered.*

**9.1.3. Influence of properties of bonds**

In the following analysis it was assumed that only bonds fail, that is, the fibres are assumed to be strong enough to avoid fibre failure. Under these circumstances the influence of the properties of the bonds on the fracture behaviour of 2D networks is studied. The bond properties taken into consideration are stiffness, strength and degree of ductility, the last property being quantified by  $n_s$ , the number of slips before complete failure, and by  $\lambda_1$  and  $\lambda_2$ , see Figure 3.7.

Starting out by considering one single linear elastic spring, the effect of changing spring properties can be seen in Figure 9.15. In a) two springs of equal stiffness but different strength are compared, and in b) the springs are equal in strength but differ in stiffness. From the  $F$ - $\Delta u$ -relationships it can be seen that if the spring strength  $F$  is doubled and the stiffness  $k$  is kept constant, both the ultimate force and ultimate extension  $\Delta u$  are doubled, while the fracture energy,  $w$ , increases four times. If instead the spring stiffness is doubled and the strength is kept constant, as in b), the ultimate force does not change but both ultimate extension and fracture energy reach only half their original values.

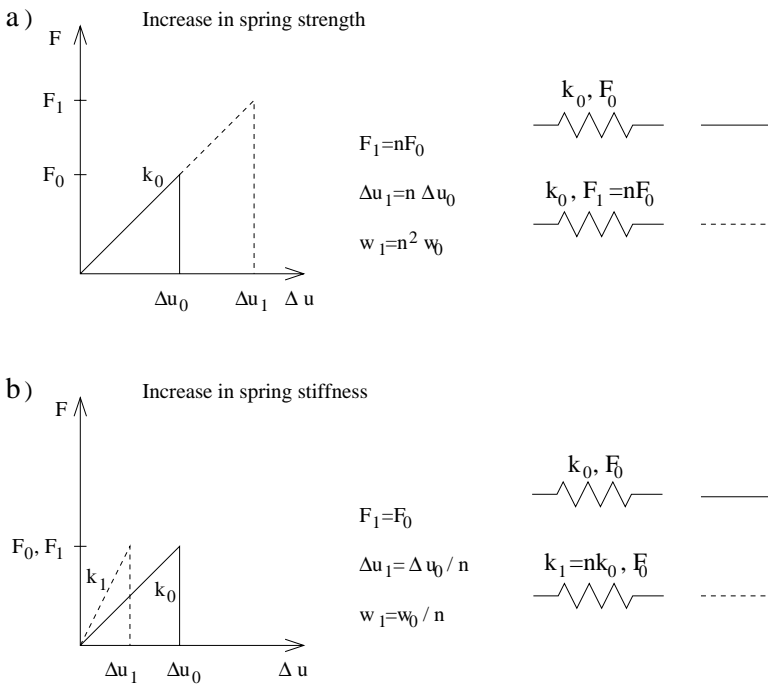


Figure 9.15: a) Effect of modified spring strength. b) Effect of modified spring stiffness.

When a network is considered instead of a single spring, the conclusions from the spring case are directly applicable to the case of change of strength, provided

that only bonds fail. This is illustrated in Figure 9.16, where the stress-strain relationship of the example network of the previous section is given, together with the corresponding curve for the same network when the strength of the bonds has been doubled (dashed line in the diagram). Doubling the strength of the bonds here means doubling of both the ultimate force and ultimate moment. As is expected from the spring case, the ultimate stress and the ultimate strain are twice the value of the example network, and the fracture energy is hence increased by a factor of four. When only fracture of bonds is considered, and the strength of the bonds is

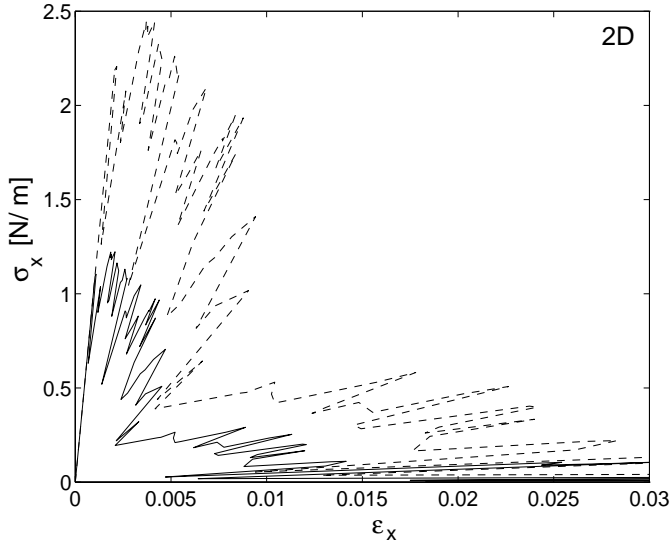


Figure 9.16: *Change in stress-strain relationship for fracture example network when the bond strength is doubled.*

modified, the fracture behaviour of the new network can be obtained from the simple relations of Figure 9.15a. From these relations it is also found that the intrinsic or characteristic length parameter of the material,  $l_{ch}$ , see (8.19), is not affected by the bond strength.

If, on the other hand, we choose to modify the spring stiffness, the situation is more complicated. This is because the relation between bond and beam stiffnesses influences the fracture behaviour. Simulations have been made on the basic 2D fracture example network geometry described in Section 8.1, with bond stiffnesses multiplied by 0.01, 0.1, 1, 10 and 100. All other parameters, including the bond strength parameters, were kept constant according to Table 8.2. The studied variation in bond stiffness is about the same as that which gives strong influence on the initial stiffness of the network according to Figure 7.9. Bond stiffness  $k$  here includes all three stiffness values  $k_x$ ,  $k_y$  and  $k_\phi$ , which are all multiplied by the same constant. Due to the considerable differences in magnitude it is not possible to show all five

curves in the same diagram. Figure 9.17 shows the stress-strain relationship of the example network, and the two networks with reduced bond stiffnesses. It is clear that the initial stiffness decreases and the maximum stress and limit strain increase as the bond stiffness decreases. Figure 9.18 shows the corresponding relationships for the example network and the two networks with higher values of stiffness. The curves for  $10k$  and  $100k$  partly coincide and are difficult to distinguish. Figures 9.19 and 9.20 show the maximum stress and fracture energies as a function of  $k/k^0$ ;  $k$  denoting the stiffness of bonds in the network studied and  $k^0$  being bond stiffness of the 2D fracture example network.

In Table 9.2 the results are given numerically, also for the initial stiffness,  $(\sigma_x/\epsilon_x)_0$ , and the characteristic length,  $l_{ch}$ . It should be noted that the computational results for the various values of  $k/k_0$  are obtained from one single network geometry.

Table 9.2: *Material property parameters and stiffness of bonds.*

$k/k_0$	$(\sigma_x/\epsilon_x)_0$ [N/m]	$\sigma_{max}$ [N/m]	$G_F$ [Nm/m]	$l_{ch}$ [m]
0.01	110	6.56	$210 \cdot 10^{-5}$	$5.4 \cdot 10^{-3}$
0.1	430	3.28	$30 \cdot 10^{-5}$	$12 \cdot 10^{-3}$
1	1100	1.22	$1.8 \cdot 10^{-5}$	$13 \cdot 10^{-3}$
10	1600	0.61	$0.36 \cdot 10^{-5}$	$16 \cdot 10^{-3}$
100	1800	0.42	$0.30 \cdot 10^{-5}$	$31 \cdot 10^{-3}$

Although the effect of changing the bond stiffness seems very large from the diagrams, it is not as great as the effect of changing the strength. In the stiffness case we obtain an increase in ultimate stress of approximately a factor 16 when the stiffness is decreased by a factor 10000. In the case of change of strength, there is direct proportionality between the increase in bond strength and network ultimate stress.

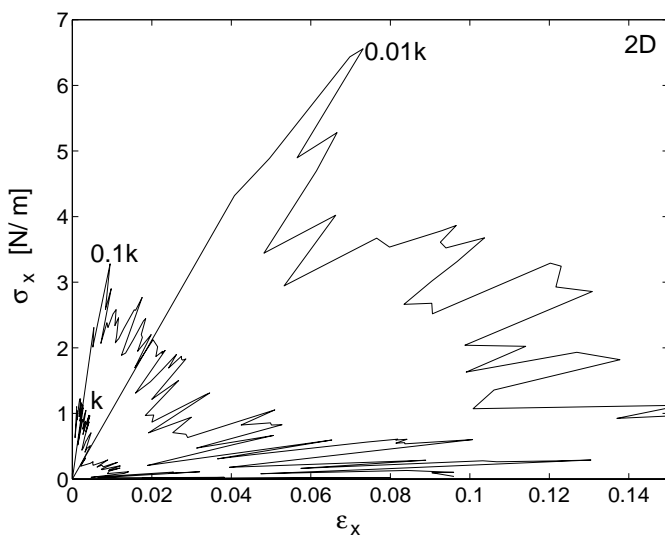


Figure 9.17: *Stress-strain relationship of example network when bond stiffness is decreased.*

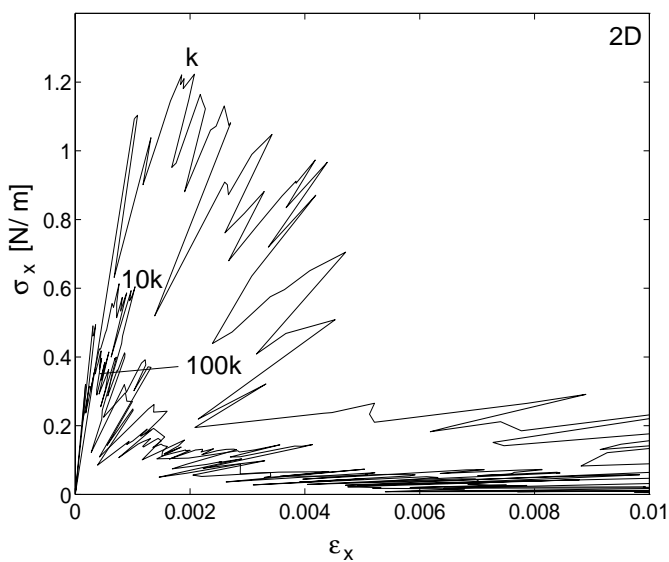


Figure 9.18: *Stress-strain relationship of example network when bond stiffness is increased.*

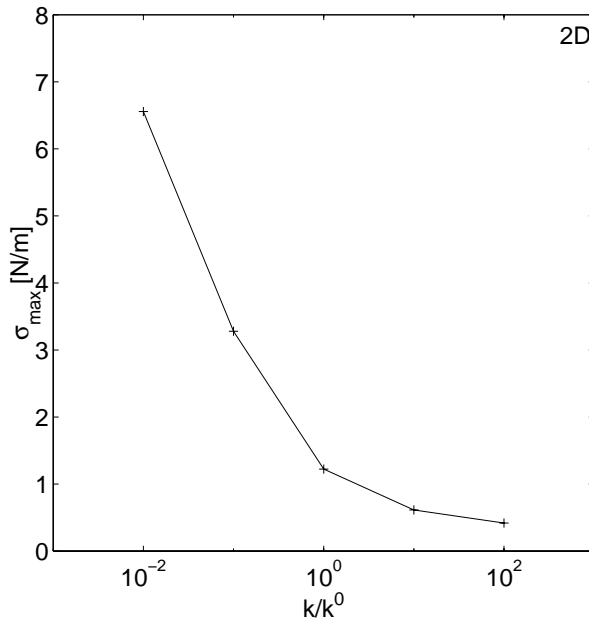


Figure 9.19: Maximum stress plotted against  $k/k^0$ .

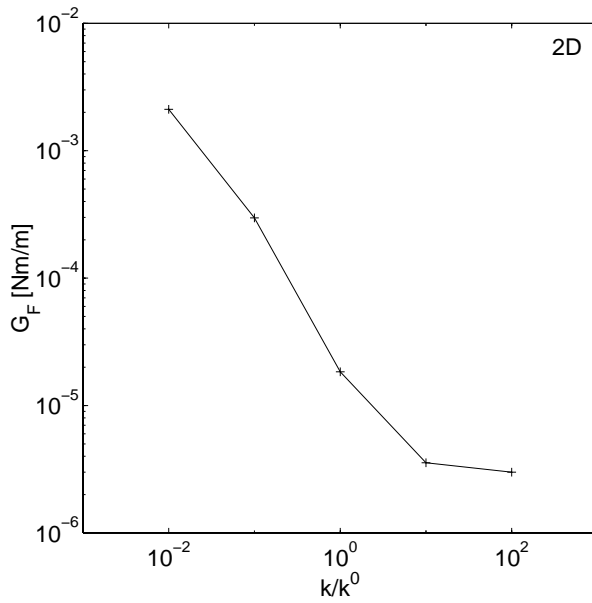


Figure 9.20: Fracture energy plotted against  $k/k^0$ .

Simulations have also been made in order to investigate the influence of the ductility of bonds on global fracture behaviour. The stick-slip behaviour of the bonds is defined in Figure 3.7. The parameters used were reduction in stiffness between two slips  $\lambda_1 = 0.5$ , and reduction in strength between two slips  $\lambda_2 = 1.0$ . The number of slips investigated before complete failure,  $n_s$ , were 1, 2 and 5. The network density was  $20 \text{ mm}^{-1}$  and the other input parameters were as listed in Table 8.2. As many as five slips before final failure of a bond may seem a lot, but the relative displacement of two fibres in a bond here is still on the microscopic level. The effect of fibres slipping and forming new bonds in a new geometric configuration remains to be accounted for.

Two simulations were made for each value of  $n_s$ . In order to speed up the calculations, more than one bond was modified in each step for the cases of  $n_s = 2$  and 5. Figure 9.21 illustrates the effect of this approximation, the first diagram showing the result for  $n_s = 2$  when only one bond is modified in each step, and the second the result when five bonds are modified in each step. The details of the curve are changed, but the overall shape is much the same. For  $n_s = 5$ , ten bonds were modified in each step.

If the results from all the simulations are plotted in the same diagram the curves interfere making interpretation difficult. In order to avoid this problem the average of the two curves in the different simulations was replaced by a hand-drawn simplified approximation. Figure 9.22 shows the two original curves together with the approximated one in the same diagram, for the case of  $n_s = 5$ .

The results of the simulations are shown in Figure 9.23. It is clear that an increase in bond ductility has a remarkable effect on the global strength and fracture energy. This is because the greater ductility allows the degree of utilisation to become more evenly distributed over the network. The stiffness of a bond that is severely stressed is reduced, allowing other less stressed bonds to take over part of the load. Ideally, one could imagine a situation where every bond in the network reaches final failure at the same time, although this would cause a very abrupt failure. The ultimate stress and fracture energy as a function of  $n_s$  are shown in Figures 9.24 and 9.25. In Table 9.3 the results for initial stiffness and characteristic length are also given.

Table 9.3: *Material property parameters and ductility of bonds.*

$n_s$	$(\sigma_x/\epsilon_x)_0$ [N/m]	$\sigma_{max}$ [N/m]	$G_F$ [Nm/m]	$l_{ch}$ [m]
1	25000	22	$6.8 \cdot 10^{-5}$	$3.5 \cdot 10^{-3}$
2	25000	30	$14 \cdot 10^{-5}$	$3.9 \cdot 10^{-3}$
5	25000	56	$120 \cdot 10^{-5}$	$9.6 \cdot 10^{-3}$

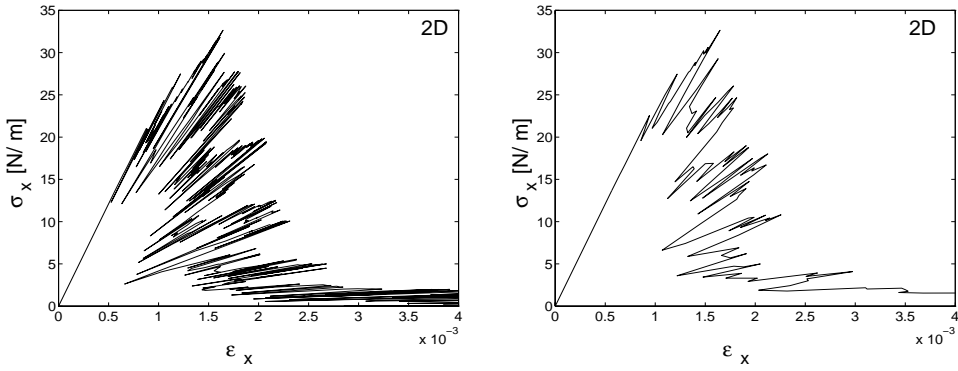


Figure 9.21: *Stress-strain relationship for the same network when 1 and 5 bonds have been broken in each step.*

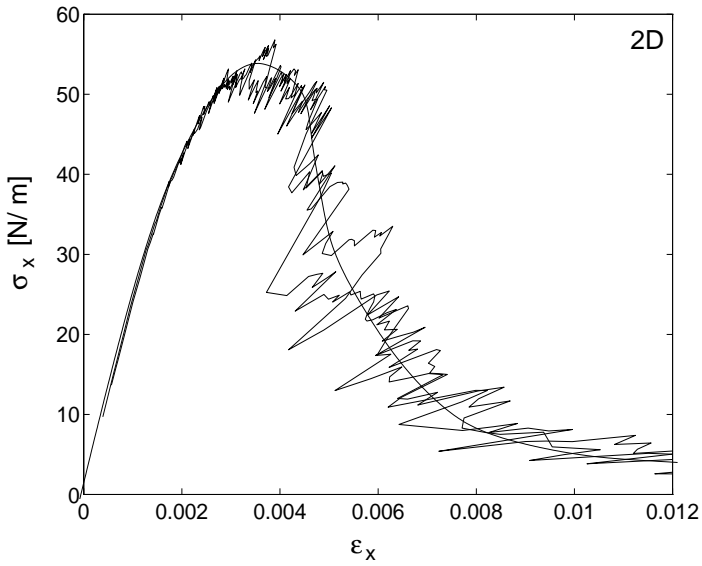


Figure 9.22: *Two stress-strain curves obtained from simulations together with the corresponding hand-drawn approximation.*

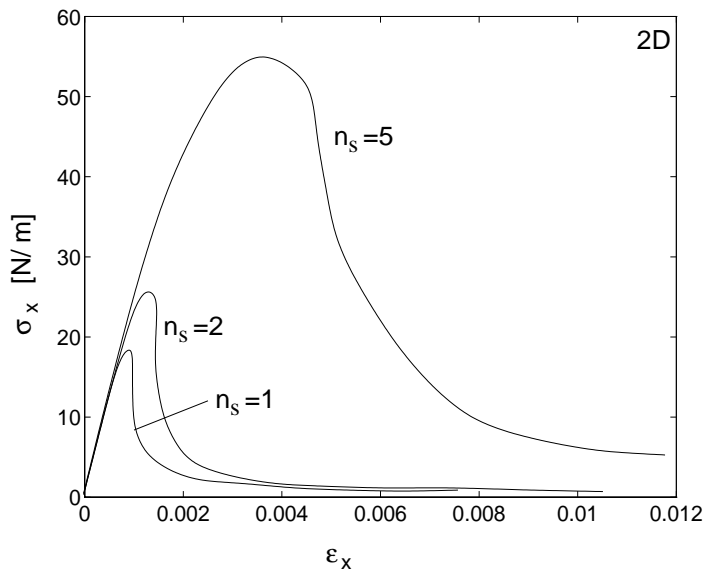


Figure 9.23: *Stress-strain relationships for  $n_s = 1, 2$  and 5.*

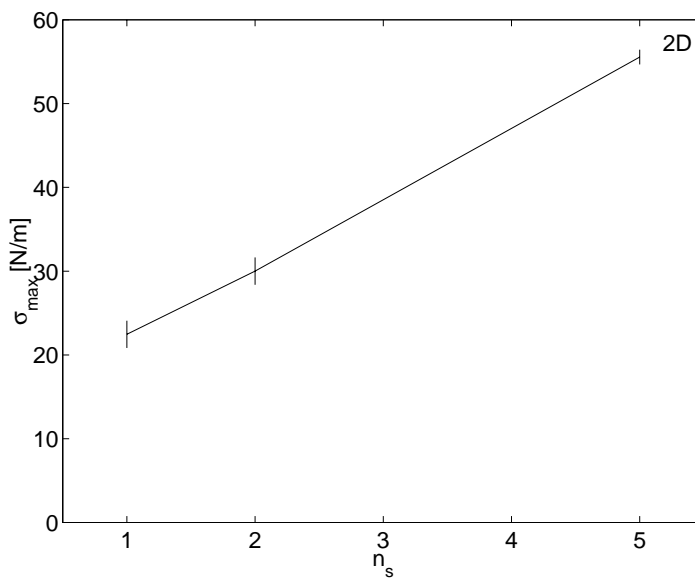
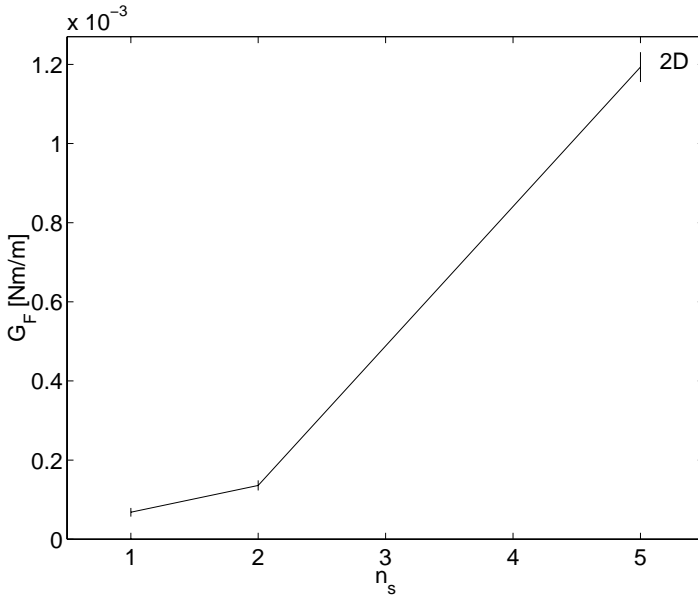


Figure 9.24: *Maximum stress plotted against  $n_s$ .*

Figure 9.25: *Fracture energy plotted against  $n_s$ .*

#### 9.1.4. Influence of network density

The influence of network density on the fracture behaviour of a 2D network has been examined by simulating a series of networks of density  $\rho = 8.7, 15$  and  $20 \text{ mm}^{-1}$ . Bond failure is assumed, and the other properties of the networks correspond to those of the 2D fracture example network. Five simulations were performed for each value of network density, and the average of the results is given in the following figures. The stress-strain relationships for the different densities are all given in Figure 9.26, despite large differences in both maximum stress and strain. To facilitate interpretation of the figure, hand-drawn approximations have been used, as described above. As  $\rho$  increases, the networks become considerably stronger, and also more brittle. The maximum stress and fracture energy, average and standard deviation, are shown as a function of network density in Figures 9.27 and 9.28.

In the work of Åstrom and Niskanen, [2], where the bonds were assumed to be rigid, it was concluded that the strength of a network is proportional to the elastic modulus of the network multiplied by the ultimate shear strain in a bond. From Figure 9.29 it is clear that the results of the present simulations agree with previous work, [2], in that the maximum stress of a network divided by the initial stiffness is almost exactly constant. If the bonds are linearly elastic, the ratio between fibre and bond stiffness is kept constant and failure is allowed to occur only in the bonds, it is obvious that the strength will also be proportional to the ultimate strain of the

bonds, see Figure 9.16. If the ultimate strain of the bonds is increased by increasing  $n_s$  from 1 to 2 and then to 5, an increase in network strength is again observed, although it is not proportional to the ultimate strain, see Figure 9.19.

In Table 9.4 the computational results for initial stiffness, strength, fracture energy and characteristic length are given numerically. It is interesting to note that the fairly moderate increase in density from  $15 \text{ mm}^{-1}$  to  $20 \text{ mm}^{-1}$  gives more than a two-fold increase in stiffness, strength and fracture energy. In the region from  $8.7 \text{ mm}^{-1}$  to  $15 \text{ mm}^{-1}$  the effect on stiffness and strength is even greater. The theoretical percolation density of the network is  $5.7/2.0=2.9 \text{ mm}^{-1}$ . Since the strength is low already at  $\rho = 8.7 \text{ mm}^{-1}$ , the sensitivity of the strength to density is probably very small in the region from the percolation point up to about  $8 \text{ mm}^{-1}$ .

From Table 9.4 it is also interesting to note that the coefficient of variation for the various properties is greater at low density. This is in agreement with the more heterogeneous character of the geometry of networks with low density. Also, the variation of the intrinsic material length parameter,  $l_{ch}$ , with density is consistent. The lowest value,  $2.9 \text{ mm}$ , at the highest density,  $\rho = 20 \text{ mm}^{-1}$ , may correspond to the more brittle character of more homogeneous materials. The variation of  $l_{ch}$  with density seems also to reflect the general absolute size of the micro-structure of the material. Although the fibre length is the same for the different networks, the free fibre segment length as well as the size of the open areas, the ‘pores’, is much smaller at a density of  $\rho = 20 \text{ mm}^{-1}$  than at  $\rho = 8.7 \text{ mm}^{-1}$ .

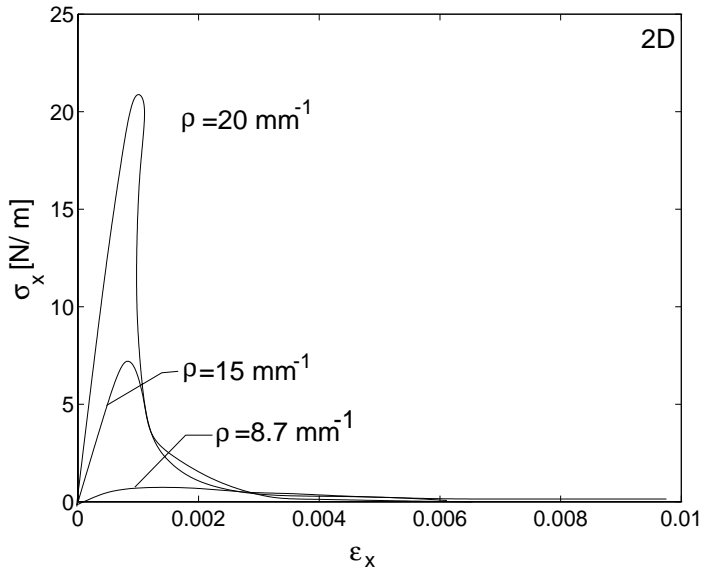


Figure 9.26: *Stress-strain relationships for different network densities.*

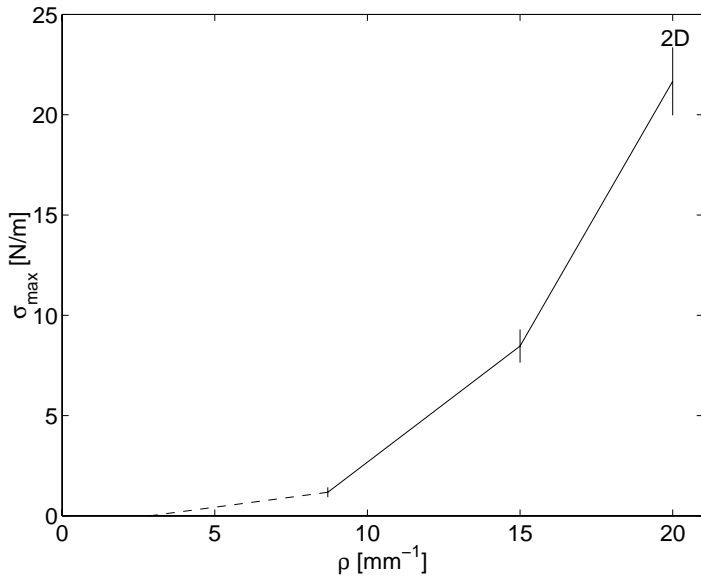


Figure 9.27: Maximum stress plotted against  $\rho$ .

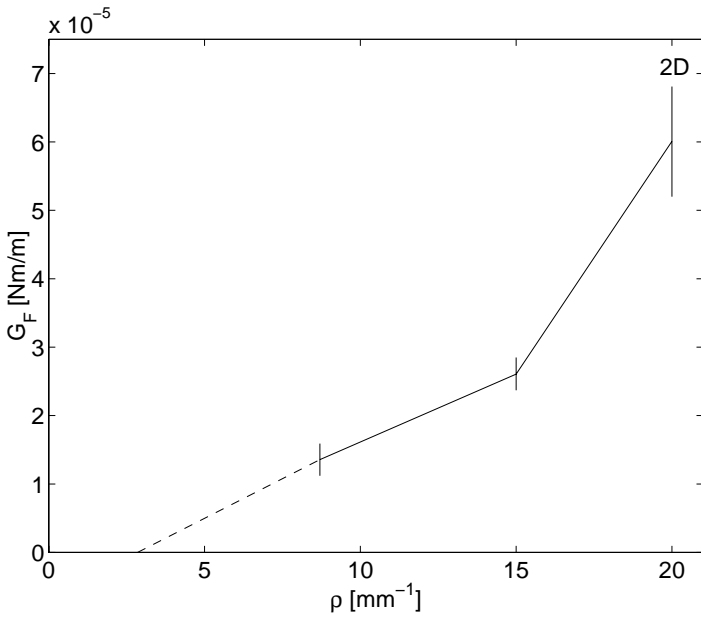


Figure 9.28: Fracture energy plotted against  $\rho$ .

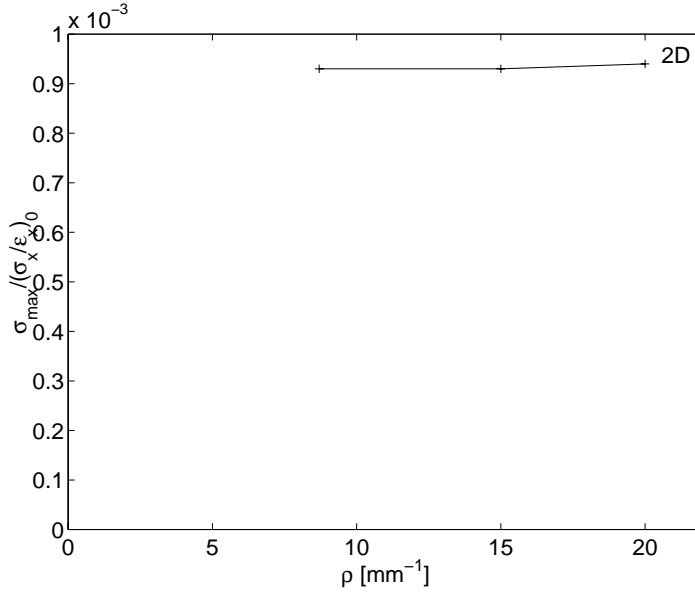


Figure 9.29: Maximum stress divided by initial stiffness plotted against  $\rho$ .

Table 9.4: Average and coefficient of variation, (c.o.v.), of material properties at different densities.

$\rho$ [mm <sup>-1</sup> ]	$(\sigma_x/\epsilon_x)_0$ [N/m]		$\sigma_{max}$ [N/m]		$G_F$ [Nm/m]		$l_{ch}$ [m]
	Average	c.o.v.	Average	c.o.v.	Average	c.o.v.	
8.7	1271	0.45	1.2	0.41	$1.35 \cdot 10^{-5}$	0.35	$11.9 \cdot 10^{-3}$
15	9126	0.19	8.4	0.19	$2.61 \cdot 10^{-5}$	0.18	$3.4 \cdot 10^{-3}$
20	23018	0.09	21.7	0.15	$6.01 \cdot 10^{-5}$	0.27	$2.9 \cdot 10^{-3}$

### 9.1.5. Simulation of complex 2D example network

This section gives an example of a simulation of a 2D network of curled fibres of varying length. The length distribution of the fibres is the same as shown in Figure 7.32 in Section 7.6, approximately representing the length distribution of a CTMP pulp. The radius of curvature of the fibres is 1.4 mm. At a fibre crossing the probability of a bond is 0.4, and each bond is assumed to exhibit a stick-slip performance. The number of slips before complete failure is five, and at each slip the stiffness is reduced by a factor of 0.5, while the strength is unaffected. The orientation distribution is uniform. The network density is  $22.1 \text{ mm}^{-1}$ , giving an average free fibre segment length of 0.18 mm. This corresponds to a three-dimensional fibre fluff of density  $80 \text{ kg/m}^3$ , if it is assumed that the fibres are randomly distributed in space, see [20]. Failure of bonds only is considered and ten bonds are modified in each step. The input parameters of the network are summarized in Table 9.5.

Table 9.5: *Input parameters for the complex 2D example network.*

Parameter	Value and unit
$l_f$	see Figure 7.32
$\kappa$	$714 \text{ mm}^{-1}$
$A_f$	$2.5 \cdot 10^{-10} \text{ m}^2$
$I_f$	$0.2 \cdot 10^{-20} \text{ m}^4$
$E_f$	$35 \cdot 10^9 \text{ Pa}$
$\sigma_{ult}$	100 MPa
$\tau_{ult}$	50 MPa
$k_{x1} = k_{y1}$	8750 N/m
$k_{\phi 1}$	$2.8 \cdot 10^{-7} \text{ Nm/rad}$
$F_{ult1}$	$3.5 \cdot 10^{-3} \text{ N}$
$M_{ult1}$	$5.6 \cdot 10^{-9} \text{ Nm}$
$n_s$	5
$\lambda_1$	0.5
$\lambda_2$	1.0
$L$	4.2 mm
$\rho$	$22.1 \text{ mm}^{-1}$
$N_\alpha$	$\frac{1}{\pi}, \quad 0 < \alpha < \pi$
$s$	0.4
$V_h$	$17.6 \text{ mm}^2$

Figure 9.30 shows an illustration of the network, which consists of 1800 active beam elements and 1005 bonds, and the approximate active part is 70%. The number of degrees of freedom in the finite element model is 6366.

Figure 9.31 shows the stress-strain relationship of the network. There are 39 steps before maximum stress is reached, and after 95 steps the network has failed

completely.  $(\sigma_x/\epsilon_x)_0 = 1.29 \cdot 10^3$  N/m,  $\sigma_{max} = 5.81$  N/m,  $G_F = 20 \cdot 10^{-5}$  Nm/m and  $l_{ch} = 7.6 \cdot 10^{-3}$  m.

Figure 9.32 shows the locations of the failed bonds after 16, 39 70 and 95 steps. The first column indicates bonds that have slipped at least once, the second indicates at least three slips and the third indicates five slips, which corresponds to completely failed bonds. It can be seen that bonds slip throughout the network, but the completely failed bonds tend to be concentrated along a localized fracture zone. Maximum load is reached after 39 steps. At this point, 210 bonds have been modified and one has reached final failure. This first final failure corresponds to maximum load, and reveals that the stress-strain relationship begins to show sawtooth behaviour. After 95 steps, 380 bonds have been modified, and 53 have failed completely.

Figure 9.33 shows the bonds that fail while the stress is increasing (first row), and the bonds that fail while the stress is decreasing (second row). Although the side of the square, 4.2 mm, is only 1.5 times the distance between the end-points of the longest fibres, 2.8 mm, there is a weak tendency towards localization.

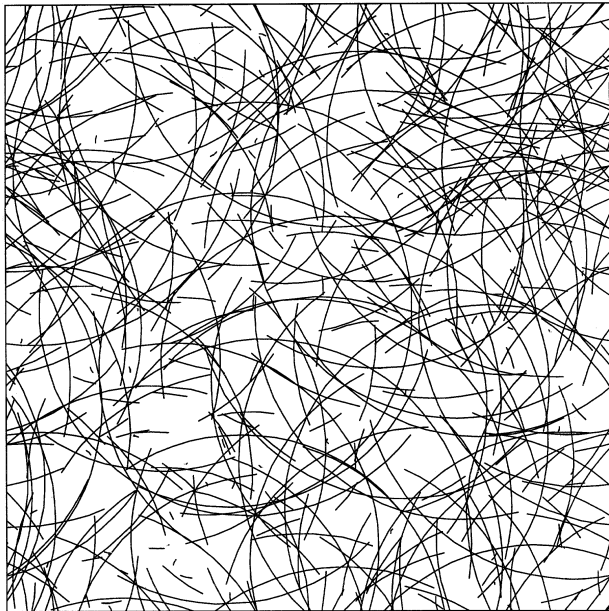


Figure 9.30: *Complex 2D example network geometry.*

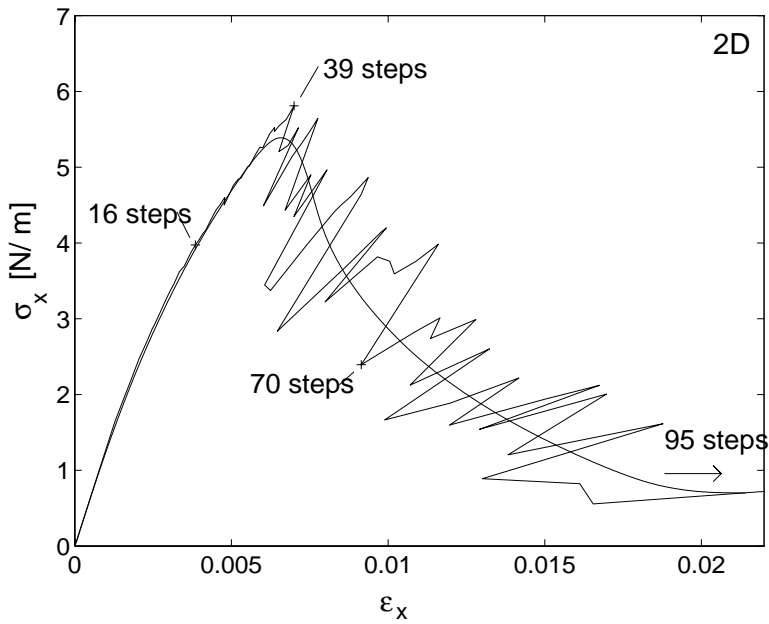


Figure 9.31: *Stress-strain relationship of the complex 2D example network.*

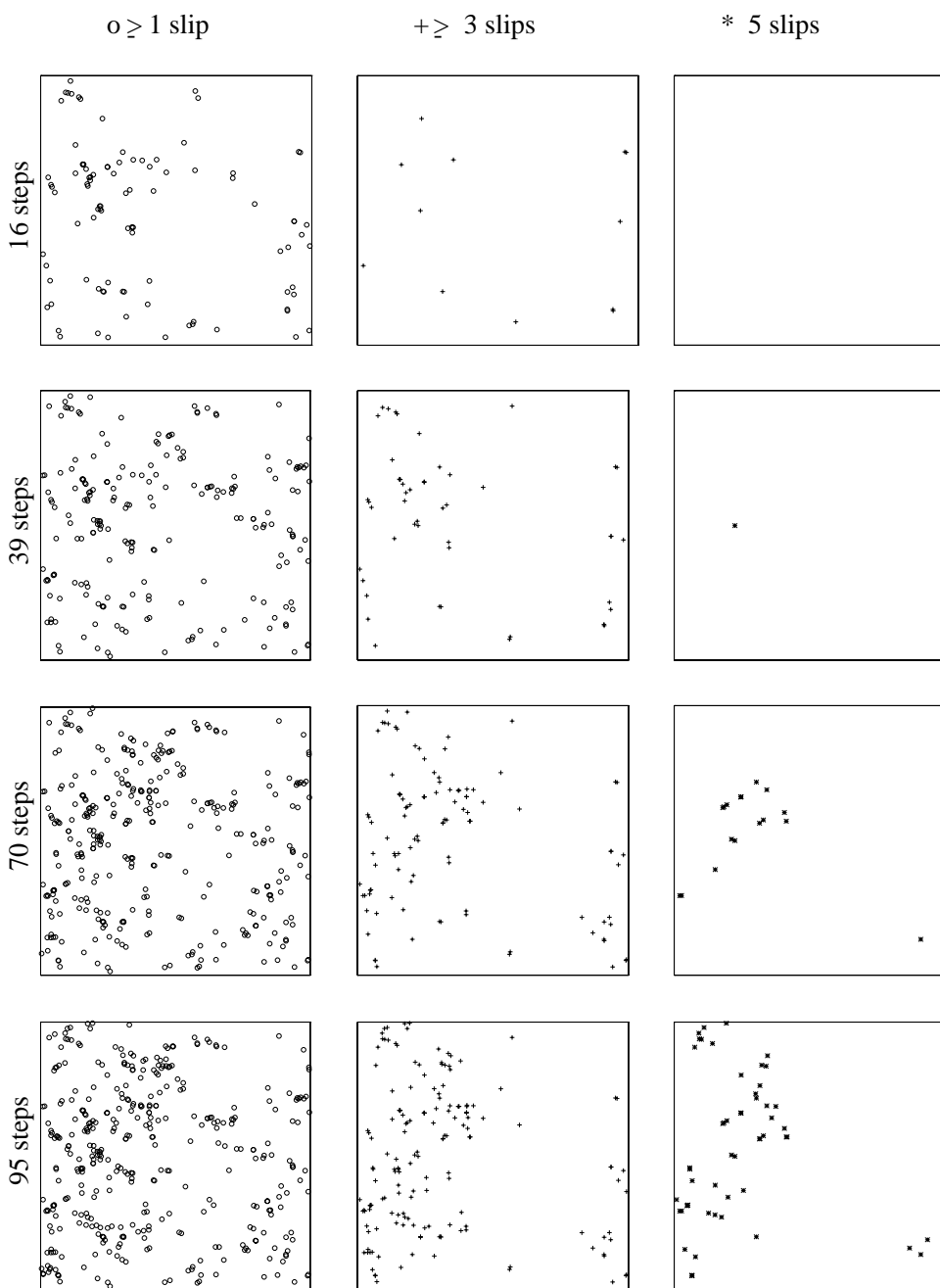


Figure 9.32: Location of failed bonds after 16, 39, 70 and 95 steps.

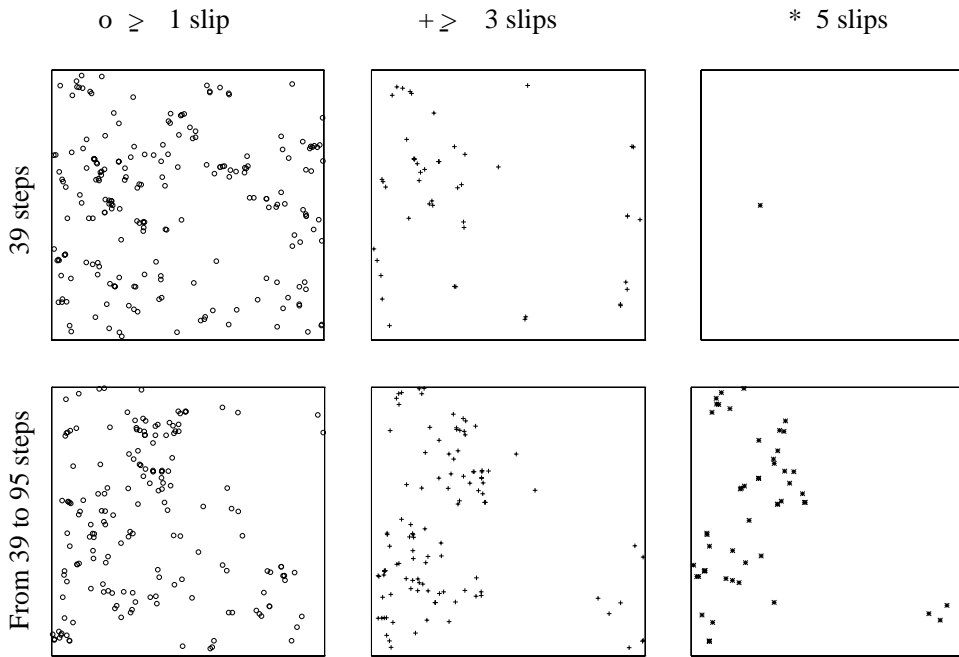


Figure 9.33: Location of failed bonds on the ascending and descending parts of the stress-strain curve.

## 9.2. Fracture in 3D networks

### 9.2.1. Influence of network density

The influence of network density on the fracture behaviour of 3D networks has been examined by simulating a series of networks of densities  $\rho=75, 87.5, 100, 112.5, 125$  and  $137.5 \text{ mm}^{-2}$ . Apart from network density, the other properties of the networks correspond to those of the 3D fracture example network. To reduce the computational time, five bonds were allowed to slip in each step. Five simulations were made for each value of network density, and the averages of the results are given in the following figures. The stress-strain relationships for the different densities are all given in Figure 9.34. Hand-drawn approximations have been used, according to the principle described in Section 9.1.3. As  $\rho$  increases, the networks become stronger, they reach maximum stress at a lower strain and the curves show a steeper descent after maximum load. The change in the stress-strain curves as network density increases is similar to that for 2D networks, Figure 9.26, except that the tendency towards reaching maximum stress at a lower strain for higher density is stronger for 3D networks. The maximum stress and fracture energy are plotted

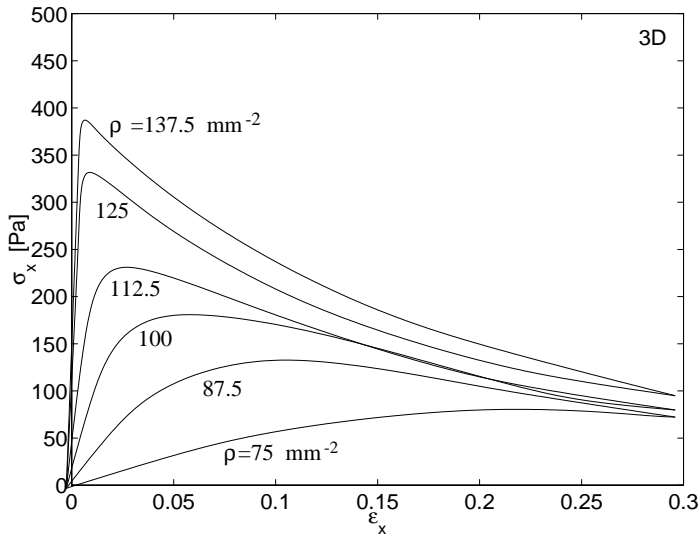


Figure 9.34: *Stress-strain relationship for different densities.*

against  $\rho$  in Figures 9.35 and 9.36. When the fracture energy was calculated, the part of the stress-strain curve where the strain exceeded 1.0 was disregarded, in order to avoid the influence of the last points where the results were deemed unreliable.

From Figure 9.37 it is clear that for the networks simulated here, the maximum stress divided by the initial stiffness is not independent of network density, as was the case for the 2D networks (Figure 9.29). The average free fibre segment lengths

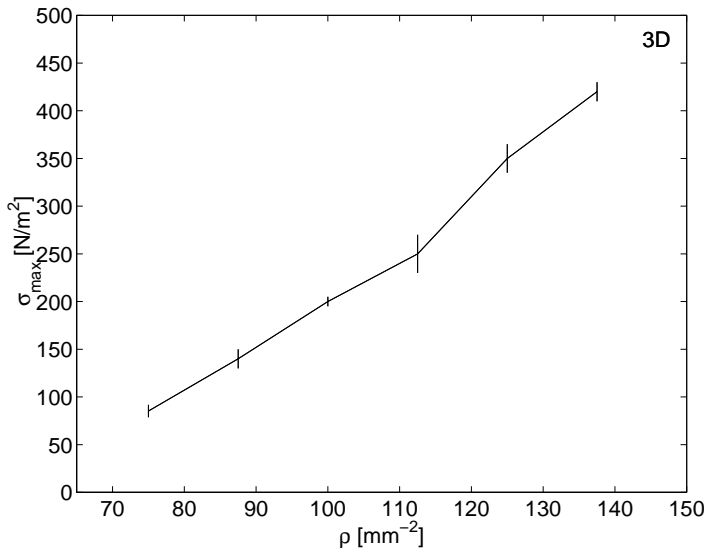


Figure 9.35: Maximum stress plotted against  $\rho$ .

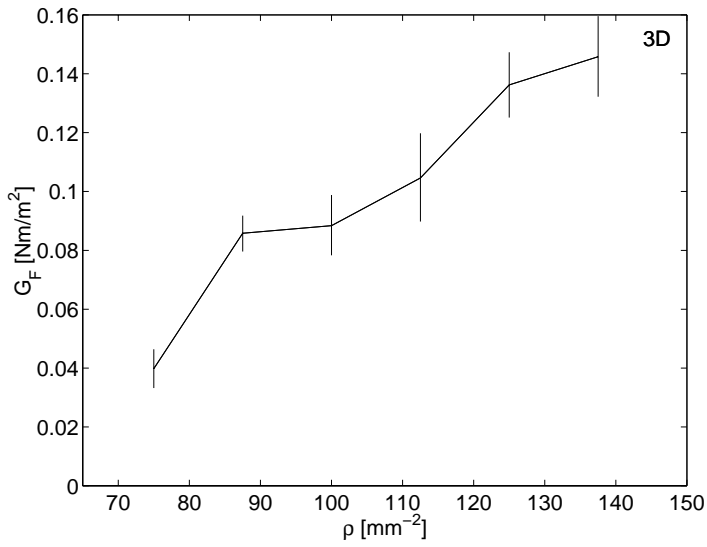


Figure 9.36: Fracture energy plotted against  $\rho$ .

are, however, different for the 2D and 3D networks. For the 2D networks simulated in Section 9.1.4, the average free fibre segment length varied from 0.18 to 0.08 mm and for the 3D networks the corresponding values ranged from 0.42 to 0.23 mm. For the two highest densities in Figure 9.37 the values of  $\sigma_{max}/(\sigma_x/\epsilon_x)_0$  are almost the same, indicating that the constancy of  $\sigma_{max}/(\sigma_x/\epsilon_x)_0$  with respect to density is not valid for densities close to the percolation threshold.

In Table 9.6 the computational results for initial stiffness, strength, fracture energy and characteristic length are given numerically. It is interesting to note that the the intrinsic material length parameter,  $l_{ch}$ , here increases with density, as opposed to the 2D simulation results of Table 9.4. As for  $\sigma_{max}/(\sigma_x/\epsilon_x)_0$ , the difference in the values for the two highest densities is small. The fact that the dependence of  $l_{ch}$  on  $\rho$  differs from that of 2D networks may be due to the larger free fibre segment length.

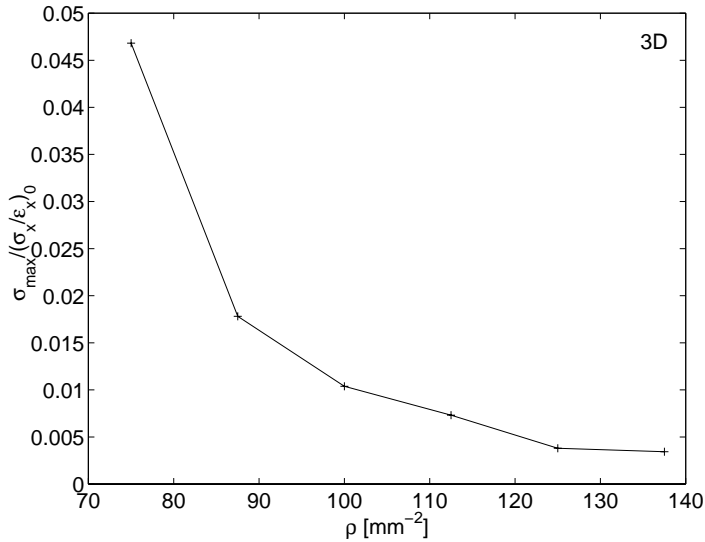


Figure 9.37: *Maximum stress divided by initial stiffness, plotted against  $\rho$ .*

### 9.2.2. Influence of fibre orientation

Simulations were made to investigate the influence of the orientation distribution of the fibres on the fracture behaviour of the network. It was previously concluded, in Section 5.2, that the fibre orientation distribution does not have much influence on the number of bonds. Results in Section 7.5 showed that both the in-plane and out-of-plane initial stiffness increase when the network becomes more planar. This section presents results from fracture simulations performed on networks with  $L_z/L_x$  ratios of 1.0 and 0.8, i.e., networks similar to the first two networks in Figure 7.29.

Table 9.6: Average and coefficient of variation, (c.o.v.), of material properties at different densities.

$\rho$ [mm <sup>-2</sup> ]	$(\sigma_x/\epsilon_x)_0$ [Pa]		$\sigma_{max}$ [Pa]		$G_F$ [Nm/m <sup>2</sup> ]		$l_{ch}$ [m]	
	Average	c.o.v.	Av.	c.o.v.	Average	c.o.v.	Average	c.o.v.
75.0	1820	0.27	85	0.15	0.0390	0.34	$9.9 \cdot 10^{-3}$	0.34
87.5	7860	0.25	140	0.14	0.0858	0.14	$32 \cdot 10^{-3}$	0.31
100.0	19300	0.12	200	0.06	0.0886	0.23	$41 \cdot 10^{-3}$	0.21
112.5	34200	0.27	250	0.17	0.1050	0.28	$59 \cdot 10^{-3}$	0.34
125.0	92000	0.22	350	0.10	0.1360	0.16	$100 \cdot 10^{-3}$	0.25
137.5	122000	0.06	420	0.06	0.1460	0.19	$100 \cdot 10^{-3}$	0.13

Networks with smaller  $L_z/L_x$  ratios have not been simulated since the number of degrees of freedom increases rapidly as the network is compressed. The only input parameters which differ from the 3D basic fracture example network are  $L_z$  and the distribution of  $\beta$  for the networks where  $L_z/L_x=0.8$ . In this case  $\beta$  is distributed according to (7.3). Five networks for each  $L_z/L_x$  ratio were simulated and were subjected to uniaxial tension in the  $x$ -,  $y$ - and  $z$ -directions, each simulation starting from an undamaged network. Five bonds were allowed to slip in each step. When the fracture energy was calculated the part of the stress-strain curve where the strain exceeded 1.0 was disregarded, as in the above.

The results from the simulations are shown in Figure 9.38 and Table 9.7. The values of  $\sigma_{max}$ ,  $G_f$  and  $l_{ch}$  for the  $L_z/L_x=1.0$  networks are approximately equal for uniaxial strain in the  $x$ -,  $y$ - and  $z$ -directions, as is expected since the orientation distribution is uniform. The limit strain, however, is more scattered. Since the results are approximately equal, the stress-strain curves representing uniaxial strain in the three different directions are plotted as one curve in Figure 9.38. For the networks where  $L_z/L_x=0.8$ , the same applies to strain in the  $x$ - and  $y$ -directions, and these results are presented as one curve in Figure 9.38. Straining in the  $z$ -direction gives, however, different results and is represented by the middle curve in the figure.

When the same number of fibres form a network in a cell of smaller height, and the fibres have a stronger tendency to be oriented in a plane, more bonds are formed and the free fibre segments become shorter. This gives an effect on the stress-strain curve similar to that of higher network density, where the maximum stress is higher and is reached at a lower level of strain. The  $L_z/L_x=0.8$  networks also become stronger for strain in the  $z$ -direction, indicating that the effect of shorter fibre segments is more important than the fact that fewer fibres are oriented in the  $z$ -direction, as was also the case for initial stiffness. From Table 9.7 it is not possible to make a distinction between the in-plane and out-of-plane directions for the values of  $G_f$  and  $l_{ch}$  for  $L_z/L_x=0.8$ , but the difference in the stress-strain curve can be seen clearly in Figure 9.38.

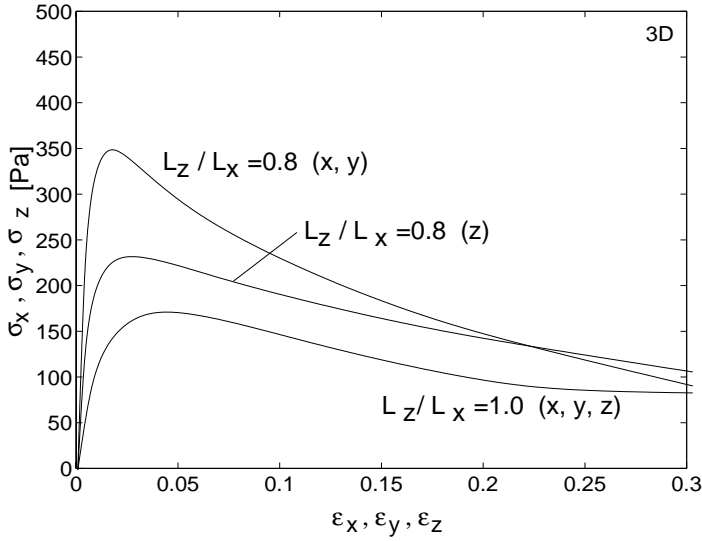


Figure 9.38: Stress-strain relationship for networks with different values of  $L_z/L_x$  and strain in different directions.

Table 9.7: Average and coefficient of variation, (c.o.v.), of material properties for networks with different values of  $L_z/L_x$  and strain in different directions.

$L_z/L_x$	Dir.	$\sigma_{max}$ [Pa]		$\epsilon_{lim}$		$G_F$ [Nm/m <sup>2</sup> ]		$l_{ch}$ [m]	
		Av.	c.o.v.	Average	c.o.v.	Average	c.o.v.	Average	c.o.v.
1.0	$x$	200	0.06	0.047	0.68	0.089	0.23	0.041	0.21
1.0	$y$	180	0.07	0.040	0.68	0.091	0.17	0.051	0.42
1.0	$z$	210	0.05	0.048	0.74	0.113	0.26	0.049	0.20
0.8	$x$	400	0.06	0.012	0.42	0.141	0.26	0.091	0.23
0.8	$y$	370	0.16	0.021	0.71	0.135	0.22	0.101	0.21
0.8	$z$	270	0.06	0.019	0.45	0.152	0.28	0.088	0.27

### 9.2.3. Influence of properties of bonds

The stiffness and strength properties of the bonds have influence on the fracture of a network. The conclusions reached without any simulations in Section 9.1.3 are valid also for 3D networks. That is, if  $E_f$ ,  $G_f$ ,  $k_n$  and  $k_t$  are divided by a constant, network strain is multiplied by the same constant but the stress is unaffected, see Figure 9.15b. If  $\sigma_{adh}$  is multiplied by a constant both stress and strain are multiplied by the same constant, as in Figure 9.15a. To obtain the effect on the stress-strain

curve for the case when only bond stiffness is changed, simulations are, however, necessary. Figure 9.39 shows results from simulations on one single network where the bond stiffness values,  $k_n$  and  $k_t$ , were as in the 3D basic fracture example network, 1/10 of these values and 1/100 of these values. The network density was  $125 \text{ mm}^{-2}$  and the fibre curl was set to 0.84. The curves in the figure are hand-drawn approxi-

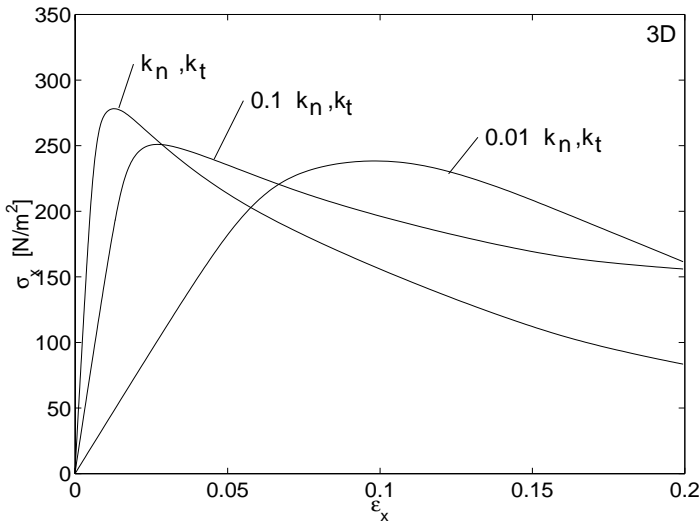


Figure 9.39: *Stress-strain relationships for different values of bond stiffness.*

mations. A lower bond stiffness gives as expected a less stiff network. The limit strain increase as bond stiffness decreases, and there is also a small decrease in maximum stress.

In the 2D networks the bond ductility had considerable influence on the stress-strain relationship. This was not found for the 3D networks. The bonds were assumed to be ductile only in compression. In the simulations, where the networks were subjected to uniaxial tension, almost all the bonds failed in tension, and thus in a brittle manner. Because of this, there was no noticeable effect of bond ductility in 3D. Figure 9.40 shows an example of the stress distribution in the bond elements in the first computational step, for a network with input parameters as in the 3D fracture example network. The stress state for each bond is indicated by '+', in the  $\sigma_n$ - $\tau$  plane. The total number of bonds was 1216, and five of them were allowed to slip in the first step. For those five bonds a circle is added around the '+'. The fracture criterion is also illustrated in the figure. The average degree of utilisation for the five elements for unit uniaxial strain was 200, giving a strain value of 0.005 for the first point on the stress-strain curve.

One problem with the bond model used is that a bond can sustain an arbitrarily large load in compression. In particular for networks of highly curled fibres there

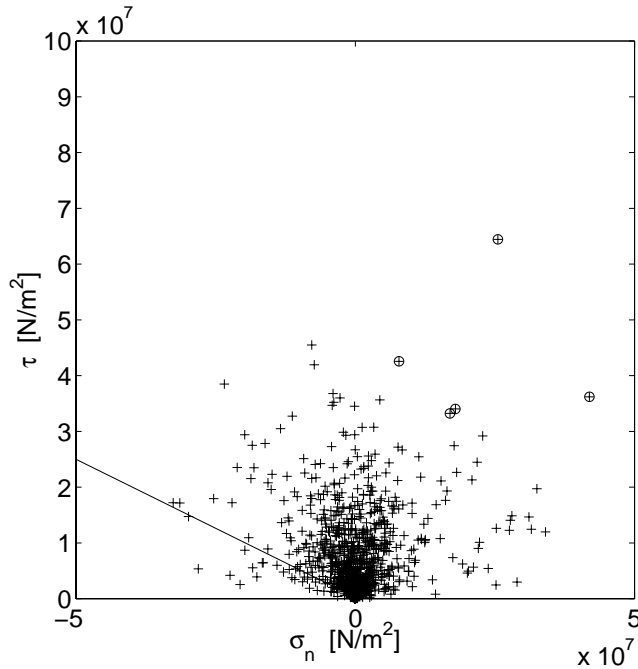


Figure 9.40: *Stress distribution in the bonds for the first step.*

is the risk that when the network is almost failed, a structure consisting of curled fibres hooked into each other around the cell remains. In a real fluff this would lead to large deformations in the fibres, finally causing tension and fracture in the bonds. In the small displacement computational model the forces are, however, always calculated from the original geometry. One approximate way of taking the real process into account would be to define a compressive fracture stress for the bonds.

#### 9.2.4. Influence of fibre length

The fibre length distribution was found to have a considerable influence on the elastic stiffness. The influence of fibre length on the fracture behaviour was also examined. The basis of the simulations is the cumulative population distribution of fibre length, shown in Figure 9.41. This distribution was constructed to fit the values of arithmetic and weighted mean fibre lengths which were measured for the pulp described in Section 9.2.5. The arithmetic mean fibre length of the pulp was 1.4 mm and the length-weighted mean fibre length was 2.3 mm. Since it is desirable to keep the maximum fibre length low, and thereby the cell size and number of degrees of freedom, the distribution was constructed so that the maximum fibre

length was 4 mm. To compensate for the longest fibres in the pulp, 6% of the fibres was given a length of 4 mm. Simulations were performed for a network density of  $125 \text{ mm}^{-2}$  for six different fibre length distributions; constant fibre lengths of 1.0 mm, 1.4 mm and 2.3 mm, the length distribution of Figure 9.41 and length distributions where all the fibre lengths from the distribution in Figure 9.41 were divided by two and three respectively. The two latter distributions approximately take account of shorter effective fibre length due to kinks. The other input parameters were as in the 3D fracture example network. Three networks were simulated for each length distribution, except for the latter two, for which only two simulations were carried out. Eight bonds were allowed to slip in each step. In these simulations the longest fibres were twice the cell length. This may cause problems, such as a false simulation-induced increase in network stiffness. It was, however, not possible to increase the cell size due to lack of computer capacity.

Figure 9.42 shows the stress-strain relationships for the six different length distributions and Table 9.8 gives the numerical values of maximum stress, limit strain, fracture energy and characteristic length. For the three constant fibre lengths, it is clear that longer fibres give a stronger network and a lower value of limit strain. The stress-strain curve for networks with a fibre length distribution as in Figure 9.41 lies between the curves for 1.4 and 2.3 mm fibres, i.e., if this fibre length distribution is to be represented by one constant fibre length, a value between the mean and weighted mean value should be used. It is interesting to note that the curve for 2.3 mm fibres lies above the curve for distributed fibre length, implying that more is lost with the shorter fibres than is gained with the longer fibres in the distribution. The curves for 1 mm fibres and the network in which the fibre lengths in Figure 9.41 were divided by two are difficult to separate, one difference being, however, that the limit strain is higher for the 1 mm fibre network. This conclusion is unfortunately unreliable due to the large scattering of the limit strain results. Figure 9.43 shows maximum stress as a function of fibre length for the three constant fibre lengths. For the case simulated there is direct proportionality between maximum stress and fibre length. The limit strain as a function of fibre length, shown in Figure 9.44, is decreasing, but not linearly.

Table 9.8: Average and coefficient of variation, (c.o.v.), of material properties for networks with different fibre length distributions. A: fibre lengths as in Figure 9.41. B: fibre lengths as in Figure 9.41, divided by two. C: fibre lengths as in Figure 9.41, divided by three.

$l_f$ [mm]	$\sigma_{max}$ [Pa]		$\epsilon_{lim}$		$G_F$ [Nm/m <sup>2</sup> ]		$l_{ch}$ [m]	
	Average	c.o.v.	Average	c.o.v.	Average	c.o.v.	Average	c.o.v.
2.3	970	0.10	0.002	0.25	0.28	0.26	0.41	0.27
1.4	530	0.05	0.006	0.18	0.21	0.31	0.22	0.33
1.0	320	0.35	0.015	0.75	0.14	0.34	0.11	0.13
A	720	0.09	0.002	0.38	0.21	0.39	0.30	0.58
B	330	0.12	0.010	0.71	0.13	0.04	0.12	0.22
C	190	0	0.044	0.51	0.053	0.08	0.025	0.18

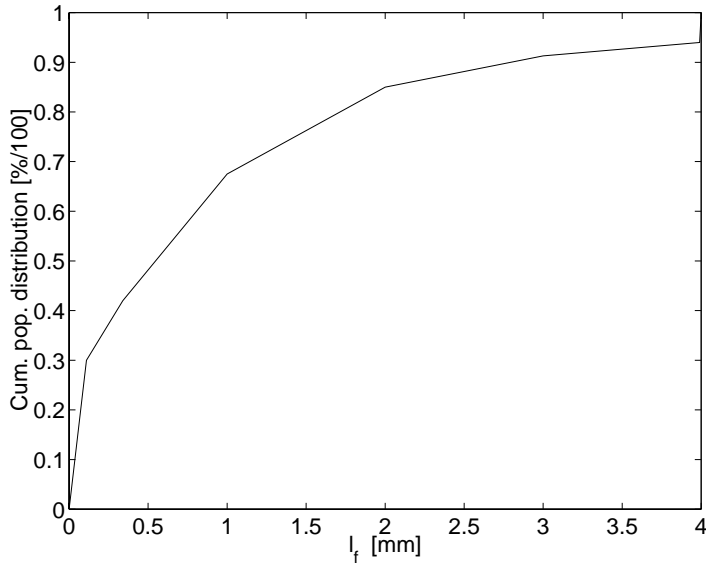


Figure 9.41: Cumulative population distribution of  $l_f$ .

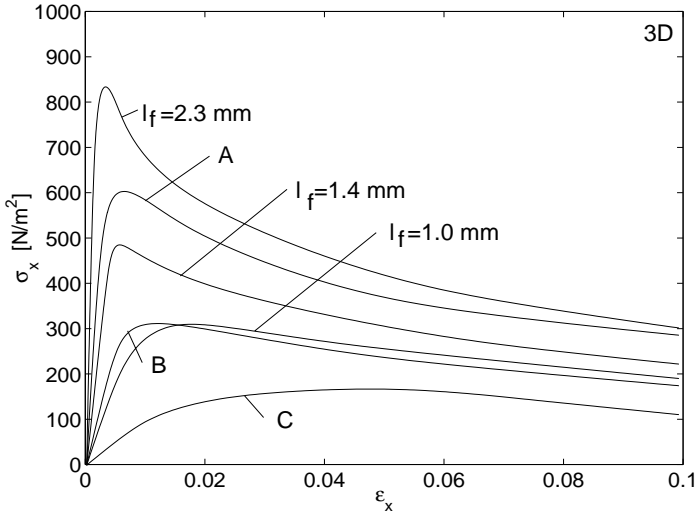


Figure 9.42: Stress-strain relationship for different fibre length distributions. A: fibre lengths as in Figure 9.41. B: fibre lengths as in Figure 9.41, divided by two. C: fibre lengths as in Figure 9.41, divided by three.

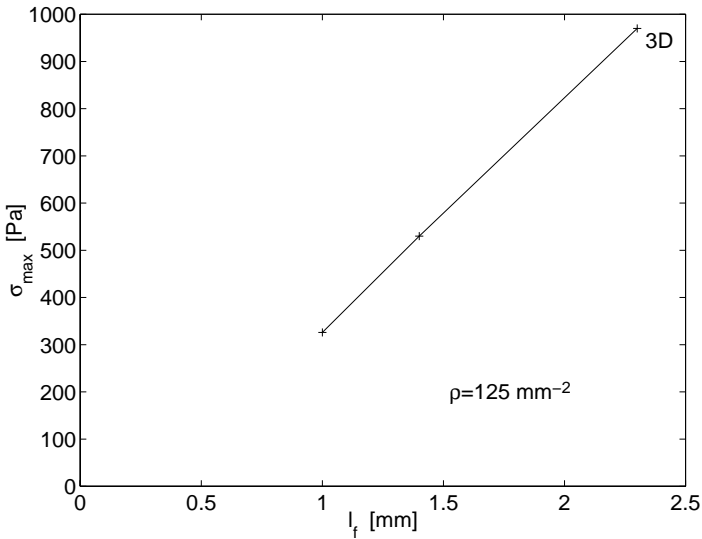


Figure 9.43: Maximum stress for different constant fibre lengths.

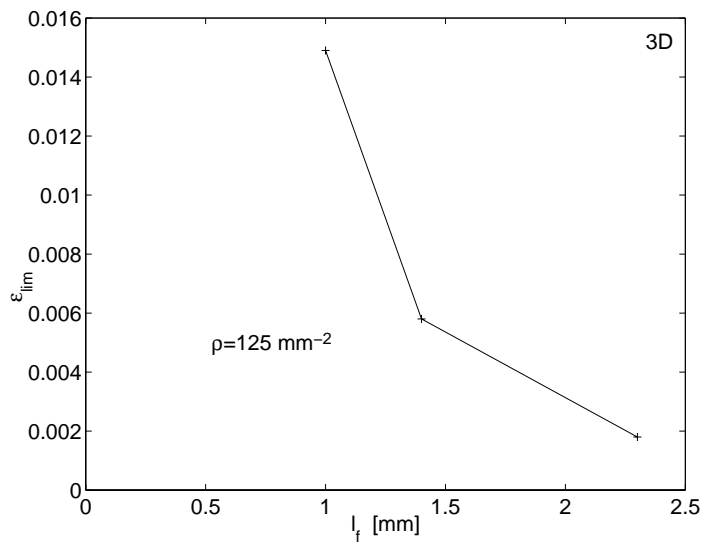


Figure 9.44: *Limit strain for different constant fibre lengths.*

### 9.2.5. Comparison with experimental results

To evaluate the accuracy of the model and to study the calibration of input data for a specific material, simulation results were compared with experimental results from tests on a fluff material. The tests were performed by SCA Research [56]. The chemical pulp used for the fluff specimens was geometrically characterized by the STFI-Fibermaster. The arithmetic mean fibre length was 1.4 mm and the weighted mean fibre length was 2.3 mm. On calculating these mean fibre lengths, fibres shorter than 0.11 mm were disregarded. The arithmetic mean value for fibre curl was 0.88, and the length-weighted value was 0.84. There were on average about 3 kinks per fibre. The width and length of the specimens were both 80 mm, and the test span was 60 mm. The average bulk of the specimens was 20.2 g/cm<sup>3</sup> and the specimens were strained at a constant speed of 1 mm/s. Figure 9.48 shows ten measured stress-strain curves.

A network cell of size 2x2x2 mm<sup>3</sup> with properties similar to the tested fluff was simulated. The length distribution illustrated in Figure 9.41 corresponds to the mean and weighted mean values of the fibre length of the tested fluff. On assuming the density of the fibre material to be 1600 kg/m<sup>3</sup> and using the fibre cross-sectional area of the basic example networks a bulk value of 20.2 g/cm<sup>3</sup> gives a network density of 125 mm<sup>-2</sup>. The length-weighted mean value of fibre curl,  $c=0.84$ , was chosen for the simulations. With the input values above, and values from the 3D fracture example network for the other parameters, the stress-strain curve shown in Figure 9.45 was obtained. In this simulation only one bond was allowed to slip in each step, which explains the saw-tooth appearance. It is obvious that the maximum stress is reached at a very low strain compared with the experimental results; about 0.3% compared with 8%.

In Section 9.2.1 it was shown that a lower network density gives maximum stress at a higher strain. This network density effect can also be obtained by changing the interaction distance,  $e$ , or the degree of interaction,  $s$ . It doesn't, however, appear to be realistic to change either of these parameters, from a physical point of view. The limit strain is also affected by the stiffnesses of the components of the network. If, for example,  $E_f$ ,  $G_f$ ,  $k_n$  and  $k_t$  were to be decreased by a factor of ten, the strain at maximum stress would be increased by a factor of ten. The values of  $E_f$  and  $G_f$  are believed to be fairly well known and accurate, and there should, thus, not be a need for calibration of these parameters. The values of  $k_n$  and  $k_t$ , are on the other hand only crude estimates. From Section 9.2.3 it can be seen that a decrease in only  $k_n$  and  $k_t$  changes the simulated stress-strain curve towards the experimental curve, but the values of  $k_n$  and  $k_t$  alone can hardly explain the deviation.

A parameter which has influence on the limit strain is the fibre length distribution. The results in Section 9.2.4 show that longer fibres give a distinct increase in maximum stress and a decrease in limit strain. A possible explanation of the discrepancy between Figures 9.45 and 9.48 is that a typical fibre acts as several shorter fibres from a mechanical point of view, due to kinks. Figure 9.47 shows results from simulations where all the fibres were assumed to be 1.1 mm long. The bond stiffness

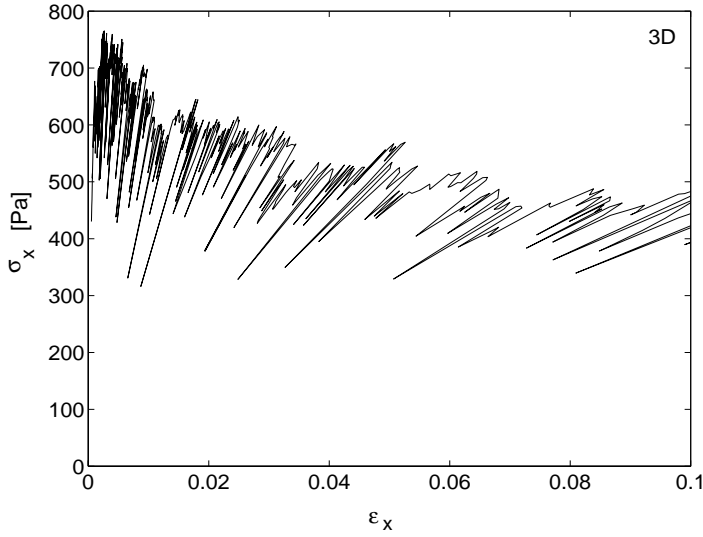


Figure 9.45: *Stress-strain relationship for a network with fibre lengths according to Figure 9.41,  $c=0.84$  and  $\rho=125 \text{ mm}^{-2}$ .*

values were set to  $k_n = 3.0 \cdot 10^{11} \text{ Pa/m}$  and  $k_t = 3.0 \cdot 10^{10} \text{ Pa/m}$  and  $\sigma_{adh}$  was set to  $6.5 \cdot 10^5 \text{ Pa}$ . All input values are given in Table 9.9 and Figure 9.46 shows an example of a simulated network geometry. For this case, the simulated values of maximum stress and limit strain are close to the experimental ones, see Table 9.10. The experimental values are averages from 25 tests, and not only from the ten tests for which the stress-strain curves are shown in Figure 9.48. Handdrawn approximations of the average stress-strain curves from experiments and simulations, respectively, are given in Figure 9.49. The strains are quite large in these simulations, probably making small displacement theory unreliable for the largest strains.

The post-peak parts of the curves can not be compared directly, due to the different specimen sizes. The test specimen is  $60 \times 80 \times 9 \text{ mm}^3$ , corresponding to 30 serially coupled elements of 180 cells coupled in parallel, in total 5400 simulated cells. When the load on the test specimen decreases, most of the specimen contracts while a fracture zone expands. In the simulated cell, most of the cell can be regarded as a fracture zone and it is therefore not relevant to compare the strain for the two cases.

The average strain at fracture, which was defined to occur at 50% of maximum load in the experiments was 14%, corresponding to 8.4 mm elongation. If the fracture zone is assumed to be 2 mm wide, and the irreversible strain outside the fracture zone is estimated to be roughly 2%, corresponding to 1.16 mm elongation, the elongation of the fracture zone is 7.24 mm, corresponding to a strain of 360%. This reasoning would have been more relevant if the experiment had been carried out

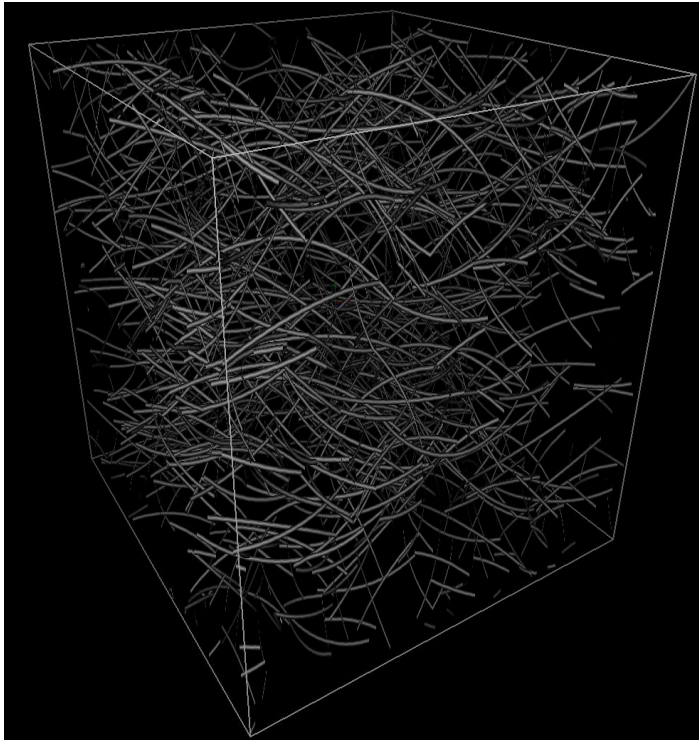
on a specimen corresponding to 30 simulated cells in a row. The fracture process would then probably have been more brittle giving a smaller strain in the fracture zone. When many cells are coupled in parallel, there is a redistribution of load from weaker to stronger zones giving a more ductile fracture with a higher fracture strain.

Table 9.9: *Input parameters for simulations that were compared with experiments.*

Parameter	Value and unit
$l_f$	1.1 mm
$c$	0.84
$A_f$	$2.5 \cdot 10^{-10} \text{ m}^2$
$I_f, J_{zf}$	$2.0 \cdot 10^{-21} \text{ m}^4$
$J_{yjf}$	$2.0 \cdot 10^{-21} \text{ m}^4$
$K_{vf}$	$3.5 \cdot 10^{-20} \text{ m}^4$
$E_f$	$35 \cdot 10^9 \text{ Pa}$
$G_f$	$2.6 \cdot 10^9 \text{ Pa}$
$A_b$	$3.1 \cdot 10^{-10} \text{ m}^2$
$k_n$	$3.0 \cdot 10^{11} \text{ Pa/m}$
$k_t$	$3.0 \cdot 10^{10} \text{ Pa/m}$
$\sigma_{adh}$	$6.5 \cdot 10^5 \text{ Pa}$
$\mu$	0.5
$n_s$	1
$\lambda_1$	1.0
$\lambda_2$	1.0
$\lambda_3$	1.0
$L_x, L_y, L_z$	2 mm
$\rho$	$125 \text{ mm}^{-2}$
$N_\alpha$	$\frac{1}{\pi}, \quad 0 < \alpha < \pi$
$N_\beta$	$\cos \beta, \quad 0 < \beta < \frac{\pi}{2}$
$N_\gamma$	$\frac{1}{\pi}, \quad 0 < \gamma < \pi$
$e$	$20 \cdot 10^{-6} \text{ m}$
$s$	1.0
$V_h$	$8.0 \text{ mm}^3$

Table 9.10: *Maximum stress and limit strain from experiments and simulations.*

	$\sigma_{max}$ [Pa]	$\epsilon_{lim}$
Experiments	520	0.075
Simulations	500	0.077

Figure 9.46: *Example of network with input as in Table 9.9.*

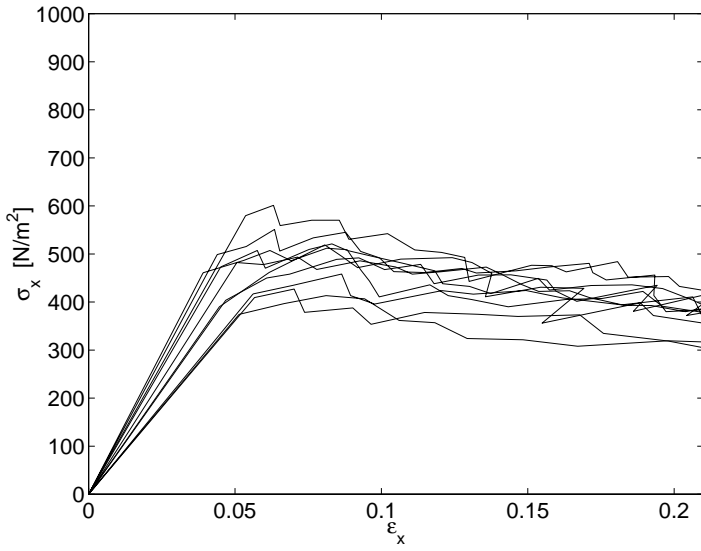


Figure 9.47: *Stress-strain curves for cellulose fibre fluff obtained from simulations.*

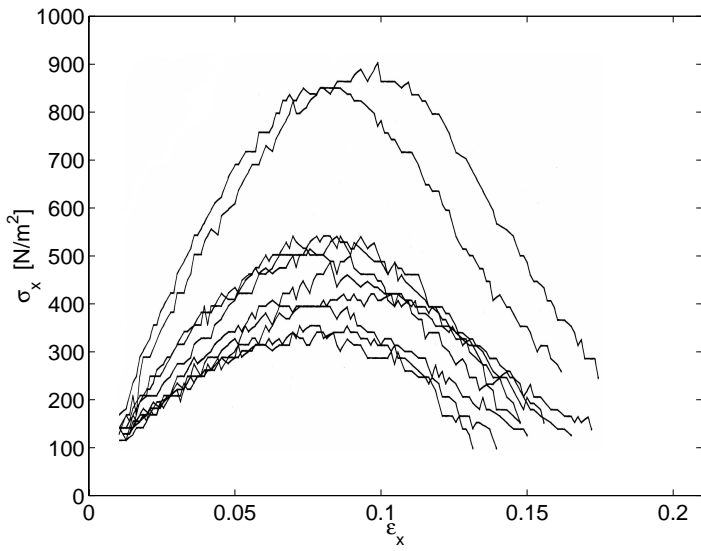


Figure 9.48: *Stress-strain curves for cellulose fibre fluff obtained from experiments.*

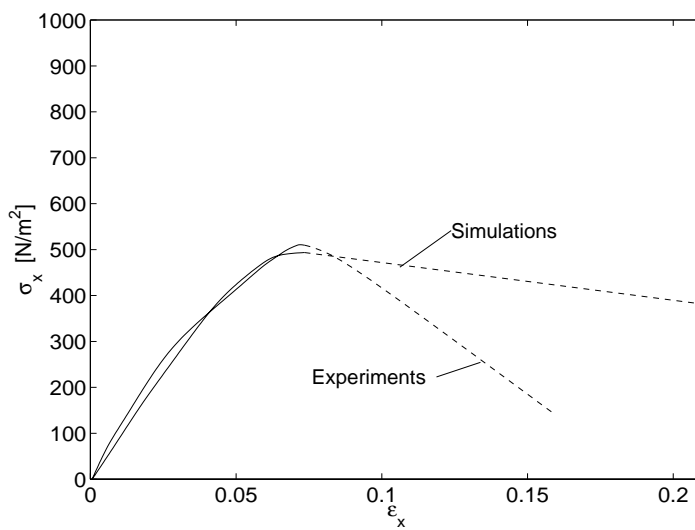


Figure 9.49: Average stress-strain curves for cellulose fibre fluff obtained from experiments and simulations.



## 10. NUMERICAL CONSIDERATIONS

When numerical simulations are performed some computer-related issues must be dealt with. Firstly, it must be established that the correct solution to the problem is obtained. For example, an ill-conditioned system matrix can arise in several ways. This must be prevented since it often causes erroneous results. A correct solution is, however, not sufficient. It is also desirable to have as short a computational time as possible, to be able to perform as many and as extensive simulations as possible, given limited computer resources.

### 10.1. Correctness of solutions

The system stiffness matrix can become ill conditioned if there is a large difference in magnitude between the coefficients in the matrix. This problem may arise from differences in stiffness between the different components of the network or extremely short beam elements.

The character of a dry-shaped cellulose fibre material is in general such that the inter-fibre bonds are much weaker than the fibres, and the fibres themselves are weaker in bending than in axial deformation. The differences in stiffness are, however, not so great that we can disregard the deformation of the stiffer components by, for example, considering the fibres to be rigid, or rigid in the axial direction. This means that we have a system of equations in which the coefficients are of various orders of magnitude, which implies numerical problems in the solution procedure. This problem is further emphasized by the fact that we often want to perform parameter studies over wide ranges of the various material properties. To reduce the effects of these phenomena, the coefficients of the stiffness matrix were rescaled. By rescaling the dimension of length, a better-conditioned system matrix can often be achieved, as is exemplified in [20].

Extremely short beam elements can also cause numerical problems. Since the fibres are independently positioned when the network is generated, it is possible for the distance between two bond sites on a fibre to be arbitrarily short. Since beam length is raised to the power three in the denominator of the beam stiffness matrix, these coefficients become extremely large and may cause numerical problems. In studies where the bonds are assumed to be rigid, e.g. [3, 22], this problem has been overcome by merging two closely neighboring bonds into one. The use of this method is, however, not straightforward when the bond is represented by a compliant element. Instead, the beam is slightly modified by moving one of its nodes a short distance. This is also physically reasonable, since the centres of two

fibres cannot be closer to each other than one fibre width. In most of the 3D simulations a bond was moved a distance equal to  $1/5000$  of the mean fibre length if a beam element was shorter than  $1/5000$  of the mean fibre length. In the 2D simulations beams which were shorter than  $1/100$  of the mean fibre segment length were modified by moving one end a distance equal to  $1/10$  of the mean fibre segment length. This causes a slight distortion of this fibre, as well as of the fibre connected at the displaced node. The short fibre segments occur relatively often in pairs or triplets, in the form of triangles, in which case the local distortion of the network becomes somewhat greater. This is, however, not believed to have an appreciable effect on the final solution since the distortion is very local and occurs quite rarely, and in 3D networks very rarely.

## 10.2. Speed of simulations

The software used for the 2D simulations consisted of a Fortran code for the generation of the network geometry and Matlab/Calfem, [37, 9], routines for the FEM analysis. For the 3D simulations Matlab was used for both network generation and FEM analysis. Matlab was chosen because of its flexibility and because code can be generated and debugged quickly. Matlab is, however, not known for high-speed performance, and some weak points had to be dealt with.

One time-consuming part of the program is the detection of bond sites in three dimensions. The complexity of the problem increases as the square of the number of fibres, making it very important that what must be done very many times does not take too long a time. Matlab Compiler [38], was used to produce C code for this subroutine. Matlab Compiler is most efficient for code using real scalars and many loops. The code for the detection of connections does not contain many loops, but does contain many trigonometric functions which leads to time-consuming call-backs to Matlab from the C code. However, the compiled code performs better than the original one, and contributes to making the detection of bonds feasible.

Another problem is the assembling of element stiffness matrices into the sparse global stiffness matrix. Here, the problems are not caused by the inherent properties of the assembling process itself, but rather by Matlab's inefficient way of expanding sparse matrices when assembling is performed in a straightforward manner. This problem was overcome by using an improved assembling method which creates vectors containing all the information on the positions and values of the elements of the stiffness matrix. The contributions from all the elements are then entered into the stiffness matrix in one single operation, which is much faster than entering them one by one but, on the other hand, requires more memory.

The solution of the sparse system of equations is also time-consuming for large systems. Instead of using the standard Matlab sparse solver, a direct solver provided by SGI, which was optimized for the hardware used, was utilized.

# 11. CONCLUDING REMARKS

## 11.1. Summary and conclusions

A network mechanics model for describing dry-shaped materials made of cellulose fibres has been proposed. 2D and 3D versions of the model have been implemented, and various parameter studies have been performed.

The network is composed of fibres, which are modelled as beams of constant curvature made of linear elastic material. Length, cross-sectional properties, curvature, elastic modulus and strength parameters for the fibres constituting the network are given in terms of arbitrary statistical distributions.

Where fibres cross there may be a fibre-fibre interaction. The inter-fibre bonds are modelled by an assembly of springs. Stiffness and strength properties of the bonds are given in terms of arbitrary statistical distributions, and the probability of a bond at a fibre crossing point is another input parameter. The bonds can be assigned linear or non-linear behaviour. The non-linear model corresponds to stick-slip performance in the bond.

The fibres are positioned at random in the cell, and oriented according to a statistical distribution. The network density is assigned a deterministic value for a cell of specified size and governs the number of fibres. The geometry is periodic, i.e., the cell under consideration is regarded as one of many identical cells making up a global structure of infinite size. Loading is applied by a set of cyclic boundary conditions such that each point on the boundary of a cell is in equilibrium with the corresponding point of the neighbouring cell. At the same time, geometric compatibility is achieved at each boundary point. In addition to this method of loading, the more conventional method where straight boundaries are assumed to remain straight was also implemented.

The geometric output parameters considered were the number of fibre crossings and the ratio that quantifies the mechanically active part of the network. It was verified that the number of crossings obtained from simulations agreed with the number predicted by a theoretical formula from the literature, except for the case of curled fibres where the formula fails, and a new one was given for the special case of arc-shaped curled fibres. For densities above the percolation point, the mechanically active part was found to be well-approximated by the part of the network that is not free fibre ends. This quantity is easily calculated using well-known equations.

A general concept for subjecting a cell with periodic geometry to a load and, through the use of a least-squares method obtaining the homogenized elastic parameters for an elastic material structure has been developed. The method is in-

dependent of the kind of heterogeneous material inside the cell, as long as it is of periodic structure, and was used to obtain the isotropic stiffness parameters  $E$  and  $\nu$ , as well as the corresponding transversely isotropic or orthotropic parameters for two- and three-dimensional elasticity.

Several simulations were performed in order to obtain the global elastic stiffness properties of a network. 2D and 3D example networks with representative properties were used, and the input parameters varied in order to elucidate their influence on global elastic stiffness.

Simulations show that the use of cyclic boundary conditions allows the simulation of smaller cells than does the use of conventional boundary conditions. For the case of constant fibre length, a cell length of 1.2 times the fibre length seems to be adequate to avoid a false, simulation-induced, size dependence of the initial stiffness. The conventional conditions with straight boundaries seem to give too high a network stiffness, even when the length of the cell is several times the length of a fibre.

The influence of the individual stiffness components on the global initial stiffness has been examined. It was found that the transversal spring stiffness was of greater importance than the rotational spring stiffness of the bonds in a 2D network and that the axial stiffness of straight fibres is more important than the bending stiffness. For 3D networks, the transversal spring stiffness had a stronger influence on the stiffness than the normal spring stiffness.

Simulations show that curled fibres give a less stiff network. For higher network densities this is, in the first place, due to the fibres not extending along a straight path with the bonds along a straight line. For lower network densities the smaller axial stiffness of curled beam segments is also of importance.

If there is a preferred orientation for the fibres, the network becomes stiffer in this direction. Simulations of networks of a constant number of fibres, ranging from an isotropic cube to a thin, transversely isotropic, almost planar network show that the in-plane stiffness increases as the network becomes more planar, but also that the out-of-plane stiffness increases, indicating that the effect of shorter free fibre segments is more important than that of fewer fibres being oriented in the out-of-plane direction.

With constant network density, long fibres give a stiffer network than short ones, and for a statistical distribution in length the weighted mean fibre length seems to be a more relevant parameter than the arithmetic mean fibre length.

A study of the influence of network density and the number of fibre-to-fibre interaction points on the homogenized stiffness properties shows that the elastic modulus rises rapidly with density, but Poisson's ratio is less affected.

Fracture criteria have been introduced and the non-linear fracture process of networks analysed. The fracture process has been quantified in terms of global stress versus strain performance, maximum stress, fracture energy, intrinsic length and localization of fracture.

Some results regarding sample size dependence of fracture properties have been given and a comparison made with Weibull theory. It could be concluded that the

result of a fracture simulation is always size-dependent, and that Weibull theory is not applicable due to assumptions concerning heterogeneity and material properties not being fulfilled.

The characteristics of fibre and bond failure have been investigated by simulating a 2D network. The failure of a fibre segment has a greater influence on the fracture process than the failure of a bond, since when bond failures are considered the fibres must be pulled out of the network. For dry-shaped materials containing no adhesive, bond failure is dominant.

In the case of bond failure, simulations have shown that increased strength of the bonds result in a stronger and more ductile network. For 2D networks ductile bonds gave a much stronger and more ductile network. For 3D networks the influence of bond ductility was, however, negligible since the bond was assumed to fail in a non-brittle manner only for compressive normal stress, and most of the bonds fail in tension when the network is subjected to uniaxial tension.

As for network density, a higher density gives a stronger but more brittle network for both 2D and 3D networks. Long fibres resulted in a stronger network for which the maximum stress was reached at a lower strain than for short fibres.

2D and 3D networks showed many qualitative similarities, but also some differences, the main one being that ductile bonds had a much greater influence on 2D networks. Some differences were probably caused by the fact that the simulated 2D networks generally had shorter free fibre segment lengths than the 3D networks.

For 3D networks it was possible to make a quantitative comparison with experimental results. When the fibre length distribution was adjusted to approximately account for a shorter effective fibre length due to kinks in the fibre, reasonable agreement was found between the simulated and experimental stress-strain relationships up to maximum stress. The post-peak parts of the curves require further analysis before a relevant comparison can be made, since the experiments were performed on a specimen that was much larger than the simulated cell. This means that the size effects due to strain localization and heterogeneity in the material must be taken into account.

## 11.2. Future developments

Possible future work on network mechanics models for cellulose fibre materials should include both further simulations within the present model and the development of new or completed models. Further simulations with the present model would involve the many variations of input data which have not yet been studied, and further simulations for the verification of the model and comparisons with experimental results. One parameter which could be given more attention is the degree of heterogeneity, and its influence on the mechanical properties of a network.

As for further development of the model, there are several possibilities. One of them is a new strategy for the generation of the network geometry. In the present model the fibres are positioned independently of each other. A more representative geometry would probably be obtained if the manufacturing process of fibres falling

and making contact with other fibres could be modelled. An alternative method might be to take the network geometry directly from experimental observations, if available. An, as yet, unexplored area is the effect of initial stresses in the network, originating from the manufacturing process. Initial stresses may very well be an important factor for the fibre-to-fibre interaction. Initial stresses might be obtained from more realistic geometry generation, or could be approximated by some modification of the bond model. The modelling of the fibres can be improved by considering kinks, which affect the fibre geometry and have low or zero bending stiffness. The results obtained with the present model suggest that defect zones in the fibre, which make a fibre act like separate fibres may be important for the mechanical behaviour of a network. The model could also be refined by including large-displacement theory and time-dependent effects, but it is believed that the modifications mentioned above would be of greater practical interest in the modelling of fluff.

## A. GENERATION OF FIBRES

The position, geometry and orientation of a fibre are given by the input variables  $\mathbf{m}$ ,  $l_f$ ,  $c$ ,  $\alpha$ ,  $\beta$  and  $\gamma$ , see Section 4.2. These variables are also defined in Table A.1.

Table A.1: *Input variables defining fibre position, geometry and orientation.*

$\mathbf{m}$	Coordinates for the mid-point of the fibre.
$l_f$	Length of the fibre.
$c$	Curl index of the fibre.
$\alpha$	The unit vector directed as the line between the end points of the fibre is denoted $\mathbf{d}$ . $\alpha$ is the angle between the projection of $\mathbf{d}$ onto the $xy$ -plane and the $x$ -axis.
$\beta$	$\beta$ is the angle between $\mathbf{d}$ and the $xy$ -plane.
$\gamma$	$\mathbf{s}$ is a unit vector that is perpendicular to $\mathbf{d}$ , and whose projection onto the $xy$ -plane is parallel to the $x$ -axis. $\gamma$ is the angle between $\mathbf{s}$ and the normal from $\mathbf{d}$ towards the fibre.

From the input variables, the variables suitable for computational purposes,  $\mathbf{c}$ ,  $r$ ,  $\theta_a$ ,  $\theta_b$ ,  $\mathbf{u}$  and  $\mathbf{v}$ , see Section 4.2 and Figure 4.4, are calculated as is illustrated in the flow chart in Figure A.1. The numbers in circles in the figure refer to the steps which are explained below.

1. The unit vector directed as the line between the end points of the fibre is denoted  $\mathbf{d}$ , see Figure A.2a.  $\mathbf{d}$  is chosen so that its  $z$ -component  $\geq 0$ . The angle between  $\mathbf{d}$  and the  $xy$ -plane is  $\beta$  and the angle between the projection of  $\mathbf{d}$  on the  $xy$ -plane and the  $x$ -axis is  $\alpha$ . This gives:

$$\mathbf{d} = (\cos \beta \cos \alpha, \cos \beta \sin \alpha, \sin \beta)(\cos^2 \beta \cos^2 \alpha + \cos^2 \beta \sin^2 \alpha + \sin^2 \beta)^{-\frac{1}{2}} \quad (\text{A.1})$$

2. The vector  $\mathbf{s}$  is used as a reference axis for the angle  $\gamma$ , which defines the position of a curved fibre around its own axis, see Figure A.2a.  $\mathbf{s}$  is chosen to be the unit vector that is perpendicular to  $\mathbf{d}$  and whose projection onto the  $xy$ -plane is parallel to and directed along the  $x$ -axis. We use the fact that the scalar product of two perpendicular vectors is equal to zero, (A.2), and that the projection of  $\mathbf{s}$  onto the  $xy$ -plane, (A.3), must have a component in the  $y$ -direction that is equal to zero.

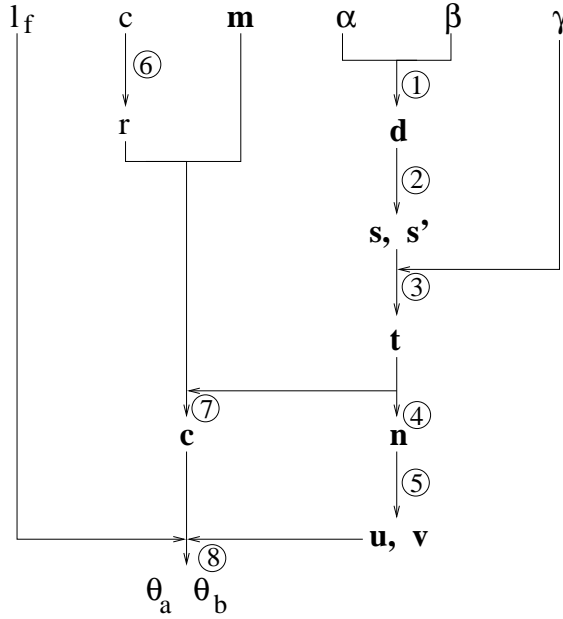


Figure A.1: Flow chart showing the calculation of fibre parameters.

That is:

$$\mathbf{d} \cdot \mathbf{s} = 0 \quad , \quad (\text{A.2})$$

$$\mathbf{s} - \mathbf{s} \cdot (0, 0, 1)(0, 0, 1) \text{ must be of the form } (a, 0, 0), a \text{ arbitrary} \quad . \quad (\text{A.3})$$

This yields

$$\mathbf{s} = (d_z, 0, -d_x) \frac{1}{\sqrt{d_x^2 + d_z^2}} \quad , \quad (\text{A.4})$$

where  $d_x$  and  $d_z$  denote the first and third components of  $\mathbf{d}$ . For the special case of  $\mathbf{d}$  in the  $xy$ -plane  $\mathbf{s}$  is chosen to be the unit vector in the  $xy$ -plane which is perpendicular to  $\mathbf{d}$  and has a positive  $x$ -component.

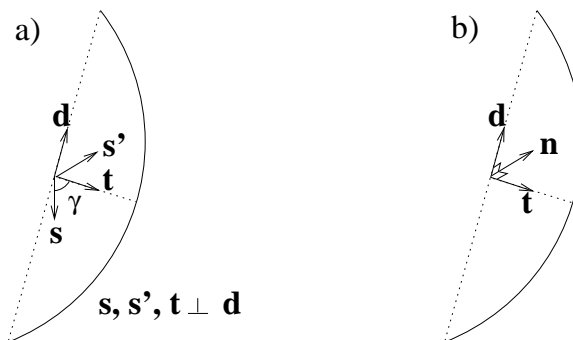
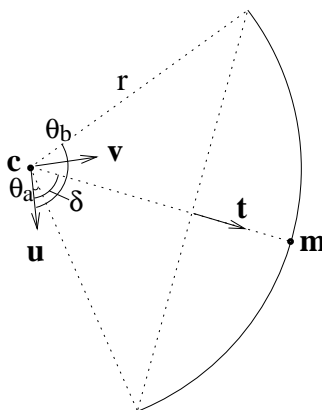
$$\mathbf{s} = (d_y, -d_x, 0), \text{ if } s_x < 0 \text{ then } \mathbf{s} = (-d_y, d_x, 0) \quad . \quad (\text{A.5})$$

$\mathbf{s}'$  is the vector that makes  $(\mathbf{d}, \mathbf{s}, \mathbf{s}')$  an ortho-normal base. The definition of the vector product yields

$$\mathbf{s}' = \mathbf{d} \times \mathbf{s} \quad . \quad (\text{A.6})$$

**3.**  $\mathbf{t}$  is the unit vector that is perpendicular to  $\mathbf{d}$  and points from the line between the fibre end points to the fibre. The position of the fibre, and thus the direction of  $\mathbf{t}$ , is given by the angle  $\gamma$ , see Figure A.2a.

$$\mathbf{t} = \cos \gamma \mathbf{s} + \sin \gamma \mathbf{s}' \quad (\text{A.7})$$

Figure A.2: *Illustrations of notations used in steps 1-4.*Figure A.3: *Illustration of notations used in steps 5-8.*

4.  $\mathbf{n}$  is the unit normal vector to the plane of the fibre, which has  $z$ -component  $n_z > 0$ , see Figure A.2b. Since both  $\mathbf{d}$  and  $\mathbf{t}$  are in the plane of the fibre, the vector product is used to obtain  $\mathbf{n}$  which is perpendicular to both of them.

$$\mathbf{n} = \mathbf{d} \times \mathbf{t}, \text{ if } n_z < 0 \text{ then } \mathbf{n} = -\mathbf{n} . \quad (\text{A.8})$$

5.  $\mathbf{u}$  and  $\mathbf{v}$  are perpendicular unit vectors in the plane of the fibre, see Figure A.3.  $\mathbf{u}$  is chosen so that its projection onto the  $xy$ -plane is parallel to the  $x$ -axis. In analogy with step 2 we have

$$\mathbf{n} \cdot \mathbf{u} = 0 , \quad (\text{A.9})$$

$$\mathbf{u} - \mathbf{u} \cdot (0, 0, 1)(0, 0, 1) \text{ must be of the form } (a, 0, 0), a \text{ arbitrary} . \quad (\text{A.10})$$

This yields

$$\mathbf{u} = (n_z, 0, -n_x) \frac{1}{\sqrt{n_x^2 + n_z^2}} , \quad (\text{A.11})$$

where  $n_x$  and  $n_z$  denote the first and third components of  $\mathbf{n}$ . For the special case of  $\mathbf{n}$  in the  $xy$ -plane  $\mathbf{u}$  is chosen to be

$$\mathbf{u} = (n_2, -n_1, 0), \text{ if } u_x < 0 \text{ then } \mathbf{u} = (-n_2, n_1, 0) . \quad (\text{A.12})$$

$\mathbf{v}$  is the vector that makes  $(\mathbf{n}, \mathbf{u}, \mathbf{v})$  an on-base. The definition of the vector product yields

$$\mathbf{v} = \mathbf{n} \times \mathbf{u} . \quad (\text{A.13})$$

6. The curvature of the fibre is obtained from (3.5) by means of tabulated corresponding values of  $c$  and  $\kappa$ . The radius of curvature of the fibre is denoted  $r$ , and is simply obtained by inversion of the curvature,  $\kappa$ .

$$r = \frac{1}{\kappa} \quad (\text{A.14})$$

7.  $\mathbf{c}$  is the centre point of the circle of which the fibre is a part. From Figure A.3 we can see that

$$\mathbf{c} = \mathbf{m} - t\mathbf{r} . \quad (\text{A.15})$$

8.  $\theta_a$  and  $\theta_b$  are the angles relative to  $\mathbf{u}$  at the beginning and end of the fibre, see Figure A.3. The fibre is defined by a counter-clockwise rotation from  $\theta_a$  to  $\theta_b$ . The total sector angle of the fibre is

$$\alpha_{tot} = \frac{l_f}{r} . \quad (\text{A.16})$$

From the definition of scalar product we can calculate  $\delta$ , which denotes the angle from  $\mathbf{u}$  to the radius from  $\mathbf{c}$  to  $\mathbf{m}$ ,

$$\delta = \arccos(\mathbf{t} \cdot \mathbf{u}) . \quad (\text{A.17})$$

This finally gives

$$\theta_a = \delta - \frac{\alpha_{tot}}{2} , \quad (\text{A.18})$$

$$\theta_b = \delta + \frac{\alpha_{tot}}{2} . \quad (\text{A.19})$$

An arbitrary point on the fibre can now be denoted  $\mathbf{x}$  and obtained from

$$\mathbf{x} = \mathbf{c} + r \cos \theta \cdot \mathbf{u} + r \sin \theta \cdot \mathbf{v}, \quad \theta_a \leq \theta \leq \theta_b . \quad (\text{A.20})$$

## B. ANALYSIS OF CONNECTEDNESS OF NETWORKS

The first thing that must be established is what is meant by a connected network. When studying a global network, made up of many cells, a network is considered to be connected if it is of such geometry that it can sustain a load in an arbitrary direction. For the individual cell this implies that there must be a locally connected structure within the cell, which is connected with itself across the left-right, back-front and up-down boundaries. Figure B.1 shows some schematic examples of connected and unconnected 2D networks. Note in particular example three, which represents a cell structure which is not connected with itself although it is locally connected and linked to all cell boundaries.

The criterion described above is a sufficient condition for connectedness of a network, but it is not necessary. This can be seen in Figure B.2, which shows a network that is connected, but still does not satisfy the criterion stated above. The implementation applies the criterion above, and should a network of the type shown in Figure B.2 occur, it is thus falsely classified as not connected.

Graph theory, cf. [8], is used to determine whether a network satisfies the criterion described above or not. The network is viewed as a graph, with beam elements as edges which connect nodes (inter-fibre bonds or points on the boundary). A graph can be described by an incidence matrix, in which a 1 in position  $(i, j)$  means ‘connection between nodes  $i$  and  $j$ ’, that is ‘a beam element between bonds  $i$  and  $j$ ’, and a 0 denotes no connection. The first step is to sort the graph into connected graphs. A connected graph is a graph in which there is a path between every pair of nodes. This is done as follows: Choose an arbitrary node. Incorporate into this node all nodes that have paths to it. Choose a new starting node, which has not previously been classified as a member of a connected graph, and incorporate all nodes that have paths to it. Repeat this until every node is part of a connected graph. In the implementation this is done by means of manipulations in the incidence matrix.

We now have a number of connected graphs. The next step is to go through these and check if any of them satisfies the conditions stated above. If there is a bond at every fibre crossing there can only be one connected graph that satisfies the conditions in 2D networks. In a 3D network, as well as in a 2D network where there is not a bond at every crossing there is a theoretical possibility that there may be two or more independent connected structures. This possibility is not taken into account in the implementation. If a connected graph is found, which is also connected with itself across the borders, it must be completed with possible parts

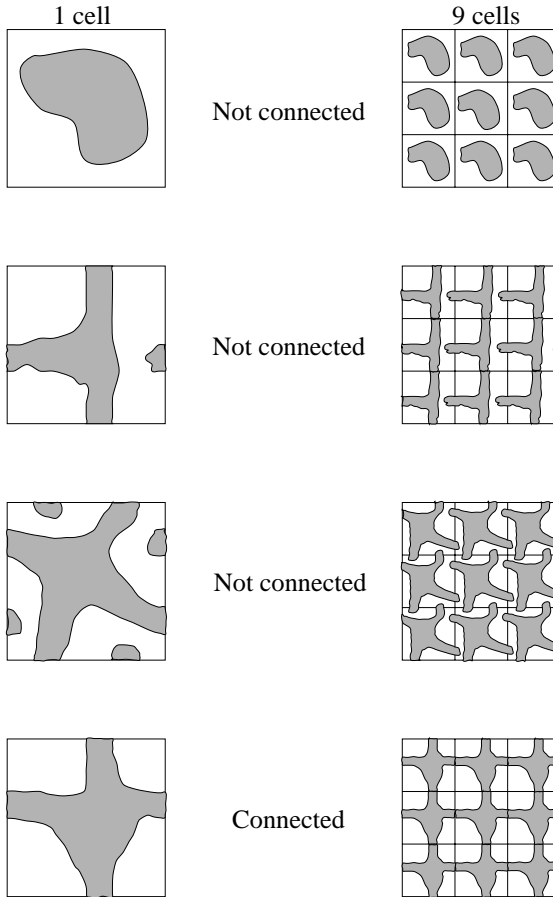


Figure B.1: *Examples of connected and unconnected 2D networks.*

that it is connected to across borders, but not inside the cell. The rest of the connected graphs, if any, are ‘islands’, i.e. clusters of fibres with no contact with the rest of the global network. Those are removed and thus disregarded in the mechanical analysis.

Clusters of fibres that are attached to the rest of the network by only one fibre are detected as follows. For every beam element: Remove the beam element and go through the procedure described above. If there are now two connected graphs, the one that does not satisfy the conditions in the beginning is a ‘peninsula’.

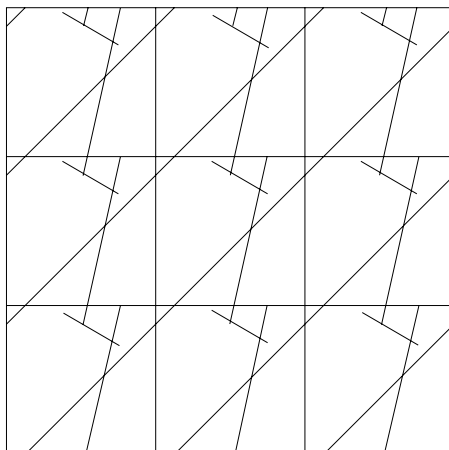


Figure B.2: *A connected network which is difficult to detect.*



## C. EFFECTIVE BENDING STIFFNESS OF A SPIRAL BEAM

Assume a spiral beam with moments of inertia  $I_{x'}$  and  $I_{y'}$  around its principal axes, which completes one revolution in a distance  $l$ . We want to know the moments of inertia of the non-spiral beam which yield the same angle change  $\Delta\phi_x = u'(l) - u'(0)$  when subjected to moment  $m_x$ , as in Figure C.1.

The bending stiffness of a spiral beam varies along the  $z$ -axis. Therefore, we start by computing the change in  $\phi_x$  per unit length as a function of  $z$  for a spiral beam segment of length  $l$  subjected to moment  $m_x$ . We begin by considering the change

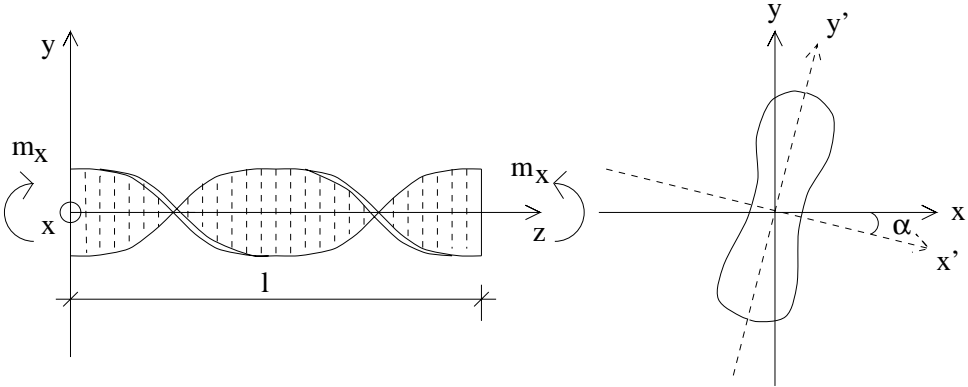


Figure C.1: *Spiral beam segment and cross section.*

in angle per unit length around the principal axes of the beam cross section,  $x'$ ,  $y'$ , which are rotated an angle  $\alpha$  relative to the nominal  $x$ - and  $y$ -axes.

$$\frac{d\phi_{x'}}{dz} = \frac{m_x \cos \alpha}{EI_{x'}} \quad \frac{d\phi_{y'}}{dz} = \frac{m_x \sin \alpha}{EI_{y'}} \quad (\text{C.1})$$

From this we can calculate the change in angle per unit length around the  $x$ -axis.

$$\frac{d\phi_x}{dz} = \frac{m_x}{E} \left( \frac{\cos^2 \alpha}{I_{x'}} + \frac{\sin^2 \alpha}{I_{y'}} \right) \quad (\text{C.2})$$

To obtain the total change in angle we integrate over the revolution length,  $l$ .

$$\Delta\phi_x = \int_0^l \frac{d\phi_x}{dz} dz = \frac{m_x}{E} \int_0^l \left( \frac{\cos^2 \alpha}{I_{x'}} + \frac{\sin^2 \alpha}{I_{y'}} \right) dz \quad (\text{C.3})$$

Since

$$\alpha = \frac{z}{l} 2\pi \quad (\text{C.4})$$

and

$$dz = \frac{l}{2\pi} d\alpha, \quad (\text{C.5})$$

(C.3) gives

$$\Delta\phi_x = \frac{m_x l}{2\pi E} \int_0^{2\pi} \left( \frac{\cos^2 \alpha}{I_{x'}} + \frac{\sin^2 \alpha}{I_{y'}} \right) d\alpha = \frac{m_x l}{2\pi E} \left( \frac{\pi}{I_{x'}} + \frac{\pi}{I_{y'}} \right) = \frac{m_x l}{2E} \left( \frac{1}{I_{x'}} + \frac{1}{I_{y'}} \right). \quad (\text{C.6})$$

For a non-spiral cross section with moment of inertia  $I_e$  around the  $x$ -axis, the change in angle along the length  $l$  when subjected to the moment  $m_x$  is:

$$\Delta\phi_x = \frac{m_x l}{EI_e} \quad (\text{C.7})$$

By setting  $\Delta\phi_x$  for spiral and non-spiral beams equal, and solving for  $I_e$  we obtain

$$I_e = \frac{m_x l}{E \frac{m_x l}{2E} \left( \frac{1}{I_{x'}} + \frac{1}{I_{y'}} \right)} = \frac{2I_{x'} I_{y'}}{I_{x'} + I_{y'}}. \quad (\text{C.8})$$

For a rectangular cross section of width  $b$  and depth  $h$  this yields

$$I_e = \frac{2 \frac{bh^3}{12} \frac{b^3 h}{12}}{\frac{bh^3}{12} + \frac{b^3 h}{12}} = \frac{b^3 h^3}{6(b^2 + h^2)}. \quad (\text{C.9})$$

## D. TRANSFORMATION OF THE $\mathbf{D}$ MATRIX

The transformation of the constitutive matrix  $\mathbf{D}$  when the coordinate system is rotated is derived using the transformation relations of second order tensors. We have two coordinate systems  $\mathbf{x} = (x_1, x_2, x_3)$  and  $\mathbf{x}' = (x'_1, x'_2, x'_3)$ . When  $\mathbf{x}$  is rotated into  $\mathbf{x}'$  a second-order tensor  $T_{pq}$  is transformed as, [35]:

$$T'_{ij} = a_i^p a_j^q T_{pq} \quad (\text{D.1})$$

where  $a_k^r = \cos(x'_k; x_r)$ . The inverse relation is

$$T_{pq} = a_i^p a_j^q T'_{ij} . \quad (\text{D.2})$$

The nine components of  $a_k^r$  for the cases of rotation  $\alpha_1$  about the  $x_1$ -axis,  $\alpha_2$  about the  $x_2$ -axis and  $\alpha_3$  about the  $x_3$ -axis, can be identified from Figure D.1 to have the values given in Table D.1.

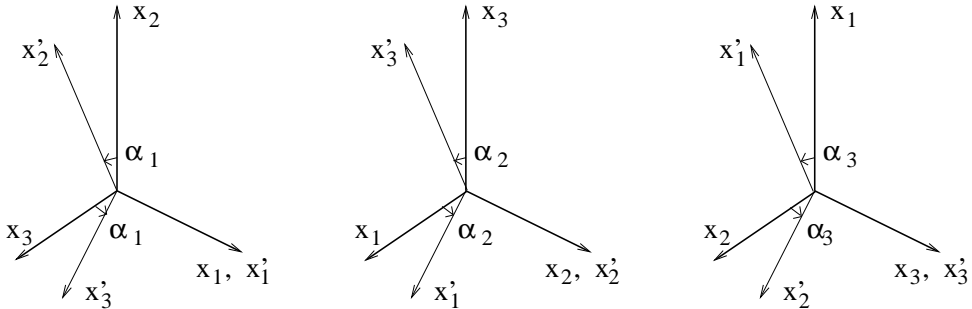


Figure D.1: Rotations about the  $x_1$ -,  $x_2$ - and  $x_3$ -axes.

From (D.1) and Table D.1 the transformation relation for tensorial strain for rotation about the  $x_1$ -axis can be calculated. Denoting  $\sin \alpha_1$  by  $s$  and  $\cos \alpha_1$  by  $c$  this yields in matrix form:

Table D.1: Components of  $a_k^r$  for rotations about the  $x_1$ -,  $x_2$ - and  $x_3$ -axes.

$a_k^r$	$\alpha_1$	$\alpha_2$	$\alpha_3$
$a_1^1$	1	$\cos \alpha_2$	$\cos \alpha_3$
$a_2^1$	0	0	$-\sin \alpha_3$
$a_3^1$	0	$\sin \alpha_2$	0
$a_1^2$	0	0	$\sin \alpha_3$
$a_2^2$	$\cos \alpha_1$	1	$\cos \alpha_3$
$a_3^2$	$-\sin \alpha_1$	0	0
$a_1^3$	0	$-\sin \alpha_2$	0
$a_2^3$	$\sin \alpha_1$	0	0
$a_3^3$	$\cos \alpha_1$	$\cos \alpha_2$	1

$$\begin{bmatrix} \epsilon'_{11} \\ \epsilon'_{22} \\ \epsilon'_{33} \\ \epsilon'_{12} \\ \epsilon'_{13} \\ \epsilon'_{23} \\ \epsilon'_{21} \\ \epsilon'_{31} \\ \epsilon'_{32} \end{bmatrix} = \begin{bmatrix} 1 & 0 & 0 & 0 & 0 & 0 & 0 & 0 & 0 \\ 0 & c^2 & s^2 & 0 & 0 & sc & 0 & 0 & sc \\ 0 & s^2 & c^2 & 0 & 0 & -sc & 0 & 0 & -sc \\ 0 & 0 & 0 & c & s & 0 & 0 & 0 & 0 \\ 0 & 0 & 0 & -s & c & 0 & 0 & 0 & 0 \\ 0 & -sc & sc & 0 & 0 & c^2 & 0 & 0 & -s^2 \\ 0 & 0 & 0 & 0 & 0 & 0 & c & s & 0 \\ 0 & 0 & 0 & 0 & 0 & 0 & -s & c & 0 \\ 0 & -sc & sc & 0 & 0 & -s^2 & 0 & 0 & c^2 \end{bmatrix} \begin{bmatrix} \epsilon_{11} \\ \epsilon_{22} \\ \epsilon_{33} \\ \epsilon_{12} \\ \epsilon_{13} \\ \epsilon_{23} \\ \epsilon_{21} \\ \epsilon_{31} \\ \epsilon_{32} \end{bmatrix} \quad (\text{D.3})$$

The corresponding relation for the engineering strain,  $\epsilon$ , can be obtained by use of the symmetry of  $\epsilon$  and the fact that  $\gamma_{xy} = \epsilon_{12} + \epsilon_{21}$ ,  $\gamma_{xz} = \epsilon_{13} + \epsilon_{31}$  and  $\gamma_{yz} = \epsilon_{23} + \epsilon_{32}$ .

$$\begin{bmatrix} \epsilon'_x \\ \epsilon'_y \\ \epsilon'_z \\ \gamma'_{xy} \\ \gamma'_{xz} \\ \gamma'_{yz} \end{bmatrix} = \begin{bmatrix} 1 & 0 & 0 & 0 & 0 & 0 \\ 0 & c^2 & s^2 & 0 & 0 & sc \\ 0 & s^2 & c^2 & 0 & 0 & -sc \\ 0 & 0 & 0 & c & s & 0 \\ 0 & 0 & 0 & -s & c & 0 \\ 0 & -2sc & 2sc & 0 & 0 & c^2 - s^2 \end{bmatrix} \begin{bmatrix} \epsilon_x \\ \epsilon_y \\ \epsilon_z \\ \gamma_{xy} \\ \gamma_{xz} \\ \gamma_{yz} \end{bmatrix} \quad (\text{D.4})$$

The transformation relation for tensorial stress is equivalent to (D.3), and the corresponding relation for the engineering stress  $\sigma$  is obtained by use of the symmetry of  $\sigma$ :

$$\begin{bmatrix} \sigma'_x \\ \sigma'_y \\ \sigma'_z \\ \sigma'_{xy} \\ \sigma'_{xz} \\ \sigma'_{yz} \end{bmatrix} = \begin{bmatrix} 1 & 0 & 0 & 0 & 0 & 0 \\ 0 & c^2 & s^2 & 0 & 0 & 2sc \\ 0 & s^2 & c^2 & 0 & 0 & -2sc \\ 0 & 0 & 0 & c & s & 0 \\ 0 & 0 & 0 & -s & c & 0 \\ 0 & -sc & sc & 0 & 0 & c^2 - s^2 \end{bmatrix} \begin{bmatrix} \sigma_x \\ \sigma_y \\ \sigma_z \\ \sigma_{xy} \\ \sigma_{xz} \\ \sigma_{yz} \end{bmatrix} \quad (\text{D.5})$$

(D.4) is written in the form:

$$\boldsymbol{\epsilon}' = \mathbf{T}(\alpha_1)\boldsymbol{\epsilon} \quad (\text{D.6})$$

The inverse relation is

$$\boldsymbol{\epsilon} = \mathbf{T}(-\alpha_1)\boldsymbol{\epsilon}' . \quad (\text{D.7})$$

From (D.4) and (D.5) it can be seen that the corresponding relations for  $\boldsymbol{\sigma}$  are

$$\boldsymbol{\sigma}' = \mathbf{T}^T(-\alpha_1)\boldsymbol{\sigma} \quad (\text{D.8})$$

and

$$\boldsymbol{\sigma} = \mathbf{T}^T(\alpha_1)\boldsymbol{\sigma}' . \quad (\text{D.9})$$

Using (D.8), (6.1) and (D.7) gives:

$$\boldsymbol{\sigma}' = \mathbf{T}^T(-\alpha_1)\boldsymbol{\sigma} = \mathbf{T}^T(-\alpha_1)\mathbf{D}\boldsymbol{\epsilon} = \mathbf{T}^T(-\alpha_1)\mathbf{D}\mathbf{T}(-\alpha_1)\boldsymbol{\epsilon}' = \mathbf{D}'\boldsymbol{\epsilon}' . \quad (\text{D.10})$$

That is,

$$\mathbf{D}' = \mathbf{T}^T(-\alpha_1)\mathbf{D}\mathbf{T}(-\alpha_1) , \quad (\text{D.11})$$

or with the notation of Section 6.6,

$$\mathbf{D}' = \mathbf{T}_1(\alpha_x)\mathbf{D}\mathbf{T}_1^T(\alpha_x) \quad (\text{D.12})$$

with

$$\mathbf{T}_1(\alpha_x) = \begin{bmatrix} 1 & 0 & 0 & 0 & 0 & 0 \\ 0 & c^2 & s^2 & 0 & 0 & 2sc \\ 0 & s^2 & c^2 & 0 & 0 & -2sc \\ 0 & 0 & 0 & c & s & 0 \\ 0 & 0 & 0 & -s & c & 0 \\ 0 & -sc & sc & 0 & 0 & c^2 - s^2 \end{bmatrix} . \quad (\text{D.13})$$

The transformation matrices  $\mathbf{T}_2$  and  $\mathbf{T}_3$  for rotation about the  $x_2$ - and  $x_3$ -axes are obtained analogously from (D.1) and Table D.1.

$$\mathbf{T}_2(\alpha_y) = \begin{bmatrix} c^2 & 0 & s^2 & 0 & -2sc & 0 \\ 0 & 1 & 0 & 0 & 0 & 0 \\ s^2 & 0 & c^2 & 0 & 2sc & 0 \\ 0 & 0 & 0 & c & 0 & -s \\ sc & 0 & -sc & 0 & c^2 - s^2 & 0 \\ 0 & 0 & 0 & s & 0 & c \end{bmatrix} \quad (\text{D.14})$$

and

$$\mathbf{T}_3(\alpha_z) = \begin{bmatrix} c^2 & s^2 & 0 & 2sc & 0 & 0 \\ s^2 & c^2 & 0 & -2sc & 0 & 0 \\ 0 & 0 & 1 & 0 & 0 & 0 \\ -sc & sc & 0 & c^2 - s^2 & 0 & 0 \\ 0 & 0 & 0 & 0 & c & s \\ 0 & 0 & 0 & 0 & -s & c \end{bmatrix}, \quad (\text{D.15})$$

$s$  and  $c$  now denoting the sine and cosine of  $\alpha_y$  and  $\alpha_z$ .

## REFERENCES

- [1] Andersson, S.R. and Rasmuson A. *Dry and Wet Friction of Single Pulp and Synthetic Fibres*. Journal of Pulp and Paper Science, 23(1) pp. J5-J11, 1997.
- [2] Åström, J.A. and Niskanen, K.J. *Simulation of network fracture*. Proceedings of the 1991 International Paper Physics Conference, TAPPI, 1991.
- [3] Åström, J.A. and Niskanen, K.J. *Symmetry-Breaking Fracture in Random Fibre Networks*. Europhys. Lett., 21(5), pp. 557-562, 1993.
- [4] Åström, J.A., Saarinen, S., Niskanen, K.J. and Kurkijrvi, J. *Microscopic mechanics of fibre networks*. J. Appl. Phys. 75(5), pp. 2383-2392, 1994.
- [5] Baum, G.A. *Elastic Properties of paper*. In: Design Criteria for Paper Performance, STFI-meddelande A 969, 1987.
- [6] Berg, A. and Svensson, U. *Computer simulations and analysis of fracture performance in a heterogeneous material structure*. M.Sc. diploma work, Report TVSM-5050, Lund University, Division of Structural Mechanics, Lund, Sweden, 1991. (In Swedish).
- [7] Blom, G. *Statistikteori med tillämpningar*. Studentlitteratur, Lund, Sweden, 1984. (In Swedish).
- [8] Böiers, L-C. *Föreläsningar i grafteori*. Matematiska Institutionen, Lund University, Lund, Sweden, 1991. (In Swedish).
- [9] *CALFEM - A finite element toolbox to MATLAB, Version 3.2*. Lund University, Division of Structural Mechanics and Department of Solid Mechanics, Lund, Sweden, 1995.
- [10] Campbell, J.G. *Structural interpretation of paper elasticity*. Appita, 16(5) pp. 130-137, 1963.
- [11] Cox, H.L. *The elasticity and strength of paper and other fibrous materials*. British Journal of Applied Physics, Vol. 3, pp. 72-79, 1952.
- [12] Deng, M. and Dodson, C.T.J. *Paper: An engineered stochastic structure*. Tappi Press, Atlanta, USA, 1994.
- [13] Department of building materials *Kompendium i byggnadsmateriallära FK*. Lund University, Lund, Sweden, 1986. (In Swedish).

- [14] Feldman, H., Jayaraman, K. and Kortschot, M.T. *A Monte Carlo Simulation of Paper Deformation and Failure*. Journal of Pulp and Paper Science, 22(10) pp. J386-J392, 1996.
- [15] *Formelsamling i hållfasthetslära*. Royal Inst. of Technology, Department of Solid Mechanics, Stockholm, Sweden, 1986. (In Swedish).
- [16] Gustafsson, P.J. *Fracture Mechanics Studies of Non-Yielding Materials such as Concrete*. Report TVBM-1007, Ph.D. thesis, Lund University, Division of Building Materials, Lund, Sweden, 1985.
- [17] Gustafsson, R. *Dynamic analysis of networks: Estimation of stiffness of paper from wave propagation velocity*. M.Sc diploma work, Report TVSM-5064, Lund University, Division of Structural Mechanics, Lund, Sweden, 1996. (In Swedish).
- [18] Hahn, H.T. *A Derivation of Invariants of Fourth Rank Tensors*. J. Composite Materials, Vol. 8, pp. 2-14, 1974.
- [19] Hamlen, R.C. *Paper structure, mechanics, and permeability: Computer-aided modeling*. Ph.D. thesis, University of Minnesota, USA, 1991.
- [20] Heyden, S. *A network model applied to cellulose fibre materials*. Licentiate thesis, Report TVSM-3018, Lund University, Division of Structural Mechanics, Lund, Sweden, 1996.
- [21] Heyden, S. and Gustafsson P.J. *Simulation of Fracture in a Cellulose Fibre Network*. Journal of Pulp and Paper Science, 24(5) pp. 160-165, 1998.
- [22] Jangmalm, A. *Network modelling of the elastic properties of paper*. Licentiate thesis, Dep. of Solid Mechanics, Royal Institute of Technology, Stockholm, Sweden, 1996.
- [23] Kallmes, O. and Corte, H. *The structure of paper, I. The Statistical Geometry of an Ideal Two Dimensional Fiber Network*. Tappi, Vol. 43, pp. 737-752, 1960.
- [24] Kallmes, O.J., Stockel, I.H. and Bernier, G.A. *The Elastic Behaviour of Paper*. Pulp Pap. Mag. Can. 64(10) pp. T449-T456, 1963.
- [25] Kallmes, O.J. and Perez, M. *A new theory for the load/elongation properties of paper*. In: Trans. Brit. Paper and Board Makers' Assoc. Sympos. Consol. Paper Web, pp. 779-800, Cambridge, 1965.
- [26] Kallmes, O., Bernier, G. and Perez, M. *A mechanistic theory of the load-elongation properties of paper: Parts 1-4*. Pap. Technol. Ind. 18(7) pp. 222-228; (8) pp. 243-245; (9) pp. 283-285; (10) pp. 328-331, 1977.
- [27] Kärenlampi, P. *Effect of Distributions of Fibre Properties on Tensile Strength of Paper: A Closed-Form Theory*. Journal of Pulp and Paper Science, 21(4) pp. J138-J143, 1995.

- [28] Kärenlampi, P. *Tensile Strength of Paper: A Simulation Study*. Journal of Pulp and Paper Science, 21(6) pp. J209-J214, 1995.
- [29] Kollmann, F.F.P. and Cote, W.A. *Principles of Wood Science and Technology, I, Solid Wood*. Springer-Verlag, Berlin, 1968.
- [30] Kolseth, P. and de Ruvo, A. *An Attempt to Measure the Torsional Strength of Single Wood Pulp Fibers*. In: General Constitutive Relations fo Wood and Wood-Based Materials. Report of Workshop sponsored by The National Science Foundation; Engineering Mechanics Section; Solid Mechanics Program, pp. 57-74, 1978.
- [31] Komori, T. and Makishima, K. *Numbers of Fiber-to-Fiber Contacts in General Fiber Assemblies*. Textile Research Journal, Vol. 47, pp. 13-17, 1977.
- [32] Krenk, S. *A General Format for Curved and Non-Homogeneous Beam Elements*. Computers & Structures, 50(4), pp. 449-454, 1994.
- [33] Lindemann, J. and Dahlblom, O. *FibreScope - A real-time fibre network post processor*. Lund University, Division of Structural Mechanics, Lund, Sweden. (Under development.)
- [34] Lucisano, M. *Forming of Quasirandom Laboratory Paper Sheets*. M.Sc. diploma work, Dep. of Pulp and Paper Technology, Royal Institute of Technology, Stockholm, Sweden 1998.
- [35] Malvern, L.E. *Introduction to the mechanics of a continuous medium*. Prentice-Hall, Englewood Cliffs, New Jersey, 1969.
- [36] *Maple V*. Waterloo Maple inc., Canada.
- [37] *MATLAB - The language of technical computing*. The Math Works Inc, Natick, Ma, USA, 1998.
- [38] *MATLAB Compiler*, The Math Works Inc, Natick, Ma, USA, 1998.
- [39] Nilsen, N. and Niskanen, K. *A 3D simulation for paper structure*. In: Progress in Paper physics -A Seminar, STFI, Stockholm, Sweden, 1996.
- [40] Niskanen, K.J. *Strength and fracture of paper*. KCL Paper Science Centre, Finland, 1993.
- [41] Oden, J.T. and Ripperger, E.A. *Mechanics of elastic structures*. McGraw-Hill, 1981.
- [42] Olsson, P. *Visualisation of deformation and fracture in a fibre network*. M.Sc. diploma work, Report TVSM-5086, Lund University, Division of Sructural Mechanics, Lund, Sweden, 1999. (In Swedish).

- [43] Ottosen, N.S. and Petersson, H. *Introduction to the finite element method*. Prentice-Hall, U.K., 1992.
- [44] Page, D.H. *A Theory for the Tensile Strength of Paper*. Tappi 52(4), pp. 674-681, 1969.
- [45] Page, D.H., Seth, R.S. and De Grace, J.H. *The elastic modulus of paper: Parts 1-3*. Tappi 62(9), pp. 99-102 (1979); 63(6) pp. 113-116 (1980); 63(10) pp. 99-102, 1980.
- [46] Perkins, R.W. and Mark, R.E. *On the structural theory of the elastic behavior of paper*. Tappi 59(12), pp. 118-120, 1976.
- [47] Persson, K. *Material model for paper, experimental and theoretical aspects*. M.Sc. diploma work, Lund University, Division of Solid Mechanics, Lund, Sweden, 1991.
- [48] Popov, E.P. *Mechanics of materials*. Prentice-Hall, Englewood Cliffs, New Jersey, 1978.
- [49] Qi, D. *Microstructural model for a three-dimensional fiber network*. Tappi 80(1), pp. 283-292, 1997.
- [50] Qi, D. *Three-dimensional generalized anisotropic Cox-type structural model of a fiber network*. Tappi 80(11), pp. 165-171, 1997.
- [51] Räsänen, V.I., Alava, M.J., Nieminen, R.M. and Niskanen, K.J. *Elastic-plastic behaviour in fibre networks*. Nordic Pulp and Paper Research Journal 11(4), pp. 243-248, 1996.
- [52] Räsänen, V.I., Heyden, S., Gustafsson, P.J., Alava, M.J. and Niskanen, K.J. *Simulation of the effect of a reinforcement fiber on network mechanics*. Nordic Pulp and Paper Research Journal 12(3), pp.162-166, 1997.
- [53] Ramasubramanian, M.K. and Perkins, R.W. *Computer Simulation of the Uniaxial Elastic-Plastic Behaviour of Paper*. Journal of Engineering Materials and Technology, Vol. 110, pp. 117-123, 1988.
- [54] Rigdahl, M., Westerlind, B. and Hollmark, H. *Analysis of cellulose networks by the finite element method*. Journal of Materials Science, Vol. 19, pp 3945-3952, 1984.
- [55] Salomonsson, A. *A model for dry-shaped cellulose fibre materials*. M.Sc. diploma work, Report TVSM-5051, Lund University, Division of Structural Mechanics, Lund, Sweden, 1992. (In Swedish).
- [56] SCA Research, Sundsvall, Sweden.

- [57] Stahl, D.C. and Cramer, S.M. *A Three-Dimensional Network Model for a Low Density Fibrous Composite*. J. Engineering Materials and Technology, Vol. 120, pp. 126-130, 1998.
- [58] Thomsson, L. *Simulering av formfaktorns inverkan på de elastiska konstanterna hos fibernätverk av cellulosa*. M.Sc. diploma work, Dep. of Solid Mechanics, Royal Institute of Technology, Stockholm, Sweden 1995. (In Swedish).
- [59] Toll, S. and Månson, J.-A. E. *Elastic Compression of a Fiber Network*. Journal of Applied Mechanics, Vol. 62, pp. 223-226, 1995.
- [60] Tryding, J. *In-Plane Fracture in Paper*. Ph.D. thesis, Report TVSM-1008, Lund University, Division of Structural Mechanics, Lund, Sweden, 1996.
- [61] Van den Akker, J.A. *Some theoretical considerations on the mechanical properties of fibrous structures*. In: Trans. Brit. Paper and Board Makers' Assoc. Sympos. Consol. Paper Web, pp. 205-241, London, 1962.
- [62] [www.ktx.com](http://www.ktx.com)
- [63] [www.VRML.org](http://www.VRML.org)
- [64] Yang, C-F. *Plane modeling and analysis of fiber system*. Ph.D. thesis, University of Washington, USA 1975.
- [65] Zienkiewicz, O.C. and Taylor, R.L. *The finite element method, fourth edition, Vol.1*. McGraw-Hill, London 1989.